



UNIVERSITAT  
POLITÈCNICA  
DE VALÈNCIA



DEPARTAMENTO  
DE INGENIERÍA  
ELECTRÓNICA

---

# Control of electromagnetic energy by metamaterials

---

THESIS FOR THE DEGREE OF DOCTOR OF  
PHILOSOPHY

Ana Díaz Rubio

Academic advisors:

Jose Sánchez-Dehesa Moreno-Cid

Jorge Carbonell

July 2, 2015



RESUMEN DE LA TESIS DOCTORAL

# Control de energía electromagnética mediante metamateriales

por

**Ana Díaz Rubio**

Doctor Ingeniero de Telecomunicación por el Departamento de Ingeniería  
Electrónica

Universidad Politécnica de Valencia, Valencia, Julio 2015

Los metamateriales son estructuras periódicas cuyas celdas unidad son muy pequeñas en comparación con la longitud de onda a la frecuencia de trabajo. Bajo estas condiciones, estos materiales artificiales pueden considerarse como medios homogéneos cuyos parámetros constitutivos dependen de las características de las celdas unidad que los componen. La aparición de los metamateriales abrió un nuevo campo de investigación que ha generado multitud de trabajos en las líneas de microondas, óptica y acústica.

En este contexto, el objetivo principal de esta tesis es el estudio de nuevas estructuras basadas en metamateriales que permitan el control de la energía electromagnética. En particular, plantea nuevas soluciones para problemas de localización y absorción de ondas electromagnéticas. La tesis ha sido desarrollada en el Grupo de Fenómenos Ondulatorios de la Universidad Politécnica de Valencia y en colaboración con el Grupo de Metamateriales Acústicos y Electromagnéticos de la Universidad de Exeter.

Los problemas estudiados en la primera parte de esta tesis son la concentración de energía para su posterior absorción, la transferencia inalámbrica de potencia y nuevos sistemas capaces de ser empleados como sensores de posición. Para la solución de estos problemas se emplean un nuevo tipo de estructuras cilíndricas, multicapa y anisótropas conocidas como Cristales Fotónicos Radiales. La dependencia radial de los parámetros constitutivos de los materiales que componen cada una de sus capas genera, en estas estructuras, un comportamiento similar al de los cristales fotónicos unidimensionales. Entre los resultados obtenidos con estas estructuras, cabe destacar la primera demostración experimental de un resonador basado en Cristales

Fotónicos Radiales.

La absorción de ondas electromagnéticas por capas delgadas de materiales con pérdidas es el segundo tema tratado en esta tesis. El objetivo principal es el estudio teórico y experimental del aumento de la absorción en capas delgadas mediante el uso de estructuras periódicas bidimensionales, también llamadas metasuperficies. En concreto, se han estudiado los efectos de una red cuadrada de cavidades coaxiales sobre la que se coloca una capa delgada de un material con pérdidas. Como resultado, se consigue un aumento de la absorción que permite obtener picos de absorción total. El estudio semi-analítico de esta estructura ha permitido obtener expresiones que controlan la posición del pico de absorción y su amplitud; las cuales han permitido desarrollar una metodología de diseño para sistemas de absorción total.

RESUM DE LA TESI DOCTORAL

## **Control de energía electromagnética mitjançant metamateriales**

por

**Ana Díaz Rubio**

Doctor en Ciències pel Departament de Enginyeria Electrònica  
Universidad Politécnica de València, València, Juliol 2015

Els metamateriales són estructures periòdiques en els que les cel·les unitat són molt xicotetes en comparació amb la longitud d'ona a la freqüència de treball. Tenint en consideració aquestes condicions, aquestos materials artificials poden considerar-se com a mitjans homogenis en els que els paràmetres constitutius depenen de les característiques de les cel·les unitat que els componen. A més, l'aparició dels metamateriales va obrir un nou camp d'investigació que ha generat multitud de treballs en les línies de microones, òptica i acústica.

En aquest context, l'objectiu principal d'aquesta tesi és l'estudi de noves estructures basades en metamateriales que permeten el control de l'energia electromagnètica. En particular, planteja noves solucions per a problemes de localització i absorció d'ones electromagnètiques. La tesi ha sigut realitzada en el Grup de Fenòmens Ondulatoris de la Universitat Politècnica de València i en col·laboració amb el Grup de Metamateriales Acústics i Electromagnètics de la Universitat d'Exeter.

Els problemes analitzats en la primera part de la tesi són la concentració d'energia per a la seua posterior absorció, la transferència inalàmbrica de potència i nous sistemes capacos de ser empleats com a sensors de posició. Per a la solució dels problemes identificats s'utilitza un nou tipus d'estructures cilíndriques, multicapa i anisòtropes conegudes com a Cristalls Fotònics Radials. La dependència radial dels paràmetres constitutius dels materials que componen cadascuna de les seues capes genera, en aquestes estructures, un comportament semblant al dels Cristalls Fotònics Unidimensionals. Entre els resultats obtinguts, cal destacar la primera demostració experimental d'un ressonador basat en Cristalls Fotònics Radials.

Pel que respecta a la segon part de la tesi, l'absorció d'ones electromagnètiques per capes primes de materials amb pèrdues és tema tractat. L'objectiu principal és l'estudi teòric i experimental de l'augment de l'absorció en capes primes per mitjà de l'ús d'estructures periòdiques bidimensionals, també denominades metasuperfícies. En concret, s'han examinat els efectes d'una xarxa quadrada de cavitats coaxials sobre la qual es col·loca una capa prima d'un material amb pèrdues. Com a resultat, s'aconsegueix un augment de l'absorció que permet obtindre pics d'absorció total. Així mateix, l'estudi semi-analític d'aquesta estructura ha permés obtindre expressions que controlen la posició del pic d'absorció i la seua amplitud; les quals han permés desenvolupar una metodologia de disseny per a sistemes d'absorció total.

ABSTRACT OF THE DOCTOR THESIS

# **Control of electromagnetic energy by metamaterials**

by

**Ana Díaz Rubio**

Doctor of Philosophy in the Electronic Engineering department  
Politecnia University of Valencia, Valencia, July 2015

Metamaterials are periodic structures whose unit cells are small compared to the wavelength at the operating frequency. Under these conditions, these artificial materials can be considered as homogeneous media whose constitutive parameters depend on the characteristics of the unit cells. The discovery of metamaterials opened a new research field that has produced many works with microwaves, optical waves and acoustic waves.

In this context, the main goal of this thesis is the study of new structures based on metamaterials that allow controlling of electromagnetic energy. In particular, new solutions for localization and absorption of electromagnetic waves are proposed. The thesis has been developed in the Wave Phenomena Group of the Polytechnic University of Valencia and in collaboration with the Group of Acoustic and Electromagnetic Metamaterials at the University of Exeter.

The problems studied in the first part of this thesis are energy harvesting for subsequent absorption, wireless power transfer and new systems that can be used as position sensors. To solve these problems a new type of cylindrical, multilayer and anisotropic structures known as Radial Photonic Crystals are used. The radial dependence of the constitutive parameters generates, in these structures, a behavior like a one dimensional photonic crystals. Among the results obtained with these structures, it is included the first experimental demonstration of a Radial Photonic Crystals based resonator.

Absorption of electromagnetic waves by thin layers of lossy materials is the second topic of this thesis. The main target is the theoretical and experimental study of the absorption enhancement in thin layers by using two-dimensional periodic structures, also called metasurfaces. Specifically,

we studied the effects of a square lattice of coaxial cavities covered by a thin layer of lossy material. As a result, an enhancement of the absorption peaks that can produce total absorption is achieved. The semi-analytical study of this structure has allowed obtaining expressions that control the position of the absorption peak and its amplitude; which have helped to develop a design methodology for total absorption systems.





## AGRADECIMIENTOS

En primer lugar, me gustaría dar las gracias a mis directores de tesis Pepe y Jorge. Gracias a Pepe por haberme dado la oportunidad de realizar la tesis en su grupo. Jorge, gracias por el esfuerzo realizado para dirigir esta tesis.

Quiero agradecer de un modo muy especial a Daniel Torrent toda la ayuda que me ha brindado. Gracias por haber sido un compañero de trabajo, un amigo y por haberme guiado cuando me he sentido perdida. Ha sido todo un placer trabajar a tu lado y aprender de ti.

I would like to express my gratitude to Alastair Hibbins, who nicely received me in his research group. It was a motivating and useful experience. I am really grateful to Ben Tremain for the help with my experiments.

Llegar a un sitio nuevo, donde nadie te conoce y que te abran las puertas de una casa, de una familia, de un hogar . . . es algo que no tiene precio y que agradeceré eternamente. Mil gracias Ana y Pablo. Y por supuesto a mis peques, Erik y Max, por robarme tantas sonrisas y darme tanto cariño. Con vosotros no me sentaría sola ni un segundo.

A mis niñas, Rossi y Jessi. Hace 10 años empezamos una nueva aventura juntas y hoy seguimos estando juntas en la distancia. Gracias Jessi, por seguir ahí después de tanto tiempo separadas y porque sigues siendo la misma que conocí. Rossi, gracias por responder a mis llamadas de S.O.S, por esas cervecitas y por ser tan buena.

Gracias a todas esas personas que han estado a mi lado desde siempre y que habéis compartido conmigo todos los momentos importantes. A “la Isa”: por todo, porque no hay una razón en especial, siempre has estado y estarás ahí para todo, mil gracias amore!!!! A “la Patri”: porque aunque has estado lejos mucho tiempo eres capaz de volver y conseguir que parezca que el tiempo no ha pasado. A “la Ana Antón”: por ser como eres, por hacerme desconectar y darme tantos buenos momentos. Gracias a Moi y a Sergio: porque sois únicos; espero que cada paso que dé y en cada sitio que tenga que estar, tenga más visitas vuestras. Y por supuesto gracias a Martín: porque eres un fenómeno; es imposible no quererte. Gracias a todos vosotros por recordarme de dónde vengo.

A Manolo, porque siempre me has hecho sentir parte de la familia. Durante estos años has estado muy pendiente de mí y me has cuidado como si

fuera una hija. Gracias!!!

A mi tío Daniel, porque desde siempre has sido mi referente. Tú me inculcaste el amor por la ciencia con tus conversaciones, tus libros, pero sobre todo con tu pasión. Son pocas las personas que quieren algo de ese modo y yo he tenido la suerte de tenerte a ti a mi lado.

No hay palabras que me permitan expresar todo lo que debo agradecer a mis padres, Gloria y Hermes. Me habéis dado la opción de crecer y jamás me habéis puesto límites. Me habéis enseñado que el esfuerzo, el sacrificio y el trabajo duro son la clave para conseguir lo que uno desea. Por muy orgullosos que os sintáis por mis resultados, no superará el orgullo que es para mí tener unos padres como vosotros.

A mi chica, mi hermaneta, mi bombón, mi Eleneta. Creo que nunca serás consciente de lo importante que has sido para mí en este último año. No has sido solo mi hermana, has sido mi amiga y todas esas comidas juntas han sido vitales para terminar esta etapa. Te quiero.

Borja, solo tú sabes lo dura que ha sido esta etapa. Has aguantado los malos momentos a mi lado y has sabido compartir los buenos momentos con la gente que me importa. Crees en mí más que nadie, más de lo que yo lo hago. Sin ti hubiera tirado la toalla y este momento no sería posible. Y como no podía ser de otro modo, a ti va dedicada esta tesis.



A Borja.



# CONTENTS

---

<b>1</b>	<b>Introduction</b>	<b>3</b>
1.1	Motivation . . . . .	4
1.2	Methodology and Procedures . . . . .	5
1.3	Structure of the Thesis . . . . .	7
<b>I</b>	<b>Localization of Electromagnetic Waves</b>	<b>11</b>
<b>2</b>	<b>Principles of periodic media</b>	<b>13</b>
2.1	Wave Equations . . . . .	14
2.1.1	Two-dimensional periodic systems . . . . .	15
2.1.2	Boundary conditions . . . . .	16
2.2	Direct and Reciprocal Lattice . . . . .	18
2.3	Bloch Theorem . . . . .	20
2.4	Photonic Band Structure . . . . .	21
2.5	Metamaterials . . . . .	23
<b>3</b>	<b>Radial Photonic Crystals</b>	<b>25</b>
3.1	Cylindrical Multilayer Shells and the Bloch Theorem . . . . .	26
3.2	Photonic Band Structure and Transmission Spectra . . . . .	29
3.3	Analysis of the RPC Resonant Modes . . . . .	36
3.3.1	Fabry-Perot like modes . . . . .	36
3.3.2	Cavity modes . . . . .	36
3.3.3	Whispering gallery modes . . . . .	38
<b>4</b>	<b>RPC applications</b>	<b>43</b>
4.1	Energy Harvesting . . . . .	44

4.2	Wireless Power Transfer . . . . .	53
4.3	Position Sensors . . . . .	68
4.3.1	Analysis of the frequency shift . . . . .	82
<b>II</b>	<b>Absorption of Electromagnetic Waves</b>	<b>93</b>
<b>5</b>	<b>Absorption Mechanisms in Thin Layers</b>	<b>95</b>
5.1	Introduction . . . . .	96
5.2	Coaxial Grating . . . . .	98
<b>6</b>	<b>Absorption Enhancement by a Coaxial Grating</b>	<b>101</b>
6.1	Mode Matching Analysis . . . . .	102
6.1.1	General case . . . . .	103
6.1.2	Absorption analysis . . . . .	106
6.1.3	Monomode approximation . . . . .	108
6.2	Modes in Coaxial Cavities . . . . .	114
6.2.1	TEM modes . . . . .	115
6.2.2	TE modes . . . . .	118
6.2.3	TM modes . . . . .	120
6.3	Numerical Experiments . . . . .	123
6.3.1	Low-frequency absorption. . . . .	123
6.3.2	Other absorption mechanisms . . . . .	129
<b>7</b>	<b>Experimental verification of Total Absorption</b>	<b>135</b>
7.1	Design Methodology . . . . .	136
7.2	Experimental setup . . . . .	139
7.3	Results . . . . .	140
7.4	Discussion . . . . .	146
<b>8</b>	<b>Concluding Remarks</b>	<b>157</b>
8.1	Summary and Conclusions . . . . .	158
8.2	Future Work . . . . .	158



<b>III</b>	<b>Appendix</b>	<b>161</b>
<b>A</b>	<b>Mathematical notes</b>	<b>163</b>
A.1	Bessel Functions . . . . .	163
A.1.1	Properties . . . . .	165
A.2	Chebyshev Identity . . . . .	165
<b>B</b>	<b>Reduced Parameters of Radial Photonic Crystals</b>	<b>167</b>
<b>C</b>	<b>Homogenization of the SRR Unit Cells</b>	<b>171</b>
C.1	Transmission Matrix . . . . .	171
C.2	Effective Parameters of SRR Unit Cells . . . . .	174
<b>D</b>	<b>Merits of the Author</b>	<b>179</b>
D.1	International Journals . . . . .	179
D.2	International Meetings and Conferences . . . . .	180
D.3	National Meetings and Conferences . . . . .	181
D.4	Patents . . . . .	182



# LIST OF FIGURES

---

1.1	Impact of the RPC applications . . . . .	5
2.1	1D and 2D PhCs. . . . .	17
2.2	Direct and reciprocal lattice . . . . .	18
2.3	PBS of 1D PhCs . . . . .	22
2.4	PBS of 2D PhCs . . . . .	23
2.5	Classification of EM metamaterials . . . . .	24
3.1	2D cylindrical multilayer structure . . . . .	26
3.2	CPC constitutive parameters . . . . .	27
3.3	RPC constitutive parameters . . . . .	30
3.4	Plane wave amplitudes in an infinite RPC . . . . .	30
3.5	Plane wave amplitudes in a finite RPC . . . . .	33
3.6	PBS and transmission coefficients in a RPC . . . . .	35
3.7	Field distribution of the RPC resonant modes . . . . .	37
3.8	External WG mode in a RPC . . . . .	39
3.9	Internal WG mode in a RPC . . . . .	41
4.1	RPC design for EH . . . . .	44
4.2	FP mode properties . . . . .	46
4.3	Cavity mode properties . . . . .	47
4.4	WG mode properties (outer layer) . . . . .	48
4.5	WG mode properties (inner layer) . . . . .	50
4.6	WG modes excited by a point source . . . . .	52
4.7	Scheme of a WPT system . . . . .	54
4.8	Frequency splinting of the coupled modes. . . . .	58
4.9	RPC design for WPT . . . . .	59

4.10	Resonant modes for WPT . . . . .	60
4.11	E-field patterns of the coupled modes . . . . .	61
4.12	Eigenvalue analysis of the WPT . . . . .	63
4.13	Coupling to loss ratio with RPCs . . . . .	64
4.14	WPT with RPCs . . . . .	65
4.15	Coupling between two shells . . . . .	67
4.16	RPC constitutive parameters for sensors . . . . .	68
4.17	Profiles of reduced constitutive parameter. . . . .	69
4.18	Implementation scheme of the RPC shell . . . . .	71
4.19	Schematic view of the measurement setup . . . . .	72
4.20	2D parabolic reflector . . . . .	73
4.21	Configuration of the emitting source. . . . .	74
4.22	2D chamber verification . . . . .	75
4.23	Schematic for the measurements. . . . .	76
4.24	E-field magnitude for a plane wave illuminating an RPC . . . . .	77
4.25	Real E-field of a point source inside the RPC . . . . .	79
4.26	E-field magnitude for a point source outside the RPC . . . . .	79
4.27	Real E-field for a point source illuminating 2 RPCs . . . . .	80
4.28	RPC position sensor . . . . .	81
4.29	Parameter Extraction. Region . . . . .	85
4.30	Extracted coefficient . . . . .	87
4.31	Lorentzian Fit . . . . .	87
4.32	Extracted coefficient . . . . .	88
4.33	Unit cells . . . . .	89
4.34	Frequency shift. Change in constitutive parameters. . . . .	90
4.35	Extracted coefficient with the air gap . . . . .	91
5.1	Traditional absorbers . . . . .	96
5.2	Absorption enhancement . . . . .	97
5.3	Coaxial metasurface for absorption enhancement . . . . .	99
6.1	Metasurface covered by a lossy thin layer . . . . .	102
6.2	Coaxial cavity. . . . .	115
6.3	Coaxial TEM mode . . . . .	117
6.4	Solution for the TE modes . . . . .	119
6.5	TE <sub>11</sub> mode . . . . .	120

6.6	Analysis of the $TE_{11}$ cutoff frequency . . . . .	121
6.7	Solution for the TM modes . . . . .	122
6.8	$TM_{01}$ mode . . . . .	122
6.9	Monomode model . . . . .	124
6.10	Absorption spectra. Cavity length . . . . .	125
6.11	Absorption spectra. Outer radius . . . . .	126
6.12	Absorption spectra. Inner radius . . . . .	127
6.13	Absorption spectra. Losses in the dielectric . . . . .	128
6.14	Absorption spectra. Dielectric thickness . . . . .	129
6.15	Absorption spectra. Non-Bravais lattice . . . . .	130
6.16	Absorption spectra. Guided modes . . . . .	133
6.17	Absorption spectra. Guided modes (incidence angle) . . . . .	134
7.1	Design 1 . . . . .	138
7.2	Design 2 . . . . .	138
7.3	Coaxial Grating . . . . .	140
7.4	Scheme of the experimental setup . . . . .	141
7.5	Photograph of the experimental setup . . . . .	141
7.6	Experiment. Angle of incidence. . . . .	142
7.7	Cavity length effect . . . . .	144
7.8	Study of the dielectric thickness effects . . . . .	146
7.9	Dielectric thickness effects . . . . .	147
7.10	Air gap . . . . .	148
7.11	Airgap study. Amplitude . . . . .	152
7.12	Airgap study. Frequency . . . . .	154
7.13	Cavity length effect. Airgap . . . . .	155
7.14	Dielectric thickness effect. Airgap . . . . .	156
A.1	Bessel functions of the first kind . . . . .	164
A.2	Bessel functions of the second kind . . . . .	164
B.1	Reduced profile resonances . . . . .	169
C.1	Transmission Matrix . . . . .	172
C.2	SRR unit cell . . . . .	175
C.3	Retrieved parameters . . . . .	176



## LIST OF TABLES

---

4.1	Extracted parameters from the unit cells . . . . .	70
4.2	Design parameters of the SRRs . . . . .	70
4.3	Lorentzian fit . . . . .	86
4.4	Extracted parameters from the unit cells with air gap . . . . .	89
7.1	Sample dimensions . . . . .	139
7.2	Effect of an air gap . . . . .	153
B.1	Reduced profile . . . . .	169

# ACRONYMS

---

- **1D/2D/3D** One-/ Two-/ Three-Dimensional
- **EH** Energy Harvesting
- **FEM** Finite Elements Method
- **FP** Fabry-Perot
- **MM** Modal Matching
- **PBG** Photonic Bandgap
- **PBS** Photonic Band Structure
- **PhC** Photonic Crystal
- **RPC** Radial Photonic Crystal
- **RWC** Radial Wave Crystal
- **SRR** Split Ring Resonator
- **TMM** Transfer Matrix Method
- **WG** Whispering Gallery
- **WPT** Wireless Power Transfer





# 1

## INTRODUCTION

---

This is an introductory chapter in which the goals of the thesis are explained. Moreover, the methods and procedures employed throughout this work are briefly described. Finally, the structure of the thesis is presented and the different chapters of the manuscript are summarized.

### Contents

---

<b>1.1 Motivation</b> . . . . .	<b>4</b>
<b>1.2 Methodology and Procedures</b> . . . . .	<b>5</b>
<b>1.3 Structure of the Thesis</b> . . . . .	<b>7</b>

---

## 1.1 Motivation

Controlling electromagnetic waves and managing their energy are a challenging problems with a huge number of applications. The work carried out in this thesis has been supported by the Spanish government under the TEC-2010-19751 project and the project *Engineering Metamaterials* of the CONSOLIDER program. The objective of both projects was designing new devices inspired on metamaterials. In the framework of these projects, this thesis is focused on the study of advanced artificial structures for the management of electromagnetic energy. More specifically, we have studied theoretical and experimentally highly anisotropic and inhomogeneous structures (Radial Photonic Crystals) and artificial thin surfaces (metasurfaces) for their potential application in the localization and absorption of electromagnetic waves, specially in the microwave regime. This manuscript is divided in two main parts.

The first part reports a comprehensive study of Radial Photonic Crystals and their application for the localization of electromagnetic waves. Radial Waves Crystals are a new type of structures with cylindrical symmetry and crystal-like behavior predicted by members of the Wave Phenomena group, where this thesis has been developed [1]. The results obtained with Radial Waves Crystals showed extraordinary resonant properties with acoustic and electromagnetic fields, Radial Sonic Crystals and Radial Photonic Crystal respectively. Motivated by these previous results, the thesis began with a deep study of the Radial Photonic Crystal and their resonant properties. Then, these properties were employed for developing a new path in the design of devices for the management of electromagnetic energy. Particularly, we focused on the use of Radial Photonic Crystal in *Energy Harvesting* and *Wireless Power Transfer*. We chose these applications for different reasons. On the one hand, these applications need completely different resonant properties and it is a proof of the wide range of applications in which the Radial Photonic Crystal can be employed. On the other hand, these are applications which are attracting an increasing interest, like it is shown in Fig.1.1 where we can see the evolution of citations on these topics. Moreover, due to the complexity of the Radial Wave Crystal structures, we were interested in the first practical realization of a Radial Photonic Crystal and its experimental

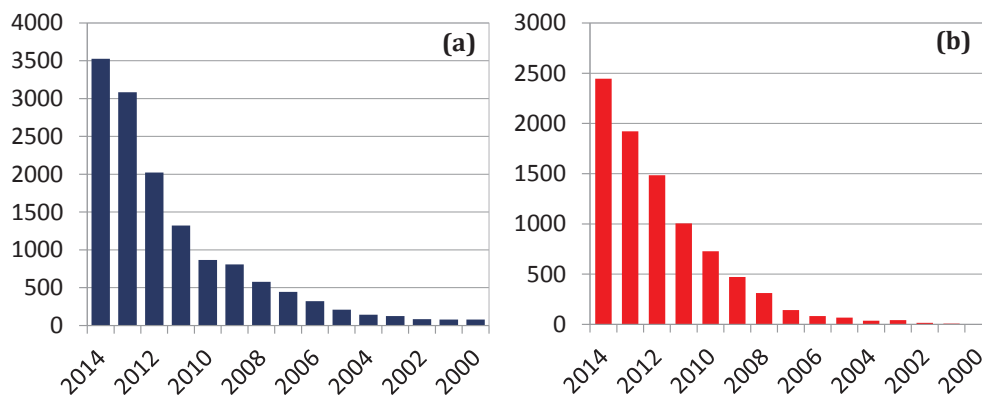


Figure 1.1: Number of citations per year in papers under the search: (a) *wireless power transfer* and (b) *energy harvesting electromagnetic waves*. Source: Web Of Science.

characterization.

The second part of the thesis deals with the absorption of electromagnetic waves by thin layers. Particularly, it is focused on the absorption enhancement produced by metasurfaces. The motivation for tackling this topic is the theoretical analysis of a simple structure which allows understanding the different mechanisms which produce the absorption enhancement. The results of the study can be applied for explaining the absorption phenomenon in more complex structures. Particularly, we focused on the study of the absorption enhancement produced by a metallic metasurface on the backside of a lossy thin dielectric layer. We studied how the metasurface affects to the absorption spectra. In the last part of the thesis, we experimentally verified the theoretical findings.

## 1.2 Methodology and Procedures

This section explains the methods employed for the development of this research work. The topics covered in this thesis have been developed with three different procedures: analytical methods, numerical simulations and experimental demonstrations. Each procedure and the data analysis are detailed below.

### Analytical Methods

The different topics tackled by this thesis have been studied under a theoretical point of view by analytical models. These models have allowed a deep knowledge of the studied structures and, in some cases, simplifications which have allowed obtaining design criteria. In particular, two analytical methods have been employed: Transfer Matrix Method and Mode Matching Method. The main features of these methods are:

1. *Transfer Matrix Method.* We have used this method for the analysis of the Radial Photonic Crystals, which is a 2D dimensional problem dealing with anisotropic and inhomogeneous materials. Applying the boundary conditions at the interfaces of the Radial Photonic Crystals, we have obtained the Band diagram and the transmission coefficients of these periodic structures.
2. *Mode Matching Method.* This method has been used in the second part of the thesis, during the study of the absorption by thin layers. With this method, we have solved the 3D problem of a thin dielectric layer covered by a metallic grating. Using a monomode approximation inside the cavities of the metallic grating, we have proposed design criteria for total absorption structures.

Both theoretical models have been implemented using Matlab.

### Numerical Simulations

With the purpose of demonstrating our analytical models and for the analysis of complex systems, difficult to perform with analytical methods, two commercial software packages were employed:

1. *COMSOL.* With this finite element solver, we have solved two kinds of 2D problems in the first part of the thesis. On the one hand, eigen frequency studies of the Radial Photonic Crystals for obtaining their resonant frequencies. On the other hand, frequency domain studies with point sources to obtain the response of the Radial Photonic Crystals.
2. *Ansys HFSS.* We have used this 3D finite element solver in both parts of the thesis. In the first part, we have done the study of a periodic

array of Split Ring Resonator for extracting the effective parameters and the study of RPC shells implemented with these resonators. In the second part, we have simulated the absorption produced by the periodic system formed by a metallic grating and a dielectric layer over it.

### Experimental Demonstrations

Each part of the thesis has an experiment which demonstrates the concepts under study. Two experimental setups have been specifically developed to demonstrate the theoretical predictions:

1. *2D E-field mapping.* This kind of measurements has been done for the characterization of Radial Photonic Crystals. To this purpose, we have fabricated our own 2D chamber and developed a software, with LabView, for the automatic data acquisition.
2. *Absorption measurements.* The characterization of the absorption has been performed with transmission measurements in free space at different frequencies. Noteworthy, the use of collimating mirrors for exciting the samples with plane waves.

### Data Analysis

The results from the analytical models, numerical simulations and experiments are processed to allow an easy comparison between them. The analysis of the data and the graphics have been done using Matlab.

## 1.3 Structure of the Thesis

This thesis is organized in two parts and eight chapters. The distribution of the chapters and the content of each one are summarized as follows:

**Chapter 1** starts with the motivation of the thesis. Next, a brief review of the state of the art is presented. Finally, the third section describes the structure and the organization of the thesis.

The first part of the thesis, entitled **Localization of Electromagnetic Waves**, reports the main resonant features of highly anisotropic and inhomogeneous structures. More specifically, the work is focused on a new type of

structures with cylindrical symmetry and crystal-like behavior named *Radial Wave Crystals*. This part includes three chapters.

**Chapter 2** introduces a revision of the theoretical principles needed for working with electromagnetic periodic media. Concepts like wave equations, boundary conditions and Bloch theorem are reviewed.

**Chapter 3** studies in detail the concept of *Radial Photonic Crystal*, pointing out the fulfilling of the requirements for applying the Bloch theorem. A comparison with the *Circular Photonic Crystals* has been performed. Moreover, the resonant modes generated in these structures are also studied.

**Chapter 4** presents the potential applications where the resonant properties of the *Radial Photonic Crystal* can be employed. Three different cases are reviewed: energy harvesting, wireless energy transfer and position sensors.

The second part, entitled **Absorption of Electromagnetic Waves**, studies thin absorbing layers for electromagnetic waves. The study is divided in three chapters.

**Chapter 5** provides a brief introduction to the problematic of the thin absorbing layers and proposes an alternative to enhance the absorption using artificial thin surfaces.

**Chapter 6** presents theoretically our proposal. In this chapter, an analytic model has been developed using a monomode approximation. A complete study of the system has been carried out. Moreover, this model allows obtaining a simple method for designing total absorption systems.

**Chapter 7** describes the experimental demonstration of the whole absorption system. The main theoretical findings extracted from our model are experimentally confirmed.

**Chapter 8** summarizes the conclusion remarks extracted from the two parts of the thesis. Furthermore, future research lines identified from this work are presented.

In addition, three appendixes have been included with useful information for the development of this work.

**Appendix A** collects mathematical concepts used in the development of the theoretical models. Bessel Functions and their main properties are presented, and besides, Chebyshev Identity is explained.

**Appendix B** explains the retrieval method used for the homogenization

of the *Split Ring Resonators* (SRR) unit cells. This method is used in the experimental characterization of the Radial Photonic Crystal.

**Appendix C** lists the merits of the author. The appendix includes the contributions to international journals and the conference proceedings resulting from oral and poster presentations in international and national conferences.

Finally, in **Bibliography** section, a list of the works cited throughout this thesis is include. In this list, the works are numbered sequentially in order of appearance.





# Part I

LOCALIZATION OF  
ELECTROMAGNETIC WAVES



# 2

## PRINCIPLES OF PERIODIC MEDIA

---

The work presented in this thesis studies different properties of the electromagnetic wave propagation in periodic media. This chapter summarizes some theoretical principles needed for working with periodic media. First, the wave equation is derived from the Maxwell's equations, paying special attention to the two-dimensional (2D) problem. Then, the direct and reciprocal lattices of the periodic media are introduced. Moreover, the eigenvalue problem of the wave equation is presented and it is used to prove Bloch's theorem. In chapter 2.4, the band structure and the concept of photonic bandgap are presented. Finally, we will introduce the concept of metamaterial and the main features of these artificial structures.

### Contents

---

<b>2.1</b>	<b>Wave Equations</b>	<b>14</b>
2.1.1	Two-dimensional periodic systems	15
2.1.2	Boundary conditions	16
<b>2.2</b>	<b>Direct and Reciprocal Lattice</b>	<b>18</b>
<b>2.3</b>	<b>Bloch Theorem</b>	<b>20</b>
<b>2.4</b>	<b>Photonic Band Structure</b>	<b>21</b>
<b>2.5</b>	<b>Metamaterials</b>	<b>23</b>

---

## 2.1 Wave Equations

For studying the propagation of electromagnetic waves, we have to start with Maxwell equations. Considering a source free medium, the relation between electric and magnetic fields can be expressed by the Maxwell equations, in the SI units, as:

$$\nabla \times \mathbf{E}(\mathbf{r}, t) = -\frac{\partial}{\partial t} \mathbf{B}(\mathbf{r}, t), \quad (2.1a)$$

$$\nabla \times \mathbf{H}(\mathbf{r}, t) = \frac{\partial}{\partial t} \mathbf{D}(\mathbf{r}, t), \quad (2.1b)$$

$$\nabla \cdot \mathbf{D}(\mathbf{r}, t) = 0, \quad (2.1c)$$

$$\nabla \cdot \mathbf{B}(\mathbf{r}, t) = 0. \quad (2.1d)$$

These equations relate the electric field ( $\mathbf{E}$ ), the magnetic field ( $\mathbf{H}$ ), the electric displacement ( $\mathbf{D}$ ) and the magnetic induction ( $\mathbf{B}$ ). Moreover, the relations between  $\mathbf{E}$  and  $\mathbf{D}$  and between  $\mathbf{H}$  and  $\mathbf{B}$  are obtained from the constitutive equations. The constitutive equations in vacuum conditions are:

$$\mathbf{D} = \varepsilon_0 \mathbf{E}, \quad (2.2a)$$

$$\mathbf{B} = \mu_0 \mathbf{H}, \quad (2.2b)$$

where  $\varepsilon_0$  is the vacuum permittivity and  $\mu_0$  the permeability. In an isotropic media the constitutive parameters  $\varepsilon$  and  $\mu$  are constant. In this case, the constitutive equations for the electric field,  $\mathbf{D} = \varepsilon \mathbf{E}$ , and the magnetic field,  $\mathbf{B} = \mu \mathbf{H}$  only depend on a scalar value.

Along this manuscript the time dependence of the electromagnetic fields takes the form

$$\mathbf{E}(r, t) = \mathbf{E}(r) e^{-i\omega t}, \quad (2.3a)$$

$$\mathbf{H}(r, t) = \mathbf{H}(r) e^{-i\omega t}, \quad (2.3b)$$

where  $\omega$  is the angular frequency, and  $\mathbf{E}(r)$  and  $\mathbf{H}(r)$  represent the eigenfunction of the wave equations. The harmonic time dependence of the electromagnetic fields allows to write the Eq.(2.1a) and Eq.(2.1b) equations as:

$$\nabla \times \mathbf{E}(\mathbf{r}) = i\omega \mathbf{B}(\mathbf{r}), \quad (2.4a)$$

$$\nabla \times \mathbf{H}(\mathbf{r}) = -i\omega \mathbf{D}(\mathbf{r}). \quad (2.4b)$$

Taking the curl of Eq.(2.4a) and using the constitutive relation for the magnetic field, we obtain:

$$\nabla \times \nabla \times \mathbf{E}(\mathbf{r}) = i\omega \mu \nabla \times \mathbf{H}(\mathbf{r}). \quad (2.5)$$

Now introducing Eq.(2.4b) and using the vector operator identity  $\nabla \times (\nabla \times \mathbf{A}) = \nabla(\nabla \cdot \mathbf{A}) - \nabla^2 \mathbf{A}$ , we have

$$\nabla(\nabla \cdot \mathbf{E}(\mathbf{r})) - \nabla^2 \mathbf{E}(\mathbf{r}) - k^2 \mathbf{E}(\mathbf{r}) = 0, \quad (2.6)$$

with  $k^2 = (\omega/c)^2$  being  $c = c_0/\sqrt{\mu\epsilon}$ . From Eq.(2.1c) we know that  $\nabla \cdot \mathbf{E}(\mathbf{r}) = 0$ , so that

$$\nabla^2 \mathbf{E}(\mathbf{r}) + k^2 \mathbf{E}(\mathbf{r}) = 0. \quad (2.7)$$

This wave equation is known as **Helmholtz's equation**. The same procedure can be employed to obtain the Helmholtz's equation for the magnetic fields.

Finally, if we consider a periodic distribution of isotropic materials, the constitutive parameters,  $\epsilon(r)$  and  $\mu(r)$ , will be periodic functions with the same periodicity that the lattice. Under these conditions, the wave equation for the electric and magnetic fields are:

$$\Theta_E \mathbf{E}(\mathbf{r}) \equiv \frac{1}{\epsilon(r)} \nabla \times \left\{ \frac{1}{\mu(r)} \nabla \times \mathbf{E}(\mathbf{r}) \right\} = \omega^2 \mathbf{E}(\mathbf{r}) \quad (2.8a)$$

$$\Theta_H \mathbf{H}(\mathbf{r}) \equiv \frac{1}{\mu(r)} \nabla \times \left\{ \frac{1}{\epsilon(r)} \nabla \times \mathbf{H}(\mathbf{r}) \right\} = \omega^2 \mathbf{H}(\mathbf{r}) \quad (2.8b)$$

where  $\Theta_E$  and  $\Theta_H$  represent the differential operators of these equations.

### 2.1.1 Two-dimensional periodic systems

This section particularizes the previous analysis for 2D periodic systems. An schematic representation of a 2D problem is depicted in the figure 2.1.b. The system is periodic in  $\hat{x}$  and  $\hat{y}$  directions and invariant along  $\hat{z}$ , such that  $\epsilon(\mathbf{r})$ ,  $\mu(\mathbf{r})$ ,  $\mathbf{E}(\mathbf{r})$  and  $\mathbf{H}(\mathbf{r})$  do not depend on the  $z$ -coordinate. Considering that

the waves travel on the  $x$ - $y$  plane ( $\mathbf{k}$  parallel to this plane) we can decouple the vectorial equation in two independent sets of equations.

The first set corresponds with  $E_x = E_y = 0$  and  $E_z \neq 0$  and it is known as  $TE$  polarization. The Maxwell equations leads to

$$\frac{\partial}{\partial y} E_z(\mathbf{r}) = i\omega\mu(r)H_x(\mathbf{r}), \quad (2.9a)$$

$$\frac{\partial}{\partial x} E_z(\mathbf{r}) = -i\omega\mu(r)H_y(\mathbf{r}), \quad (2.9b)$$

$$\frac{\partial}{\partial x} H_y(\mathbf{r}) - \frac{\partial}{\partial y} H_x(\mathbf{r}) = -i\omega\varepsilon(\mathbf{r})E_z(\mathbf{r}), \quad (2.9c)$$

where  $\mathbf{r}$  is the position in the  $x$ - $y$  plane (cylindrical coordinates). The wave equation for the  $TE$  polarization can be obtained combining these equations for removing  $H_x(\mathbf{r})$  and  $H_y(\mathbf{r})$ .

$$-\frac{1}{\varepsilon(\mathbf{r})} \left\{ \frac{\partial}{\partial x} \frac{1}{\mu(\mathbf{r})} \frac{\partial}{\partial x} - \frac{\partial}{\partial y} \frac{1}{\mu(\mathbf{r})} \frac{\partial}{\partial y} \right\} E_z(\mathbf{r}) = \omega^2 E_z(\mathbf{r}). \quad (2.10)$$

The second case, known as  $TM$  polarization, is characterized by  $H_x = H_y = 0$  and  $H_z \neq 0$ . With the same procedure that for the  $TE$  polarized waves, the set of equation is

$$\frac{\partial}{\partial y} H_z(\mathbf{r}) = -i\omega\mu(r)E_x(\mathbf{r}), \quad (2.11a)$$

$$\frac{\partial}{\partial x} H_z(\mathbf{r}) = i\omega\mu(r)E_y(\mathbf{r}), \quad (2.11b)$$

$$\frac{\partial}{\partial x} E_y(\mathbf{r}) - \frac{\partial}{\partial y} E_x(\mathbf{r}) = i\omega\varepsilon(\mathbf{r})H_z(\mathbf{r}), \quad (2.11c)$$

and the wave equation for  $H_z(\mathbf{r})$  is

$$-\frac{1}{\mu(\mathbf{r})} \left\{ \frac{\partial}{\partial x} \frac{1}{\varepsilon(\mathbf{r})} \frac{\partial}{\partial x} - \frac{\partial}{\partial y} \frac{1}{\varepsilon(\mathbf{r})} \frac{\partial}{\partial y} \right\} H_z(\mathbf{r}) = \omega^2 H_z(\mathbf{r}) \quad (2.12)$$

### 2.1.2 Boundary conditions

To apply the boundary conditions at the interface between two different media we can decompose the electromagnetic fields in the normal components to the surface ( $\mathbf{E}_n$ ,  $\mathbf{H}_n$ ,  $\mathbf{D}_n$  and  $\mathbf{B}_n$ ) and the tangential components to the

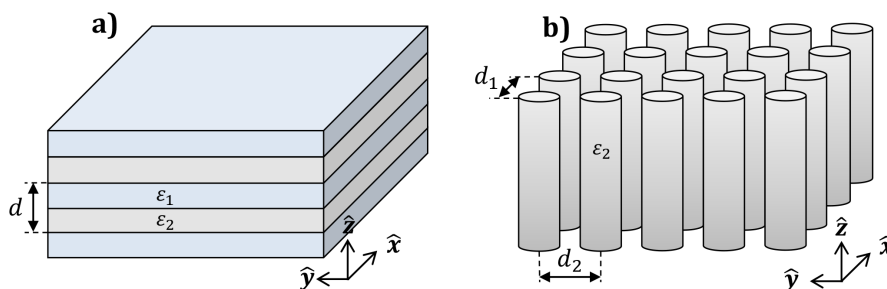


Figure 2.1: Schematic representation of 1D and 2D photonic crystals. a) 1D PhC where the different colours represent layers with different dielectric constants. The system has no dependence in the  $z$  and  $x$  direction. b) 2D PhC made with a periodic distribution of dielectric rods. The system is invariant in  $z$  direction

surface ( $\mathbf{E}_t$ ,  $\mathbf{H}_t$ ,  $\mathbf{D}_t$  and  $\mathbf{B}_t$ ). The boundary conditions impose the continuity of the tangential electric and magnetic fields:

$$\mathbf{E}_t^{(1)} = \mathbf{E}_t^{(2)}, \quad (2.13)$$

$$\mathbf{H}_t^{(1)} = \mathbf{H}_t^{(2)}, \quad (2.14)$$

and also the continuity of the normal components:

$$\mathbf{D}_n^{(1)} = \mathbf{D}_n^{(2)}, \quad (2.15)$$

$$\mathbf{B}_n^{(1)} = \mathbf{B}_n^{(2)}, \quad (2.16)$$

where (1) and (2) refer to the change of the dielectric and magnetic properties of the materials at both sides of the interface boundary.

For the case of the 2D problem using cylindrical coordinates we can apply the boundary condition for the  $TE$  and  $TM$  modes. First, if we consider the  $TE$  modes (i.e the components different than zero are  $E_z$ ,  $H_r$  and  $H_\theta$ ) the continuity conditions of the tangential components imply that:

$$\mathbf{E}_z^{(1)} = \mathbf{E}_z^{(2)}, \quad (2.17)$$

$$\frac{1}{\mu^{(1)}} \frac{\delta}{\delta r} \mathbf{E}_z^{(1)} = \frac{1}{\mu^{(2)}} \frac{\delta}{\delta r} \mathbf{E}_z^{(2)}, \quad (2.18)$$

where  $\mu^{(1)}$  and  $\mu^{(2)}$  are the permeabilities in each medium. For the  $TM$  modes the components involved are  $H_z$ ,  $E_r$  and  $E_\theta$ . In a similar way to the



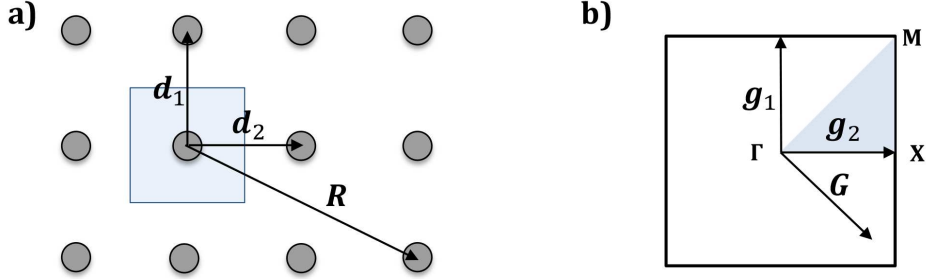


Figure 2.2: Photonic crystal with a squared distribution. a) Real lattice. The unit cell is shown with the blue square. b) Brillouin zone of the squared lattice. The irreducible zone and the special points ( $\Gamma$ ,  $M$ ,  $X$ ) are plotted.

*TE* modes

$$\mathbf{H}_z^{(1)} = \mathbf{H}_z^{(2)}, \quad (2.19)$$

$$\frac{1}{\varepsilon^{(1)}} \frac{\delta}{\delta r} \mathbf{H}_z^{(1)} = \frac{1}{\varepsilon^{(2)}} \frac{\delta}{\delta r} \mathbf{H}_z^{(2)}. \quad (2.20)$$

being  $\varepsilon^{(1)}$  and  $\varepsilon^{(2)}$  the permittivities of the two different media.

## 2.2 Direct and Reciprocal Lattice

*Photonic Crystals* (PhC) are obtained from a building unit which is periodically repeated in space. The translational symmetry that describes the periodicity in crystals can be expressed as a linear combination of three independent vectors ( $\mathbf{d}_1$ ,  $\mathbf{d}_2$  and  $\mathbf{d}_3$ ) which are called *lattice vectors*, like it is shown in Figure 2.2.(a) where a square lattice of cylindrical scatters is represented. These vectors define the *unit cell*. The lattice vectors, and thus the unit cell, can be selected in various ways for the same periodic distribution. Independently of the unit cell choice, the volume of the cell remains constant and is given by  $V = \mathbf{d}_1 \cdot (\mathbf{d}_2 \times \mathbf{d}_3)$ .

Once the lattice vectors are chosen according to the symmetry of the structure, any unit cell can be described by

$$\mathbf{R} = l_1 \mathbf{d}_1 + l_2 \mathbf{d}_2 + l_3 \mathbf{d}_3 \quad (2.21)$$

where  $l_\alpha$  ( $\alpha = 1, 2, 3$ ) are integers. Moreover any point in a unit cell can be reached with the nearest  $\mathbf{R}$  vector, and adding to it the corresponding

fractions of the lattice vectors:

$$\mathbf{r} = \mathbf{R} + \mathbf{r}' = (l_1 \mathbf{d}_1 + l_2 \mathbf{d}_2 + l_3 \mathbf{d}_3) + (x \mathbf{d}_1 + y \mathbf{d}_2 + z \mathbf{d}_3). \quad (2.22)$$

being  $x, y, z$  the dimensionless fractions of the axes.

Now, if we consider a periodic crystal formed by dielectric rods like in Figure 2.2.(b), the translational symmetry of the structure has to be reflected in the dielectric function. This means that the dielectric function fulfils:

$$\varepsilon(\mathbf{r} + \mathbf{R}) = \varepsilon(\mathbf{r}). \quad (2.23)$$

In this case, the periodic function can be analyzed by Fourier transform as follows [2]:

$$\varepsilon(\mathbf{r}) = \int u(\mathbf{q}) e^{i\mathbf{q} \cdot \mathbf{r}} d\mathbf{q}. \quad (2.24)$$

That is, the function  $\varepsilon(\mathbf{r})$  can be expressed as a combination of plane waves with amplitude  $u(\mathbf{q})$  and wave vector  $\mathbf{q}$ . The translational symmetry in the dielectric function [see Eq.(2.23)] requires that:

$$\varepsilon(\mathbf{r} + \mathbf{R}) = \int u(\mathbf{q}) e^{i\mathbf{q} \cdot \mathbf{r}} e^{i\mathbf{q} \cdot \mathbf{R}} d\mathbf{q} = \int u(\mathbf{q}) e^{i\mathbf{q} \cdot \mathbf{r}} d\mathbf{q}. \quad (2.25)$$

This relation imposes that  $u(\mathbf{q}) e^{i\mathbf{q} \cdot \mathbf{R}} = u(\mathbf{q})$ . This requirement can be satisfied only if  $u(\mathbf{q}) = 0$  or  $e^{i\mathbf{q} \cdot \mathbf{R}} = 1$ . Then  $u(\mathbf{q}) = 0$  except for the values where  $e^{i\mathbf{q} \cdot \mathbf{R}} = 1$ . The  $\mathbf{q}$  vectors verifying this condition form the *reciprocal lattice*,  $\mathbf{G}$ . The vectors of this lattice are:

$$\mathbf{G} = m_1 \mathbf{g}_1 + m_2 \mathbf{g}_2 + m_3 \mathbf{g}_3 \quad (2.26)$$

The reciprocal lattice need to fulfil  $\mathbf{G} \cdot \mathbf{R} = n2\pi$  which implies that  $\mathbf{a}_i \cdot \mathbf{b}_j = 2\pi \delta_{ij}$ . Finally, for a direct lattice defined by its primitive vectors ( $\mathbf{d}_1, \mathbf{d}_2$  and  $\mathbf{d}_3$ ), its reciprocal lattice can be constructed by:

$$\mathbf{g}_1 = 2\pi \frac{\mathbf{d}_2 \times \mathbf{d}_3}{\mathbf{d}_1 \cdot (\mathbf{d}_2 \times \mathbf{d}_3)} \quad (2.27a)$$

$$\mathbf{g}_2 = 2\pi \frac{\mathbf{d}_3 \times \mathbf{d}_1}{\mathbf{d}_2 \cdot (\mathbf{d}_3 \times \mathbf{d}_1)} \quad (2.27b)$$

$$\mathbf{g}_3 = 2\pi \frac{\mathbf{d}_1 \times \mathbf{d}_2}{\mathbf{d}_3 \cdot (\mathbf{d}_1 \times \mathbf{d}_2)} \quad (2.27c)$$

## 2.3 Bloch Theorem

A system has *continuous* translational symmetry when it is unchanged by a translation through any displacement  $\mathbf{d}$ . Photonic crystals do not have continuous translational symmetry, they have *discrete* translational symmetry. This means that they are not invariant under translation in any distance, only for some fixed step length [3]. As it was explained before, the basic step vector is called *primitive lattice vector*,  $\mathbf{R}$  [see Eq.(2.21)]. The discrete translation operator is defined as:

$$T_{\mathbf{R}}\psi(\mathbf{r}) = \psi(\mathbf{r} + \mathbf{R}), \quad (2.28)$$

being  $\psi(\mathbf{r})$  an arbitrary function. The eigenfunction of this operator can be found as

$$T_{\mathbf{R}}\psi(\mathbf{r}) = \lambda(\mathbf{R})\psi(\mathbf{r}), \quad (2.29)$$

where  $\lambda(\mathbf{R})$  represents the eigenvalues. Applying a translation operator over the previous expression we obtain

$$T_{\mathbf{R}}T_{\mathbf{R}'}\psi(\mathbf{r}) = \lambda(\mathbf{R})T_{\mathbf{R}'}\psi(\mathbf{r}) = \lambda(\mathbf{R})\lambda(\mathbf{R}')\psi(\mathbf{r}). \quad (2.30)$$

Now, taking into account that for any lattice vector  $T_{\mathbf{R}}T_{\mathbf{R}'} = T_{\mathbf{R}+\mathbf{R}'}$ , we can write

$$T_{\mathbf{R}}T_{\mathbf{R}'}\psi(\mathbf{r}) = T_{\mathbf{R}+\mathbf{R}'}\psi(\mathbf{r}) = \lambda(\mathbf{R} + \mathbf{R}')\psi(\mathbf{r}). \quad (2.31)$$

Equations (2.30) and (2.31) imply that the eigenvalues have to fulfil  $\lambda(\mathbf{R})\lambda(\mathbf{R}') = \lambda(\mathbf{R} + \mathbf{R}')$  which means that the eigenfunction of the discrete translational operator is of the form:

$$\lambda(\mathbf{R}) = e^{i\mathbf{k}\cdot\mathbf{R}}, \quad (2.32)$$

where the vector  $\mathbf{k}$  can be expressed in terms of the reciprocal lattice as

$$\mathbf{k} = k_1\mathbf{g}_1 + k_2\mathbf{g}_2 + k_3\mathbf{g}_3 \quad (2.33)$$

The differential operator defined in Eq.(2.8a) is invariant under translations,  $\Theta(\mathbf{r}) = \Theta(\mathbf{r} + \mathbf{R})$ . Then applying the translation operator to this eigenvalue equation we can write

$$\begin{aligned} T_{\mathbf{R}}\Theta(\mathbf{r})\mathbf{E}_{\mathbf{k}}(\mathbf{r}) &= \Theta(\mathbf{r} + \mathbf{R})\mathbf{E}_{\mathbf{k}}(\mathbf{r} + \mathbf{R}) \\ &= \Theta(\mathbf{r})\mathbf{E}_{\mathbf{k}}(\mathbf{r} + \mathbf{R}) \\ &= \Theta(\mathbf{r})T_{\mathbf{R}}\mathbf{E}_{\mathbf{k}}(\mathbf{r}) \end{aligned} \quad (2.34)$$

This means that the translation operation commutes with  $\Theta$ , so the eigenfunction of the operator  $T_{\mathbf{R}}$  is simultaneously an eigenfunction of the differential operator  $\Theta$ :

$$\Theta \mathbf{E}_{\mathbf{k}}(\mathbf{r}) = \left(\frac{\omega_{\mathbf{k}}}{c}\right)^2 \mathbf{E}_{\mathbf{k}}(\mathbf{r}) \quad (2.35)$$

$$T_{\mathbf{R}} \mathbf{E}_{\mathbf{k}}(\mathbf{r}) = \lambda(\mathbf{R}) \mathbf{E}_{\mathbf{k}}(\mathbf{r}) \quad (2.36)$$

Now applying an arbitrary lattice translation  $\mathbf{R}$  to the eigenfunction  $\mathbf{E}_{\mathbf{k}}(\mathbf{r})$  one obtains:

$$T_{\mathbf{R}} \mathbf{E}_{\mathbf{k}}(\mathbf{r}) = \mathbf{E}_{\mathbf{k}}(\mathbf{r} + \mathbf{R}) = \lambda(\mathbf{R}) \mathbf{E}_{\mathbf{k}}(\mathbf{r}) = e^{i\mathbf{k} \cdot \mathbf{R}} \mathbf{E}_{\mathbf{k}}(\mathbf{r}) \quad (2.37)$$

which leads to the *Bloch's theorem*. Bloch proved that waves in periodic media propagate without scattering with a certain wavevector  $\mathbf{k}$  and their behavior is governed by a periodic envelope function multiplied by a planewave:

$$\mathbf{E}_{\mathbf{k}}(\mathbf{r}) = e^{i\mathbf{k} \cdot \mathbf{r}} \mathbf{e}_{\mathbf{k}}(\mathbf{r}) \quad (2.38)$$

where  $\mathbf{e}_{\mathbf{k}}(\mathbf{r} + \mathbf{R}) = \mathbf{e}_{\mathbf{k}}(\mathbf{r})$ .

## 2.4 Photonic Band Structure

The *Photonic Band Structure* (PBS) of a PhC describes the eigenvalue distribution in frequency,  $\omega_n(\mathbf{k})$ . Due to the periodicity of this system, the wave propagation is forbidden at certain frequency ranges. The ranges of frequencies where no electromagnetic modes propagate are called *Photonic Bandgaps* (PBGs). Under certain conditions, the PBG extends over all possible directions, in this case it is called *complete band gap*.

In Figure 2.3, the simplest case of a PBS is represented, a 1D PhC made of alternating layers with different dielectric constants [3]. A schematic representation of the system is shown in Figure 2.1.a, where the lattice vector is defined as  $d\hat{\mathbf{z}}$ . The waves propagate in  $\hat{\mathbf{z}}$  direction (on-axis propagation,  $\mathbf{k} = k_z$ ). In this 1D system the reciprocal vectors are  $\mathbf{G} = n\frac{2\pi}{a}\hat{\mathbf{z}}$  ( $n = 0, \pm 1, \pm 2, \dots$ ) and the Brillouin zone is defined as  $-\pi/d < k_z < \pi/d$  being the limits of the PBS. In the first case, Figure 2.3.a, a multilayer system is shown in which all the layers have the same dielectric properties, so it behaves like a bulk material ( $\varepsilon_1 = \varepsilon_2 = 13$ ). The modes lie on the light line and are given by  $\omega(k) = ck/\sqrt{\varepsilon}$ . In Figure 2.3.b, the PBS of a multilayer system

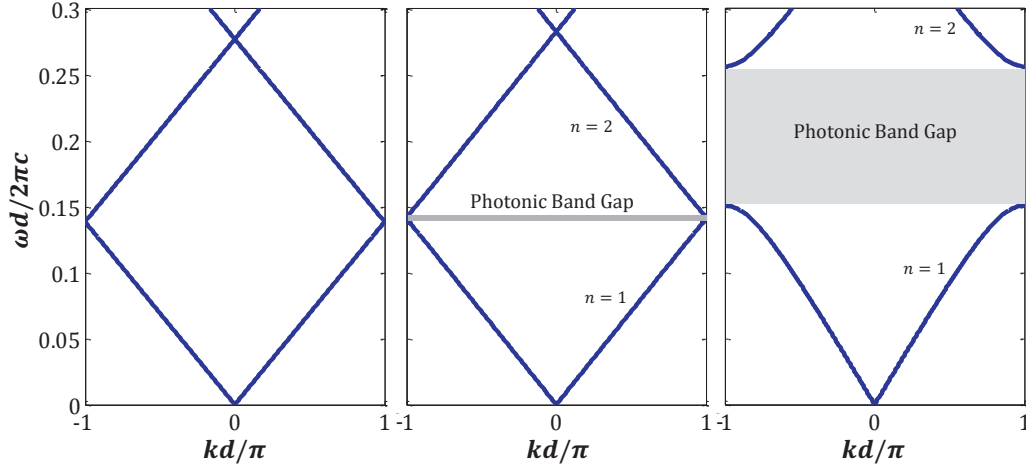


Figure 2.3: Band diagram for an on-axis propagation in a 1D PhCs calculated with the Transfer Matrix Method [4]. a) Every layer has the same dielectric constant  $\varepsilon_1 = \varepsilon_2 = 13$ . b) Layers with different dielectric constants,  $\varepsilon_1 = 12$  and  $\varepsilon_2 = 13$ . c) Layers with different dielectric constants,  $\varepsilon_1 = 1$  and  $\varepsilon_2 = 13$

slightly different dielectric constants in the material ( $\varepsilon_1 = 12$  and  $\varepsilon_2 = 13$ ) is shown. The shadowed area represents the frequency range where appear a PBG where the wave propagation is not allowed. Each band, denoted with  $n = 1, 2$ , represents one eigenmode. Finally, in Fig.2.3.c, the PBS of a multilayer system with a strong contrast in the dielectric properties ( $\varepsilon_1 = 1$  and  $\varepsilon_2 = 13$ ) is plotted. Note that the increase of the dielectric contrast produces broadening of the PBG, increasing the number of frequencies in which there is no propagation.

This idea can be extended to the 2D case. To do that, it is necessary taking into account that now the system is periodic in two directions ( $\hat{x}$  and  $\hat{y}$ ) and homogeneous in the third one ( $\hat{z}$ ). In the 2D problem, the splitting between TE and TM polarizations is possible and the PBSs associated with each one are different. Figure 2.4 shows the PBS for each polarization in a squared distribution of rod with  $\varepsilon_d = 8.9$  embedded in air when  $k_z = 0$ . The PBG is represented over the directions of maximum symmetry of the Brillouin zone (see Fig.2.21). In this system there is a complete PBG for the TE modes which is represented with the shadow area, but there is no PBG for the TM modes.

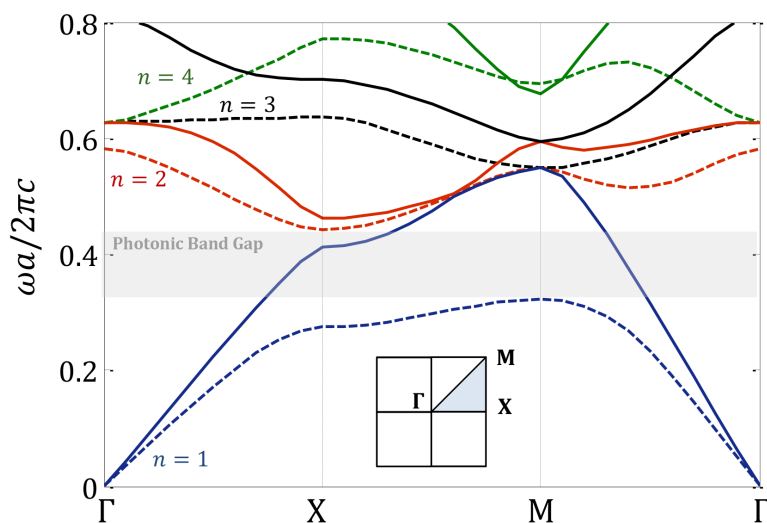


Figure 2.4: Band diagram for TM modes (solid lines) and TE modes (dashed lines) in a 2D-photonic crystal made of dielectric rods ( $\epsilon_d = 8.9$ ) embedded in air. The rod, with radius is  $0.2d$ , are placed in a squared lattice. [5]

## 2.5 Metamaterials

Metamaterials are artificial structures whose building elements are arranged periodically on a subwavelength scale. Thus, under the subwavelength regime, the periodic material can be considered as a homogeneous material whose constitutive parameters can be obtained applying homogenization theories. By using electrically small inclusions, compared to the operation wavelength, one can create artificial materials with unusual characteristics not found in natural materials [6] [7]. The special properties and the possibility of tailoring their constitutive parameters have put metamaterials on the focus of many works in the last years.

In a general way, metamaterials can be classified on the basis of the behavior of their constitutive parameters,  $\mu$  and  $\epsilon$ , which define the propagation properties inside the material. Figure 2.5 represents the classification of the metamaterials. Metamaterials defined as double positive (DPS) materials have  $\epsilon > 0$  and  $\mu > 0$ . Metamaterials with one of its constitutive parameters negative are known as epsilon-negative (ENG), when  $\epsilon < 0$  and  $\mu > 0$ , or mu-negative materials (MNG), when  $\epsilon > 0$  and  $\mu < 0$ . Finally, double negative

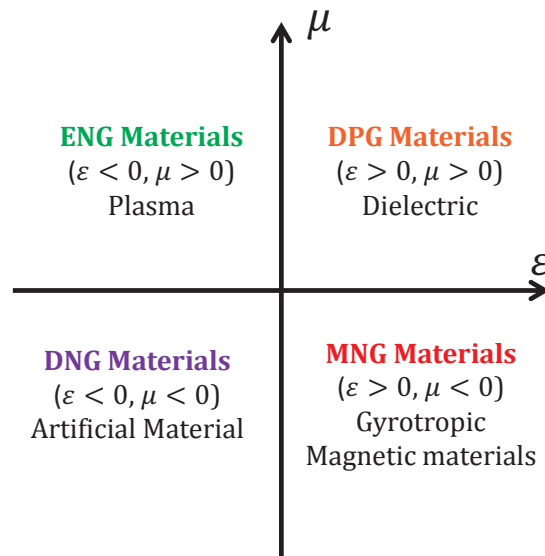


Figure 2.5: Classification of electromagnetic (EM) metamaterials [6]. Double positive (DPS), epsilon-negative (ENG), mu-negative (MNG) and double negative (DNG) materials.

(DNG) materials are characterized by having both constitutive parameters negative ( $\varepsilon < 0$  and  $\mu < 0$ ). Metamaterials have opened a way for designing new materials, being possible to obtain not only new DPS, MNG or ENG materials, also DNG materials [8].

These artificial materials have given the opportunity for many interesting applications which were not possible with natural materials. For example, W. Cai *et al.* proposed a perfect lenses based on metal-dielectric composites that allows subwavelength resolution [9]. Metamaterials have been used for the design of optical cloaks [10], making possible to avoid the perturbations produced by an object on an impinging wave. Also, EM absorption can be enhanced by using metamaterial, being possible to obtain perfect absorbers [11].

# 3

## RADIAL PHOTONIC CRYSTALS

---

The idea of a *Radial Photonic Crystal*, RPC, was introduced by D. Torrent and J. Sánchez-Dehesa in 2009 [1] [12]. Having anisotropic and radial dependent constitutive parameters, RPCs are multilayer structures which are invariant under radial translation and verify the Bloch's theorem. RPCs are different to the so called *Circular Photonic Crystals* (CPCs) where the Bloch's Theorem cannot be applied [13] [14].

This chapter describes the main features of 2D RPCs. First section discusses the applicability of the Bloch's theorem in cylindrical multilayer structures and justifies the radial dependence of the constitutive parameters in the RPCs. Then the PBS is calculated for an infinite RPC and the transmission in a RPC shell with a finite number of periods is calculated. Finally, an analysis of the resonant modes allowed in the RPC shell is presented.

### Contents

---

<b>3.1</b>	<b>Cylindrical Multilayer Shells and the Bloch Theorem . . . . .</b>	<b>26</b>
<b>3.2</b>	<b>Photonic Band Structure and Transmission Spectra . . . . .</b>	<b>29</b>
<b>3.3</b>	<b>Analysis of the RPC Resonant Modes . . . . .</b>	<b>36</b>
3.3.1	Fabry-Perot like modes . . . . .	36
3.3.2	Cavity modes . . . . .	36
3.3.3	Whispering gallery modes . . . . .	38

---



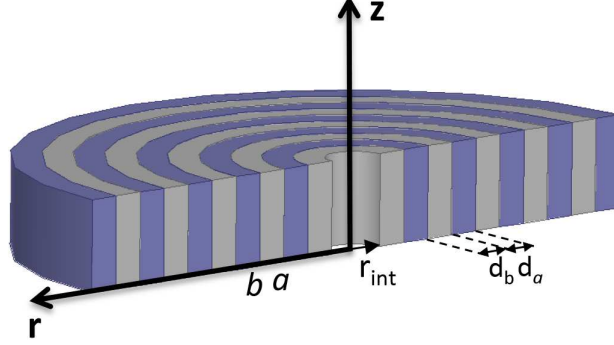


Figure 3.1: Schematic representation of a 2D cylindrical multilayer structure formed by two different materials  $a$  and  $b$  with periodicity  $d = d_a + d_b$ . The structure has a void cavity filled with the same material that the background.

### 3.1 Cylindrical Multilayer Shells and the Bloch Theorem

Considering a 2D system, both CPC and RPC are cylindrical multilayer structures. In Figure 3.1, a schematic representation of these structures is shown. To understand the originality of the RPCs and the most important differences with the CPCs, we start with the study of the propagation of  $TE$ -polarized waves in the CPC.

CPCs are composed by a radial periodic arrangement of cylindrical layer with isotropic and homogeneous materials. An example of the constitutive parameters in these structures is represented in Fig. 3.2. In these 2D structures and considering the  $TE$  polarization,  $\mathbf{E} = E_z \hat{\mathbf{z}}$ , the wave equation defined in Eq. (2.8a) can be written as follows:

$$\frac{1}{r\varepsilon(r)} \left\{ -\frac{\partial}{\partial r} \left( \frac{r}{\mu(r)} \frac{\partial}{\partial r} \right) + \frac{1}{r\mu(r)} \frac{\partial^2}{\partial \theta^2} \right\} \mathbf{E}(r, \theta) = \omega^2 \mathbf{E}(r, \theta), \quad (3.1)$$

where the constitutive parameters follow the periodicity of the system, so  $\varepsilon(r) = \varepsilon(r + d)$  and  $\mu(r) = \mu(r + d)$  (see Fig. 3.2). The electric field in an arbitrary point of the space can be factorized as:

$$\mathbf{E}(r, \theta) = \sum_q \mathbf{E}_q(r) e^{iq\theta}, \quad (3.2)$$

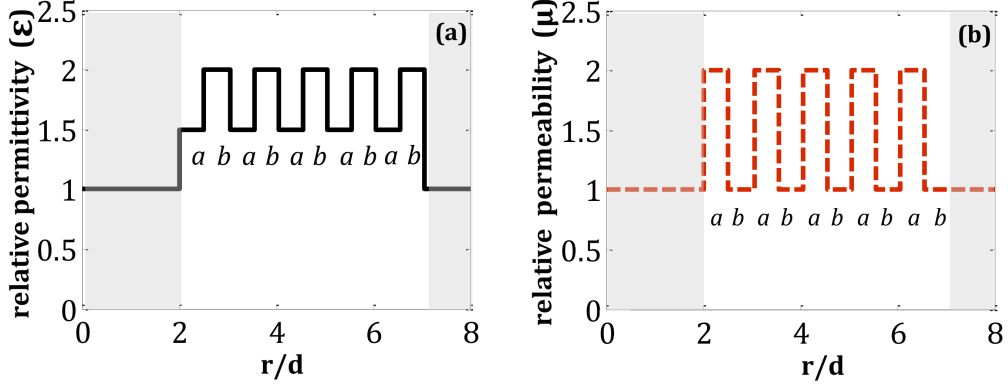


Figure 3.2: Constitutive parameters of a CPC with 5 periods (10 layers): (a) permittivity,  $\varepsilon$  and (b) permeability  $\mu$ . The layers are characterized by:  $\varepsilon_a = 1.5$ ,  $\mu_a = 2$ ,  $\varepsilon_b = 2$ ,  $\mu_b = 1$  and  $d_a = d_b$ .

where  $q = 0, 1, 2, \dots$  represents the angular variation. Using separation of variables, we obtain that the electric field  $\mathbf{E}_q(r)$  has to accomplish the following wave equation:

$$\left\{ -\frac{1}{r\varepsilon(r)} \frac{\partial}{\partial r} \left( \frac{r}{\mu(r)} \frac{\partial}{\partial r} \right) + \frac{q}{r^2\varepsilon(r)\mu(r)} \right\} \mathbf{E}_q(\mathbf{r}) = \omega^2 \mathbf{E}_q(\mathbf{r}). \quad (3.3)$$

The differential operator that takes part in this wave equation is not invariant under translation of the form  $r \rightarrow r + nd$ , being  $n$  an integer. Note that the term  $r/\mu(r)$  and  $r\mu(r)$  cannot be simultaneously periodic. As a consequence of that, the Bloch theorem cannot be applied to these structures.

By assuming that each layer is made with an anisotropic material whose constitutive parameters can be expressed in a tensorial form as

$$\boldsymbol{\varepsilon} = \begin{pmatrix} \varepsilon_r(r) & 0 & 0 \\ 0 & \varepsilon_\theta(r) & 0 \\ 0 & 0 & \varepsilon_z(r) \end{pmatrix}, \boldsymbol{\mu} = \begin{pmatrix} \mu_r(r) & 0 & 0 \\ 0 & \mu_\theta(r) & 0 \\ 0 & 0 & \mu_z(r) \end{pmatrix}, \quad (3.4)$$

the wave equation can be re-written as

$$\left\{ -\frac{1}{r\varepsilon_z(r)} \frac{\partial}{\partial r} \left( \frac{r}{\mu_\theta(r)} \frac{\partial}{\partial r} \right) + \frac{q}{r^2\varepsilon_z(r)\mu_r(r)} \right\} \mathbf{E}_q(\mathbf{r}) = \omega^2 \mathbf{E}_q(\mathbf{r}). \quad (3.5)$$

Now, the coefficients  $r/\mu_\theta(r)$ ,  $r\mu_r(r)$  and  $r\varepsilon_z(r)$  can be made simultaneously

periodic by ensuring that

$$\frac{r + nd}{\mu_\theta(r + nd)} = \frac{r}{\mu_\theta(r)}, \quad (3.6a)$$

$$(r + nd) \mu_r(r + nd) = r \mu_r(r), \quad (3.6b)$$

$$(r + nd) \varepsilon_z(r + nd) = r \varepsilon_z(r). \quad (3.6c)$$

These conditions establish that the constituent parameters have to fulfill the relations (3.7a), (3.7b) and (3.7c), where  $\hat{\mu}_\theta(r)$ ,  $\hat{\mu}_r^{-1}(r)$ ,  $\hat{\varepsilon}_z^{-1}(r)$  are periodic functions.

$$\mu_\theta(r) = r \hat{\mu}_\theta(r), \quad (3.7a)$$

$$\mu_r^{-1}(r) = r \hat{\mu}_r^{-1}(r), \quad (3.7b)$$

$$\varepsilon_z^{-1}(r) = r \hat{\varepsilon}_z^{-1}(r). \quad (3.7c)$$

In a structure periodic along the radial direction which is composed by two media,  $a$  and  $b$  with thickness  $d_a$  and  $d_b$  respectively (see Fig.3.1), we can define the vector  $X(r) \equiv [\mu_\theta(r), \mu_r^{-1}(r), \varepsilon_z^{-1}(r)]$  which contains the constituent parameters in a layer. Therefore the constitutive parameters in the structure can be expressed as:

$$X(r) = \begin{cases} r \hat{X}_a & \text{if } (n-1)d < r < (n-1)d + d_a \\ r \hat{X}_b & \text{if } (n-1)d + d_a < r < nd \end{cases} \quad (3.8)$$

where  $d = d_a + d_b$ ,  $n$  is an integer and  $\hat{X}_{a,b} \equiv [\hat{\mu}_{\theta_{a,b}}(r), \hat{\mu}_{r_{a,b}}^{-1}(r), \hat{\varepsilon}_{z_{a,b}}^{-1}(r)]$  represents the periodic functions which compose the constitutive parameters in each layer. The following set of constitutive parameters ensure the RPC condition is:

$$\mu_{\theta a}(r) = \hat{\mu}_{\theta a} r = \frac{2r}{d}, \quad \mu_{\theta b}(r) = \hat{\mu}_{\theta b} r = \frac{r}{d}, \quad (3.9a)$$

$$\mu_{r a}(r) = \frac{\hat{\mu}_{r a}}{r} = \frac{0.25d}{r}, \quad \mu_{r b}(r) = \frac{\hat{\mu}_{r b}}{r} = \frac{0.5d}{r}, \quad (3.9b)$$

$$\varepsilon_{z a}(r) = \frac{\hat{\varepsilon}_{z a}}{r} = \frac{d}{1.5r}, \quad \varepsilon_{z b}(r) = \frac{\hat{\varepsilon}_{z b}}{r} = \frac{d}{r}. \quad (3.9c)$$

These parameters are represented in Fig. 3.3. Note that the inner void cavity is necessary to avoid the divergence of the constitutive parameters. Under these conditions, the new differential operator is invariant under translation in  $\hat{r}$  and the Bloch's theorem can be applied in cylindrical coordinates.

We can express the wave equation in each layer by introducing the Eq. (3.8) in Eq. (B.2).

$$\frac{\partial^2 E_q(r)}{\partial r^2} + [\omega^2 \hat{\epsilon}_{iz} \hat{\mu}_{i\theta} - q^2 \frac{\hat{\mu}_{i\theta}}{\hat{\mu}_{ir}}] E_q(r) = 0, \quad (3.10)$$

These equations have plane-wave solutions and the dispersion relation in each layer can be expressed as:

$$k_{iq}^2 = [\omega^2 \hat{\epsilon}_{iz} \hat{\mu}_{i\theta} - q^2 \frac{\hat{\mu}_{i\theta}}{\hat{\mu}_{ir}}], \quad i = a, b. \quad (3.11)$$

Applying the Bloch's theorem, the general solution for the electric field is

$$E_q(r) = \sum_G e^{iKr} e^{iGr} \quad (3.12)$$

where  $G = 2\pi n/d$  is the reciprocal lattice and  $K$  represent a Bloch wave vector.

For the TM mode the same procedure can be followed but with the magnetic field. In this case, the vector  $X(r) \equiv [\varepsilon_\theta(r), \varepsilon_r^{-1}(r), \mu_z^{-1}(r)]$  the wave equation for the magnetic field is

$$\frac{\partial^2 H_q(r)}{\partial r^2} + [\omega^2 \hat{\mu}_{iz} \hat{\epsilon}_{i\theta} - q^2 \frac{\hat{\epsilon}_{i\theta}}{\hat{\epsilon}_{ir}}] H_q(r) = 0, \quad (3.13)$$

where,

$$k_{iq}^2 = [\omega^2 \hat{\mu}_{iz} \hat{\epsilon}_{i\theta} - q^2 \frac{\hat{\epsilon}_{i\theta}}{\hat{\epsilon}_{ir}}], \quad i = a, b. \quad (3.14)$$

## 3.2 Photonic Band Structure and Transmission Spectra

This section, reports a theoretical study of the wave propagation in RPCs. We use the TMM to obtain the photonic band structure and the transmission spectra. This method has been widely used for the study of 1D periodic media [4]. In our case due to the complexity of the RPCs some modifications have to be introduced [15].

According to Eq. (3.10), the electric fields inside each layer of the RPC shell can be expressed as a sum of incident plane wave and reflected plane waves as follows:

$$E_q(r) = [(C_q^+)_{ln} e^{ik_{iq}(r'-nd)} + (C_q^-)_{ln} e^{-ik_{iq}(r'-nd)}] e^{iq\theta}, \quad (3.15)$$

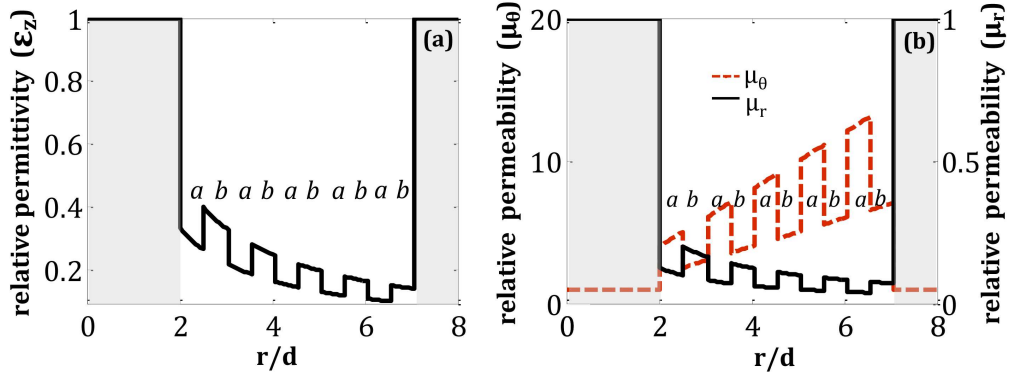


Figure 3.3: Profiles of the constitutive parameters in RPC with 5 periods (10 layers) with  $d_a = d_b$ : (a) permittivity,  $\epsilon_z$  and (b) permeability  $\mu_\theta$  and  $\mu_r$ . Material *a*:  $\hat{\mu}_{a\theta} = 2/d$ ,  $\hat{\mu}_{ar} = 0.25d$  and  $\hat{\epsilon}_{az} = d/1.5$ . Material *b*:  $\hat{\mu}_{b\theta} = 1/d$ ,  $\hat{\mu}_{br} = 0.5d$  and  $\hat{\epsilon}_{bz} = d/1$ .

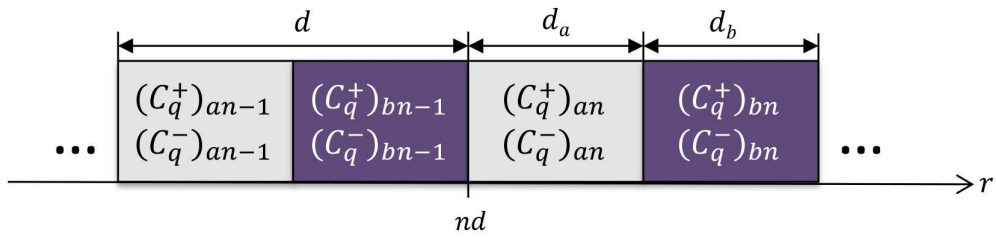


Figure 3.4: Infinite slab. Plane wave amplitudes associated with the  $n^{\text{th}}$  unit cell and its neighboring cells.

where the wave numbers  $k_{lq}$  are defined in the Eq. (3.11),  $r' = r - r_i n t$ ,  $n = 1, 2, \dots, N$  and  $l$  defines the materials  $a$  and  $b$ . Figure 3.4 shows the definition of wave amplitudes.

The electric fields in two consecutive layers are related through the corresponding boundary conditions. Thus, for the  $TE$  polarized modes under study, the boundary conditions are reported in Eq. (2.17) and Eq. (2.18). These conditions are imposed at the interfaces of the unit cell. Therefore, the matrix relating the complex amplitudes of the plane waves in a b-layer with those of the equivalent layer of the next unit cell is:

$$\begin{pmatrix} (C_q^+)_{bn-1} \\ (C_q^-)_{bn-1} \end{pmatrix} = \begin{pmatrix} A & B \\ C & D \end{pmatrix} \begin{pmatrix} (C_q^+)_{bn} \\ (C_q^-)_{bn} \end{pmatrix}, \quad (3.16)$$

where the transmission matrix ABCD elements are:

$$A = e^{-ik_{bq}d_b} \left[ \cos(k_{aq}d) - \frac{1}{2}i \left( \frac{\hat{\mu}_{\theta b} k_{aq}}{\hat{\mu}_{\theta a} k_{bq}} - \frac{\hat{\mu}_{\theta a} k_{bq}}{\hat{\mu}_{\theta b} k_{aq}} \right) \sin(k_{aq}d_a) \right], \quad (3.17)$$

$$B = e^{ik_{bq}d_b} \left[ -\frac{1}{2}i \left( \frac{\hat{\mu}_{\theta b} k_{aq}}{\hat{\mu}_{\theta a} k_{bq}} - \frac{\hat{\mu}_{\theta a} k_{bq}}{\hat{\mu}_{\theta b} k_{aq}} \right) \sin(k_{aq}d_a) \right], \quad (3.18)$$

$$C = e^{-ik_{bq}d_b} \left[ \frac{1}{2}i \left( \frac{\hat{\mu}_{\theta b} k_{aq}}{\hat{\mu}_{\theta a} k_{bq}} - \frac{\hat{\mu}_{\theta a} k_{bq}}{\hat{\mu}_{\theta b} k_{aq}} \right) \sin(k_{aq}d_a) \right], \quad (3.19)$$

$$D = e^{ik_{bq}d_b} \left[ \cos(k_{aq}d) + \frac{1}{2}i \left( \frac{\hat{\mu}_{\theta b} k_{aq}}{\hat{\mu}_{\theta a} k_{bq}} - \frac{\hat{\mu}_{\theta a} k_{bq}}{\hat{\mu}_{\theta b} k_{aq}} \right) \sin(k_{aq}d_a) \right]. \quad (3.20)$$

Taking into account that inside the RPC we can apply the Bloch's theorem, the periodic condition can be written as:

$$\begin{pmatrix} (C_q^+)_{bn} \\ (C_q^-)_{bn} \end{pmatrix} = e^{iKd} \begin{pmatrix} (C_q^+)_{bn-1} \\ (C_q^-)_{bn-1} \end{pmatrix}. \quad (3.21)$$

It follows from the Eqs. (3.16) and (3.21) that the column vector for the Bloch wave satisfies the following eigenvalue problem:

$$\begin{pmatrix} A & B \\ C & D \end{pmatrix} \begin{pmatrix} (C_q^+)_{bn} \\ (C_q^-)_{bn} \end{pmatrix} = e^{iKd} \begin{pmatrix} (C_q^+)_{bn} \\ (C_q^-)_{bn} \end{pmatrix}. \quad (3.22)$$

The eigenvalue of the translational matrix is given by

$$e^{iKd} = \frac{1}{2}(A + D) - \sqrt{\left[\frac{1}{2}(A + D)\right]^2 - 1}. \quad (3.23)$$

The dispersion relation is given by

$$\begin{aligned} \cos(Kd) = \cos(k_{aq}d_a) \cos(k_{bq}d_b) + \\ \frac{1}{2} \left( \frac{\hat{\mu}_{\theta b} k_{aq}}{\hat{\mu}_{\theta a} k_{bq}} + \frac{\hat{\mu}_{\theta a} k_{bq}}{\hat{\mu}_{\theta b} k_{aq}} \right) \sin(k_{aq}d_a) \sin(k_{bq}d_b) \end{aligned} \quad (3.24)$$

The solution for this equation using the parameters described in Eqs.(4.1) is displayed in Fig. 3.6(a), where  $q$  denotes the symmetry order of the modes in the corresponding band. Note that each band contains modes with well-defined symmetry. In addition, note that modes with coefficient  $q > 0$  have a cutoff frequency higher than zero. Also, part of the  $q = 1$  band (with dipolar symmetry modes) is inserted within the first band gap of mode  $q = 0$  (with monopolar modes).

Let us stress that by changing the material parameters in Eq. (4.1) it is possible to perform band gap engineering and design photonic structures that fit our needs. For example, in Fig. 3.6(a) we observe that part of the modes with dipolar symmetry ( $q = 1$ ) are in the band gap of the rest of modes. This implies that only dipolar modes will be excited by external sources in the frequency region  $[0.38, 0.55]$  (in reduced units). This feature can be extremely useful for designing photonic devices based on finite size RPCs.

Now, considering a finite slab with  $N$  periods, the electric field inside the RPC shell will be defined as in Eq. (3.15) and, in turn, the electric field in the homogeneous and isotropic media can be represented by a linear combination of Bessel and Hankel functions:

$$E_q = \left[ C_{iq}^+ H_q(k_i r) + C_{iq}^- J_q(k_i r) \right] e^{iq\theta}, \quad (3.25)$$

where  $k_i^2 = \omega^2 \varepsilon_i \mu_i$  with  $i = 1, 2$ .  $J_q(kr)$  and  $H_q(kr)$  are the Bessel and Hankel function of order  $q$  (See Appendix A.1). Material 1 and 2 are the materials inside the inner and in the external background, respectively. Note that this expression allows us to obtain the field produced by external sources

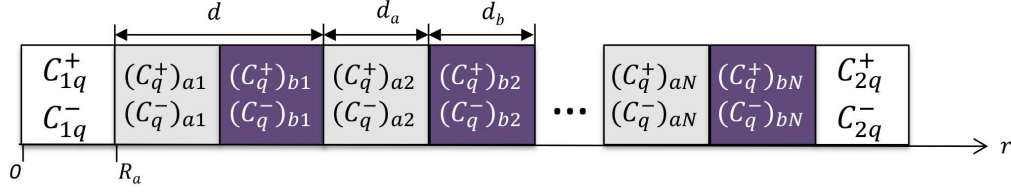


Figure 3.5: Finite slab. Amplitudes associated with each layer in a slab with  $N$  periods.

located at any position inside the cavity ( $r < r_{int}$ ). Figure 3.5 shows the field amplitude in this system.

For the case of a RPC shell made of  $N$  unit cells, the following relation applies:

$$\begin{pmatrix} (C_q^+)_{b1} \\ (C_q^-)_{b1} \end{pmatrix} = \begin{pmatrix} A & B \\ C & D \end{pmatrix}^N \begin{pmatrix} (C_q^+)_{bN} \\ (C_q^-)_{bN} \end{pmatrix}. \quad (3.26)$$

The continuity conditions at the interface between the inner cavity (medium 1) and the RPC shell produce the following transition matrix:

$$\begin{pmatrix} C_{1q}^+ \\ C_{1q}^- \end{pmatrix} = \frac{i\pi\mu_1}{2} \begin{pmatrix} J'_q(k_1 R_a) & -J_q(k_1 R_a) \\ -H'_q(k_1 R_a) & H_q(k_1 R_a) \end{pmatrix} \begin{pmatrix} 1 & 1 \\ Z_1 & -Z_1 \end{pmatrix} \begin{pmatrix} (C_q^+)_{b0} \\ (C_q^-)_{b0} \end{pmatrix}, \quad (3.27)$$

where

$$Z_1 = i \frac{\mu_1 k_{bq}}{k_1 \hat{\mu}_{\theta b} R_a}. \quad (3.28)$$

The boundary conditions at the interface between the RPC shell and the external background (medium 2) give the second transmission matrix:

$$\begin{pmatrix} (C_q^+)_{bN} \\ (C_q^-)_{bN} \end{pmatrix} = \frac{1}{2} \begin{pmatrix} 1 & 1 \\ 1 & -1 \end{pmatrix} \begin{pmatrix} H_q(k_2 R_b) & J_q(k_2 R_b) \\ Z_2 H'_q(k_2 R_b) & Z_2 J'_q(k_2 R_b) \end{pmatrix} \begin{pmatrix} C_{2q}^+ \\ C_{2q}^- \end{pmatrix}, \quad (3.29)$$

with

$$Z_2 = -i \frac{k_2 \hat{\mu}_{\theta b} R_b}{\mu_2 k_{bq}}. \quad (3.30)$$

Finally, the complex amplitudes of the  $E$  field in the inner cavity and in the external background are related by the end-to-end relation:

$$\begin{pmatrix} C_{1q}^+ \\ C_{1q}^- \end{pmatrix} = \begin{pmatrix} M_{11} & M_{12} \\ M_{21} & M_{22} \end{pmatrix} \begin{pmatrix} C_{2q}^+ \\ C_{2q}^- \end{pmatrix}, \quad (3.31)$$



$$M = \frac{i\pi\mu_1}{4 \sin Kd} \begin{pmatrix} J'_q(k_1 R_a) & -J_q(k_1 R_a) \\ -H'_q(k_1 R_a) & H_q(k_1 R_a) \end{pmatrix} \begin{pmatrix} A_N & B_N \\ C_N & D_N \end{pmatrix} \times \begin{pmatrix} H_q(k_2 R_b) & J_q(k_2 R_b) \\ Z_2 H'_q(k_2 R_b) & Z_2 J'_q(k_2 R_b) \end{pmatrix}. \quad (3.32)$$

The  $N$  power of the matrix follows the following relation

$$\begin{pmatrix} A_N & B_N \\ C_N & D_N \end{pmatrix} = \begin{pmatrix} A & B \\ C & D \end{pmatrix}^N = \begin{pmatrix} AU_{N-1} - U_{N-2} & BU_{N-1} \\ CU_{N-1} & DU_{N-1} - U_{N-2} \end{pmatrix}, \quad (3.33)$$

where  $U_N = \sin(N+1)Kd / \sin(Kd)$ . The  $ABCD$  matrix elements are calculated as:

$$A_N = \left[ 2 \cos(Kd) + \left( \frac{\hat{\mu}_{\theta b} k_{aq}}{\hat{\mu}_{\theta a} k_{bq}} - \frac{\hat{\mu}_{\theta a} k_{bq}}{\hat{\mu}_{\theta b} k_{aq}} \right) \sin(k_{aq} d_a) \sin(k_{bq} d_b) \right] \sin(NKd) - 2 \sin((N-1)Kd) \quad (3.34)$$

$$B_N = -2i \left[ \cos(k_{aq} d_a) \sin(k_{bq} d_b) + \frac{\hat{\mu}_{\theta a} k_{bq}}{\hat{\mu}_{\theta b} k_{aq}} \sin(k_{aq} d_a) \sin(k_{bq} d_b) \right] \quad (3.35)$$

$$C_N = -2Z_1 i \left[ \cos(k_{aq} d_a) \sin(k_{bq} d_b) + \frac{\hat{\mu}_{\theta b} k_{bq}}{\hat{\mu}_{\theta a} k_{bq}} \sin(k_{aq} d_a) \sin(k_{bq} d_b) \right] \quad (3.36)$$

$$D_N = Z_1 \left[ 2 \cos(Kd) - \left( \frac{\hat{\mu}_{\theta b} k_{aq}}{\hat{\mu}_{\theta a} k_{bq}} - \frac{\hat{\mu}_{\theta a} k_{bq}}{\hat{\mu}_{\theta b} k_{aq}} \right) \sin(k_{aq} d_a) \sin(k_{bq} d_b) \right] \sin(NKd) - 2 \sin((N-1)Kd) \quad (3.37)$$

The  $M$  matrix is employed to determine the transmittance,  $T_q$  and the reflectance  $R_q$  of modes with  $q$  symmetry from the RPC shell. Their expressions are

$$T_q = \frac{1}{M_{11}} \quad (3.38)$$

and

$$R_q = \frac{M_{21}}{M_{11}}. \quad (3.39)$$

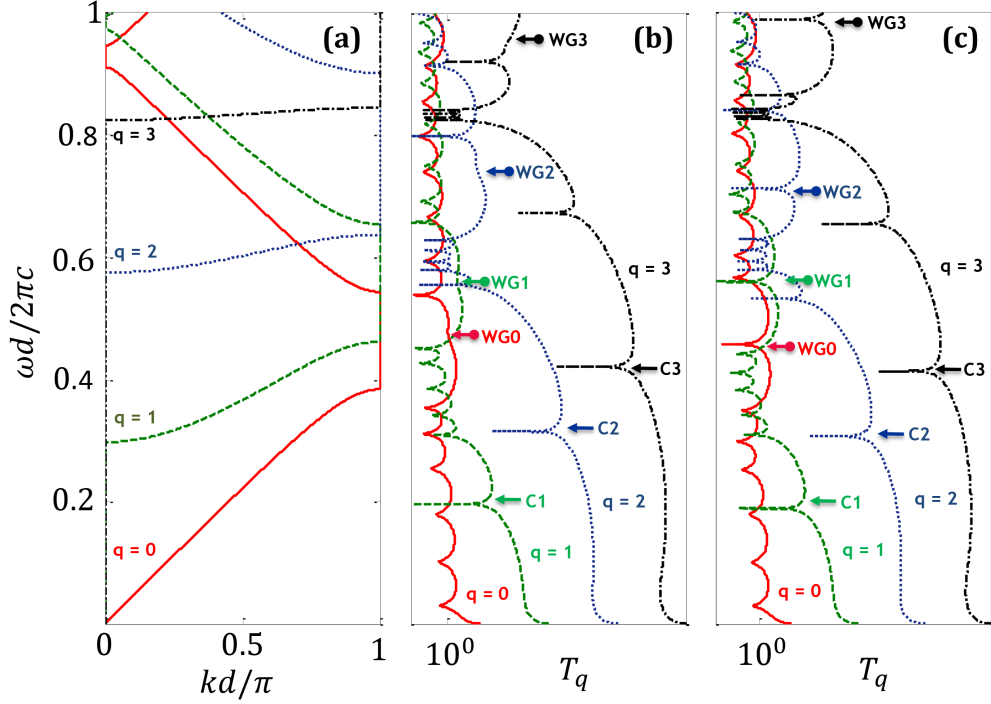


Figure 3.6: (Color online) (a) Photonic band structure for the radial photonic crystal described in Sec. II. (b) Calculated transmission coefficients  $T_q$  for the five period metamaterial shell described in Fig. 3.3. (c) Calculated transmission coefficients  $T_q$  for a structure similar to Fig. 1 but with inverted a and b layer order (abab... changes to baba...).

Let us recall that these coefficients always refer to the radial propagation direction. The quality factor,  $Q$  of a given resonant mode can also be obtained from the matrix element  $M_{11}(\omega)$  and involves the calculation of the complex frequencies  $\omega_R$  that cancel this matrix element:  $M_{11}(\omega_R) = 0$ , where  $\omega_R = \omega_0 - i\alpha$ . Then, the  $Q$  factor can be calculated from the real and imaginary parts of the resonance frequency as  $Q = \frac{\omega_0}{2\alpha}$ . In the rest of this chapter, unless otherwise indicated,  $Q$  factors are calculated following this procedure.

The transmission properties of the shell are depicted in Fig. 3.6(b) and Fig. 3.6(c). The difference between both cases only comes from the layer ordering. In Fig. 3.6(b), layer profiles exactly follow the data in Fig. 3.3, whereas in Fig. 3.6(c) the order between a and b layers is inverted. Thus, in Fig. 3.6(b), the inner layer is of a type and outer layer is of b type, but in

Fig. 3.6(c) it is the opposite. The different curves represent the transmittance coefficients  $T_q$  for the total transmitted electrical field,  $E_z^t$ , whose expression is

$$E_z^t = \sum_q A_q^0 T_q H_q(k_0 r) e^{iq\theta}, \quad (3.40)$$

where  $A_{0q}$  represent the amplitudes of the incident wave modes,  $T_q$  give information about the interaction between EM waves and the RPC shell. Note that a given  $T_q$  curve is specifically related to the allowed band with the same  $q$  symmetry in the dispersion diagram shown in Fig.3.6(a). The peaks observed in a selected  $T_q$  spectrum represent the resonant modes with  $q$  symmetry in the shell.

### 3.3 Analysis of the RPC Resonant Modes

The resonant modes associated with these RPC shells can be characterized as Fabry-Perot, cavity, and whispering gallery modes. The Fabry-Perot-like modes are located in the RPC shell, cavity modes exist at the central cavity whose features are equivalent to those predicted for cylindrical cavities and whispering gallery modes are the third type of resonant modes existing in these structures and they are localized close to the interfaces at the inner and outer boundaries of the RPC shell with the background. This main purpose of this section is the study of these resonances.

#### 3.3.1 Fabry-Perot like modes

If the deeps of coefficients  $T_q$  appear at frequencies within the photonic bands of the corresponding dispersion relation [see Fig. 3.6(a)], they are produced by a Fabry-Perot (FP) interference phenomenon due to the shell finite thickness. Figure 3.7(a) plots, as an example, the E-field pattern of a FP mode with dipolar symmetry ( $q = 1$ ). Note that the field is mainly located inside the shell; i.e., within positions  $r_{int} < r < 5d$ . The FP-like resonances have been widely studied in previous works. For a detailed discussion of their properties and their potential application the reader is addressed to the references [1] and [16].

#### 3.3.2 Cavity modes

When the deeps in  $T_q$  appear within the bandgap of the photonic band with a given symmetry, they represent modes that are confined in the central

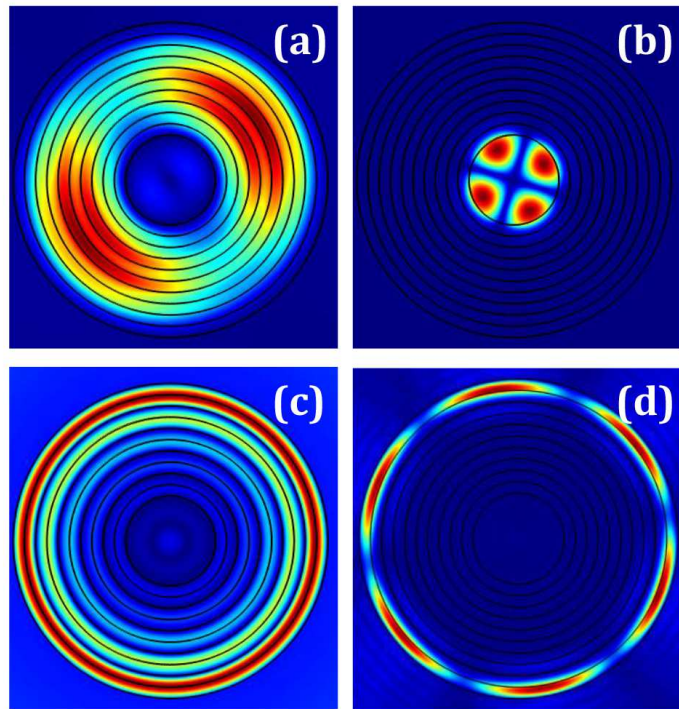


Figure 3.7: Resonant modes found in the 5 period RPC-shell described in Fig. 1: (a) Fabry-Perot like mode with symmetry  $q = 1$  and frequency 0.3101 (in reduced units), (b) cavity mode with symmetry  $q = 2$  and frequency 0.3157 (C2 in Fig.3.6(b)), (c) whispering gallery mode with symmetry  $q = 0$  and frequency 0.4724 (WG0 in Fig. 3.6(b)), and (d) whispering gallery mode with symmetry  $q = 3$  and frequency 0.9442 (WG3 in Fig. 3.6(b)).

void region. For example, Fig. 3.6(b) shows that deep C1 appearing in the profile of the spectrum  $q = 1$  (dashed line) corresponds to a cavity mode with dipolar symmetry. C1 has frequency 0.1971 which is below the cutoff of the corresponding band in Fig. 3.6(a). In a similar manner, deeps C2 and C3 with frequencies 0.3157 and 0.4156, respectively, are due to the presence of cavity modes with quadrupolar ( $q = 2$ ) and hexapolar symmetry ( $q = 3$ ). Figure 3.7(b) displays as an example the E-field pattern corresponding to the cavity mode with quadrupolar symmetry ( $q = 2$ ). Let us stress that cavity modes are strictly related to the size of the inner cavity and, as it is shown in Fig.3.7(b), they are strongly localized inside the cavity.

### 3.3.3 Whispering gallery modes

In addition to the resonant modes previously described we have observed additional features in the transmission spectra that have been associated to whispering gallery (WG) modes. The shoulders annotated in Fig. 3.6(b) as WG0, WG1, WG2 and WG3 are produced by resonant modes characterized for having their E-field mainly localized in the last layer of the shell, as it is usual for the WG described in the literature. The frequencies of modes WG0, WG1, WG2 and WG3 have been obtained independently using a method based on finite elements and their values are 0.4724, 0.5607, 0.7667 and 0.9442 (in reduced units). These values are in agreement with the frequencies at which the shoulders appear in the corresponding  $T_q$  (with  $q = 0$  to 3).

The WG modes are characterized by two main properties. On the one hand, their frequencies are always within the bandgap of the photonic bands with the same symmetry. On the other hand, they appear in a truncated RPC with a void cavity at its center. In other words, the structures sustaining WG modes are anisotropic shells having two boundaries with the background. For the case under study here, the external and inner borders are at  $r_{ext} = 7d$  and  $r_{int} = 2d$ , respectively. Figures 3.7(c) and 3.7(d) plot, as two typical examples, the E-field patterns of WG-type modes with symmetries  $q = 0$  and  $q = 3$ , respectively; WG0 and WG3 in Fig. 3.6(b). It is shown that E-fields are mainly localized at the shell inner and outer layers, respectively.

Figure 3.8(a) specifically shows the E-field profile, along the diameter crossing the horizontal axis, for the mode WG0 with frequency 0.4724. A comparison with the profiles of the components of the refractive index tensor,

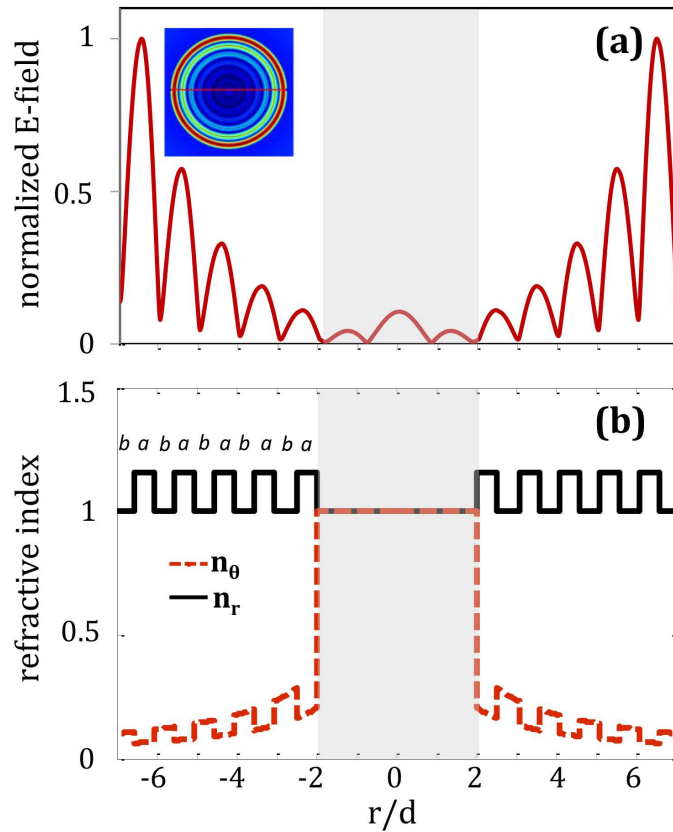


Figure 3.8: (a) The E-field profile along a diameter section of a WG mode located at the outer layer of the 5 period RPC shell described in Fig. 3.3. The monopolar mode  $WG_0$  with frequency 0.4724 is depicted. Note how the field amplitude exponentially decreases with the separation from the external boundary. The inset shows the E-field pattern in 2D for comparison purposes. (b) Radial dependence of the radial and angular components of the refractive index tensor.

which are shown in Fig. 3.8(b), indicates that localization takes place in the last period, where the last layer is b-type (with  $n_r = 1$ ). At this point it is interesting to remain that the so called Tamm states were observed at the interface between a multilayered dielectric structure and the background. The Tamm states are strongly localized at the last layers of the multilayers due to the high contrast between the refractive index of the last layers and the background. In contrast, our WG modes, these being a kind of surface states with circular symmetry, are slightly localized and, therefore, highly radiative.

WG modes localized in the shell inner layer can be also obtained by simply inverting the sequence of alternating a- and b-type layers. Figure 3.9(a) shows the case of a WG mode with monopolar symmetry ( $q = 0$ ) that has been obtained using an inner layer b-type and an outer layer a-type. The inset shows the 2D field pattern of this mode that resonates at 0.4575 (in reduced units), a value very close to that of the WG0 mode localized in the outer layer of the shell. The high concentration of field observed inside the cavity is due to the leaky nature of this mode in combination with the fact that its wavelength is commensurate with the cavity diameter ( $\phi = 2r_{int}$ ); i.e.,  $\phi \approx 3\lambda/2$ . The radial E-field profile shown in Fig. 3.9(a) in comparison with the radial dependence of components  $n_r$  and  $n_\theta$  (as shown in Fig. 3.9(b)) let us to conclude that localization of these types of modes is strongly related with regions with high  $n_\theta$ .

It has been pointed out that a main feature of WG modes found in RPC shells is that they are strongly radiative. In other words, they have very low Q-factors, a property of paramount interest in building devices for energy harvesting. The Q-factors of WG modes are specifically studied in the next section in comparison with the Q-factors of cavity and FP resonances.

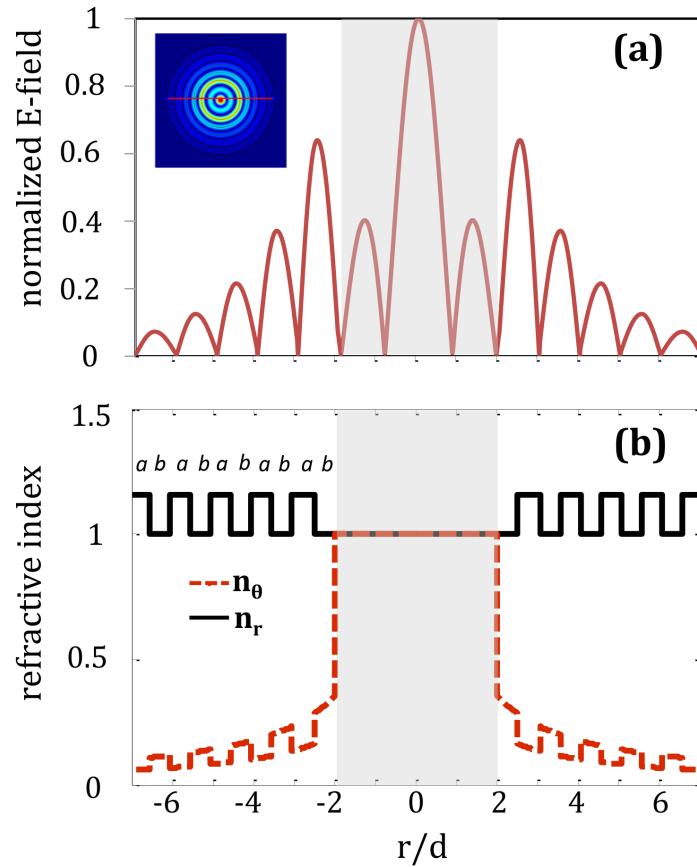


Figure 3.9: (a) The E-field profile along a diameter section of a WG mode located at the inner layer of the 5 period RPC shell with inverted sequence (*a*-type and *b*-type layers have been exchanged with respect to Fig. 3.3). The monopolar WG0 mode with frequency 0.4575 is depicted. Note the high concentration of the field in the cavity due to the leaky nature of this mode. The insets show the E-field pattern in 2D for comparison purposes. (b) Radial dependence of the radial and angular components of the refractive index tensor.





# 4

## RPC APPLICATIONS

---

It has been shown that RPC shells have rich resonant properties which can be tailored to adjust the behavior for different applications. In this chapter, we will present three different applications in which the RPC resonant properties can be employed.

First, in section 4.1, we will comprehensively study the use of WGMs for increasing the EM field concentration and enhancing energy harvesting. Then, in section 4.2, we will review the requirements needed in wireless power transfer systems and we will propose a solution for the Wireless Power Transfer problem by means of the FP modes of the RPC. Finally, in section 4.3, the use of the RPC shell as position sensors will be theoretically and experimentally studied.

### Contents

---

<b>4.1</b>	<b>Energy Harvesting</b> . . . . .	<b>44</b>
<b>4.2</b>	<b>Wireless Power Transfer</b> . . . . .	<b>53</b>
<b>4.3</b>	<b>Position Sensors</b> . . . . .	<b>68</b>
4.3.1	Analysis of the frequency shift . . . . .	82

---

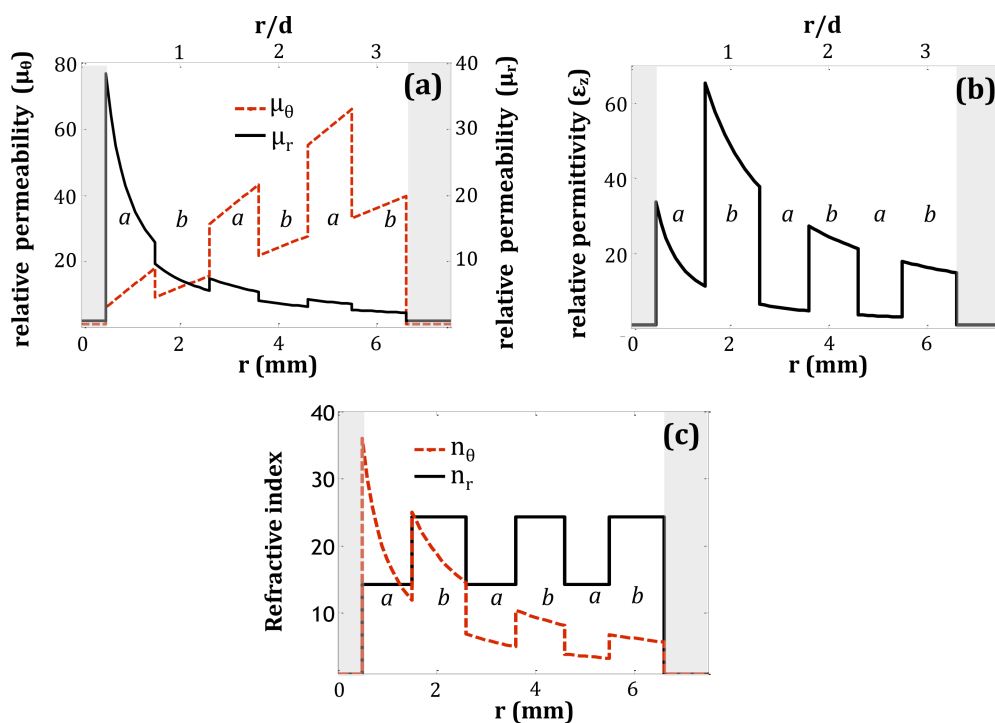


Figure 4.1: Profiles of the constitutive parameters defining an anisotropic metamaterial shell made of three periods of alternating materials and having a central cavity with radius  $r_{int} = d/4$ . (a) Radial and angular permeabilities  $\mu_r$  and  $\mu_\theta$ , (b) permittivity  $\epsilon_z$ , and (c) radial and angular components of the refractive index  $n_r$  and  $n_\theta$ , respectively.

## 4.1 Energy Harvesting

Energy absorption and harvesting are topics deeply studied in the last years for their use with acoustic, electromagnetic or thermal energy. For harvesting energy it is necessary a system which concentrates the surrounding energy and allows its conversion to AC voltage by a conversion medium. In this work, the concept of energy harvesting is considered as the ability of a given structure of exchanging and trapping EM energy from the surrounding medium. In this sense, artificially structured materials have shown potential advantages as concentrator devices due to their exotic properties which are not found in natural materials [17] [18]. In the literature, it has been demonstrated that low- $Q$  resonant modes in spherical nanoshells can be used for

facilitating the coupling of light and improve the absorption [19]. Also, 2D magnetic shells have been proposed for collecting the energy in the void core and boosting the energy harvest [20]. In this section, an specific configuration of RPC-shells that enhances the energy exchange between their resonant WG modes with the background EM fields will be studied.

A metamaterial shell is here designed for operating at frequencies around  $f = 3$  GHz (i.e., for wavelengths around  $\lambda = 100$  cm). The shells under study have radial period  $d = 2$  mm, ( $d_a = d_b = d/2$ ), the central cavity has radius  $r_{int} = 0.5$  mm ( $r_{int} = d/4$ ), and the constitutive parameters of its layers are:

$$\mu_{ra}(r) = \frac{9.6d}{r}, \quad \mu_{rb}(r) = \frac{7.2d}{r}, \quad (4.1a)$$

$$\mu_{\theta a}(r) = \frac{24r}{d}, \quad \mu_{\theta b}(r) = \frac{12r}{d}, \quad (4.1b)$$

$$\varepsilon_{za}(r) = \frac{8.4d}{r}, \quad \varepsilon_{zb}(r) = \frac{49d}{r}. \quad (4.1c)$$

These parameters are selected to produce WG modes with extremely low Q-factors. The profiles for these parameters together with those of the components of the refractive index tensor are described in Fig.4.1(a) to Fig. 4.1(c).

For the sake of comparison, the Q-factors of the FP-like modes and cavity modes have been also calculated as a function of the number  $N$  of double layers. Results have been obtained using the TMM described in Chapter 3 and have been compared with the ones calculated using a commercial software (COMSOL). Only radiation losses are considered in all the calculations. The possible dissipative losses associated with materials have been neglected in this study.

Figures 4.2(a) and 4.2(b) show the results obtained for the frequencies and Q-factors, respectively, of the FP-like modes. Modes with monopolar ( $q = 1$ ), dipolar ( $q = 2$ ) and hexapolar ( $q = 3$ ) symmetry are studied. The FP-like mode for a given symmetry corresponds with the lowest frequency mode within the pass band. Note the excellent agreement between the values calculated with the TMM (dashed lines) and the COMSOL simulations (continuous lines). The main feature of these modes is the slight variation of the frequency as a function of the number of layers (upper panel) and also small variation of the Q-factor (less than one order of magnitude). The high values

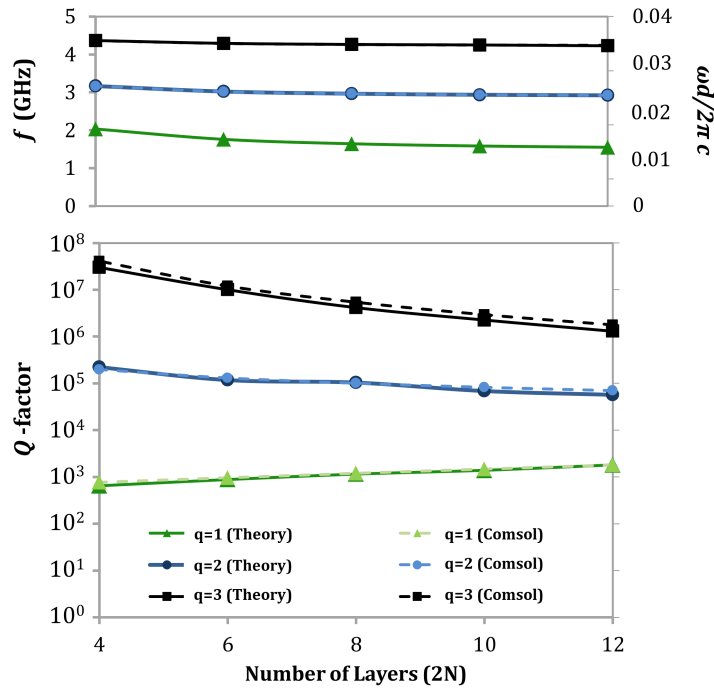


Figure 4.2: Frequency variation (a) and quality factor  $Q$  variation (b) as a function of the number  $N$  of periods for the Fabry-Perot resonances located in the shell described in Fig. 4.1. The radius of the cavity being  $r_{int} = 0.5$  mm. Results from a commercial software (COMSOL) are compared with the transfer matrix method (TMM).

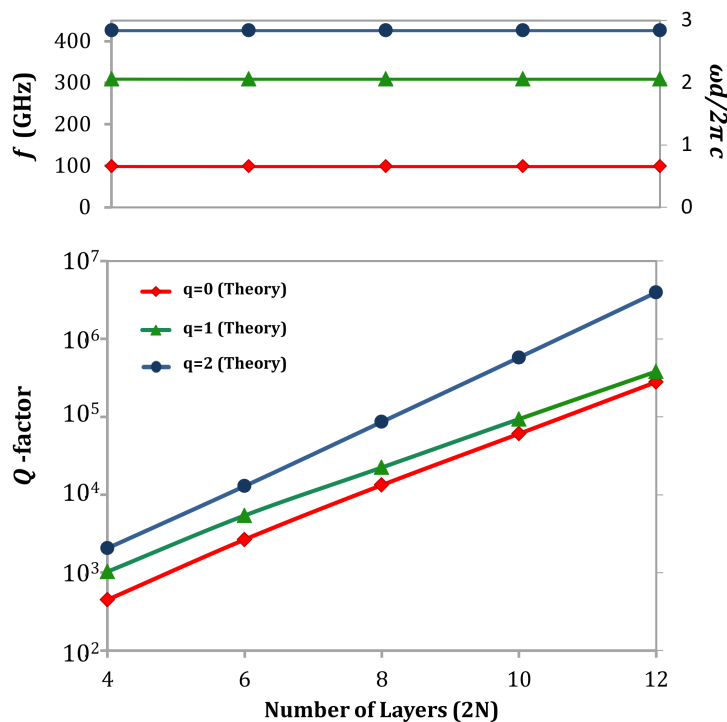


Figure 4.3: Frequency variation (a) and quality factor  $Q$  variation (b) as a function of the number  $N$  of periods for the modes located in the inner void cavity of the shell described in Fig. 4.1. The radius of the cavity being  $r_{int} = 0.5$  mm. Results are obtained with the transfer matrix method (TMM).

and almost constant of the  $Q$ -factor make these modes not appropriate for use in field concentrators for the energy harvesting.

Figure 4.3 shows the results corresponding to cavity modes. Figure 4.3(a) shows that their frequencies remain constant as a function of  $N$  and are very high in comparison with that of FP modes. High frequency values are due to the small dimension of the cavity. For this case only TMM calculations are reported since the commercial software, which is based on finite elements method, is not efficient with large electrical size objects. Figure 4.3(b) shows that their  $Q$ -factors exponentially increase with  $N$ , which can be understood as a consequence of the exponential decaying behavior of the E-field within the photonic bandgap. Due to the extremely high  $Q$ -factors of the cavity modes, the exchange of energy between the cavity and the background is not

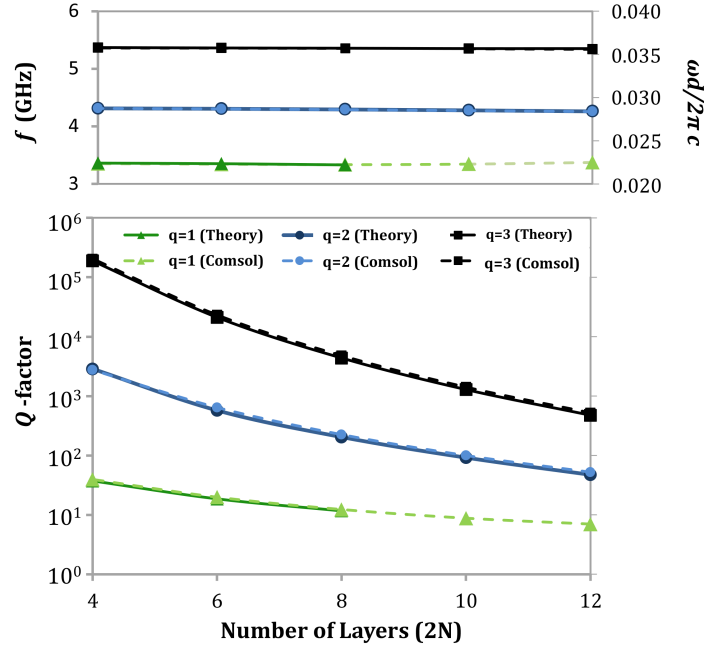


Figure 4.4: Frequency variation (a) and quality factor  $Q$  variation (b) as a function of the number  $N$  of periods for the outer interface whispering gallery resonances located in the shell described in Fig. 4.1. The radius of the cavity being  $r_{int} = 0.5$  mm. Results from a commercial software (COMSOL) are compared with the transfer matrix method (TMM).

avored, so these modes cannot be used for energy harvesting.

Figure 4.4 reports the properties of WG modes localized at the outer surface as a function of  $N$ . Figure 4.4(a) shows that their frequencies have a negligible dependence with the shell thickness. Their values for  $N = 2$  (4 layers) are 3.35 GHz (WG1), 4.29 GHz (WG2) and 5.36 GHz (WG3). Again, results obtained with our analytical TMM are well supported by the numerical experiments using COMSOL.

Figure 4.4(b) indicates that the  $Q$  factors decrease with the thickness of the shell, an interesting feature that can be useful for energy harvesting. We may provide an intuitive explanation for this observed feature. The decreasing values of  $Q$  when the size of the shell increases are related to the occurrence of WGMs in the band gaps of the multilayer shell. It is clear that in the respective band gap propagation of the EM wave of the WG mode

in the radial direction and towards the center of the structure is prohibited (WGMs only travel in the angular direction). This is one of the requirements for the existence of these modes.

When we consider finite size shells, thicker multilayers that produce the exponential tails of the E field towards the center will not reach the inner cavity and lose localization in comparison with thinner shells. It is observed in Fig. 4.4 how the  $Q$  factors converge to an apparently common value for an increasing number of layers. This common value is necessarily the one corresponding to the surface mode weakly localized at the interface between the background with the semi-infinite structure. Note that mode WG1 has the lowest  $Q$ -factor among all the modes analyzed here. For the higher order WGMs, their  $Q$  factors are 2 orders of magnitude lower than those calculated for the FP-like modes with similar order. In comparison with the  $Q$  factors obtained for cavity modes C1 and C2, WG1 has a  $Q$  factor comparable with that of C1 at  $N = 2$ , while WG2 has a  $Q$  factor 2 orders of magnitude larger (at  $N = 2$ ). However, for increasing shell thickness WGMs strongly decrease their  $Q$  factor up to values several orders of magnitude lower than that of the cavity modes. It can be concluded that WGMs associated with a thick enough metamaterial shell are the best candidates to guarantee an efficient energy exchange with the EM waves to/from the background.

A very remarkable property of these modes is that their frequencies, as in the case of cavity modes, do not vary with the shell thickness. This would seem counter-intuitive since the frequency of WG modes in cylindrical cavities made of isotropic dielectric medium depends of the optical path determined by the cavity perimeter; that is  $\ell = n \times 2\pi R$ , where  $n$  is the refractive index and  $R$  the cavity radius. For the anisotropic and inhomogeneous shell under consideration, Fig. 4.1(c) shows that  $n_r$  is constant within each layer of types  $a$  or  $b$ , their values alternate in consecutive layers between  $n_{ra} = 15$  and  $n_{rb} = 25$ . Since the external layer (of  $b$ -type) has a higher refractive index, compared to the background or the closest shell layer (of  $a$ -type) it may guide some energy in the angular direction. Conditions exist for these modes to be propagative within the external  $b$ -layer, and this time again resonant modes appear due to the finite size of the perimeter of this external layer. Refractive index in this perimeter varies as  $n_\theta = \sqrt{\varepsilon_z \mu_r} \propto \frac{cte}{r}$ , which is an inverse function of the radial distance, and with  $ct$  being a constant value



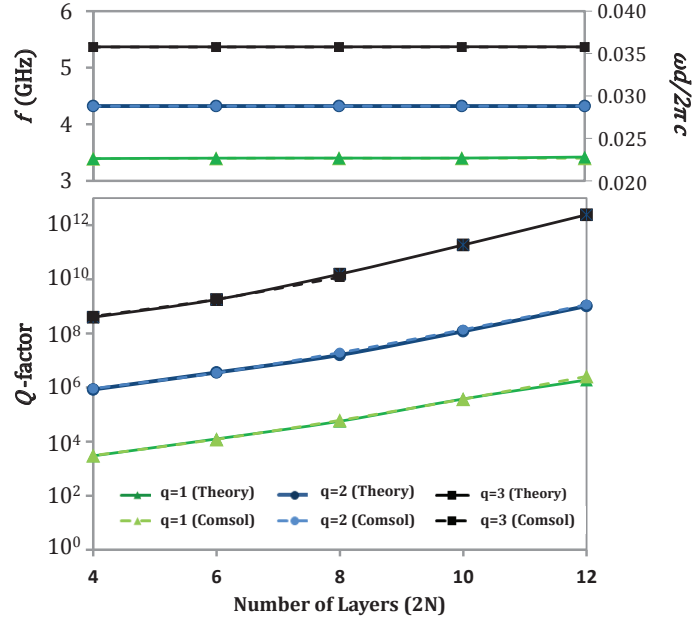


Figure 4.5: Frequency variation (a) and quality factor  $Q$  variation (b) as a function of the number  $N$  of periods for the inner interface whispering gallery resonances located in the shell described in Fig. 4.1. The radius of the cavity being  $r_{int} = 0.5$  mm. Results from a commercial software (COMSOL) are compared with the transfer matrix method (TMM).

depending on the  $a$ - or  $b$ -type layer. Now, this refractive index with inverse radial dependence makes that the 'optical path' ( $\sim n_\theta \times 2\pi r = ct$ ) of the outer layer is independent of the size (or number of layers) of the shell. This explains the constant resonant frequencies of the whispering gallery modes.

If the layer order is inverted (i.e., higher  $n_\theta$  value for the inner interface layer), the previously observed WGMs are transferred to that interface. The behavior of these modes is described in Fig. 4.5 and is coherent with the previous discussion. Again, the resonant frequencies of the WGM of the inner interface are independent of the size of the shell. This behavior is obvious for this configuration since the circular dimension of the inner layer is kept constant when adding external layers. Resonant frequencies are only slightly shifted with respect to those of Fig. 4.4. In coherence also with the previous discussion, the  $Q$  factors obtained increase with the number of

layers since the exponential tail is smaller at a larger distance from the inner surface. In other words, the internal WGMs will be increasingly isolated with respect to external background and, therefore, the radiation losses will be smaller (i.e., higher  $Q$  factors). However, the  $Q$ -factor variation with the number of layers is not exponential as it was in the case of cavity modes (see Fig.4.3). In this case, the RPC shells with less layers will have a better behavior as a energy harvesting device.

Finally, let us discuss the case of two degenerate WGMs obtained for a single shell, one being located at the outer boundary and the other at the inner boundary. This case is achieved considering a shell with an odd number of layers (seven layers equivalent to three periods and one additional  $b$ -type layer); the total diameter being equal to  $\phi = 15mm$ . Figure 4.6 reports how a point source located at a distance  $r_{source} = 20mm (\equiv 10d)$  from the shell center illuminates the shell for three slightly different frequencies. It is shown how the WG2 mode at the outer layer is excited at 4.277 GHz, while the WG2 mode at the inner layer is excited at 4.323 GHz. Moreover, Fig. 4.6(b) shows that both modes are simultaneously excited at 4.303 GHz. The frequency differences are much smaller than those depicted in Figs. 3.8 and 3.9 since the inner void cavity size is much (electrically) smaller and there is a lower perturbation due to it. In the case depicted in Fig. 4.6(c), the resonant mode is linked to the inner interface of the shell with the cavity. In order to complete this graphical information, the  $Q$  factors of these two degenerate modes have been calculated showing a non-negligible difference. For the external WGM shown in Fig. 4.6(a) we obtained the value  $Q_{WG2_{ext}} = 503$ , whereas for the internal WGM shown in Fig. 4.6(c)  $Q_{WG2_{int}} = 1824$ . This difference is expected since the internal WGM is more isolated from the external background and, consequently, is less radiative.

As a conclusion to this section, the resonant properties of the WGM can be used for the harvesting of EM energy due to their low  $Q$ -factors which allow the energy exchange with the background. Both WGM possibilities, internal and external, have been studied in terms of the shell thickness, concluding that: (i) for the external mode, in which the energy has to be collected in the outer layer, a high number of layer favors the energy harvesting; (ii) for the internal mode, where the energy will be collected in the inner layer, the minimum number of layer will produce a better behavior as

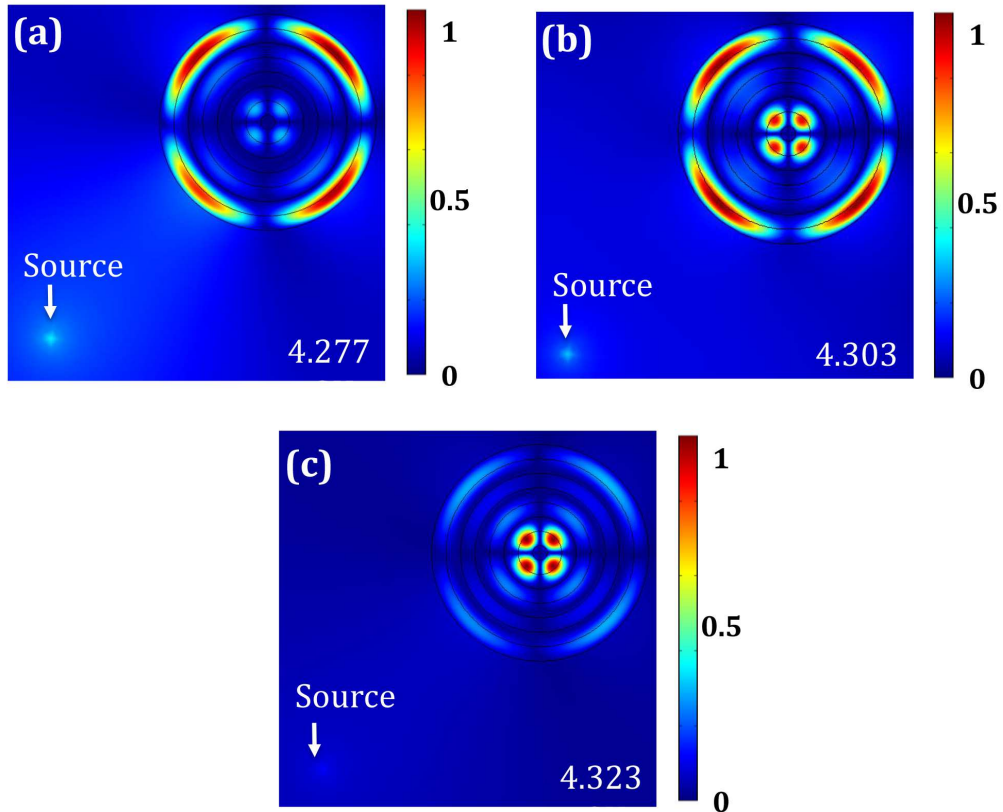


Figure 4.6: E-field patterns of an external point source illuminating a RPC shell and exciting a whispering gallery mode, (a) an external whispering gallery mode at 4.277 GHz, (b) simultaneous excitation of internal and external whispering gallery modes at 4.303 GHz, and (c) internal whispering gallery mode at 4.323 GHz. Here the total number of layers of the shell is seven, with inner and outer layers of the same  $a$  type.

energy concentrator.

## 4.2 Wireless Power Transfer

Another application which has motivated many works and in which the scientific community is devoting enormous efforts is the *Wireless Energy Transfer* (WPT). The interest in this topic is related to the development of mobile and wireless charging devices. Since times of Nicola Tesla [21], the challenge of transmitting energy without physical contact has been a hot topic. However, it has been in the last decades when the necessity of this type of technology has become evident. Nowadays, the number of electronic devices (telephones, laptops, MP3-reproducers...) that each consumer uses has increased and this fact has produced a huge dependence on charging systems, which are typically associated to wire connections. Moreover, new potential applications have been discovered in new environments where the physical connections are not possible or not appropriated (satellites or emergency systems). The study of new technologies that avoid the use of wires or other physical infrastructures for transmitting energy can improve the mobility for recharging batteries and allow uninterrupted operation. For all these reasons, the possibility of feeding or recharging electronic devices with a wireless system especially attractive.

To deal with the WPT, different types of technological schemes have been proposed [22] [23] [24]. The proposals can be divided in two groups: radiative and non-radiative energy transfer systems. The radiative solutions have important drawbacks. It is difficult to make the correct pointing and the necessary adjustments to maintain the alignment between transmitter and receiver. Furthermore, the beam can be easily blocked, interrupting the transmission of power, this can even affect (or damage) the blocking object.

For the non-radiative systems the magnetic induction [25] and the strong resonant coupling [26] [27] phenomenon have been the most studied. On the one hand, in the magnetic induction systems the primary winding (source) and the secondary winding (the device) must be close in distance, and positioned with a particular alignment. From the technical point of view, this requires a large magnetic flux coupling between windings for proper operation. On the other hand, in strong resonant coupling systems, it is fundamental to have a sub-wavelength size resonators with high quality factors ( $Q$ ). In this

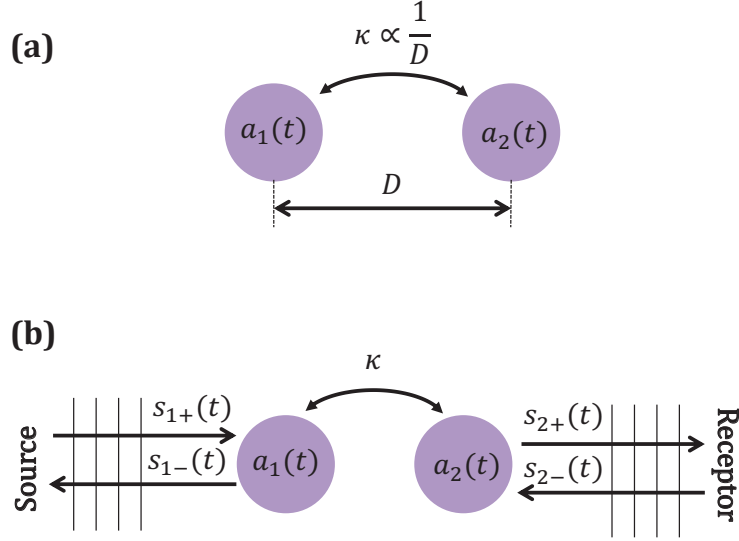


Figure 4.7: Scheme of a WPT system. (a) Mode amplitudes when the system has only two resonators and (b) when the system has two resonators, a excitation source and a collecting receptor .

section, we propose an alternative WPT system based on the strong resonant coupling phenomena which uses RPCs as resonant elements.

We start introducing the Copled Mode Theory (CMT) for the analysis of the WPT [28]. First, assuming a time dependence  $e^{-i\omega t}$ , we consider a single resonator, where the mode amplitude  $a(t)$  can be defined as follows:

$$\frac{da(t)}{dt} = -i\omega_0 a(t) - \left( \frac{1}{\tau_{rad}} + \frac{1}{\tau_{abs}} \right) a(t), \quad (4.2)$$

with  $1/\tau_{rad}$  and  $1/\tau_{abs}$  being the decay rates due to escaping power and losses in the material, respectively, and  $\omega_0$  the resonant frequency. From the energy in the system  $W(t) = |a(t)|^2$ , we can obtain the power dissipation due to the decay rates  $P_{rad}$  and  $P_{abs}$ :

$$\frac{dW(t)}{dt} = -2 \left( \frac{1}{\tau_{rad}} + \frac{1}{\tau_{abs}} \right) W = -P_{rad} - P_{abs}. \quad (4.3)$$

The power radiated to the background is  $P_{rad} = 2W/\tau_{rad} = \omega W/Q_{rad}$  and the power dissipated in the material is  $P_{abs} = 2W/\tau_{abs} = \omega W/Q_{abs}$ . The

quality factor of the resonator can be calculated as:

$$\frac{1}{Q_0} = \frac{1}{Q_{rad}} + \frac{1}{Q_{abs}}. \quad (4.4)$$

Notice that in the design of WPT systems we try to minimize the dissipated power, so we require resonators with high quality factors.

Now, the study is focused on the coupling produced between two resonators. Figure 4.7.(a) shows a schematic of a WPT scheme. If we consider the coupling between two resonators with mode amplitudes  $a_1(t)$  and  $a_2(t)$ , resonant frequencies  $\omega_1$  and  $\omega_2$  and coupling factors  $\kappa_{12}$  and  $\kappa_{21}$ , the amplitudes obey the following equations:

$$\frac{da_1(t)}{dt} = -i\omega_1 a_1(t) - \Gamma_1 a_1(t) + i\kappa_{12} a_2(t), \quad (4.5a)$$

$$\frac{da_2(t)}{dt} = -i\omega_2 a_2(t) - \Gamma_2 a_2(t) + i\kappa_{21} a_1(t), \quad (4.5b)$$

where  $\Gamma_1 = (1/\tau_{rad1} + 1/\tau_{abs1})$  and  $\Gamma_2 = (1/\tau_{rad2} + 1/\tau_{abs2})$  represent the decay rates in each resonator. Considering  $\Gamma_1 = \Gamma_2 = 0$ , energy conservation imposes that the time rate of change energy must be zero, so:

$$\frac{d|a_1|^2 + |a_2|^2}{dt} = a_1^* \kappa_{12} a_2 + a_1 \kappa_{12}^* a_2^* + a_2^* \kappa_{21} a_1 + a_2 \kappa_{21}^* a_1^* = 0 \quad (4.6)$$

The coupling coefficients have to satisfied  $\kappa_{12} + \kappa_{21}^* = 0$ . Due to the reciprocity of the system the coupling coefficients are equal and real,  $\kappa_{12} = \kappa_{21} = \kappa$ .

The matrix representation of the Equation 4.5 can be written as:

$$\dot{\mathbf{a}} \overset{\check{}}{\mathbf{G}} = \mathbf{A} \mathbf{a}, \quad (4.7)$$

where

$$\mathbf{A} = \begin{pmatrix} -i\omega_1 - \Gamma_1 & i\kappa \\ i\kappa & -i\omega_2 - \Gamma_2 \end{pmatrix}. \quad (4.8)$$

To obtain the eigenmodes, we consider that  $(a_1(t) \ a_2(t)) = (A_1 \ A_2)e^{-i\omega t}$ . In this case, to solve the equation system we have to ensure  $\det(\mathbf{A} + \lambda \mathbf{I}) = 0$ , being  $\mathbf{I}$  the identity matrix and  $\lambda = -i\omega$ . The complex frequencies are:

$$\omega_{e,o} = \frac{\omega_1 + \omega_2}{2} - i\frac{\Gamma_1 + \Gamma_2}{2} \pm \sqrt{\left(\frac{\omega_1 - \omega_2}{2} - i\frac{\Gamma_1 - \Gamma_2}{2}\right)^2 + \kappa^2}. \quad (4.9)$$

The frequency splitting produced by the coupling between the resonances is defined by  $\delta_\omega^{(1)} = \omega_e - \omega_o = \Omega_0$ , with

$$\Omega_0 = \sqrt{\left(\frac{\omega_1 - \omega_2}{2} - i\frac{\Gamma_1 - \Gamma_2}{2}\right)^2 + \kappa^2}. \quad (4.10)$$

Note that for the same frequency  $\omega_1 = \omega_2$  and the same decay rate  $\Gamma_1 = \Gamma_2$ , the splitting is  $\delta_\omega^{(2)} = |\kappa_{12}|$ . The coupling rate  $\kappa$  can be evaluated in practice from the frequency separation between even and odd modes, since it is related to the intensity of the interaction. We have used  $\kappa = (\omega_o - \omega_e)/2$ , where  $\omega_o$  and  $\omega_e$  are the angular frequencies of each mode. On the other hand, there is a rate at which energy is dissipated in the resonators, which can be quantified by means of the damping factor. In our case, we use the damping factor  $\Gamma$  related to the  $Q$  value and giving the width of the resonances. From the definition of the  $Q$ -factor, we have  $Q = \omega/2\Gamma$ . Since there are two resonant modes (even, odd), the averaged damping factor is  $\Gamma = \sqrt{\Gamma_o\Gamma_e}$ . In a practical situation, the coupling rate  $\kappa$  should be large enough in comparison with the damping factor  $\Gamma$  in order that energy is transferred at a rate higher than it is lost in the system. A figure of merit (FOM) can be defined as the coupling to loss ratio  $\kappa/\Gamma$ , which has to reach values in principle much higher than 1.

Once the system is excited by a source the schematic view of the system is represented in Fig.4.7.(b). Considering a complete WPT system, where a source is connected to the resonator 1 with a coupling factor  $\kappa_1$  and the resonator 2 is connected to the receptor with a coupling factor  $\kappa_2$  [29], the set of equations which models the system can be written as:

$$\frac{da_1(t)}{dt} = -i\omega_1 a_1(t) - \Gamma_1 a_1(t) + i\kappa_{12} a_2(t) - \kappa_1 a_1(t) + \sqrt{(2\kappa_1)} s_{+1}(t), \quad (4.11a)$$

$$\frac{da_2(t)}{dt} = -i\omega_2 a_2(t) - \Gamma_2 a_2(t) + i\kappa_{21} a_1(t) - \kappa_2 a_2(t), \quad (4.11b)$$

$$s_{-1}(t) = \sqrt{(2\kappa_1)} a_1(t) - s_{+1}(t) \quad (4.11c)$$

$$s_{-2}(t) = \sqrt{(2\kappa_2)} a_2(t). \quad (4.11d)$$

The scattering matrix elements (S-parameters) can be obtained and written as follows:

$$S_{21} = \frac{S_{-2}}{S_{+1}} = \frac{2i\kappa\sqrt{(\kappa_1\kappa_2)}}{(\Gamma_1 + \kappa_1 - i\delta_1)(\Gamma_2 + \kappa_2 - i\delta_2 + \kappa^2)}, \quad (4.12)$$

and

$$S_{11} = \frac{S_{-1}}{S_{+1}} = \frac{(\Gamma_1 - \kappa_1 - i\delta_1)(\Gamma_2 + \kappa_2 - i\delta_2 + \kappa^2)}{(\Gamma_1 + \kappa_1 - i\delta_1)(\Gamma_2 + \kappa_2 - i\delta_2 + \kappa^2)}. \quad (4.13)$$

being  $\delta_{1,2} = \omega - \omega_{1,2}$ . The conditions which maximize the efficiency of the system are: power transmission maximization (i.e  $|S_{21}|^2 \rightarrow \max$ ) and power reflection minimization (i.e  $|S_{11}|^2 \rightarrow \min$ )

Based in this analysis, Figure 4.8 shows the magnitude of the  $S_{21}$  in a complete WPT system as a function of the frequency and the coupling rate  $\kappa_{12}$ , when we consider two identical resonators with  $\kappa_1 = \kappa_2 = 1$  (perfect coupling with the source and the receptor),  $\Gamma_1 = \Gamma_2 = 0$  (no losses in the resonators) and a normalized frequency  $f_1 = f_2 = 5$ . The critical coupling is marked and we can see the *over coupled* and the *under coupled* regions. Within the over coupled region, in this example, maximum  $S_{21}$  occurs at two frequencies. In the under coupled region the  $S_{21}$  magnitude decreases exponentially when  $\kappa_{21}$  decreases. The coupling rate,  $\kappa_{12}$ , and the separation between the resonators,  $D$ , are inversely proportional.

As we have mentioned before, this section presents a proposal for the use of RPCs shells as resonant elements in a WPT system. The designed anisotropic metamaterial shell consists of alternating layers of type  $a$  and of type  $b$  whose constitutive parameters are defined as follows:

$$\mu_{ra}(r) = \frac{40d}{r}, \quad \mu_{rb}(r) = \frac{60d}{r}, \quad (4.14a)$$

$$\mu_{\theta a}(r) = \frac{35r}{d}, \quad \mu_{\theta b}(r) = \frac{20r}{d}, \quad (4.14b)$$

$$\varepsilon_{za}(r) = \frac{40d}{r}, \quad \varepsilon_{zb}(r) = \frac{60d}{r}. \quad (4.14c)$$

In this study the losses in the materials are neglected because they depend on the particular RPC implementation (SRR resonator, using natural materials with these permittivity and permeability values or using discrete elements) and this is out of the scope of this study. The design criteria



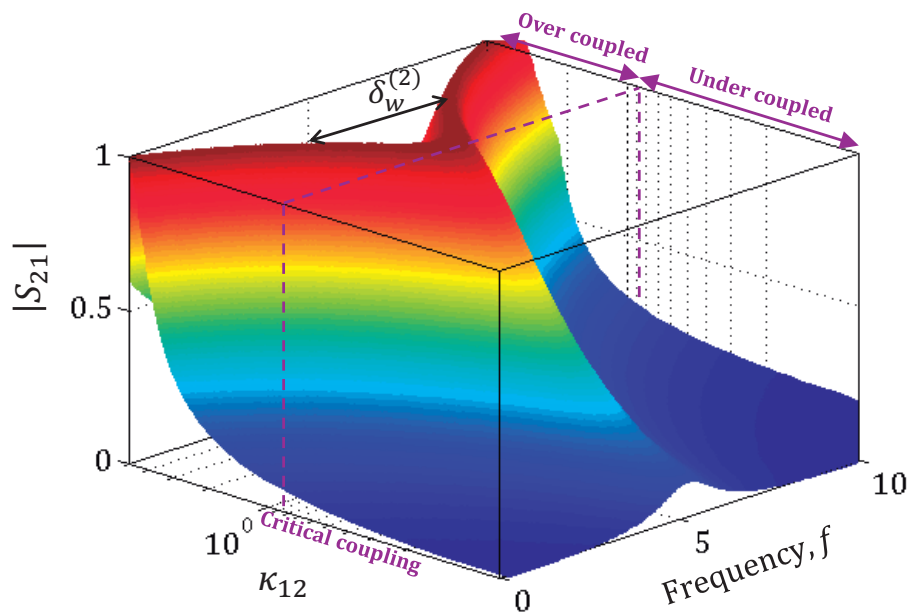


Figure 4.8:  $S_{21}$  magnitude as a function of frequency and transmitter to receptor coupling  $\kappa_{12}$ . The coupling rates with the source and the receptor  $\kappa_1 = \kappa_2 = 1$ , the decay rates in the resonator are  $\Gamma_1 = \Gamma_2 = 0$  and the resonant frequencies of the resonators are  $f_1 = f_2 = 5$

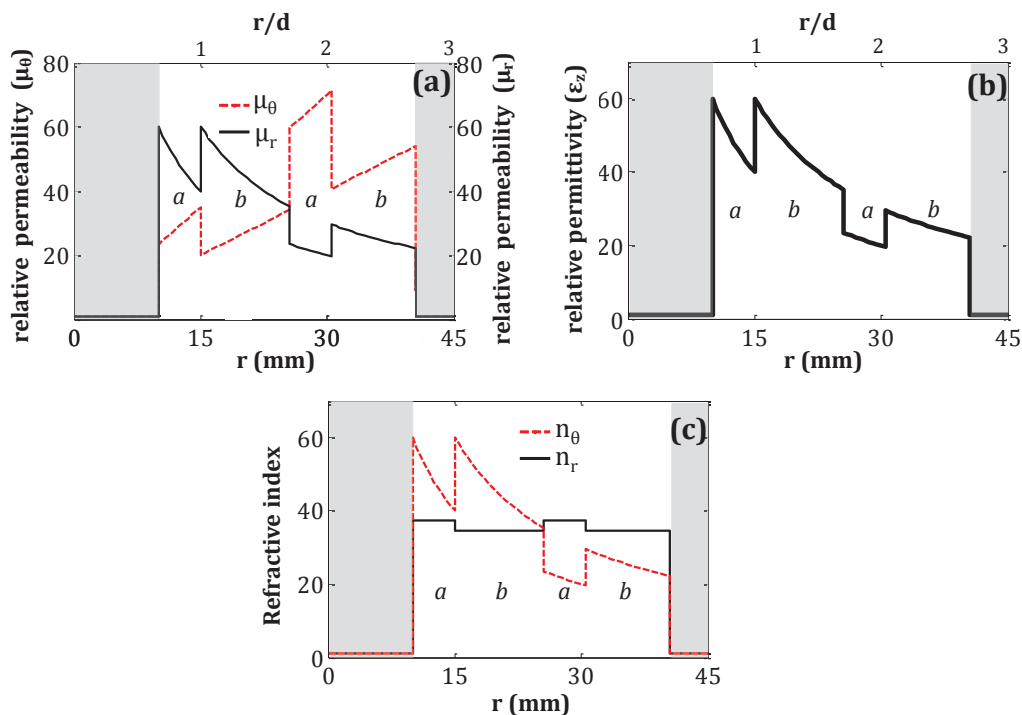


Figure 4.9: Profiles of the constitutive parameters defining an anisotropic metamaterial shell made of 2 periods of alternating materials and having a central cavity with radius  $r_{int} = 10$  mm. (a) Radial and angular permeabilities  $\mu_r$  and  $\mu_\theta$ , (b) permittivity  $\epsilon_z$ , and (c) radial and angular components of the refractive index  $n_r$  and  $n_\theta$ , respectively.

have been: (i) work with a low resonant frequency for obtaining a subwavelength size resonator, (ii) increase the quality factor for reducing the radiation losses and (iii) choose the constitutive parameters in order to make the radial impedance ( $Z_r(r) = \sqrt{\mu_r(r)/\epsilon_z(r)}$ ) identical to the vacuum impedance. These design constraints facilitate the energy transfer between the shells.

To reduce the size of the resonators, we have chosen a 4-layer resonator with inner cavity  $r_{int} = 10$  mm, radial periodicity parameter  $d = 15$  mm with  $d_a = 5$  mm and  $d_b = 10$  mm, so the external radius is  $r_{ext} = 40$  mm. The constitutive parameters described in Eq. (4.14) and particularized for these physical dimensions are displayed in Figure 4.9. Figure 4.9.(a) and Figure 4.9.(b) show that the parameter values described are not extreme as the ones proposed in [26] for dielectric structures, where  $\epsilon_r = 147.7$ .

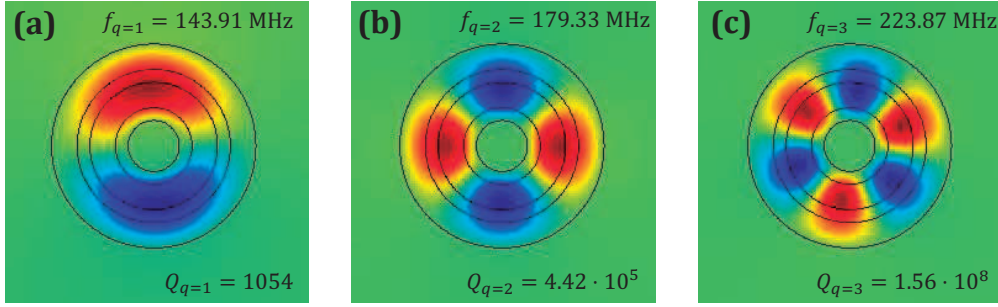


Figure 4.10: Resonant modes with different symmetry orders. (a) Dipolar modes at  $f_{q=1} = 143.91$  MHz with quality factor  $Q_{q=1} = 1054$ , (b) quadrupolar modes at  $f_{q=2} = 179.33$  MHz with quality factor  $Q_{q=2} = 4.45 \cdot 10^5$  and (c) sextupolar modes at  $f_{q=3} = 223.87$  MHz with quality factor  $Q_{q=3} = 1.56 \cdot 10^8$ .

Figure 4.10 shows the modes with symmetry orders  $q = 1, 2, 3$  allowed in our design. Value of  $q$  defines the dipolar, quadrupolar or sextupolar orders. Resonant modes are found at  $f_{q=1} = 143.91$  MHz,  $f_{q=2} = 179.33$  MHz and  $f_{q=3} = 223.87$  MHz. The quality factors associated to these resonances are  $Q_{q=1} = 1054$ ,  $Q_{q=2} = 4.45 \cdot 10^5$  and  $Q_{q=3} = 1.56 \cdot 10^8$ . From these results, we chose the mode with symmetry  $q = 2$  because the quality factor is bigger than the quality factor of the  $q = 1$  mode (less radiative losses) and the resonant frequency is smaller than the frequency for the  $q = 3$  mode (more subwavelength). So the operation frequency is  $f = 179.33$  MHz at which the free space wavelength is close to  $\lambda_0 = 1.67$  m. Taking into account the physical dimensions of the design, we can see that the shell has a sub-wavelength size at the operation frequency; i.e.,  $\lambda/r_{ext} \approx 42$ . The sub-wavelength size is paramount to operate in a strong coupling regime since evanescent components of the resonant fields are used to transfer the energy.

Once the resonant mode has been chosen, the second step in the analysis is the study of the system with two coupled shells and the study of the coupling between the resonators by means of the analysis of the resonant modes. Figure 4.11 shows the resonance modes involved in this study. First, 4.11(a) represents the resonant mode of single shell with quadrupolar symmetry. Then Figure 4.11(b) and Figure 4.11(c) are the even and odd resonant modes of a pair of coupled RPC shells, respectively. As in the previous theoretical analysis, the combination formed by these two resonant elements

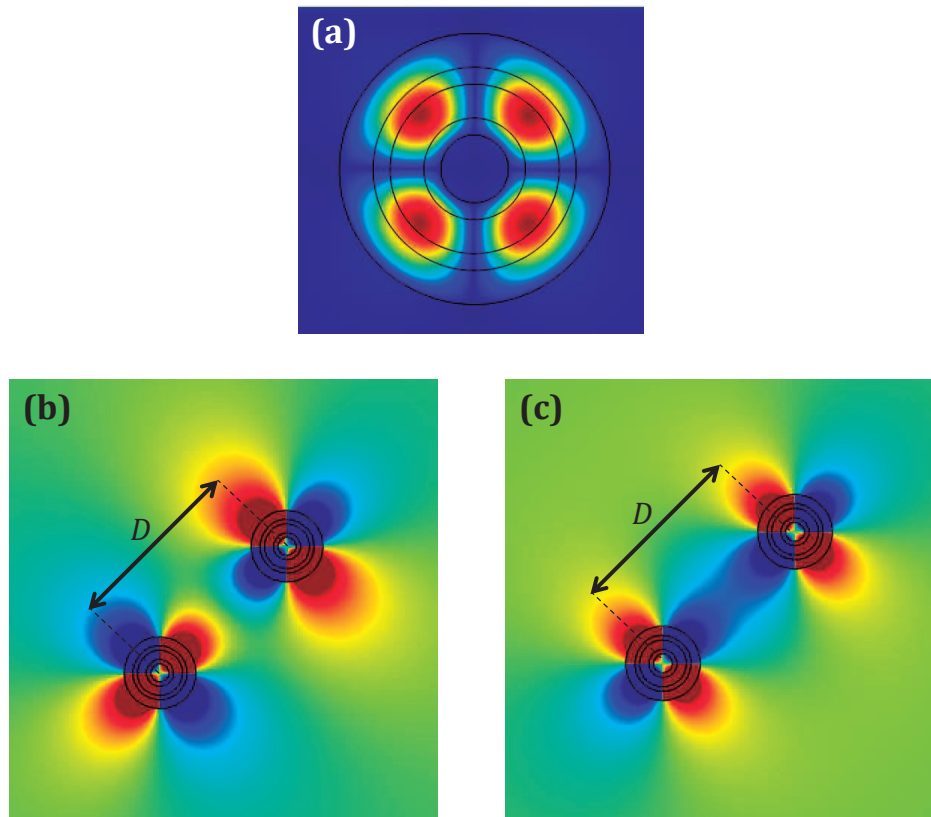


Figure 4.11: Simulated electric field patterns in normalized units of (a) the quadrupolar resonance of a single RPC at  $f_{q=2} = 179.33\text{MHz}$ . (b) and (c) represent the strongly coupled resonance pattern of a system formed by 2 resonant shells separated a distance (center to center)  $D = 200\text{mm} = 5r_{ext}$ . Resonance frequency for the even mode is  $179.32\text{MHz}$ , while it is  $179.34\text{MHz}$  for the odd mode.

creates a system with its own resonant modes and frequencies, which result from the original resonant modes of the individual element. In this case,  $D = 200 \text{ mm} = 5r_{ext}$  and the even and odd modes appear at 179.32 MHz and 179.34 MHz. Both modes share the symmetry axis formed by the line equidistant from both centers of the RPCs.

The purpose of the analysis of the combined system is to evaluate if a strong coupling regime is established between both resonant elements that can favor a wireless energy transfer. Two key parameters can be identified in order to evaluate such an interaction. On the one hand it is the coupling factor or rate  $\kappa$  between the RPCs. As we have seen, this coupling factor relates the variations of the field amplitude in the first shell  $a_1$  with the field amplitude in the second shell  $a_2$ . On the other hand, there is the rate at which energy is dissipated in the resonators, which can be quantified by means of the damping factor,  $\Gamma$ .

Our study consists in analysing the resonant system formed by two shells with split resonant frequencies. For each mode, even and odd, a coupling to loss ratio has been calculated from the respective frequencies and Q-factors. The results are summarized in Fig. 4.12, where panel (a) displays the resonant frequencies as a function of the distance between shells. It is observed that, as expected,  $f_e$  and  $f_o$  are quite different for the shorter distances and both tend to the single shell resonance frequency as distance increases. Let us recall that these are relative distances larger than the size of the shells, and at the same time they are smaller than the operation wavelength in free space.

Figures 4.12(b) and 4.12(c) report the quality  $Q$  and damping  $\Gamma$  factors (related only to radiation losses), respectively. The even mode presents more radiation losses, i.e. lower  $Q$ -factors. For the odd mode and since the damping factor presents a minimum value, a maximum value is obtained for the  $Q$ -factor. This maximum value corresponds to a separation close to four times the radius of the shells. This is an important difference between both resonant modes.

Figure 4.12(d) displays the calculated FOM, which gives the coupling to loss ratio  $\kappa/\Gamma$ . Within a wide range of distances the FOM reaches values much higher than one. All this distance range where the FOM presents values higher than one is in principle usable in view of obtaining a wireless

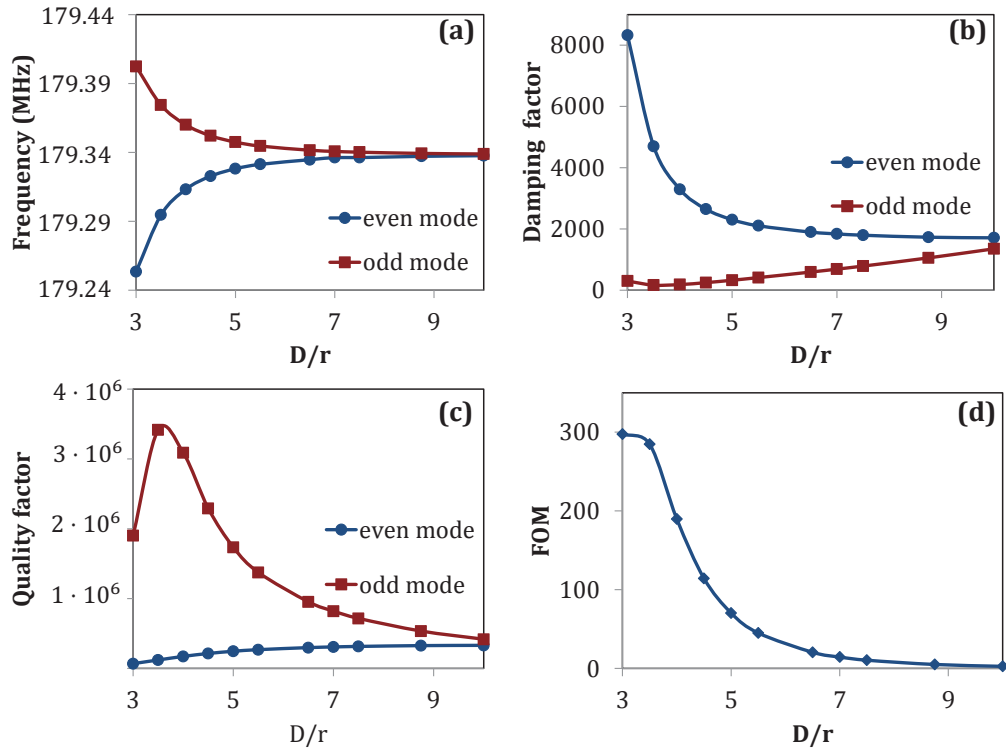


Figure 4.12: Numerical results from an eigenvalue analysis of a pair of coupled resonators with varying separation distance  $D/r_{ext}$  (ratio between the physical distance among their centers and the radius of the RPCs). (a) Resonant degenerated frequencies of the coupled RPCs system, (b) Damping factor for each resonant frequency including radiation losses (c) Calculated quality factors for both resonant modes. (d) Figure of merit (FOM) for the energy transfer calculated as the ratio between the coupling factor  $\kappa$  and the averaged damping factor  $\Gamma$ .

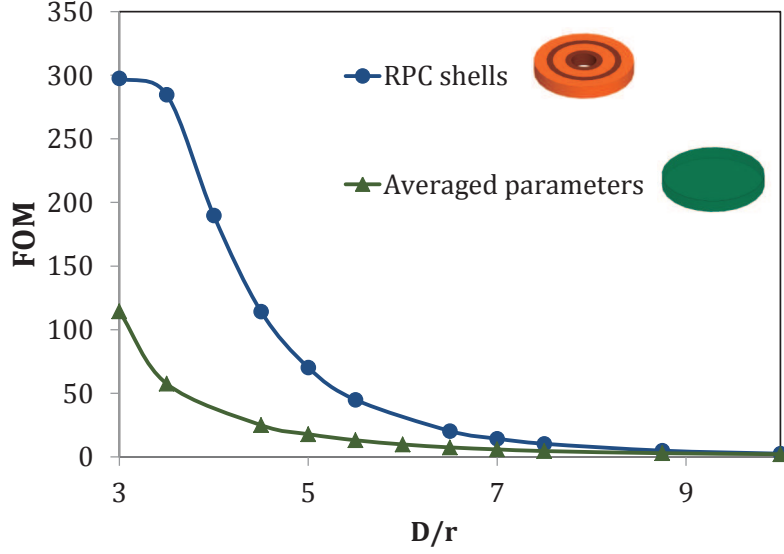


Figure 4.13: Simulated coupling to loss ratio  $FOM = \kappa/\Gamma$  for the metamaterial shells compared to homogeneous disks as a function of the normalized separation in each case.

power transfer; energy is transferred at a rate higher than the rate at which it is lost in the system, which is the target of the device.

Additionally, we have compared the efficiency of the proposed resonator structures, based on metamaterials, with other solutions already explored. Thus, the same analysis has been also carried out for homogeneous isotropic disks with the same physical dimensions of the metamaterial shells. Specifically, the constitutive parameters are the result of averaging those of the RPC metamaterial shell:  $\varepsilon_H = 30.06$ ,  $\mu_H = 33.23$ . Under these conditions, the individual resonator frequency is  $f_{q=2} = 190.09 MHz$  and the associated quality factor is  $Q_H = 1.42 \cdot 10^5$ . The two calculated FOMs as a function of the separation distance are displayed in Fig. 4.13. They demonstrate that the coupling factor between the two anisotropic metamaterial shells is higher than that for the equivalent homogeneous dielectric-magnetic disks. With the metamaterial resonators, stronger quality factors can be obtained and thereby higher FOM ( $FOM_{RPC} \gg FOM_H$ ). It is concluded that the proposed resonator structures based on metamaterials present much better performance for wireless energy transfer.

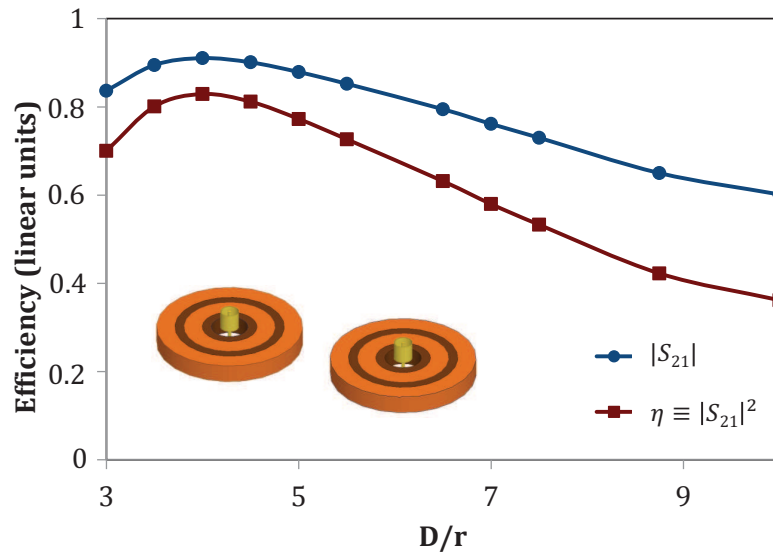


Figure 4.14: Simulated power transfer efficiency  $\eta$  and transmission coefficient  $S_{21}$  as a function of separation distance. These relative figures are defined between the two port planes of the coaxial connectors. Efficiency  $\eta$  includes the transfer rates from the connectors to the RPCs and the wireless transfer rate between the RPCs. Inset shows a schematic of the wireless energy transfer system including source and drain coaxial connectors to respectively inject and extract EM energy.



A practical application of this type of system would require inevitably additional considerations in order to assess a magnitude quantifying the transfer efficiency. For this goal, we have analyzed the problem of placing two shells in proximity under conditions that could be encountered in practice. In particular, we have analyzed the possibility of using connecting elements respectively acting as a power source and a power drain. Therefore, 3D numerical simulations including feeding and probing coaxial connectors in both shells are performed. This permits to directly obtain the power transfer efficiency figure evaluating the performance of the system. This efficiency can be estimated directly from the transmission coefficient ( $S_{21}$ ) relating the power from the transmitting port that is transferred to the receiving port. The system analyzed is composed of two identical devices including a coaxial standard connector on the shells inner cavities and each one acts respectively as power source and power drain.

A schematic of this configuration is given in Fig. 4.14. Importantly, the connectors themselves are part of the power transfer system and influence its performance. Also, the estimated efficiency by this means is a global value that includes the efficiency of the transfer between the connectors and the shells on top of the transfer efficiency between the two shells. Let us mention that the placement or geometrical design of these connecting elements is not optimized. Impedance adaptation between coaxial probe and the cavity material is the only consideration taken into account. Coaxial probes are not placed exactly at the center of the inner cavities. This is done in order to improve the excitation of the quadrupolar mode [30]. Since this mode has a null at the center of this cavity because of symmetry reasons, the center is not an optimum position for the source or load connectors. The optimal position to maximize matching between the connector and the shell has not been investigated and is therefore susceptible of improvement. In our simulations, the inner coaxial conductor is just displaced at  $r = 0.1r_{ext}$  from the center of each RPC. The presence of the connectors creates a slight perturbation in the electrical behavior of the RPCs, shifting in practice their resonant frequencies from the ones displayed in Fig. 4.11(a). However, the simulations show that this shift is very small ( $< 0.01\%$ ) and it is almost homogeneous within the considered range of separation distances.

Figure 4.14 shows the evolution of the transfer efficiency as a function of

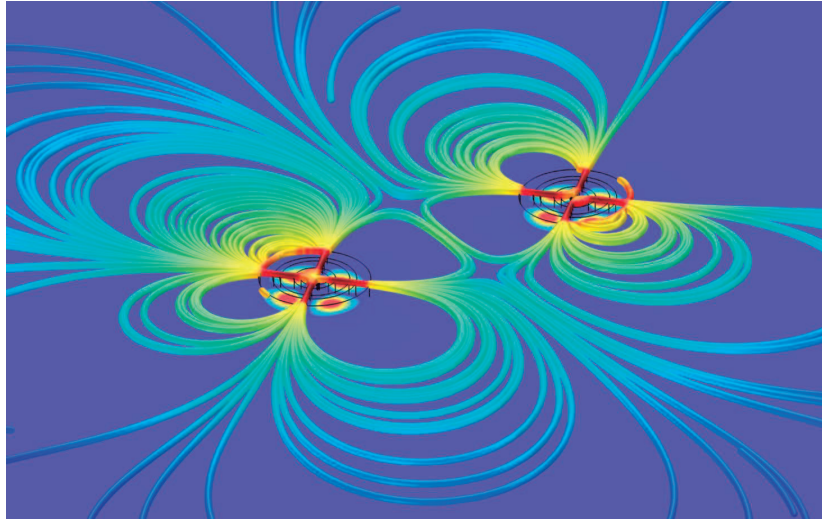


Figure 4.15: Field in a system with two RPC shells. Magnitude of the electric field and magnetic field lines.

the separation between the shells in normalized units. At each separation distance, the maximum transmission frequency is shifted (as it was already shown in Fig. 4.12(a)). The maximum transmission coefficient is obtained at each one of these peak frequencies: this maximum  $S_{21}$  value is the one reported in Fig.4.13. It can be seen that efficiency is higher for the shorter distances and it slowly decays with increasing separations. Maximum transfer efficiency close to  $\eta = 83\%$  is obtained for a separation of four times the device radius. This distance value is slightly above the one reported in Fig. 4.12(d)), because the system has been altered due to the presence of the coaxial connectors and, as it was discussed previously, resonance frequencies have also been shifted. Efficiency remains high ( $\eta > 35\%$ ) for separations up to ten times the radius of the shells. In this sense, it is interesting to note that this separation range corresponds, in terms of electrical distances to  $D/\lambda = 0.07$  (for the shortest separation) to  $D/\lambda = 0.22$  (for the largest separation). Actually, this means that in all cases we are at a short electrical distance, within the first quarter-wavelength away from the transmitting device. Hence, even reactive power can be used to couple energy from one device to the other.

Figure 4.15 allows to see the coupling mechanism between both RPC

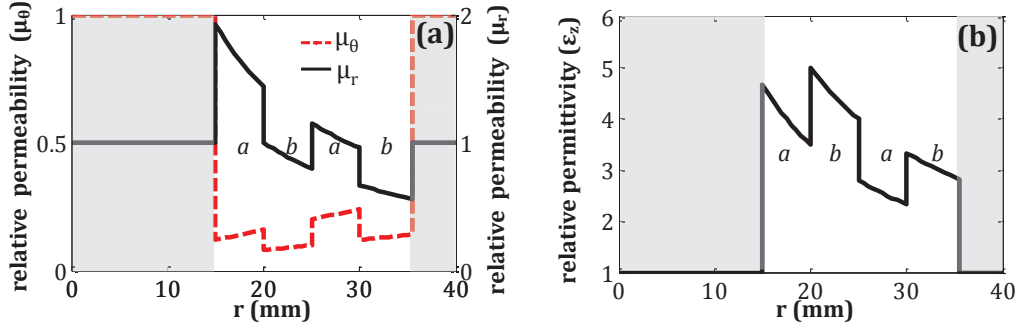


Figure 4.16: Profiles of the constitutive parameters defining an anisotropic metamaterial shell made of 2 periods of alternating materials and having a central cavity with radius  $r_{int} = 15$  mm. (a) Radial and angular permeabilities  $\mu_r$  and  $\mu_\theta$  and (b) permittivity  $\varepsilon_z$ .

shells. This figure represents the surface map of the electric field magnitude and the magnetic field lines.

### 4.3 Position Sensors

In this section, the resonant properties of the Fabry-Perot modes in the RPC shells are studied for their use as position sensors. This study is done with numerical simulations and experiments. The selected values of constitutive parameters are:

$$\mu_{ra}(r) = \frac{d}{0.347r}, \quad \mu_{rb}(r) = \frac{d}{0.5r}, \quad (4.15a)$$

$$\mu_{\theta a}(r) = \frac{0.08r}{d}, \quad \mu_{\theta b}(r) = \frac{0.04r}{d}, \quad (4.15b)$$

$$\varepsilon_{za}(r) = \frac{d}{0.143r}, \quad \varepsilon_{zb}(r) = \frac{d}{0.1r}, \quad (4.15c)$$

where  $d = d_a + d_b = 10$  mm and  $d_a = d_b = 5$  mm. The RPC shell has 2 periods (4 layers) and the void inner cavity has  $r_{int} = 15$  mm. The parameter profiles are represented in Fig. 4.16. In this section, we focus the attention on the hexapolar mode,  $q = 3$ , which appears at  $f = 3.8$  GHz. This frequency will be the operation frequency of the samples.

It is complicated to implement these microstructures due to their anisotropy and the radial dependence. Therefore, in order to fabricate a RPC sample, some simplifications allowing the feasibility of the device are used; a reduced

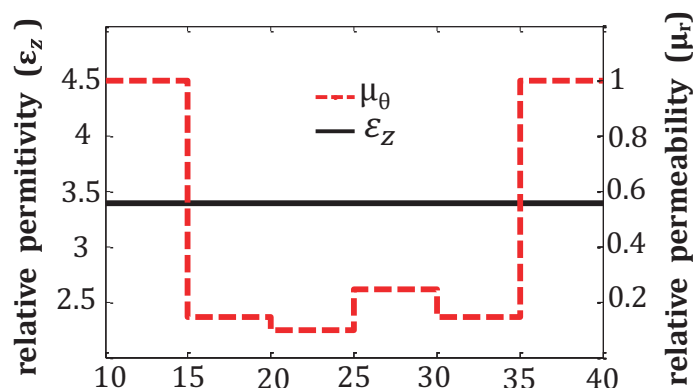


Figure 4.17: Profile of the reduced constitutive parameters. Centre of the RPC is at  $r = 0$  mm. Angular permeability (dashed line) follows a step function; permittivity (solid line),  $\epsilon_z = 3.4$  for the whole RPC shell; radial permeability (not plotted) is constant and equal to that of the background.

model is used [30]. The details of the reduced model are summarized in Appendix B. The profiles of the reduced constitutive parameter are illustrated in Fig.4.17. Angular permeability  $\mu_\theta(r)$  follows a stair-like profile in which each value is calculated like the angular permeability defined by Eqs.(B.1) in the center of the layer, permittivity is  $\epsilon_z = 3.4$  for all the RPC shell and radial permeability  $\mu_r(r)$  is constant and equal to that of the background ( $\mu_r = 1$ ).

The practical implementation of the reduced constitutive parameters of each layer is performed by a microstructure array using a unitary cell composed of a split ring resonator (SRR). The permeability of an array of SRRs can be modeled by a Lorentz-type function with the resonant frequency separating positive and negative values of the effective permeability. By designing the geometric dimensions of the SRRs, it is possible to tailor the permeability response at the design frequency of  $f = 3.8$  GHz. Table 4.1 contains the effective parameters of each layer implemented with SRRs.

Figure 4.18 displays the schemes and the final appearance of the RPC sample. Figure 4.18.(a) shows the distributions of SRRs which form each layer. The geometric dimensions of a unit cell are detailed in Fig.4.18.(b) and the physical dimensions of the SRRs which form each layer are summarized in Table 4.2.

Ring resonator	1A	1B	2A	2B
$real(\mu)$	0.1434	0.0974	0.2481	0.1468
$real(\epsilon)$	3.4137	3.4087	3.4350	3.4148

Table 4.1: Extracted parameters from the unit cells. Constitutive parameters of the ring resonators at  $f = 3.8$  GHz.

Design parameter(mm)	1A	1B	2A	2B
$a_r$	5	5	5	5
$a_\theta$	5.236	5.236	5.236	5.236
$h_t$	9	9	9	9
$r_s$	3.7	3.7	3.7	3.7
$w$	0.4	0.4	0.6	0.4
$g$	0.42	0.6	0.24	0.41
mean radius	17.5	22.5	27.5	32.5
ring/layer	21	27	33	39

Table 4.2: Design parameters of the SRRs which form each layer of the RPC shell implemented with the reduced profile defined in Table 4.1

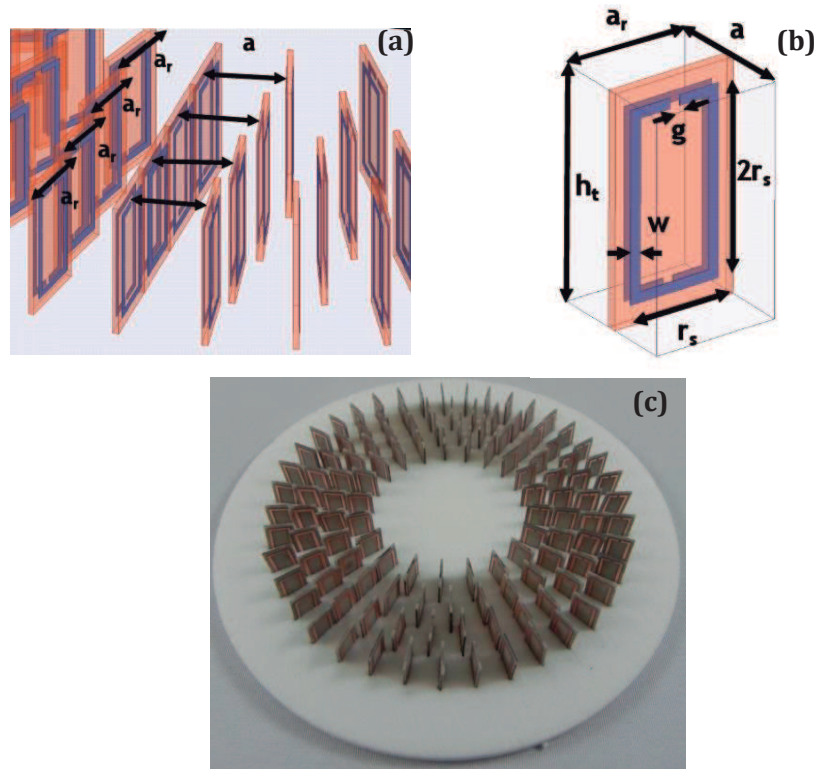


Figure 4.18: Implementation scheme of the RPC shell. (a) Details of the RPC shell implemented with SRRs, (b) SRR unit cell and (c) RPC sample.

The SRRs have been fabricated using a dielectric layer (Neltec NY9220) with a thickness of 0.381 mm and covered by  $35\mu\text{m}$  of metal. The dielectric used has low permittivity and loss [ $\epsilon_r = 2.2(1 + i0.0009)$ ]. Each SRR has been made with a combination of a chemical etch process and a laser micro-machining. Figure 4.18.(c) shows the sample including a support of Rohacell foam.

A field mapping apparatus has been developed to perform the experiments. This system comprises four parts: a 2D chamber, a Vector Network Analyzer (VNA), two linear positioning robots and a computerized control application. A scheme of the experimental setup is illustrated in Fig. 4.19. The chamber consists of by two parallel aluminum plates which are separated by a distance  $d = 10$  mm. This 2D wave guide can support the TEM mode,  $\text{TM}_n$  modes and  $\text{TE}_n$  modes. The TEM mode is the only propagation mode

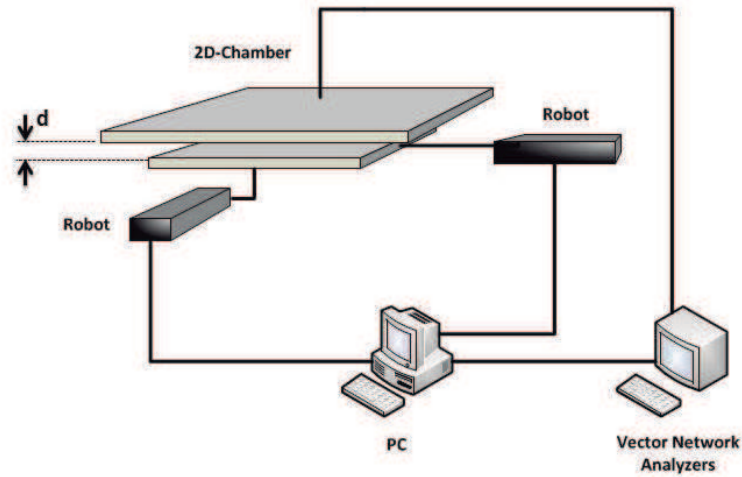


Figure 4.19: Schematic view of the measurement setup

through the guide if the space between plates,  $d$ , fulfills  $k \leq 1/d$  where  $k$  is the wave number. In our system, the separation  $d$  can be changed manually. In this experiment, the electric field is polarized perpendicularly to the chamber plates.

The top plate is  $125 \text{ cm} \times 125 \text{ cm} \times 1 \text{ cm}$  and it is fixed. To avoid a possible plate bending of the plates, it is reinforced with six girders and leans on four points at the corners. The bottom plate is  $60 \text{ cm} \times 60 \text{ cm} \times 0.8 \text{ cm}$  and can move  $60 \text{ cm}$  in two orthogonal directions. This structure creates a  $60 \text{ cm} \times 60 \text{ cm}$  measurement area allowing 2D displacements in orthogonal directions. This bottom plate is attached to a set of guide rails which make the movement possible. There are two parallel rails in each direction. Two robots control the movement of the bottom plate. In the center of the top plate, a SMA connector used as sensing probe is introduced in the chamber  $0.3 \text{ mm}$  approximately. The diameter of this SMA connector, which is used as sensing probe, is about  $1 \text{ mm}$ , so the minimum horizontal step in the horizontal plane has to be higher than that. A second SMA connector is placed at the bottom plate and penetrates in the chamber  $5 \text{ mm}$  approximately. Two possible excitation waves are implemented:

- Cylindrical wave: The connector is located at the center of the bottom plate and emits a quasi-cylindrical wave.

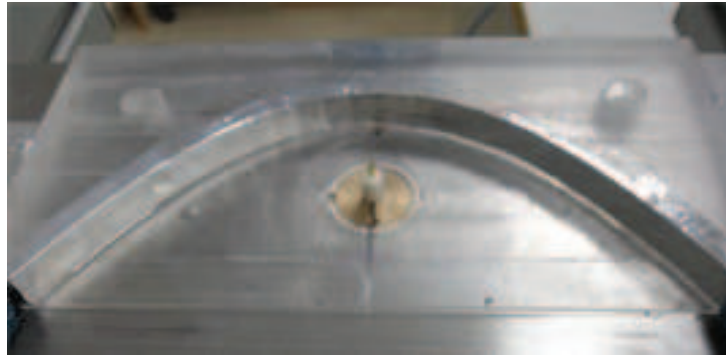


Figure 4.20: 2D parabolic reflector. Focal length is 2 cm and diameter is 12.5 cm. SMA connector is at the focal point.

- Plane Wave: The connector is placed on one side of the bottom plate and it is backed by a parabolic reflector. The parabolic reflector allows the transformation of a cylindrical wave into a plane wave. The connector is on the focal point of the parabola. The focal length of the parabolic reflector is 2 cm and the diameter is 12.5 cm. It is made with methacrylate and is wrapped with a metallic film. This device is shown in Fig. 4.20.

The detection antenna and the source antenna are connected to the Vector Network Analyzer (Rohde & Schwartz, model ZVA24) with flexible coaxial cables. The VNA allows measurements in a frequency range of 10 MHz to 24 GHz. It is controlled by means of GPIB (General Purpose Instrumentation Bus) and a home-made Labview code. To avoid the reflections at the chamber boundaries, a circular absorbing material has been placed in the chamber (see Fig 4.21). It decreases the total useful area but it reduces reflections and improves the quality of the measurements. The final useful measurement area is 28 cm  $\times$  28 cm. However, the thickness of the absorbing material is smaller than the separation between the plates; it is necessary to keep an air gap to allow the bottom plate movements. The absorbing material is shown in Fig. 4.21 for the plane wave and for the cylindrical wave (note the different shapes).

The whole setup has been tested without the samples through an empty chamber measurement. Figure 4.22 presents the measured field patterns for the two emitting sources. The E-field maps are normalized to the maximum



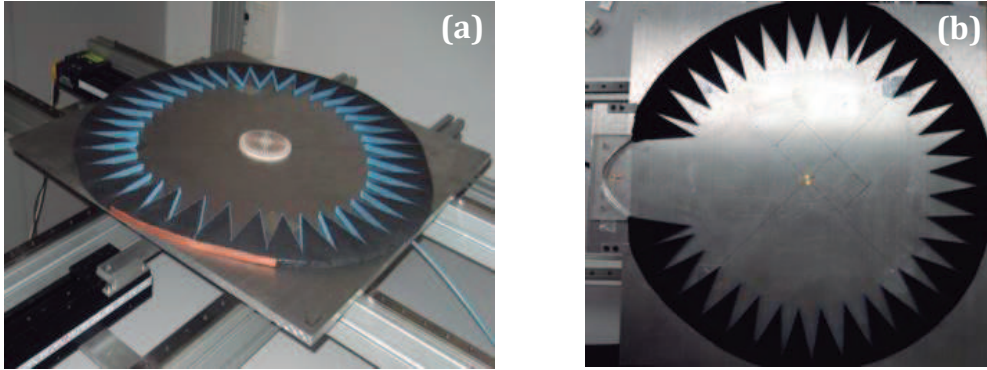


Figure 4.21: Configuration of the emitting source. (a) Setup is configured for the cylindrical wave, sample is located; (b) Setup is configured for the plane wave, parabolic reflector is located in the absorbing material aperture at the bottom plate centre.

value of the E-field. The electric field map when the chamber is excited with a punctual source [Fig. 4.22(a) and Fig. 4.22(b)] demonstrates that a cylindrical wave is generated inside the chamber. It is observed that there are reflections of the electric field at the chamber boundaries. These reflections are in large part due to the separation between the absorbing material and the top plate. For the plane wave excitation [Fig. 4.22(c) and Fig. 4.22(d)], it is observed that the wave fronts have a slight curvature. Despite of this imperfection, the wave front can be considered a quasi-plane wave excitation in the central area of the chamber.

Prior to the study of the RPCs as position sensors, we have characterized the behaviour of a RPC under different excitation sources: a plane wave, a punctual source within the void inner cavity and an external point source. These measurement types are illustrated from Fig. 4.23(a) to Fig. 4.23(c), where the samples are represented by the striped red circles and the grey circumferences represent the absorbent material.

The first measurement is schematically illustrated in Fig. 4.23(a) and corresponds to a plane wave impinging on the shell. Figure 4.24 shows the results of this study. First, in Figure 4.24.(a), the magnitude of the E-field obtained from a 2D-Comsol simulation is represented at  $f = 3.8$  GHz. In this

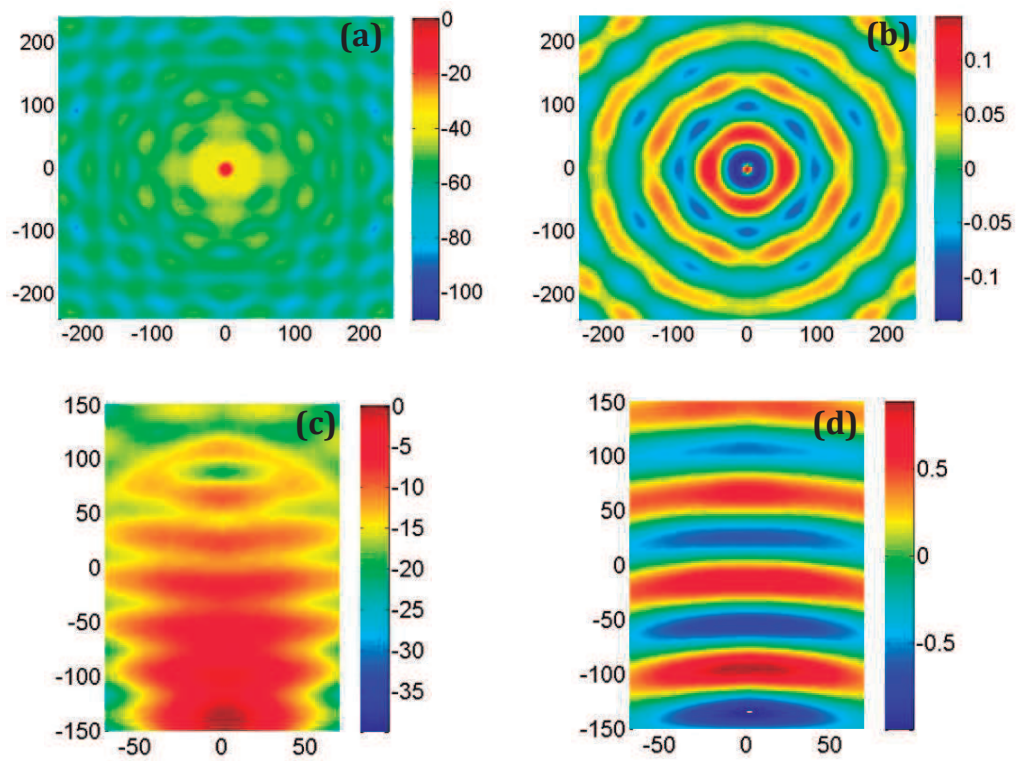


Figure 4.22: Measured E-field maps (normalized units) inside the empty chamber. (a) and (b) magnitude in dB and real part with the cylindrical wave configuration over the range of  $280 \text{ mm} \times 280 \text{ mm}$ ; (c) and (d) magnitude in dB and real part with the plane wave configuration over the range of  $300 \text{ mm} \times 240 \text{ mm}$ .

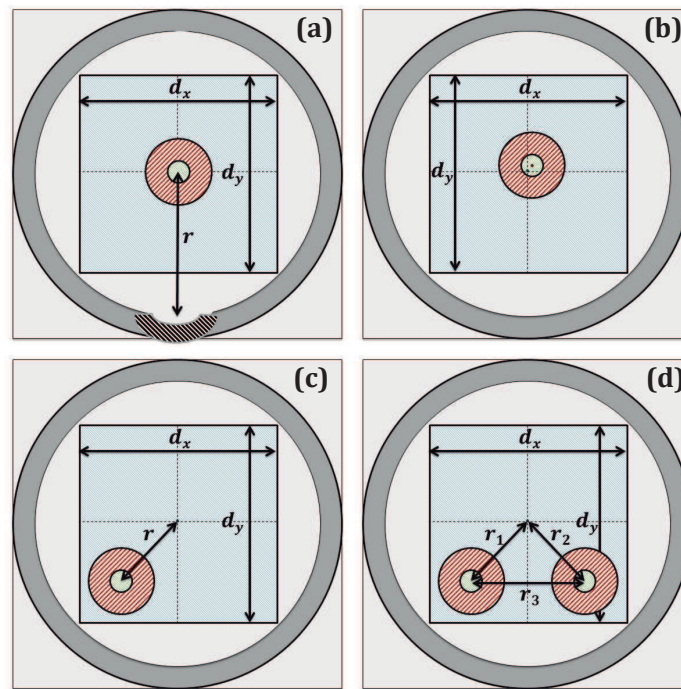


Figure 4.23: Schematic with the relevant parameters for the measurements. The measurement area is the  $d_x \times d_y$  square. The samples are represented by the striped red circle. Black circle represents the absorbing material. (a) One sample, plane wave; (b) One sample, cylindrical wave into the sample; (c) One sample, cylindrical wave out of sample; (d) Two samples, cylindrical wave out of samples.

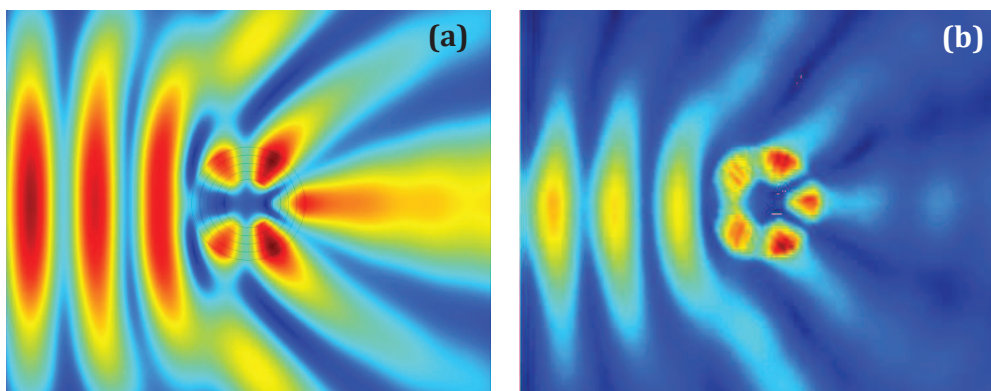


Figure 4.24: E-field complex magnitude map for a plane wave illuminating an RPC shell. (a) 2D-Comsol simulation with the reduced profile at  $f = 3.8$  GHz and (b) measurement results at  $f = 4$  GHz.

simulation, each layer of the RPC shell follows the theoretical expressions defined in Eq. (B.1). It can be noticed that the quasi-plane wave excites the  $q = 3$  mode of the shell, and besides, the result shows that the lobe which is directly illuminated by the plane wave (perpendicular to the wave front) is cancelled, so a total of five lobes appear. On the other hand, in Fig. 4.24(b), there is a representation of the experimental data when the spatial resolution is 2 mm in each direction, the measurement area is 240 mm  $\times$  300 mm and the frequency  $f = 4$  GHz. The experimental result is represented at 4 GHz, instead of 3.8 GHz, because our experimental setup modifies the behaviour of the samples in all the measurements. For this reason all measurements are obtained at  $f = 4$  GHz. This effect is discussed later. In order to compare the results, the E-field maps are normalized to the maximum value of the E-field. We have demonstrated that the Fabry-Perot modes in the RPC shells can be excited by a plane waves which can be understood as distant sources.

The next case studies a point source exciting the sample from a point inside the inner cavity. The source is located at the centre of the chamber, inside the inner cavity of the RPC, and is displaced 11 mm from the centre of the sample [see Fig. 4.23(b)]. Note that modes with symmetry  $q \geq 1$  cannot be excited if the source is placed exactly in the centre of the inner cavity. The point source excites the  $q = 3$  Fabry-Perot resonance at  $f = 3.8$  GHz. In Fig. 4.25, the real part of the E-field patterns produced

by the combination of the RPC shell and the point source inside the inner cavity are represented. For analysis purposes, the results of the experimental measurements (at  $f = 4$  GHz) are compared with the COMSOL simulations (at  $f = 3.8$  GHz) and with the HFSS simulations (at  $f = 3.8$  GHz). As we have mentioned previously, Comsol simulation solves the electric field in a 2D model, with the theoretical profiles of the constitutive parameters and HFSS simulation is a 3D model with the RPC implemented with SRRs, so it works with the reduced profile. The total measurement area is the blue square in Fig.4.23.(b) ( $240 \text{ mm} \times 240 \text{ mm}$ ) and the resolution is 2 mm in x-direction and 2 mm in the y-direction. The combination of the point source surrounded by the RPC acts as a beam-forming device, transforming the isotropic radiation of the source in a radiation pattern with six lobes. In the same way, if the exciting source has the appropriate frequency, another mode with  $q > 0$  will be excited and different patterns can be achieved. It allows using this structure to control the directionality of the source.

Notice how the response of first the HFSS simulation (SRR design) and then the fabricated shell are progressively degraded with respect to the ideal 2D Comsol simulation. Since HFSS simulations and measurements are performed on a true 3D configuration, only the top plane of the microstructure can be mapped. This top plane includes the splits of the rings that locally concentrate high E-fields.

In the third measurement with a RCP shells, the behaviour of the shell has been studied when the source is placed in the region outside the shell. Figure 4.23(c) provides a schematic view of the setup. The source remains at the centre of the chamber and the sample is located at a distance of  $r = 95$  mm from the source. Again, the measurement area is ( $240 \text{ mm} \times 240 \text{ mm}$ ) and the spatial resolution is 2 mm in each direction. If the source is placed in the region outside the shell, it is the impinging wave that causes the resonant mode of the RPC to be excited. The results are reported in Fig.4.26. As in the previous case, this figure includes the results for the Comsol and HFSS simulations at  $f = 3.8$  GHz and the experiment at  $f = 4$  GHz. The field distribution in the shell has five beams and a sixth one attenuated beam appears pointing to the source direction. One of the beams turns towards the source direction and it will be useful for locating the source position.

Now, we focus on the study of a pair of RPCs with an external source

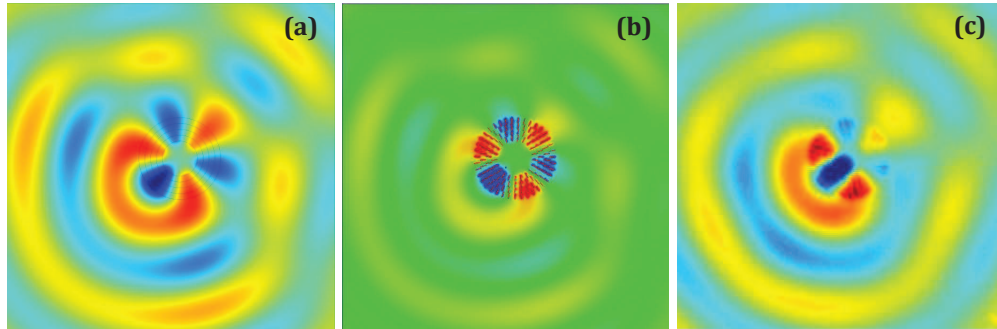


Figure 4.25: Real part of the E-field map of a point source placed inside the RPC shell (in the inner cavity) and exciting the  $q = 3$  mode. (a) 2D-Comsol simulation with the reduced profile at  $f = 3.8$  GHz; (b) 3D-HFSS simulation implemented with SRRs at  $f = 3.8$  GHz; (c) measurement results at  $f = 4$  GHz.

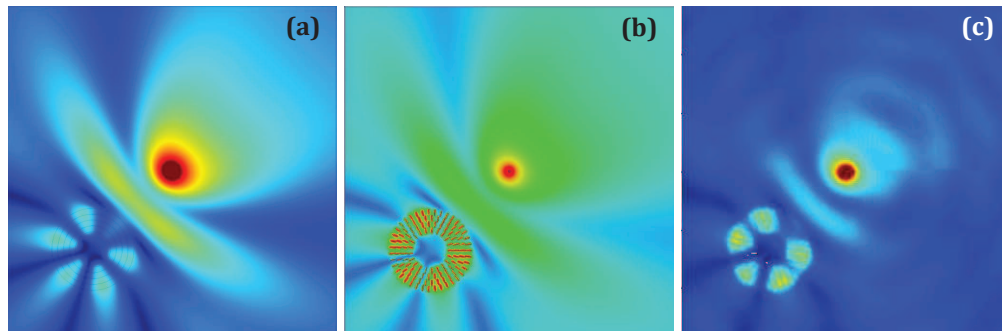


Figure 4.26: E-field complex magnitude map for a point source illuminating the RPC shell (source to center separation  $r_{int} = 95\text{mm}$ ) and exciting the  $q = 3$  mode. (a) 2D-Comsol simulation with the reduced profile at  $f = 3.8$  GHz; (b) 3D-HFSS simulation implemented with SRRs at  $f = 3.8$  GHz; (c) measurement results at  $f = 4$  GHz.

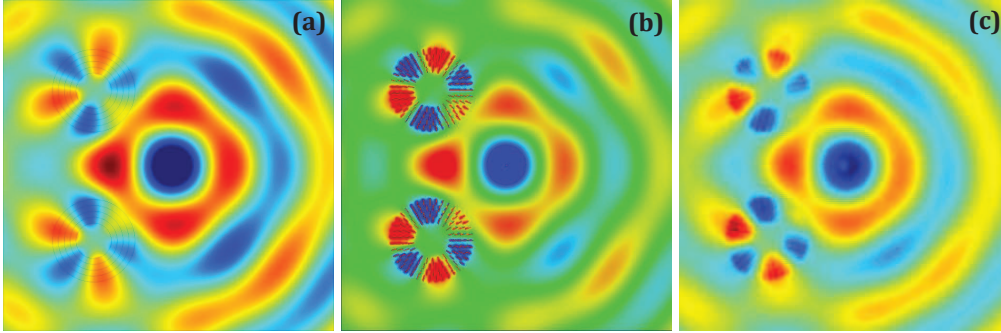


Figure 4.27: Real part of the E-field for a point source illuminating 2 RPC shells at a distance of approximately  $90\text{mm}$  to their centres and radiating. (a) Comsol simulation with the reduced profile at  $f = 3.8\text{GHz}$ ; (b) HFSS simulation implemented with SRRs at  $f = 3.8\text{GHz}$ ; (c) measurement results at  $f = 4\text{GHz}$ .

illuminating them. Figure 4.23(d) illustrates the situation of this study. The source is at the centre of the chamber and there are two shells. The shells are located at  $r_1 = r_2 = 9\text{cm}$  from the source and are separated by a distance  $r_3 = 12.8\text{cm}$ . Again, the measurement area is  $240\text{mm} \times 240\text{mm}$  and the space resolution is  $2\text{mm}$  in each direction. The results are shown in Fig. 4.27 for the Comsol and HFSS simulations ( $f = 3.8\text{GHz}$ ) and the experiment ( $f = 4\text{GHz}$ ). The behaviour is similar to that discussed earlier between a shell and an external source. Nevertheless, this time, each shell has a lobe in the direction of the source. This makes possible to use these devices in applications to determine the source position using triangulation.

Figure 4.28 explains in detail the behavior of a pair of RPC shells as position sensor. The lower panel represents an example of the E-field produced by two shells and an external point source. Over the E-field map, two white circumferences, which are sharing centres with the RPC shells, mark the E-field lines to be analysed. The representation of the E-field in these lines are in the polar graphics of the upper panel. From these graphics, the angles  $\alpha_1$  and  $\alpha_2$  can be obtained with the lowest-magnitude lobe. With these angles and knowing the distance between the shells the position of the source can be determined.

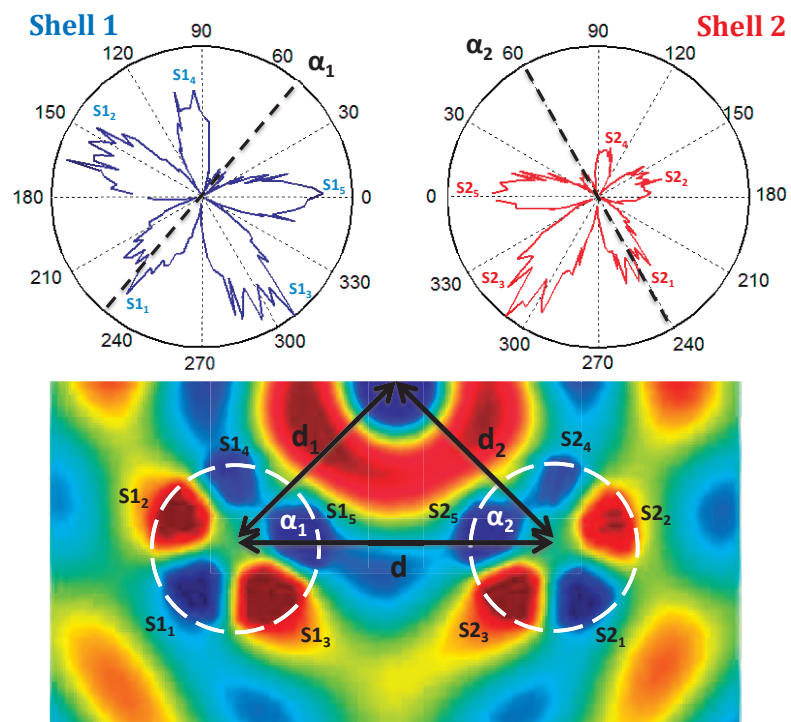


Figure 4.28: Detailed analysis of a pair of RPC shells as a position sensor.



### 4.3.1 Analysis of the frequency shift

In order to evaluate the disagreement between simulations and measurements, a complete study has been developed through the analysis of resonant mode coefficients. It aims to evaluate the behaviour of resonant modes at different frequencies. Resonant mode coefficients are extracted from measured or simulated field maps.

We consider the case of a point source illuminating the RPC shell. Fields can be expressed as a linear combination of waves emitted by the source and waves scattered by the RPC. These waves are modelled, in cylindrical coordinates, by Hankel and Bessel functions. Functions with order  $q$  represent the resonant modes with symmetry  $q$ . Two regions have to be distinguished in the field maps: the external region without the source and the inner cavity region.

In the first case, electric field in the outside region can be expressed in terms of the field produced by the punctual source ( $\psi_0$ ) and the scattered field by the RPC ( $\psi_{SC}$ ) as

$$\psi_I = \psi_0 + \psi_{SC}, \quad (4.16)$$

with

$$\psi_0 = \sum_{q=-\infty}^{+\infty} A_q^0 H_q(kr) e^{iq\theta}, \quad (4.17a)$$

$$\psi_{SC} = \sum_{q=-\infty}^{+\infty} A_q J_q(kr) e^{iq\theta}, \quad (4.17b)$$

where  $J_q$  and  $H_q$  are the Bessel and Hankel functions with order  $q$  and the constant coefficients  $A_q^0$  and  $A_q$  contain the information of the resonant modes. These coefficients are related by the transmission matrix, whose elements are defined by

$$T_q = \frac{A_q}{A_q^0}. \quad (4.18)$$

The second study analyzes the field into the inner cavity (region II). The expression for the field is:

$$\psi_{II} = \sum_{q=-\infty}^{+\infty} B_q H_q(kr) e^{iq\theta}. \quad (4.19)$$

Note that  $\psi_I$  and  $\psi_{II}$  are known from the measurements or simulations, so a multiple linear regression is applied to obtain the coefficients  $B_q$ ,  $A_q^0$  and  $A_q$ .

In a Multiple Linear Regression problem, a measured response is expressed as a linear function of multiple predictor variables. The  $i^{\text{th}}$  observation can be written as

$$y_i = \beta_0 + \beta_1 x_{i_1} + \dots + \beta_p x_{i_p} + \epsilon_i, \quad (i = 1, \dots, n), \quad (4.20)$$

where  $x_{i_j}$  is the  $j^{\text{th}}$  predictor variable for the  $i^{\text{th}}$  observation,  $\beta_j$  is the regression coefficient and  $\epsilon_i$  is the error term. A case with  $n$  observations and  $p$  predictor variables, it can be cast as:

$$Y = \beta X + \epsilon, \quad (4.21)$$

where  $Y$  is the response vector ( $n \times 1$  dimensional), the design matrix  $X$  is a matrix which packs the predictors ( $n \times p + 1$ ),  $\beta$  is the regression vector ( $p + 1$  dimensional) and  $\epsilon$  is the error vector. It represents a linear system where the unknowns are the coefficients  $\beta$ . If  $n > p$ , the system will be oversized.

$$\begin{pmatrix} y_1 \\ \vdots \\ y_n \end{pmatrix} = \begin{pmatrix} 1 & x_{1_1} & \cdots & x_{1_p} \\ \vdots & \vdots & \ddots & \vdots \\ 1 & x_{n_1} & \cdots & x_{n_p} \end{pmatrix} \begin{pmatrix} \beta_0 \\ \vdots \\ \beta_p \end{pmatrix} + \begin{pmatrix} \epsilon_1 \\ \vdots \\ \epsilon_n \end{pmatrix} \quad (4.22)$$

In order to estimate  $\beta$ , we take a least squares fitting. The residual vector elements are defined by:

$$r_i = y_i - \beta_0 + \beta_1 x_{i_1} + \dots + \beta_p x_{i_p}, \quad (i = 1, \dots, n). \quad (4.23)$$

Thus the residual vector is:

$$R = Y - \beta X. \quad (4.24)$$

This method obtains the unknown values of the parameters  $\beta$  by finding numerical values that minimize the sum of the squared difference between the observed response and the result of the model. So the problem is

$$\min \|R\|^2 = \min \|Y - \beta X\|^2, \quad (4.25)$$

where

$$\|Y - \beta X\|^2 = (Y - \beta X)^T(Y - \beta X). \quad (4.26)$$

Taking derivatives with respect to  $\beta$ , and setting these to 0, we obtain

$$-2X'(Y - X\beta) = 0, \quad (4.27a)$$

$$X'Y = X'X\beta. \quad (4.27b)$$

The regression coefficients can be obtained as

$$\hat{\beta} = (X'X)^{-1}X'Y. \quad (4.28)$$

A statistic that summarizes the quality of the fit is the residual standard deviation. It is defined by

$$\sigma = \sqrt{\frac{\sum_{i=1}^n r_i^2}{n - p - 1}}. \quad (4.29)$$

This problem can be particularized for Eqs. (4.16) and (4.19). For instance, to extract the resonant mode parameters in the cavity (region II), the values of the electric field in  $n$  points inside the cavity are collected. These points make the measured response:

$$Y = \begin{pmatrix} \psi_{II}(r_1, \theta_1) \\ \psi_{II}(r_2, \theta_2) \\ \vdots \\ \psi_{II}(r_n, \theta_n) \end{pmatrix}. \quad (4.30)$$

Then, if the sums are truncated to  $[-Q_{max}, Q_{max}]$ , the predictor variable matrix is generated as is illustrated in Eq. (4.31). In this matrix, each row represents the Hankel functions from Eq. (4.19) in a point.

$$X = \begin{pmatrix} 1 & H_{-Q_{max}}(kr_1)e^{-iQ_{max}\theta_1} & \dots & H_{Q_{max}}(kr_1)e^{iQ_{max}\theta_1} \\ 1 & H_{-Q_{max}}(kr_2)e^{-iQ_{max}\theta_2} & \dots & H_{Q_{max}}(kr_2)e^{iQ_{max}\theta_2} \\ \vdots & \vdots & \ddots & \vdots \\ 1 & H_{-Q_{max}}(kr_p)e^{-iQ_{max}\theta_p} & \dots & H_{Q_{max}}(kr_p)e^{iQ_{max}\theta_p} \end{pmatrix}. \quad (4.31)$$

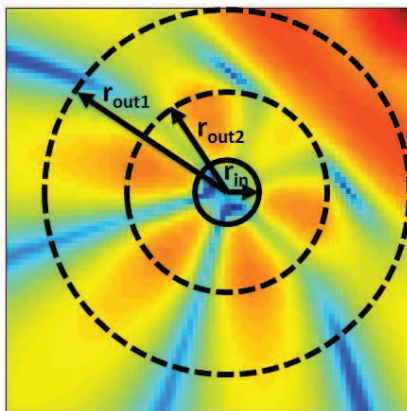


Figure 4.29: Schematic representation of the region distribution used in the analysis. Inner region is delimited by the circumference  $r_{in}$ . External region is between  $r_{out1}$  and  $r_{out2}$ .

Finally, the regression coefficient vector is formed as:

$$\beta = \begin{pmatrix} \beta_0 \\ B_{-Q_{max}} \\ B_{-Q_{max}+1} \\ \vdots \\ B_{Q_{max}} \end{pmatrix}. \quad (4.32)$$

Note that  $\beta_0$  has to be close to zero, because in Eqs. (4.16) and (4.19) there are no constant terms. The same procedure can be applied to extract the resonant mode coefficients from the region outside the shell (region I). In this case, each row of the predictor matrix will be composed by Hankel and Bessel functions and the regression vector by the  $A_q$  and  $A_q^0$  terms.

Now this method is utilized to extract the mode coefficients from the simulated and measured field maps. A simulation for the shell displaced 9.5 cm from the source has been employed to obtain these field maps. Figure 4.29.a shows the field map obtained with a Comsol simulation when the frequency is 3.8 GHz. It includes a scheme of the two regions used in this study. Specifically, the inner region is delimited by the circumference with  $r_{in} = 1.4$  cm and the external region by the external radius  $r_{out1} = 7$  cm and the inner radius  $r_{out2} = 3.5$  cm. The frequency range of this study is 3 GHz to 5 GHz.

<b>Lorentzian Fit</b>	$f_0$ (GHz)	$\Gamma$	$Q$
Simulation extraction	3.76	$8.4 \cdot 10^8$	6.39
Measurement extraction	4	$6.7 \cdot 10^8$	9.37
<b>Eigenfrequency analysis (Comsol)</b>	3.89	—	8.64

Table 4.3: Lorentzian fit.

A parameter extraction in the inner cavity (region II) has been done for each frequency. The coefficients variation is represented in Fig. 4.30. Left plot represents the analysis of the numerical simulations and right plot the analysis for the experimental data. It is observed that for frequencies lower than 3.6 GHz (shadow region) the coefficients have a different behavior than the coefficients obtained from the COMSOL simulation. This effect is due to the dispersive behavior of the SRR, around this frequency the variations in the constitutive parameters are significant. For frequencies above 3.6 GHz, although there is a frequency shift, the coefficients curves have a behavior similar to the coefficients extracted from the Comsol simulations.

At the resonance frequency of the mode  $q = 3$  the coefficient  $B_q$  has a maximum. Notice that, in this study, the same discrepancy between the simulation and the measurement appears.

In order to compare both resonances, we can analysed them using a Lorentzian fit:

$$L(f) = A_0 + \frac{A_1}{\pi} \frac{(\frac{1}{2}\Gamma)^2}{(x - x_0)^2 + (\frac{1}{2}\Gamma)^2}, \quad (4.33)$$

where  $f_0$  es the resonant frequency of the  $q = 3$  mode and the parameter  $\Gamma$  represents the width of the resonance curve, which is related to the quality factor by  $Q = \omega/2\Gamma$ . The data extracted from this analysis are summarized in Table 4.3. The resonant curve which characterizes the simulated  $B_{q3}$  coefficient is defined by  $f_0 = 3.76$  GHz and  $\Gamma = 8.4 \cdot 10^8$ . The quality factor calculated from the fitted curve is  $Q_{sim} = 6.39$ . The frequency and the quality factor are nearly equal to the obtained with Comsol. The measured coefficient  $B_{q3}$  has been fitted by a Lorentzian function with  $f_0 = 4$  GHz,  $\Gamma = 6.7 \cdot 10^8$ , so the quality factor is  $Q_{meas} = 9.37$ . Despite the  $f_0$  in both Lorentzian functions are different, the parameters  $\Gamma$  have the same order, so the width of both curves are similar.

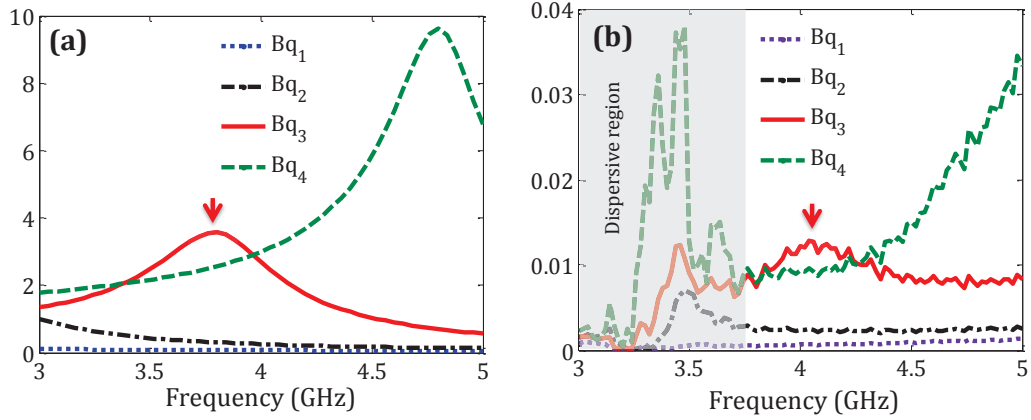


Figure 4.30: Extracted coefficients from the inner cavity field for the first 4 modes: (a) Extracted coefficients from the simulated E-field maps. (b) Extracted coefficients from the measured E-field maps. Red vertical arrows mark the point of optimal behaviour.

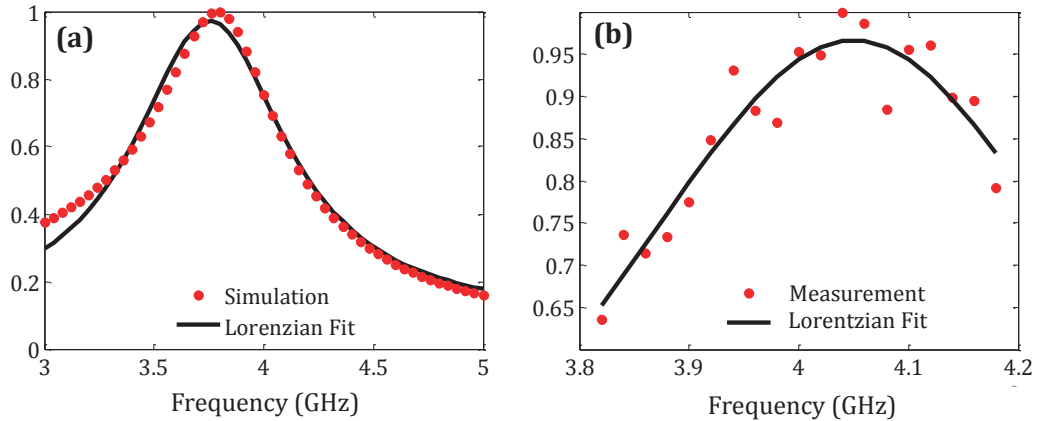


Figure 4.31:  $B_{q3}$  approached by a Lorentzian function: (a) Simulated  $B_{q3}$ , the parameters of the Lorentzian curve are:  $f_0 = 3.76GHz$ ,  $\Gamma = 8.4 \cdot 10^8$  and  $Q_{sim} = 6.39$ . (b) Measured  $B_{q3}$ , the parameters of the Lorentzian curve are:  $f_0 = 4GHz$ ,  $\Gamma = 6.7 \cdot 10^8$  and  $Q_{meas} = 9.37$ .

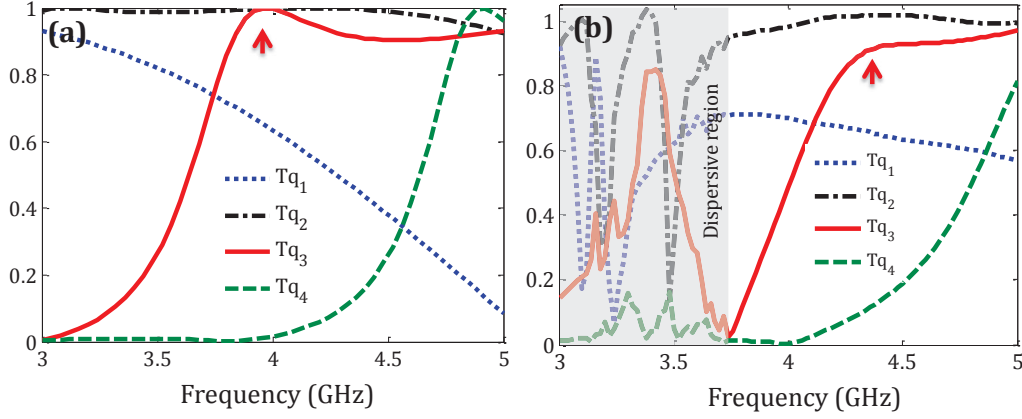


Figure 4.32: Extracted coefficients  $B_q$  from the inner cavity field for the first 4 modes: (a) Extracted coefficients from the simulated E-field maps. (b) Extracted coefficients from the measured E-field maps. Red vertical arrows mark the point of optimal behaviour.

The  $T_q$  coefficients are represented in Fig. 4.32. Left plot represents the analysis of the simulations and right plot the analysis for the measurements. As in the previous analysis, the coefficients extracted from the measurements have a wrong behaviour within the dispersive region (shadow area). Coefficients  $B_{q3}$  have a maximum value around the resonance frequency and this value is one. Note that, from the  $T_q$  definition in Eq. (4.18), this value means a total reflection of the impinging field. Moreover, we can see that  $B_{q2}$  coefficients have a high value, this is because of the point source which has an important contribution of the cuadrupolar mode [see Eq. 4.22].

In all this section, we have found a disagreement between the resonant frequencies of in simulations and measurements. The frequency shift observed in the measurements and in the coefficient extraction is caused by the experimental setup. The top plate of the 2D chamber is not in contact with the RPC sample for allowing the antenna movement. As a consequence, the air gap with 1 mm, above the sample causes a variation on the constitutive parameters [see Fig. 4.33(b)]. To evaluate the effect of this air gap, each unit cell has been simulated taking into account the air gap existing over the SRR. Using a retrieval method and the new  $S$ -parameters simulated with the air gap, the constitutive parameters are obtained. Table 4.4 gives the

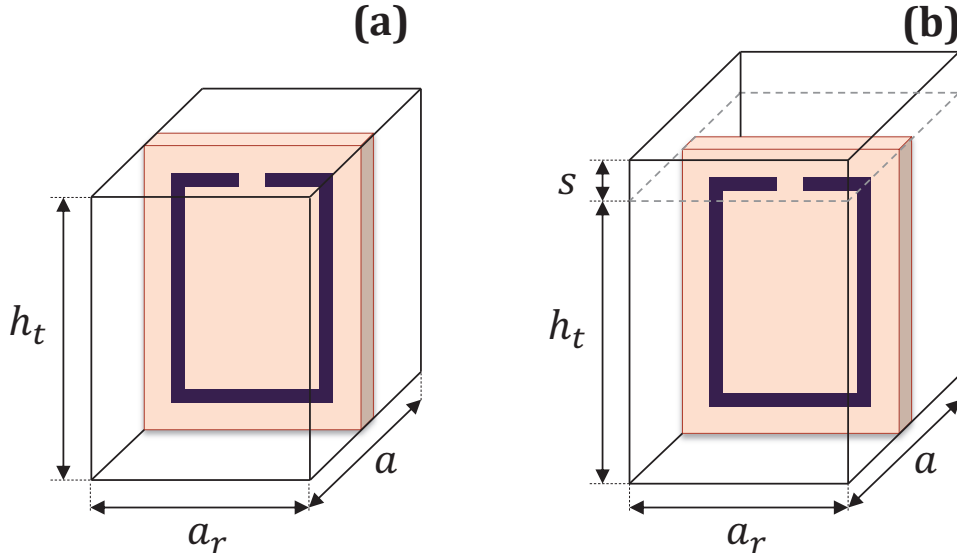


Figure 4.33: Scheme of the unit cells. (a) Unit cell employed for the design of the samples and (b) unit cell with the airgap,  $s$ , produced by the measurement setup.

results obtained at 3.8 GHz. This displacement in the constitutive parameters is shown in Fig. 4.34, where the discontinuous lines are the designed parameters and the continuous profiles are the parameters obtained inside the chamber.

This change in the constitutive parameters causes a shift in the resonance frequency of the RPC. In order to assess the frequency shift, COMSOL simulations have been used. The constitutive parameters extracted from the simulation of the ring resonators with the air gap have been introduced in

Ring resonator	1A	1B	2A	2B
$real(\mu)$	0.225	0.1885	0.321	0.2287
$real(\epsilon)$	2.834	2.833	2.848	2.834

Table 4.4: Extracted parameters from the unit cells. Constitutive parameters of the ring resonators with 1mm of air over the sample at 3.8GHz.



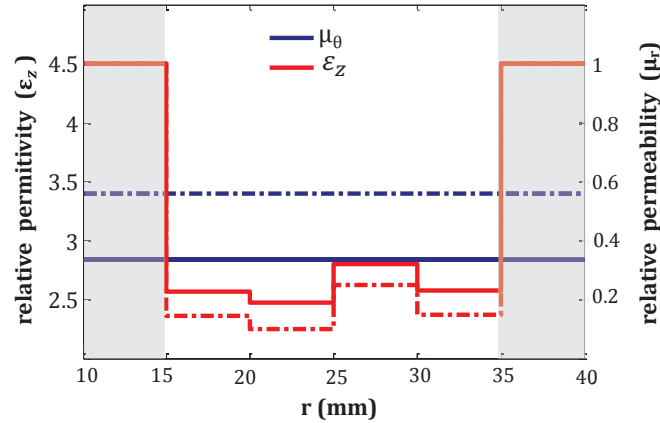


Figure 4.34: Constitutive parameter profiles. Blue lines are the permeability and red lines are the permeability. Dashed: Original design parameters. Solid: parameters with air gap

a 2D-COMSOL model and two different analysis have been performed: an eigenvalue analysis and an analysis with an external point source. First, the eigenvalue analysis shows that the resonance frequency for the mode  $q = 3$  is  $f = 3.99$  GHz that is in agreement with our experimental findings. In the second analysis, the resonance modes are studied with the parameter extraction. These results are presented in Fig. 4.35 (continuous line). Figure 4.35 compares the behavior of the mode coefficients extracted from the measurement and from the COMSOL simulations of the model with air over the sample. These analysis demonstrate that the frequency shift is caused by the experimental set-up and support our earlier observations, showing that E-field maps for a frequency  $f = 4$  GHz have the field map more defined.

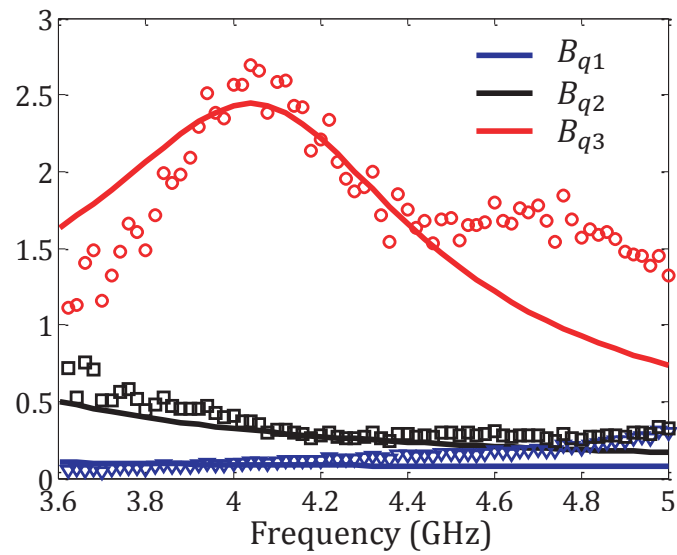


Figure 4.35: Extracted coefficients from the inner cavity field for the first 3 modes. Results from measurements are displayed with symbols; results from analytical simulation are displayed with lines.



# Part II

ABSORPTION OF  
ELECTROMAGNETIC WAVES



# 5

## ABSORPTION MECHANISMS IN THIN LAYERS

---

This section summarizes the properties of the absorption systems based on lossy thin layers. First section presents the traditional systems. Then, a review of the absorption enhancement mechanisms with periodic structures is introduced.

### Contents

---

<b>5.1</b>	<b>Introduction</b>	<b>96</b>
<b>5.2</b>	<b>Coaxial Grating</b>	<b>98</b>

---

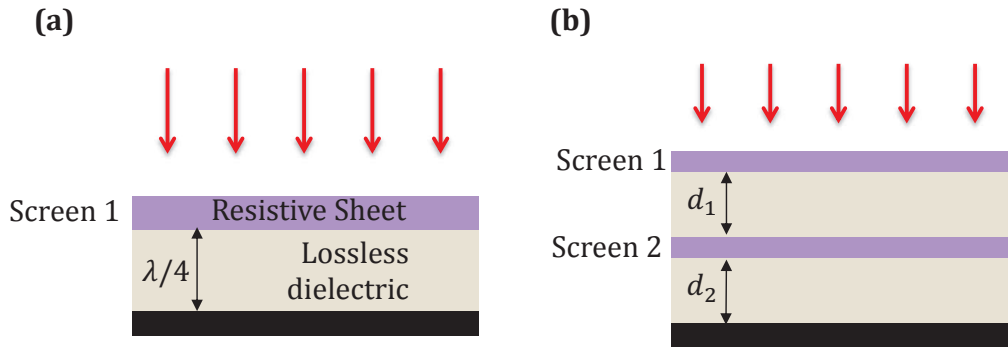


Figure 5.1: Schematic representation of traditional absorber devices: (a) Salisbury screen and (b) Jaumann absorber.

## 5.1 Introduction

Electromagnetic absorbers have attracted much interest due to the number of applications in which they are involved. The design of flat and thin materials with high absorption is still a challenge. Conventional electromagnetic absorbers are electrically thick. For example, Salisbury screen is an absorber device which is constructed by placing a thin resistive sheet at  $\lambda/4$  above a perfect conductor plane. This system is schematically represented in Fig. 5.1(a). To increase the absorption bandwidth, resistive sheets are stacked over each other at a distance of a quarter wavelength, as it is shown in Fig. 5.1(b). This solution is known as Jaumann absorber and generates wider absorption band compared to the Salisbury absorber.

The condition for considering ultra-thin absorbers is working with thickness  $\lambda/10$  or less at the operation frequency. The thickness of the lossy materials can be reduced by using periodic materials. Periodic distributions of scattering elements can be placed at the interface between the air and the absorber material. Waves will be scattered preferentially into the dielectric with larger permittivity. This solution is schematically represented in Fig. 5.2(a). Other option for reducing the thickness of the absorber material is to use a periodic arrangement of resonant elements which concentrate the field in the lossy material enhancing the absorption [see Fig. 5.2(b)]. Finally, periodic gratings can be placed on the bottom of the absorber material generating strong evanescent fields near the diffracted modes cutoff frequencies.

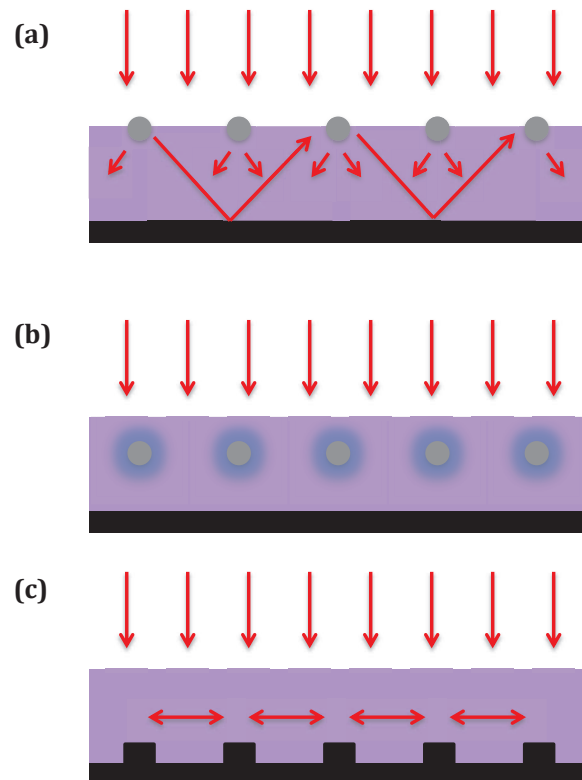


Figure 5.2: Absorption enhancement by periodic media. (a) Periodic distribution of scattering elements which favours the wave trapping at the lossy material. (b) Absorption enhancement by the excitation of resonances in a periodic distribution of resonators. (c) Excitation of the guided modes in the lossy layer by a periodic grating.



Recently, the introduction of metamaterials has opened new ways for designing absorbing materials. In the design of absorber devices based on metamaterials, a design can be considered successful when at least one of the following criteria is satisfied: (i) perfect or near unity absorption, (ii) very thin or sub-wavelength size to avoid bulky devices, and (iii) broadband operation. To these purposes, a number of options have been proposed and analyzed in the literature. Structures based on resonant patches [31] [32] have been studied at several spectral regimes. Usually, the resonant characteristics of these patches are employed to optimize absorption. Also, in combination with metallic backed planes, thin layers have been proposed including slits over dielectric layers [33] [34], holes or cavities in the metallic plane [35] [36] and even metal-dielectric multilayered structures [37]. Wide incidence angles can be explored with any of these possible element configurations [38]. Also, if the sub-wavelength thickness requirement is relaxed, performance improvements in broadband operation can be achieved [39] [40]. Although most solutions are based on periodic media, it is possible to improve the absorption properties using disordered media [41].

## 5.2 Coaxial Grating

In the following chapters, we will study the absorption produced by a metasurface on the bottom of a lossy thin layer. Particularly, the metasurface used in our study is made of annular-type cavities patterned on a metallic plate.

It has been shown that coaxial- or annular-type cavities present an enhancement of the transmission due to the TEM mode always present in this particular type of cavities [42–46]. Although annular cavity arrays have been previously studied in regards of their transmission characteristics, no studies have been performed exploring their use as building blocks for absorption enhancement.

The absorption enhancement produced by the metasurface will be comprehensively analysed. The absorption mechanism is based on the fact that the subwavelength cavities provide the resonances giving a strong concentration of EM energy which is absorbed by the thin dielectric slab on top. The fundamental mode (TEM mode) of the annular cavities has no cutoff frequency, a feature that is here employed to obtain extraordinary absorption

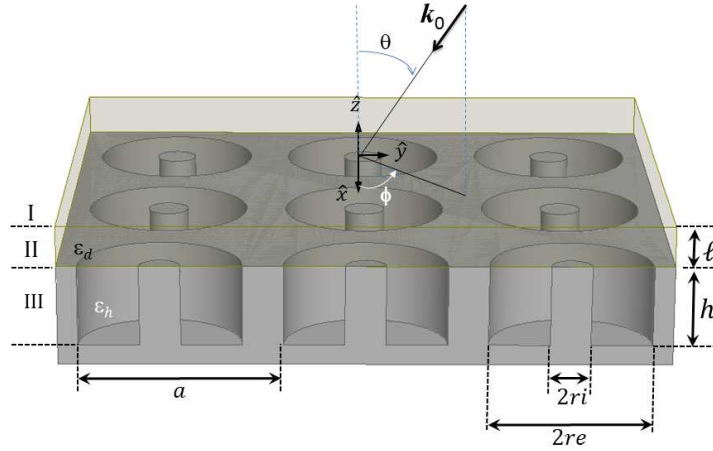


Figure 5.3: Schematic representation of the proposed structures. Region I is the background medium (air in our case), region II is a dielectric slab with thickness  $\ell$  and dielectric permittivity  $\varepsilon_d(1 + i\xi)$ . Region III is a perfectly conducting metal containing a square distribution of annular cavities with lattice period  $a$  and length  $h$  filled with a dielectric material  $\varepsilon_h$ . The external and inner radii of the annular cavities are  $r_e$  and  $r_i$ , respectively.

at low frequencies. This is an advantage in comparison with empty cavity designs where resonances are limited by the frequency cut-off determined by the cavity diameter. In comparison with metamaterial absorbers based on the repetition of metallic resonators [11], the absorption in our structures takes place on the dielectric absorbing layer on top on the metallic surface. This feature can be also considered as an advantage because of its easy fabrication; that is, the thin dielectric film is just deposited on top of the surface while the metallic resonators require a complex design together with a very accurate fabrication.



# 6

## ABSORPTION ENHANCEMENT BY A COAXIAL GRATING

---

The chapter is organized as follows. Section 6.1 introduces the structures under study and describes the model employed in their analysis. In Section 6.2, the solutions are particularized for the coaxial cavities employed in our proposal for total absorption systems. Afterwards, in Section 6.3, we discuss the absorptive properties of the structures at low frequencies. The different features of the absorptive peaks are comprehensively analyzed as a function of the structure parameters. Moreover, we study other physical mechanisms of energy absorption.

### Contents

---

<b>6.1</b>	<b>Mode Matching Analysis . . . . .</b>	<b>102</b>
6.1.1	General case . . . . .	103
6.1.2	Absorption analysis . . . . .	106
6.1.3	Monomode approximation . . . . .	108
<b>6.2</b>	<b>Modes in Coaxial Cavities . . . . .</b>	<b>114</b>
6.2.1	TEM modes . . . . .	115
6.2.2	TE modes . . . . .	118
6.2.3	TM modes . . . . .	120
<b>6.3</b>	<b>Numerical Experiments . . . . .</b>	<b>123</b>
6.3.1	Low-frequency absorption. . . . .	123
6.3.2	Other absorption mechanisms . . . . .	129

---

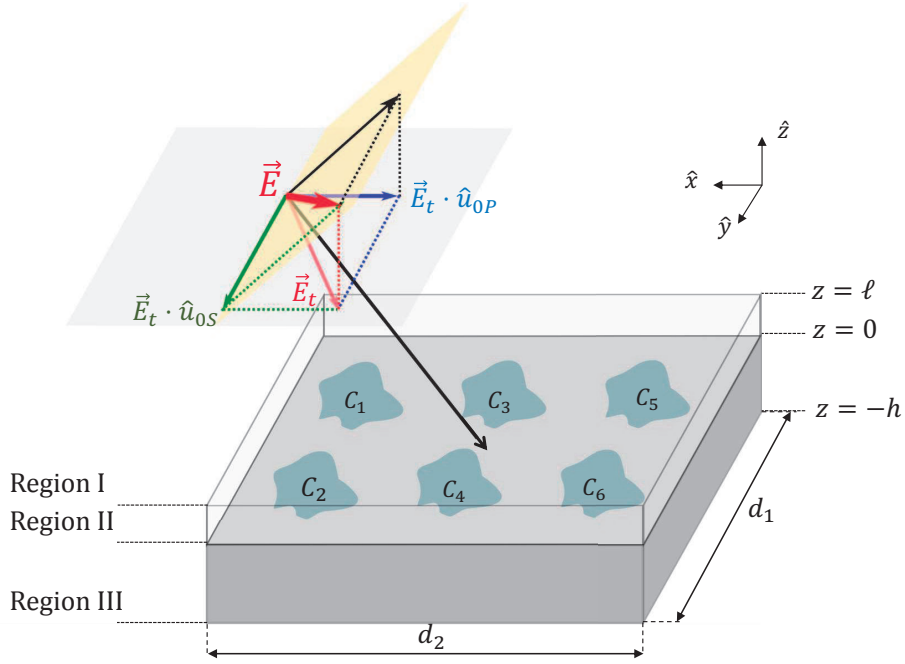


Figure 6.1: Schematic representation of metasurface covered by a lossy thin layer with thickness  $\ell$ . An arbitrary unit cell of a metasurface is represented with lattice vectors  $d_1$  and  $d_2$ . The impinging electric field vector  $\mathbf{E}$  is represented and decomposed in tangential components.

## 6.1 Mode Matching Analysis

The mode-matching technique is here employed to analyze the interaction of a plane wave impinging on a thin and lossy dielectric layer backed by the metallic metasurface.

The structure under study is schematically shown in Fig. 6.1. The EM waves propagating in air (region I) impinge on a thin dielectric slab (region II) placed on top of a metallic metasurface (region III) containing a 2D array of arbitrary cavities with length  $h$ . A unit cell of a generic metasurface is represented, being  $\mathbf{d}_1$  and  $\mathbf{d}_2$  the lattice vectors. The cavities are denoted by  $C_1, C_2 \dots C_6$  and are filled with a lossless dielectric material with permittivity  $\varepsilon_{hi}$ . The dielectric slab with complex dielectric constant  $\hat{\varepsilon}_d = \varepsilon_d(1 + i\xi)$  has thickness  $\ell$ . Furthermore, this figure represents the impinging plane wave with an oblique angle of incidence. The E-field vector is decomposed in tangential

components.

### 6.1.1 General case

It is assumed that the structure is illuminated (see Fig. 6.1) by a plane wave whose wavevector in spherical coordinates can be written as:

$$\mathbf{k}_0 = \omega/c(\sin \theta \cos \phi \hat{\mathbf{x}} + \cos \theta \sin \phi \hat{\mathbf{y}} + \cos \theta \hat{\mathbf{z}}) \quad (6.1)$$

The geometry of the problem indicates that the EM fields in the background and the dielectric layer can be decomposed in tangential and perpendicular components to the metallic surface, which defines the  $xy$  plane at  $z = 0$ . Thus, the electric and magnetic fields are given by:

$$\mathbf{E}(\mathbf{r}) = E_z \hat{\mathbf{z}} + \mathbf{E}_t, \quad (6.2)$$

$$\mathbf{B}(\mathbf{r}) = B_z \hat{\mathbf{z}} + \mathbf{B}_t. \quad (6.3)$$

The wavevector can be expressed as:

$$\mathbf{k}_0 = q_0 \hat{\mathbf{z}} + \mathbf{k}_t, \quad (6.4)$$

where  $k_0^2 = q_0^2 + |\mathbf{k}_t|^2$ . The light polarization  $\sigma$  is named  $S$  when  $\mathbf{E}_t \perp \mathbf{k}_t$  or  $P$  when  $\mathbf{E}_t \parallel \mathbf{k}_t$ . The temporal dependence  $e^{-i\omega t}$  will be implicitly assumed in the rest of the chapter for all the fields.

Due to the periodicity of the system, diffracted modes can be excited with tangential wavenumber:

$$\mathbf{k}_G = \mathbf{k}_t + \mathbf{G}, \quad (6.5)$$

being  $\mathbf{G}$  the reciprocal lattice vectors

$$\mathbf{G} = m_1 \mathbf{b}_1 + m_2 \mathbf{b}_2, \quad (6.6)$$

where  $\mathbf{b}_i$  are the primitive vectors of the reciprocal lattice and  $m_{1,2}$  are integers ( $m_{1,2} = 0, \pm 1, \pm 2, \dots$ ). The solution for  $\mathbf{E}_t$  and  $\mathbf{H}_t$  can be obtained as a linear combination of these diffracted waves, which additionally can be decomposed in two polarizations  $\sigma = S, P$ , being  $S$  and  $P$  the polarizations perpendicular and parallel, respectively, to the wavevector  $\mathbf{k}_G$ , and whose unit vectors are given by

$$\hat{\mathbf{u}}_{GS} = \frac{\hat{\mathbf{z}} \times \mathbf{k}_G}{|\mathbf{k}_G|}, \quad (6.7)$$

for the  $S$ -polarization and

$$\hat{\mathbf{u}}_{GP} = \frac{\mathbf{k}_G}{|\mathbf{k}_G|}, \quad (6.8)$$

for the  $P$ -polarization.

Therefore, the fields in region I (the air) are expressed as

$$|\mathbf{E}_t^0\rangle = A_{0\sigma_0}^- e^{-iq_0(z-\ell)} |\mathbf{k}_t\sigma_0\rangle + \sum_{G,\sigma} A_{G\sigma}^+ e^{iq_G(z-\ell)} |\mathbf{k}_G\sigma\rangle, \quad (6.9)$$

$$|-\hat{\mathbf{z}} \times \mathbf{H}_t^0\rangle = -Y_{0\sigma_0}^0 A_{0\sigma_0}^- e^{-iq_0(z-\ell)} |\mathbf{k}_t\sigma_0\rangle + \sum_{G,\sigma} Y_{G\sigma}^0 A_{G\sigma}^+ e^{iq_G(z-\ell)} |\mathbf{k}_G\sigma\rangle, \quad (6.10)$$

where  $A_{0\sigma_0}^-$  is the amplitude of the incident wave with polarization  $\sigma_0$  and  $q_G^2 = (\omega/c_0)^2 - |\mathbf{k}_G|^2$ .

Using Dirac's notation the diffracted wave with wavevector  $\mathbf{k}_G$  and polarization  $\sigma$  is denoted by the ket  $|\mathbf{k}_G\sigma\rangle$ , and their normalized expressions are

$$\langle \mathbf{r} | \mathbf{k}_G\sigma \rangle \equiv \frac{1}{\sqrt{\Omega}} e^{i\mathbf{k}_G \cdot \mathbf{r}} \hat{\mathbf{u}}_{G\sigma}, \quad (6.11)$$

where  $\Omega$  is the area of the unit cell and they accomplish  $\langle \mathbf{k}_G\sigma | r \rangle \langle r | \mathbf{k}_G\sigma \rangle = 1$ .

The modal admittances  $Y_{G\sigma}$  for the two polarizations are

$$Y_{GS}^0 = \frac{q_G}{k_\omega} \sqrt{\frac{\varepsilon_0}{\mu_0}}, \quad (6.12)$$

and

$$Y_{GP}^0 = \frac{k_\omega}{q_G} \sqrt{\frac{\varepsilon_0}{\mu_0}}, \quad (6.13)$$

where  $\varepsilon_0$  and  $\mu_0$  are, respectively, the dielectric permittivity and magnetic permeability of air.

Similarly, the tangential components of the fields in region II (the dielectric slab) are

$$|\mathbf{E}_t^d\rangle = \sum_{G,\sigma} (B_{G\sigma}^+ e^{ip_G(z-\ell)} + B_{G\sigma}^- e^{-ip_G(z-\ell)}) |\mathbf{k}_G\sigma\rangle, \quad (6.14)$$

and

$$|-\hat{\mathbf{z}} \times \mathbf{H}_t^d\rangle = \sum_{G,\sigma} Y_{G\sigma}^d \times (B_{G\sigma}^+ e^{ip_G(z-\ell)} - B_{G\sigma}^- e^{-ip_G(z-\ell)}) |\mathbf{k}_G\sigma\rangle, \quad (6.15)$$

with  $p_G^2 = k_d^2 - |\mathbf{k}_G|^2$  and  $k_d = k_0 \sqrt{\varepsilon_d \mu_d}$ .

The modal admittances for each polarization are now

$$Y_{GS}^d = \frac{p_G}{k_\omega} \sqrt{\frac{\varepsilon_d}{\mu_d}}, \quad (6.16)$$

and

$$Y_{GP}^d = \frac{k_\omega}{p_G} \sqrt{\frac{\varepsilon_d}{\mu_d}}. \quad (6.17)$$

Finally, the tangential components of the fields inside the cavities can be written as:

$$|\mathbf{E}_t^\alpha\rangle = \sum_{n,\alpha} C_{n\alpha} (e^{ik_{n\alpha}z} + \Gamma_{n\alpha} e^{-ik_{n\alpha}z}) |n\alpha\rangle, \quad (6.18)$$

$$|-\hat{\mathbf{z}} \times \mathbf{H}_t^\alpha\rangle = \sum_{n,\alpha} Y_{n\alpha} C_{n\alpha} (e^{ik_{n\alpha}z} - \Gamma_{n\alpha} e^{-ik_{n\alpha}z}) |n\alpha\rangle, \quad (6.19)$$

where the modal admittance is  $Y_{n\alpha}$ , the reflection coefficient at the cavity bottom is  $\Gamma_{n\alpha} = -e^{-2ik_{n\alpha}h}$  and  $\langle r|n\alpha\rangle$  the  $n$  mode in the  $\alpha$  cavity.

Now, we apply the boundary condition in the interfaces ( $z = \ell$  and  $z = 0$ ). At the air/dielectric interface, located at  $z = \ell$ , the continuity of the tangential components of the fields gives

$$A_{G\sigma}^+ + A_{0\sigma_0}^- \delta_{0\sigma_0} = B_{G\sigma}^+ + B_{G\sigma}^-, \quad (6.20)$$

$$Y_{G\sigma}^0 (A_{G\sigma}^+ - A_{0\sigma_0}^- \delta_{0\sigma_0}) = Y_{G\sigma}^d (B_{G\sigma}^+ - B_{G\sigma}^-). \quad (6.21)$$

At  $z = 0$ , the metal/dielectric interface, the boundary conditions impose the continuity of  $\mathbf{E}_t$  over the entire unit cell and the continuity of  $\mathbf{H}_t$  over the annular cavity. Thus, at the interface the field equations are

$$\sum_{G,\sigma} (B_{G\sigma}^+ e^{-ip_G \ell} + B_{G\sigma}^- e^{ip_G \ell}) |\mathbf{k}_G\sigma\rangle = \sum_{n,\alpha} C_{n\alpha} (1 + \Gamma_{n\alpha}) |n\alpha\rangle, \quad (6.22)$$

$$\sum_{G,\sigma} Y_{G\sigma}^d (B_{G\sigma}^+ e^{-ip_G \ell} - B_{G\sigma}^- e^{ip_G \ell}) |\mathbf{k}_G\sigma\rangle = \sum_{n,\alpha} Y_{n\alpha} C_{n\alpha} (1 - \Gamma_{n\alpha}) |n\alpha\rangle. \quad (6.23)$$



Now, (6.22) is projected with the mode  $\langle \mathbf{k}_G \sigma |$  while (6.23) is projected with cavity mode  $\langle n\alpha |$ , leading to

$$B_{G\sigma}^+ e^{-ip_G \ell} + B_{G\sigma}^- e^{ip_G \ell} = \sum_{n,\alpha} C_{n\alpha} (1 + \Gamma_{n\alpha}) \langle \mathbf{k}_G \sigma | n\alpha \rangle, \quad (6.24)$$

$$\sum_{G,\sigma} Y_{G\sigma}^d (B_{G\sigma}^+ e^{-ip_G \ell} - B_{G\sigma}^- e^{ip_G \ell}) \langle n\alpha | \mathbf{k}_G \sigma \rangle = Y_{n\alpha} C_{n\alpha} (1 - \Gamma_{n\alpha}). \quad (6.25)$$

The term  $\langle n\alpha | \mathbf{k}_G \sigma \rangle = \langle \mathbf{k}_G \sigma | n\alpha \rangle^*$  represents the overlapping integrals of the diffracted waves in the dielectric layer with the mode inside the cavities.

### 6.1.2 Absorption analysis

The study of the absorption produced by the system is done by the analysis of the energy flux. We can obtain the electromagnetic energy flux as the integral over a unit cell of the real part of the Poynting Vector:

$$\Phi = \iint_{\Omega} \Re(\mathbf{E} \times \mathbf{H}^*) d\mathbf{S} \quad (6.26)$$

The vectorial product of the electric and magnetic fields can be decomposed as follows:

$$\begin{aligned} \mathbf{E} \times \mathbf{H}^* &= (\mathbf{E}_t + \hat{\mathbf{z}}E_z) \times (\mathbf{H}_t^* + \hat{\mathbf{z}}H_z^*) = \\ &= \underbrace{(\mathbf{E}_t \times \mathbf{H}_t^*)}_{\text{Longitudinal}} + \underbrace{(\hat{\mathbf{z}}E_z \times \mathbf{H}_t^* + \mathbf{E}_t \times \hat{\mathbf{z}}H_z^*)}_{\text{Tangential}} \end{aligned} \quad (6.27)$$

It is easy to see that the flux equation can be written as:

$$\Phi = \iint_{\Omega} \Re(\mathbf{E}_t \times \mathbf{H}_t^*) d\mathbf{S}, \quad (6.28)$$

where  $d\mathbf{S} = \hat{\mathbf{z}}$  is the surface differential.

The tangential component of the electric and the magnetic fields are decomposed using the vector definition in Eqs. (6.7) and (6.8) leading to:

$$\mathbf{E}_t = \sum_G (E_{GP} \hat{\mathbf{u}}_{GP} + E_{GS} \hat{\mathbf{u}}_{GS}), \quad (6.29)$$

$$\mathbf{H}_t = \sum_G (-H_{GP} \hat{\mathbf{u}}_{GS} + H_{GS} \hat{\mathbf{u}}_{GP}), \quad (6.30)$$

Each component can be expressed as a linear combination of forward and backward propagating plane waves as follows:

$$\mathbf{E}_t \begin{cases} E_{GP} = A_{GP}^+ e^{iq_G z} + A_{GP}^- e^{-iq_G z} \\ E_{GS} = A_{GS}^+ e^{iq_G z} + A_{GS}^- e^{-iq_G z} \end{cases} \quad (6.31)$$

and

$$\mathbf{H}_t \begin{cases} H_{GP} = Y_{GS} \left( A_{GP}^+ e^{iq_G z} - A_{GP}^- e^{-iq_G z} \right) \\ H_{GS} = Y_{GP} \left( A_{GS}^+ e^{iq_G z} - A_{GS}^- e^{-iq_G z} \right) \end{cases} \quad (6.32)$$

The flux can be rewritten as

$$\Phi = \iint_{\Omega} \sum_G \Re (E_{GP} H_{GS}^* - E_{GS} H_{GP}^*) d\mathbf{S} \quad (6.33)$$

Using the expansion in forward and backward propagating waves of the electric and magnetic fields, we can see that

$$\Re (E_{GP} H_{GS}^*) = Y_{GP} \left( |A_{GP}^+|^2 - |A_{GP}^-|^2 \right) \quad (6.34)$$

and

$$\Re (E_{GS} H_{GP}^*) = -Y_{GS} \left( |A_{GS}^+|^2 - |A_{GS}^-|^2 \right). \quad (6.35)$$

Finally, the flux can be calculated as

$$\Phi = \Omega \sum_G \left[ Y_{GP} \left( |A_{GP}^+|^2 - |A_{GP}^-|^2 \right) - Y_{GS} \left( |A_{GS}^+|^2 - |A_{GS}^-|^2 \right) \right] \quad (6.36)$$

Let us consider that the total flux can be divided in the incoming flux and the out-coming flux,

$$\Phi = \Phi_{in} - \Phi_{out}, \quad (6.37)$$

where

$$\Phi_{in} = \Omega \sum_G \left( Y_{GP} |A_{GP}^-|^2 + Y_{GS} |A_{GS}^-|^2 \right) \quad (6.38)$$

and

$$\Phi_{out} = \Omega \sum_G \left( Y_{GP} |A_{GP}^+|^2 + Y_{GS} |A_{GS}^+|^2 \right) \quad (6.39)$$

Notice that in a lossless system  $\Phi_{out} = \Phi_{in}$ , so  $\Phi = 0$ . The absorption of the system can be calculated as:

$$A = 1 - \frac{\Phi_{out}}{\Phi_{in}}. \quad (6.40)$$

We can cast this equation into

$$A = 1 - \sum_G \frac{Y_{GP} |A_{GP}^+|^2 + Y_{GS} |A_{GS}^+|^2}{Y_{0\sigma_0} |A_{0\sigma_0}^-|^2}. \quad (6.41)$$

being  $A_{0\sigma_0}^-$  the amplitude of the incident plane wave with polarization  $\sigma_0$ .

### 6.1.3 Monomode approximation

We have developed a model with one cavity per unit cell in which only the fundamental mode is considered inside the cavities, it is a monomode approximation. The fundamental mode is denoted by  $|\alpha\rangle$  and, considering that it is the only mode in the cavities, Equations (6.22) and (6.23) can be simplified as:

$$|\mathbf{E}_t^\alpha\rangle = C_\alpha(e^{ikhz} + \Gamma_\alpha e^{-ikhz})|\alpha\rangle, \quad (6.42)$$

$$|-\hat{\mathbf{z}} \times \mathbf{H}_t^\alpha\rangle = Y_\alpha C_\alpha(e^{ikhz} - \Gamma_\alpha e^{-ikhz})|\alpha\rangle, \quad (6.43)$$

where the modal admittance is  $Y_\alpha$  and the reflection coefficient at the cavity bottom is  $\Gamma_\alpha$ .

Using this monomode approximation, the boundary conditions at  $z = 0$  which impose the continuity of  $\mathbf{E}_t$  over the entire unit cell and the continuity of  $\mathbf{H}_t$  over the annular cavity can be rewritten as:

$$\sum_{G,\sigma} (B_{G\sigma}^+ e^{-ip_G\ell} + B_{G\sigma}^- e^{ip_G\ell}) |\mathbf{k}_G\sigma\rangle = C_\alpha(1 + \Gamma_\alpha) |\alpha\rangle, \quad (6.44)$$

$$\sum_{G,\sigma} Y_{G\sigma}^d (B_{G\sigma}^+ e^{-ip_G\ell} - B_{G\sigma}^- e^{ip_G\ell}) |\mathbf{k}_G\sigma\rangle = Y_\alpha C_\alpha(1 - \Gamma_\alpha) |\alpha\rangle. \quad (6.45)$$

Now, applying the projection as in the previous case we arrive to:

$$B_{G\sigma}^+ e^{-ip_G\ell} + B_{G\sigma}^- e^{ip_G\ell} = C_\alpha(1 + \Gamma_\alpha) \langle \mathbf{k}_G\sigma | \alpha \rangle, \quad (6.46)$$

$$\sum_{G,\sigma} Y_{G\sigma}^d (B_{G\sigma}^+ e^{-ip_G\ell} - B_{G\sigma}^- e^{ip_G\ell}) \langle \alpha | \mathbf{k}_G\sigma \rangle = Y_\alpha C_\alpha(1 - \Gamma_\alpha). \quad (6.47)$$

The system of equations formed by Eqs. (6.20), (6.21), (6.46) and (6.47) can be solved to obtain the amplitude of the reflected waves as a function of the incident wave amplitude. To do that, we proceed as follows. From Eq. (6.46),  $B_{G\sigma}^+$  is:

$$B_{G\sigma}^+ = C_\alpha(1 + \Gamma_\alpha) \langle \mathbf{k}_G\sigma | \alpha \rangle e^{ip_G\ell} + B_{G\sigma}^- e^{2ip_G\ell}. \quad (6.48)$$

This term can be inserted in Eq. (6.47)

$$-2 \sum_{G,\sigma} \frac{Y_{G\sigma}^d}{Y_\alpha} B_{G\sigma}^- e^{ip_G\ell} \langle \alpha | \mathbf{k}_G\sigma \rangle = C_\alpha [(1 - \Gamma_\alpha) - (1 + \Gamma_\alpha)\chi^{(1)}] \quad (6.49)$$

where

$$\chi^{(1)} = \sum_{G,\sigma} \frac{Y_{G\sigma}^d}{Y_\alpha} \langle \alpha | \mathbf{k}_G \sigma \rangle \langle \mathbf{k}_G \sigma | \alpha \rangle \quad (6.50)$$

Equation (6.48) is inserted into Eqs. (6.20) and (6.21), leading to:

$$A_{G\sigma}^- \delta_{G0} + A_{G\sigma}^+ = B_{G\sigma}^- (1 - e^{2ip_G \ell}) + C_\alpha (1 + \Gamma_\alpha) \langle \mathbf{k}_G \sigma | \alpha \rangle e^{ip_G \ell} \quad (6.51)$$

$$Y_{G\sigma}^0 \left( -A_{G\sigma}^- \delta_{G0} + A_{G\sigma}^+ \right) = -Y_{G\sigma}^d B_{G\sigma}^- (1 + e^{2ip_G \ell}) + Y_{G\sigma}^d C_\alpha (1 + \Gamma_\alpha) \langle \mathbf{k}_G \sigma | \alpha \rangle e^{ip_G \ell} \quad (6.52)$$

Using Eqs. (6.51) and (6.52), the coefficients  $B_{G\sigma}^-$  and  $A_{G\sigma}^+$  can be written as a function of  $C_\alpha$ :

$$B_{G\sigma}^- = 2 \frac{Y_{G\sigma}^0}{Y_{G\sigma}^H} A_{0\sigma_0}^- \delta_{G0} + \frac{Y_{G\sigma}^d - Y_{G\sigma}^0}{Y_{G\sigma}^H} C_\alpha (1 + \Gamma_\alpha) \langle \mathbf{k}_G \sigma | \alpha \rangle e^{ip_G \ell}, \quad (6.53)$$

$$A_{G\sigma}^+ = R_d A_{0\sigma_0}^- \delta_{G0} + 2 \frac{Y_{G\sigma}^d}{Y_{G\sigma}^H} C_\alpha (1 + \Gamma_\alpha) \langle \mathbf{k}_G \sigma | \alpha \rangle e^{ip_G \ell} \quad (6.54)$$

where

$$R_d = \frac{Y_{0\sigma}^0 (1 + e^{2ip_0 \ell}) - Y_{0\sigma}^d (1 - e^{2ip_0 \ell})}{Y_{0\sigma}^0 (1 + e^{2ip_0 \ell}) + Y_{0\sigma}^d (1 - e^{2ip_0 \ell})} \quad (6.55)$$

and

$$Y_{G\sigma}^H = Y_{G\sigma}^0 (1 - e^{2ip_G \ell}) + Y_{G\sigma}^d (1 + e^{2ip_G \ell}) \quad (6.56)$$

Now, equation (6.53) is introduced into Eq. (6.49) and we obtain:

$$-4 \frac{Y_{0\sigma}^0 Y_{0\sigma}^d}{Y_\sigma^H Y_\alpha} A_{0\sigma_0}^- \langle \alpha | \mathbf{k}_0 \sigma_0 \rangle e^{ip_0 \ell} = C_\alpha \left[ (1 - \Gamma_\alpha) - (1 + \Gamma_\alpha) (\chi^{(1)} + \chi^{(2)}) \right], \quad (6.57)$$

with  $\chi^{(2)}$  being

$$\chi^{(2)} = 2 \sum_{G,\sigma} \frac{Y_\alpha}{Y_{G\sigma}^d} \frac{Y_{G\sigma}^0 - Y_{G\sigma}^d}{Y_{G\sigma}^H} e^{2ip_G \ell} \langle \alpha | \mathbf{k}_G \sigma \rangle \langle \mathbf{k}_G \sigma | \alpha \rangle \quad (6.58)$$

Therefore, the coefficient of the field inside the cavities,  $C_\alpha$ , as a function of the amplitude of the incident wave is:

$$C_\alpha = C_\alpha = -\frac{4}{M} \frac{Y_{0\sigma}^0 Y_{0\sigma}^d}{Y_{0\sigma}^H Y_\alpha} \langle \alpha | \mathbf{k}_t \sigma_0 \rangle e^{ip_0 \ell} A_0^- \quad (6.59)$$

where

$$M_{\pm}(1 - \Gamma_{\alpha}) - (1 + \Gamma_{\alpha}) (\chi^{(1)} + \chi^{(2)}) \quad (6.60)$$

The amplitude of the field in the cavities can be introduced into Eqs. ((6.53)) and ((6.54)) and we get

$$B_{G\sigma}^{-} = 2 \frac{Y_{0\sigma}^0}{Y_{0\sigma}^H} A_0^{-} \times \left[ \delta_{G,0} - \frac{2}{M} e^{ip_0\ell} \frac{Y_{G\sigma}^d - Y_{G\sigma}^0}{Y_{G\sigma}^H} \frac{Y_{0\sigma}^d}{Y_{\alpha}} (1 + \Gamma_{\alpha}) \langle \alpha | \mathbf{k}_t \sigma_0 \rangle \langle \mathbf{k}_G \sigma | \alpha \rangle e^{ip_G\ell} \right], \quad (6.61)$$

$$A_{G\sigma}^{+} = R_d A_{0\sigma_0}^{-} \delta_{G0} - 8 \frac{Y_{G\sigma}^d}{Y_{G\sigma}^H} \frac{Y_{0\sigma}^0}{Y_{\alpha}} \frac{Y_{0\sigma}^d}{Y_{0\sigma}^H} \frac{1 + \Gamma_{\alpha}}{M} \langle \mathbf{k}_G \sigma | \alpha \rangle e^{ip_0\tilde{A}\tilde{s}\tilde{A}\tilde{s}\ell} e^{ip_G\ell} \quad (6.62)$$

Finally, from Eq. ((6.20)) the coefficients  $B_{G\sigma}^{+}$

$$B_{G\sigma}^{+} = A_{0\sigma_0}^{-} \delta_{G0} + A_{G\sigma_0}^{+} B_{G\sigma_0}^{-} \quad (6.63)$$

In this work our interest is focused in frequencies below the diffraction limit and, therefore, we consider that only the fundamental mode  $\mathbf{G} = 0$  is excited. In other words, the reflection coefficient is simply

$$R_0(\omega) = A_{0P}^{+} / A_0^{-} \quad (6.64)$$

and the absorption in the dielectric slab is calculated as

$$A(\omega) = 1 - |R_0(\omega)|^2 \quad (6.65)$$

### Low-Frequency regime

For a thin dielectric slab we can assume that  $p_0\ell \ll 1$ , then  $R_d \approx -1$  and it is easy to show from (6.64) that the reflection coefficient can be simplified to

$$R_0 = - \frac{\cos k_h h + i(H_{00}^2 + \chi) \sin k_h h}{\cos k_h h - i\chi \sin k_h h}, \quad (6.66)$$

where  $H_{00}^2 = \langle \alpha | \mathbf{k}_t P \rangle \langle \mathbf{k}_t P | \alpha \rangle$ .

The lattice sum term  $\chi$  given in (6.66) is a complex quantity that is frequency dependent. It can be expressed as  $\chi(\omega) = \chi_R + i\chi_I$ . Therefore, the reflection coefficient can be given as

$$R_0 = - \frac{\cos k_h h + \chi_I \sin k_h h + i(H_{00}^2 - \chi_R) \sin k_h h}{\cos k_h h + \chi_I \sin k_h h - i\chi_R \sin k_h h} \quad (6.67)$$

and the absorption of the system is

$$A(\omega) = 1 - \frac{(\cot k_h h + \chi_I)^2 + (H_{00}^2 - \chi_R)^2}{(\cot k_h h + \chi_I)^2 + \chi_R^2}. \quad (6.68)$$

The behavior in frequency of  $\chi_I$  and  $\chi_R$  is obtained by splitting the lattice sum in  $\chi$  in the propagating ( $q_G$  and  $p_G$  real) and evanescent contributions ( $q_G$  and  $p_G$  imaginary). Since we are below the diffraction limit in both the dielectric and the background, the only propagating mode is that with  $\mathbf{G} = 0$ . Thus,

$$\chi(\omega) = \chi_0 + \sum_{G \neq 0} \chi_G, \quad (6.69)$$

where the term  $\chi_0$  is given by

$$\chi_0 = \frac{Y_{0P}^d}{Y_\alpha} \frac{Y_{0P}^0 \cos(p_0 \ell) - iY_{0P}^d \sin(p_0 \ell)}{-iY_{0P}^0 \sin(p_0 \ell) + Y_{0P}^d \cos(p_0 \ell)} H_{00}^2 \approx \frac{k_\omega}{\sqrt{k_\omega^2 - |k_t|^2}} \sqrt{\frac{\varepsilon_0}{\varepsilon_h}} H_{00}^2, \quad (6.70)$$

the last expression being obtained with the approximation  $\sin p_0 \ell \approx 0$ . Note that  $\chi_0$  is real since there are no losses neither in the background nor in the cavities.

The terms  $\chi_G$  for  $\mathbf{G} \neq 0$  cannot be simplified with the same approach since the lattice sum is infinite and the product  $p_G \ell$  grows up linearly. Also, the presence of the complex permittivity of the dielectric slab in the expressions makes difficult splitting these terms into their real and imaginary parts. To do it, we make a Taylor expansion of these terms around  $\xi = 0$ ,

$$\chi_G(\xi) \approx \chi_G(\xi = 0) + \xi \partial_\xi \chi_G(\xi = 0) \quad (6.71)$$

The first term of the expansion is found to be purely imaginary, since it is given by

$$\chi_G(\xi = 0) = H_{GG}^2 \frac{Y_{GP}^d}{Y_\alpha} \frac{Y_{GP}^0 \cos(p_G \ell) - iY_{GP}^d \sin(p_G \ell)}{-iY_{GP}^0 \sin(p_G \ell) + Y_{GP}^d \cos(p_G \ell)} \quad (6.72)$$

and, below the diffraction limit, the propagation constants  $p_G$  when  $\xi = 0$  are purely imaginary, and so are the impedance terms  $Y_{GP}^0$  and  $Y_{GP}^d$ . Then, it is easy to see that, in the above equation, the term  $H_{GG}^2$  is real, while

the fraction  $Y_{GP}^d/Y_\alpha$  is purely imaginary. The last term in the expression is real because  $\cos(p_G\ell)$  and  $i\sin(p_G\ell)$  are also real and the  $i$  factor in all the impedances cancel each other.

The second term in the expression has a more complex form, since it is the derivative  $\chi_G$  respect  $\xi$  for  $\xi = 0$  and, after some tedious but straightforward analysis, is given by

$$\chi'_G(\xi = 0) = \sum_{G \neq 0} H_{GG}^2 \frac{Y_G^d}{Y_\alpha} \times \frac{2\ell k_d^2 p_G (Y_G^{d^2} - Y_G^{0^2}) + (k_G^2 - p_G^2) (2iY_G^d Y_G^0 (1 - \cos 2p_G\ell) - (Y_G^{d^2} + Y_G^{0^2}) \sin 2p_G\ell)}{4p_G^2 (Y_G^d \cos p_G\ell - iY_G^0 \sin p_G\ell)^2}, \quad (6.73)$$

which is found to be real. Effectively, the term  $H_{GG}^2$  is real, while the following fraction is purely imaginary. Exploring the numerator of the second term, it is easy to see that all the terms are purely imaginary: the first one is linear in  $p_G$ , the second one contains the factor  $2i$  and the third one is proportional to  $\sin p_G\ell$ . This term multiplied by the first fraction gives us a real number. Finally, since the denominator is real, it is found that the full expression is real.

$$\chi_R(\omega) \approx \chi_0 + \xi \chi'_G(\xi = 0) \quad (6.74)$$

$$\chi_I(\omega) \approx -i\chi_G(\xi = 0) \quad (6.75)$$

The frequency dependence of both  $\chi_R(\omega)$  and  $H_{00}(\omega)$  is very smooth. Then it can be assumed that both are constant at low frequencies. On the contrary, it can be seen that the frequency dependence of  $\chi_I$  is predominantly linear in  $k_\omega$  with negative slope, that is

$$\chi_I = -i\chi_G(\xi = 0) \sim -i \frac{Y_G^d}{Y_\alpha} \sim -k_\omega \quad (6.76)$$

since we are under the condition  $\mathbf{G} \neq 0$  and  $p_G$  is purely imaginary.

The above considerations let us to conclude that the frequency dependence of the absorption is

$$A(\omega) = 1 - \frac{f^2(\omega) + c_1^2}{f^2(\omega) + c_2^2}, \quad (6.77)$$

where  $f(\omega)^2 = (\cot k_h h + \chi_I)^2$ .  $A(\omega)$  has a maximum as long as  $f(\omega)f'(\omega) = 0$ . But  $f'(\omega)$  is negative for the frequency region of interest and, therefore, the only possibility of having a maximum is  $f(\omega) = 0$ . So, the condition for having a peak in the absorption is

$$\cot k_h h + \chi_I(\omega) = 0. \quad (6.78)$$

In fact, this expression relates the peak position with the cavity length  $h$  and the lattice sum  $\chi_I$ , which contains only the contribution of the evanescent modes. Therefore it is concluded that the position of the peak is mainly determined by the interaction of the evanescent waves in the dielectric and the fundamental mode of the annular cavities. Also, it must be pointed out that the above condition depends on the layer's thickness  $\ell$ , but it is independent of  $\xi$ , the dissipative term of the permittivity.

The amplitude of the absorption has a frequency dependence that can be obtained from Eq. (6.67). When this amplitude fulfills the condition (6.78) the peak amplitude only depends on the term  $H_{00}^2 - \chi_R$ , which gives perfect absorption (unity amplitude) when its value is zero. In other words, the condition for having perfect absorption is

$$H_{00}^2 - \chi_R = 0. \quad (6.79)$$

This condition shows that perfect absorption depends on the value for  $\xi$  through  $\chi_R$ , but it is independent of  $h$ . Interestingly, the condition for perfect absorption is independent of the frequency at which it occurs, since it has been already mentioned that the dependence in frequency of  $H_{00}$  and  $\chi_R$  is smooth.

### Complex unit cells

Let us consider now the case in which more than one cavity is associated to one point of a Bravais lattice. In other words, we study here a periodic arrangement of cavities with  $N$  annular cavities inside the unit cell of the square lattice. The position of the  $\alpha$  aperture in the unit cell is given by a vector  $\mathbf{R}_\alpha$ , with  $\alpha = 1, 2, \dots, N$ . Under the monomode approximation we have now a set of  $N$  coefficients  $C_\alpha$ , one for each cavity, then mode matching has to be applied to every aperture, and Eqs. (6.46) and (6.47) become



$$B_{G\sigma}^+ e^{-ip_G \ell} + B_{G\sigma}^- e^{ip_G \ell} = \sum_{\beta} C_{\beta} (1 + \Gamma_{\beta}) \langle \mathbf{k}_G \sigma | \beta \rangle, \quad (6.80)$$

$$\sum_{G,\sigma} Y_{G\sigma}^d (B_{G\sigma}^+ e^{-ip_G \ell} - B_{G\sigma}^- e^{ip_G \ell}) |G\sigma\rangle \langle \alpha | \mathbf{k}_G \sigma = Y_{\alpha} C_{\alpha} (1 - \Gamma_{\alpha}). \quad (6.81)$$

After solving the system of equations defined by (6.20), (6.21), (6.80) (6.81) we get

$$A_{GP}^+ = R_0 \delta_{G,0} A_0^- - 8e^{ip_0 \ell} e^{ip_G \ell} \frac{Y_{0P}^0 Y_{0P}^d}{Y_0^H} \frac{Y_{GP}^d}{Y_G^H} \sum_{\alpha\beta} \frac{1 + \Gamma_{\alpha}}{Y_{\alpha}} M_{\alpha\beta}^{-1} \langle \beta | G_0 P \rangle \langle GP | \alpha \rangle A_0^-, \quad (6.82)$$

were the matrix elements  $M_{\alpha\beta}$  are defined as

$$M_{\alpha\beta} = (1 - \Gamma_{\alpha}) \delta_{\alpha\beta} - (1 + \Gamma_{\beta}) \chi_{\alpha\beta}, \quad (6.83)$$

and the interaction sums are given by

$$\chi_{\alpha\beta} = \sum_G H_{GG}^{\alpha\beta} \frac{Y_{GP}^d}{Y_{\alpha}} \frac{Y_{GP}^0 \cos(p_G \ell) - iY_{GP}^d \sin(p_G \ell)}{-iY_{GP}^0 \sin(p_G \ell) + Y_{GP}^d \cos(p_G \ell)}. \quad (6.84)$$

being

$$H_{GG}^{\alpha\beta} = \langle \alpha | GP \rangle \langle GP | \beta \rangle \quad (6.85)$$

## 6.2 Modes in Coaxial Cavities

The coaxial cavity geometry is shown in the Figure 6.2. The outer radius is denoted by  $r_e$  and the inner radius by  $r_i$ . The cavity is filled with a lossless dielectric material with permittivity  $\varepsilon_h$ . In this scheme, the cylindrical coordinate system employed in the analysis is also represented.

Fields inside the cavities are expressed as the superposition of TM modes ( $H_z = 0$ ), TE modes ( $E_z = 0$ ) and TEM modes ( $E_z = H_z = 0$ ). The solution for the transversal components,  $E_t$ , can be written as:

$$E_t = i \frac{q_N}{k_E^2} \nabla_t \Psi_E - i \frac{k_{\omega}}{k_M^2} \sqrt{\frac{\mu}{\varepsilon}} \hat{z} \times \nabla_t \Psi_H - \nabla_t \Psi_{TEM} \quad (6.86)$$

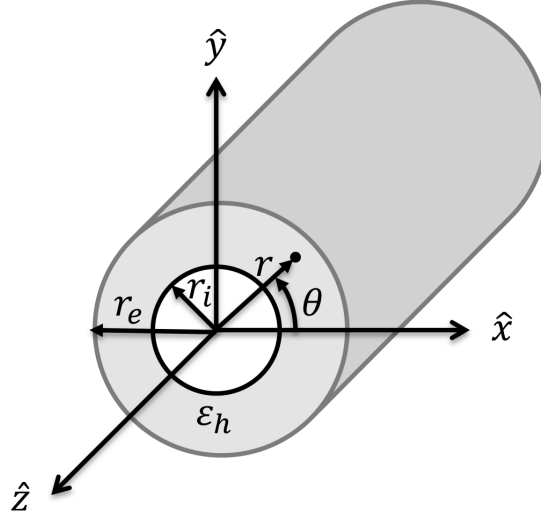


Figure 6.2: Schematic representation of the coaxial cavity.

### 6.2.1 TEM modes

TEM mode is the fundamental mode in a coaxial cavity. This mode is characterized by  $E_z = H_z = 0$  and this fact makes that the fields have to be derived by a scalar potential  $\Psi_{TEM}(r, \theta)$  which is the solution of:

$$\nabla^2 \Psi_{TEM}(r, \theta) = 0. \quad (6.87)$$

The inner conductor is at a potential  $V_0$  and the outer conductor is at zero volts, so the boundary conditions that have to be satisfied are that  $\Psi_{TEM}(r_i, \theta) = V_0$  and  $\Psi_{TEM}(r_e, \theta) = 0$ . Applying the method of separation of variables the potential can be rewritten as:

$$\Psi_{TEM}(r, \theta) = R(r)P(\theta). \quad (6.88)$$

and Eq. (6.87) can be expressed as:

$$\frac{r}{R(r)} \frac{\partial}{\partial r} \left( r \frac{\partial}{\partial r} R(r) \right) = -k_r^2, \quad (6.89)$$

$$\frac{1}{P(\theta)} \frac{\partial^2}{\partial \theta^2} P(\theta) = -k_\theta^2, \quad (6.90)$$

and

$$k_r^2 + k_\theta^2 = 0. \quad (6.91)$$

The solution for the angular function  $P(\theta)$  is:

$$P(\theta) = A \sin(k_\theta \theta) + B \cos(k_\theta \theta). \quad (6.92)$$

From the symmetry of the problem,  $k_\theta$  has to be an integer;  $k_\theta = n$ . Now, considering the boundary conditions, the potential has not to vary with  $\theta$ , so  $k_\theta = n = 0$ . Thus  $k_r = 0$  and the equations for  $R(r)$  can be reduced to

$$\frac{\partial}{\partial r} \left( r \frac{\partial}{\partial r} R(r) \right) = 0. \quad (6.93)$$

The general solution for  $R(r)$  and for  $\Psi_{TEM}$  will be

$$\Psi_{TEM} = C \ln r + D. \quad (6.94)$$

Now applying the boundary conditions, the constants  $C$  and  $D$  can be solved and the potential can be written as

$$\Psi_{TEM} = V_0 \frac{\ln r_e/r}{\ln r_e/r_i}. \quad (6.95)$$

Figure 6.3 shows the tangential electric field pattern of the TEM mode. We can see how there is not angular dependence of the electric field. Black arrows are the tangential electric field vector which is in the radial direction,  $\hat{r}$ . Red arrows represent the tangential magnetic field vector being in the angular direction,  $\hat{\theta}$

The electric field inside the coaxial apertures corresponding to the TEM mode is given by

$$\langle \mathbf{r} | \Psi_{TEM} \rangle = \nabla_t \psi_{TEM} \quad (6.96)$$

The normalization condition for the TEM mode will be

$$\langle k_{TEM} | r \rangle \langle r | k_{TEM} \rangle = \iint_{\Omega} \nabla_t \Psi_{TEM}^* \cdot \nabla_t \Psi_{TEM} d\mathbf{S} \quad (6.97)$$

and the normalized TEM mode is

$$\langle \mathbf{r} | \Psi_{TEM} \rangle = -\frac{1}{\sqrt{2\pi}} \frac{1}{\sqrt{\ln(r_e/r_i)}} \frac{1}{r} \hat{\mathbf{r}} \quad (6.98)$$

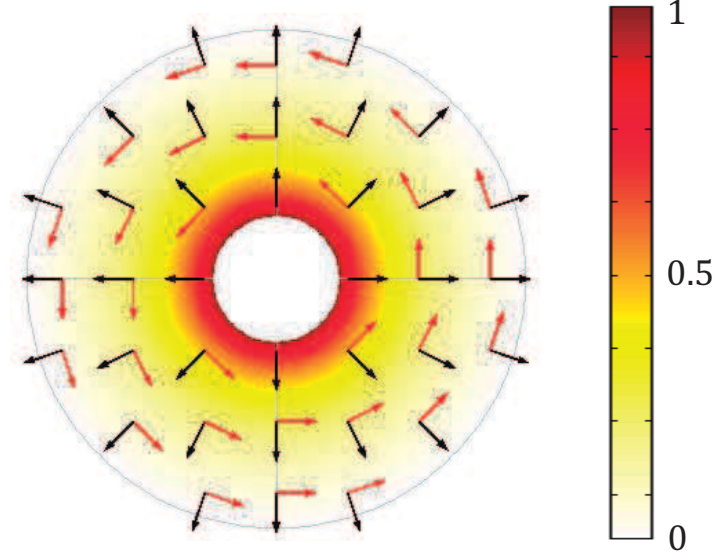


Figure 6.3: Electric field for the TEM mode. Black and red arrows represent the tangential electric and magnetic field vectors.

### Coupling integrals

The application of boundary conditions by mode-matching requires the calculation of the overlapping integrals

$$\langle \mathbf{k}_G \sigma | k_{TEM} \rangle = \iint_{\Omega_c} \langle \mathbf{k}_G \sigma | \mathbf{r} \rangle \cdot \langle \mathbf{r} | k_{TEM} \rangle d\Omega = \iint_{\Omega_c} \langle \mathbf{r} | \mathbf{k}_G \sigma \rangle^* \cdot \langle \mathbf{r} | k_{TEM} \rangle d\Omega, \quad (6.99)$$

where the surface integral is over the coaxial aperture. where  $\psi_{TEM}$  is a solution of Laplace's equation

$$\nabla^2 \psi_{TEM} = 0. \quad (6.100)$$

The calculation of the overlapping integrals (6.99) is better performed if the  $S$  and  $P$  modes above the plate are expressed as

$$\langle \mathbf{r} | \mathbf{k}_G P \rangle = \frac{1}{\sqrt{\Omega}} \frac{-i}{k_G} \nabla_t e^{i\mathbf{k}_G \cdot \mathbf{r}}, \quad (6.101)$$

and

$$\langle \mathbf{s} | \mathbf{k}_G S \rangle = \frac{1}{\sqrt{\Omega}} \frac{-i}{k_G} \hat{\mathbf{z}} \times \nabla_t e^{i\mathbf{k}_G \cdot \mathbf{r}}. \quad (6.102)$$

Then, for P-polarized waves, the overlapping integral is

$$\langle \mathbf{k}_G P | k_{TEM} \rangle = \frac{-i}{k_G \sqrt{\Omega}} \iint_{\Omega_c} \nabla_t e^{i\mathbf{k}_G \cdot \mathbf{r}} \cdot \nabla_t \psi_{TEM} d\Omega, \quad (6.103)$$

which, using Green's first identity, can be expressed as

$$\begin{aligned} \langle \mathbf{k}_G P | k_{TEM} \rangle &= \frac{i}{k_G \sqrt{\Omega}} \iint_{\Omega_c} e^{i\mathbf{k}_G \cdot \mathbf{r}} \nabla_t^2 \psi_{TEM} d\Omega \\ &- \int_{\partial\Omega_c} e^{i\mathbf{k}_G \cdot \mathbf{r}} \hat{\mathbf{r}} \cdot \nabla_t \psi_{TEM} dl. \end{aligned} \quad (6.104)$$

The first term of this integral vanishes because of  $\nabla_t^2 \psi_{TEM} = 0$ , and the second term can be easily obtained. Therefore the expression for the overlap with P-polarized waves is

$$\langle \mathbf{k}_G P | k_{TEM} \rangle = -i \frac{\sqrt{2\pi} b}{\sqrt{\Omega}} \frac{e^{i\mathbf{k}_G \cdot \mathbf{R}_\alpha}}{\sqrt{\ln(b/a)}} \frac{J_0(k_G b) - J_0(k_G a)}{k_G b}. \quad (6.105)$$

Similarly, for S-polarized waves, the overlapping integral is written as

$$\langle \mathbf{k}_G S | k_{TEM} \rangle = \frac{-i}{k_G \sqrt{\Omega}} \iint_{\Omega_c} (\hat{\mathbf{z}} \times \nabla_t e^{i\mathbf{k}_G \cdot \mathbf{r}}) \cdot \nabla_t \psi_{TEM} d\Omega. \quad (6.106)$$

Again, applying Green's first identity and using that  $\nabla^2 \psi_{TEM} = 0$  we get

$$\langle \mathbf{k}_G S | k_{TEM} \rangle = \frac{-i}{k_G \sqrt{\Omega}} \int_{\partial\Omega} \psi_{TEM} \hat{\mathbf{r}} \cdot (\hat{\mathbf{z}} \times \nabla_t e^{i\mathbf{k}_G \cdot \mathbf{r}}) dl. \quad (6.107)$$

However the above integral cancels, since boundary conditions for the TEM mode requires that  $\psi_{TEM} = 0$  on the aperture's boundary, where the above integral is performed, thus  $\langle \mathbf{k}_G S | \alpha \rangle = 0$ .

### 6.2.2 TE modes

For the TE modes or H-polarization, when  $E_z = 0$ , the magnetic field  $H_z$  can be expressed as:

$$H_z(r, \theta, z) = \Psi_H(r, \theta) e^{iq_M z}, \quad (6.108)$$

where  $\Psi_H(r, \theta)$  satisfies

$$\nabla^2 \Psi_H(r, \theta) + k_M^2 \Psi_H(r, \theta) = 0, \quad (6.109)$$

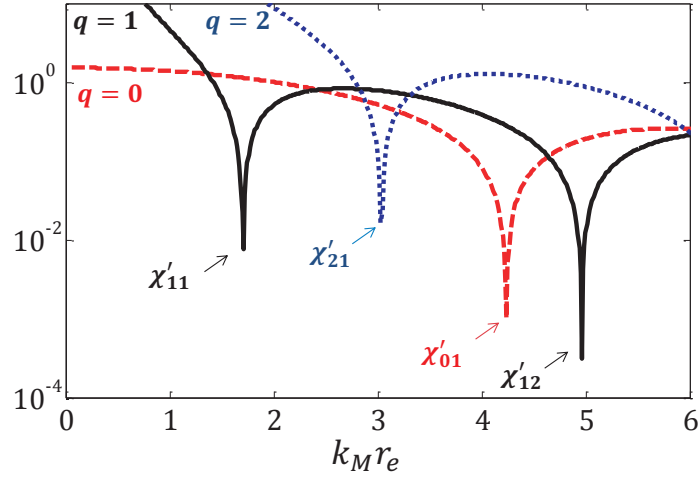


Figure 6.4: TE mode solutions for different mode orders when  $r_e = 4$  mm and  $r_i = 1$  mm.

where  $q_M^2 = k_\omega^2 - k_M^2$ . The values of  $k_M$  are the eigenvalues of the TE modes in the cavity. The solution for this equation is given by:

$$\Psi_H(r, \theta) = \sum_q \sum_n \frac{1}{N_{qn}^H} \left( J_q(k_M r) - \frac{J'_q(k_M r_i)}{Y'_q(k_M r_i)} Y_q(k_M r) \right) \begin{cases} \cos q\theta \\ \sin q\theta \end{cases} \quad (6.110)$$

where  $k_M$  must satisfy that

$$\frac{J'_q(k_M r_i)}{Y'_q(k_M r_i)} - \frac{J'_q(k_M r_e)}{Y'_q(k_M r_e)} = 0 \quad (6.111)$$

The values of  $k_M$  that satisfy this equation define the  $TE_{qn}$  modes in the coaxial cavities. Figure 6.4 represents the numerical solution for the transcendental equation when  $r_e = 4$  mm and  $r_i = 1$  mm. The solutions are denoted by  $\chi'_{qn}$ . As it is observed in Fig. 6.4, the  $TE_{11}$  mode has the lowest cutoff frequency. This is the dominant TE mode. The magnetic field pattern,  $H_z$ , of this mode is shown in Figure 6.5. Black lines represent the transversal electric field vector,  $E_t$ .

In a coaxial cavity, as we have seen before, the fundamental mode is the TEM. The  $TE_{11}$  is the mode with the lowest cutoff frequency. This cutoff frequency will define the monomode frequency range. To study the effect

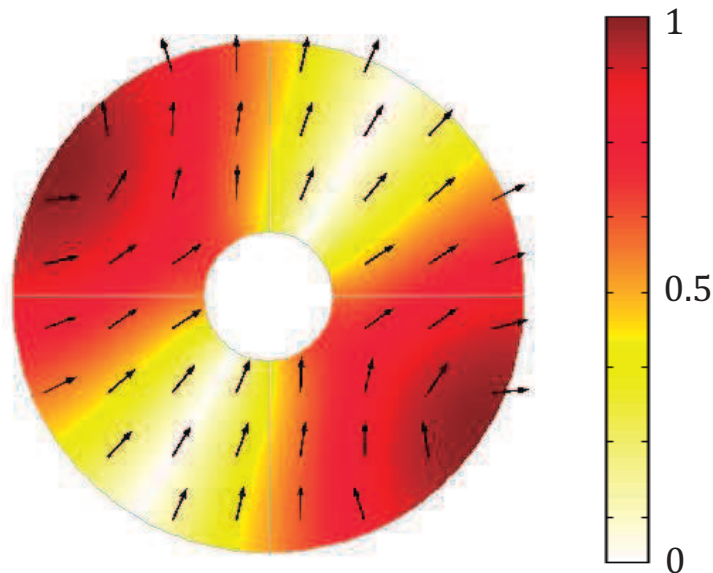


Figure 6.5: Magnetic field pattern,  $H_z$ , of the  $TE_{11}$  mode. Black arrows represent the transversal electric field vector,  $E_t$ .

of the internal and external radius in the  $TE_{11}$  cutoff frequency, we have performed two different analysis. First, we have fixed the value of the internal radius,  $r_i = 1$  mm and we have evaluated the influence of the external radius,  $r_e$ . Figure 6.6.(a) contains this analysis, showing that the cutoff frequency decreases with the internal radius. Secondly, we have fixed the value of the external radius,  $r_e = 4$  mm and we have obtained the cutoff frequency as a function of the internal radius,  $r_i$ . This result is shown in Fig.6.6(b), where we can see that the cutoff frequency also decreases when the internal radius decreases. Note that, for increasing the monomode frequency range we have to decrease the internal and the external radius.

### 6.2.3 TM modes

Solutions for the TM modes can be found in a similar manner. In this case, for a TM mode ( E-mode), where  $H_z = 0$ , the electric field can be expressed as:

$$E_z(r, \theta, z) = \Psi_E(r, \theta)e^{iq_E z}, \quad (6.112)$$

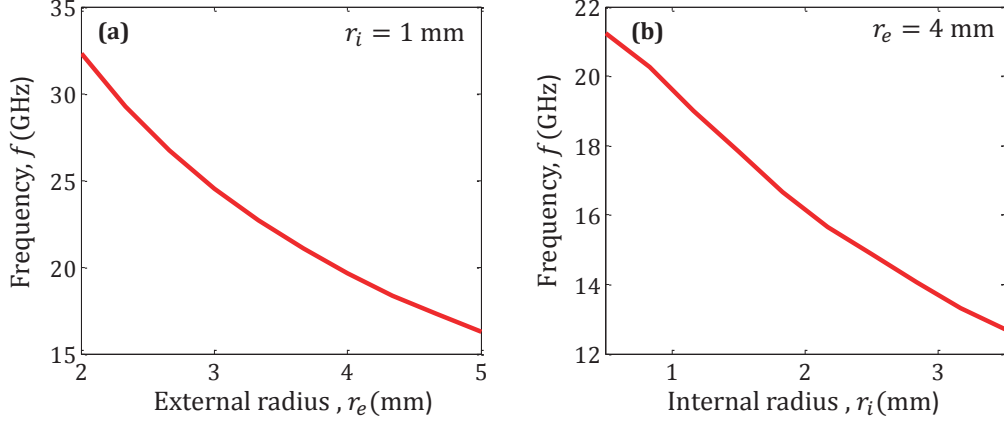


Figure 6.6: Influence of the internal and external radius in the  $TE_{11}$ . Cutoff frequency when: (a) the internal radius is  $r_i = 1$  mm for different values of  $r_e$  and (b) (a) the external radius is  $r_e = 4$  mm for different values of  $r_i$

where  $\Psi_H(r, \theta)$  satisfies

$$\nabla^2 \Psi_E(r, \theta) + k_E^2 \Psi_H(r, \theta) = 0, \quad (6.113)$$

with  $q_E^2 = k_\omega^2 - k_E^2$ . The values of  $k_E$  are the eigenvalues of the TM modes in the cavity. The solution for this equation is given by:

$$\Psi_E(r, \theta) = \sum_q \sum_n \frac{1}{N_{qn}^E} \left( J_q(k_M r) - \frac{J_q(k_M r_i)}{Y_q(k_M r_i)} Y_q(k_M r) \right) \begin{Bmatrix} \cos q\theta \\ \sin q\theta \end{Bmatrix}, \quad (6.114)$$

where  $k_E$  must satisfy that

$$\frac{J_q(k_M r_i)}{Y_q(k_M r_i)} - \frac{J_q(k_M r_e)}{Y_q(k_M r_e)} = 0 \quad (6.115)$$

The values of  $k_E$  that satisfy that condition define the  $TM_{qn}$  modes in the coaxial cavities. Figure 6.7 represent the numerical solution for the transcendental equation. The solutions are denoted by  $\chi_{qn}$ . The electric field pattern,  $E_z$ , of this mode is shown in 6.8. Black arrows represent the transversal electric field vector,  $E_t$ .



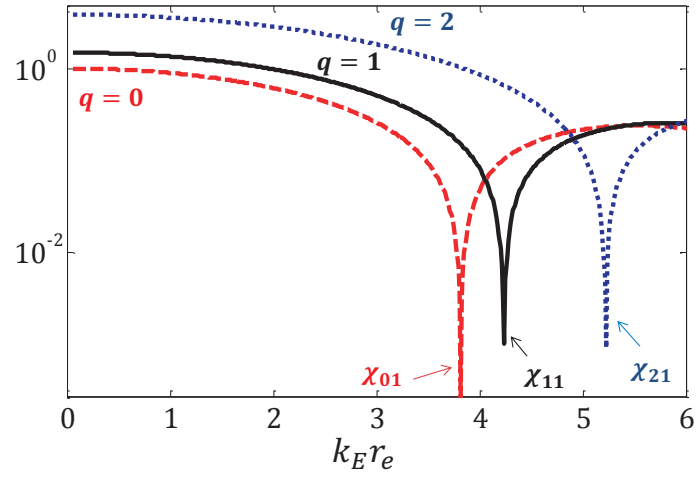


Figure 6.7: TM mode solutions for different mode orders when  $r_e = 4$  mm and  $r_i = 1$  mm.

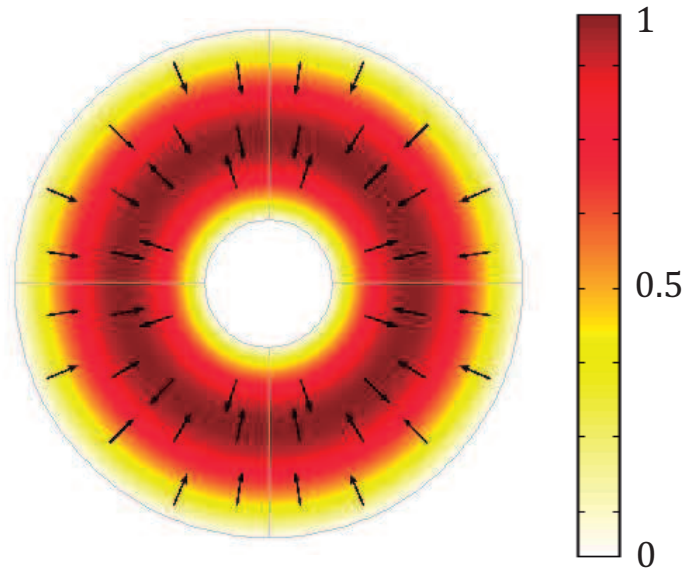


Figure 6.8: Electric field pattern,  $E_z$ , of the  $TM_{01}$  mode. Black arrows represent the transversal electric field vector,  $H_t$ .

## 6.3 Numerical Experiments

In order to support the results obtained from the analytical model full wave simulations have been performed using HFSS. The corresponding results are shown in Fig.6.9.(b) and they demonstrate that the absorptive profiles of the fundamental mode  $C_1$  and its first higher mode,  $C_2$ , are equal to those obtained from the model [see Fig.6.9(a)].

However, it is observed that the absorptive profile of peak  $G_1$ , corresponding to the hybrid mode, is not well reproduced since the model only takes into account the fundamental TEM mode and its corresponding Fabry-Perot-like modes quantized by the cavity length  $h$ . We should remark that  $G_1$  is above the cutoff frequency of the grating modes due to the periodicity of the lattice. The possible interaction of this type of modes with the evanescent modes in the coaxial cavity cannot be precisely modeled with our method. This is obvious since our model only considers the fundamental mode, the one with azimuthal mode number  $M = 0$ , and its  $N$  longitudinal excitations inside the coaxial cavities. Despite this slight disagreement, our model gives a good quantitative prediction of the peak positions at which the structure absorbs energy.

### 6.3.1 Low-frequency absorption.

Figure 6.10(a) depicts the behavior of the low frequency peak for three values of the cavity length  $h$ . Dashed, continuous and dotted lines represent the results for  $h/a = 0.3, 0.5$  and  $0.8$ , respectively. It is observed that the peak amplitude does not depend on  $h$ , but its profile becomes sharper for lower values of the frequency position. This behavior is strictly related to the fact that TEM modes in longer cavity depths have a weaker interaction with the dielectric slab. It is also clear that the position of the peak strongly depends on the length  $h$ . Moreover, this result indicates that the amplitude remains constant when the coaxial length changes. Figure 6.10(b) represents the condition (6.78) for having an absorption peak with the black line, and the horizontal dotted lines mark the coaxial lengths for which the absorption spectra are represented in the top panel. A clear correspondence is noticed between the crossing frequencies in Fig.6.10(b) and the peak positions in Fig.6.10(a).

Variation in the absorption properties with the outer and inner radius

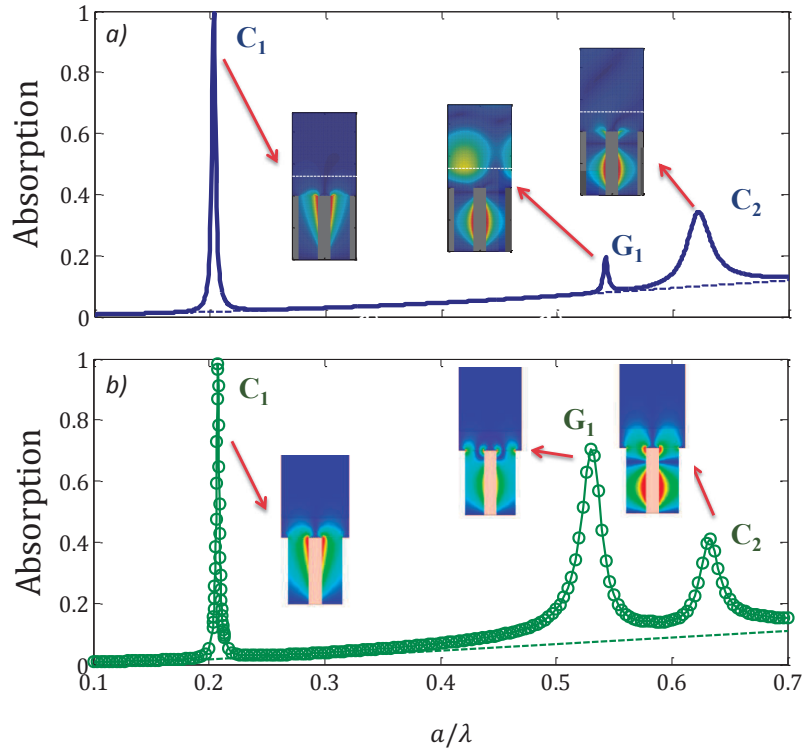


Figure 6.9: Absorbance spectrum  $A(\omega)$ . Results are obtained with a  $P$ -polarized plane wave impinging along the direction  $\phi = 0$  and  $\theta = \pi/4$ . The slab with thickness  $\ell/a = 0.3$  is a lossy dielectric with permittivity  $\varepsilon_d = 2 + i0.05$ . The metallic surface contains a square distribution of annular cavities with radii  $r_i/a = 0.1$ ,  $r_e/a = 0.4$ , and length  $h/a = 1$ . The dashed curve corresponds to the absorption of the slab with a flat metal underneath, that shows the same result at normal incidence ( $\theta = 0$ ). The insets depict the fields at the peak positions. (a) Theoretical simulation. (b) HFSS simulation.

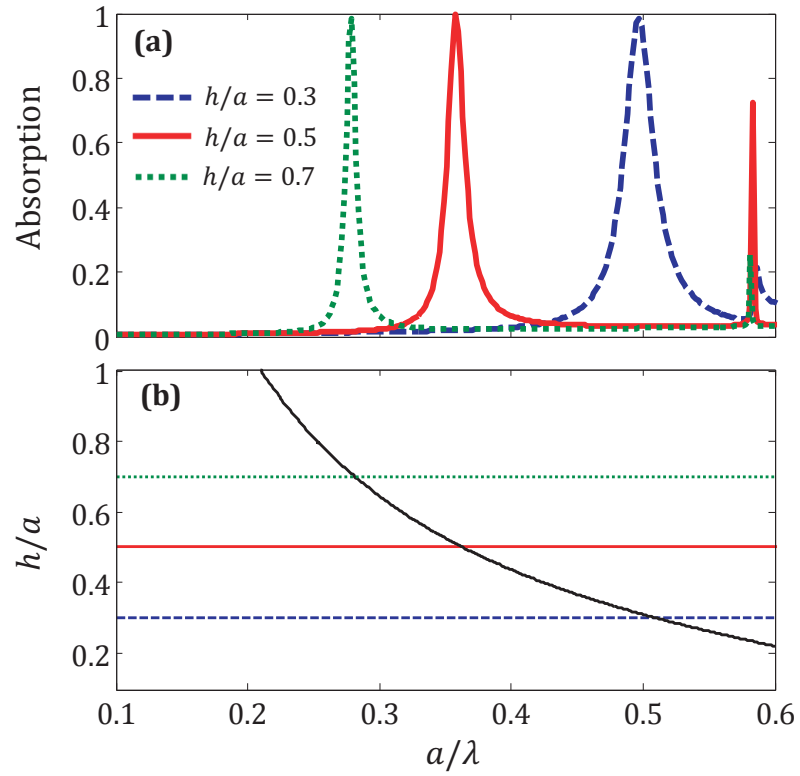


Figure 6.10: (a) Absorbance spectra for three values of cavity lengths  $h$ . (b) Frequency of the absorptive peak as a function of  $h$  (black line). Results are obtained using the incident direction  $\theta = \pi/4$ ,  $\phi = 0$  and the following parameters of the structure:  $r_i/a = 0.1$ ,  $r_e/a = 0.4$ ,  $\ell/a = 0.1$ ,  $\varepsilon_d = 2 + i0.1$ , and  $\varepsilon_h = 1$ .

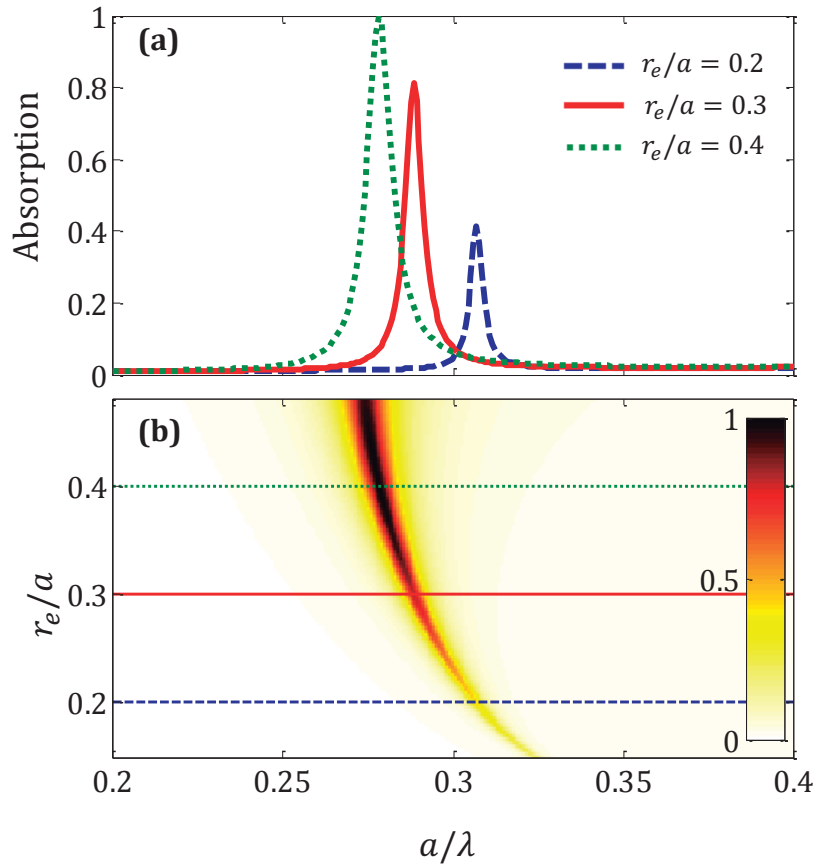


Figure 6.11: (a) Absorbance spectra  $A(\omega)$  calculated for three values of the external cavity radius  $r_e$ . (b) Absorbance enhancement as a function of  $r_e$ . The structure dimensions are  $r_i/a = 0.1$ ,  $h/a = 0.7$ ,  $\ell/a = 0.1$ , the permittivity is  $\varepsilon_d = 2 + i0.1$  and the incidence angles are  $\theta = \pi/4$ ,  $\phi = 0$ .

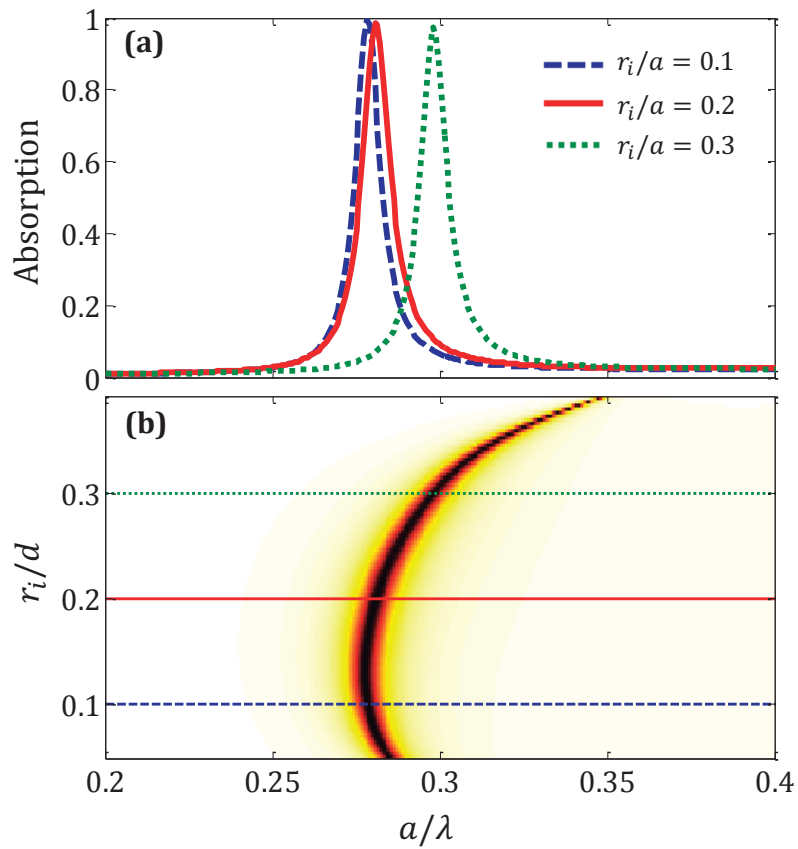


Figure 6.12: (a) Absorbance as a function of the annular inner radius  $r_i$ . The structure dimensions are  $r_e/a = 0.4$ ,  $h/a = 0.7$ ,  $\ell/a = 0.1$ . The permittivity is  $\varepsilon_d = 2 + i0.1$  and the incidence angles are  $\theta = \pi/4$ ,  $\phi = 0$ . (b) Absorbance enhancement in the active layer as a function of  $r_i$ .

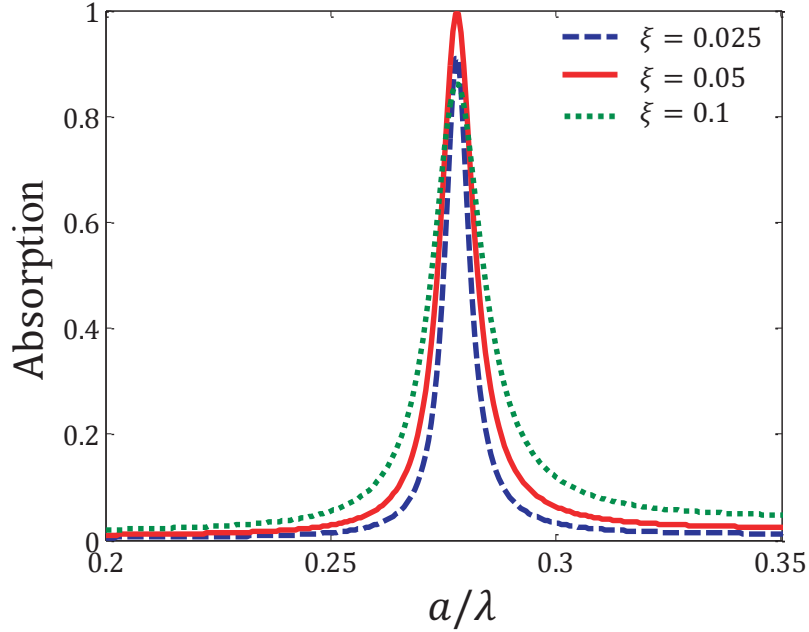


Figure 6.13: Absorbance in the dielectric slab with thickness  $\ell/a = 0.1$  for three values of  $\xi$  in its dielectric permittivity  $\varepsilon_d = 2(1+i\xi)$ . The annular cavities on the metallic metasurface have dimensions  $r_i/a = 0.1$ ,  $r_e/a = 0.4$  and  $h/a = 0.7$ . Results are obtained for the incidence angles  $\theta = \pi/4$  and  $\phi = 0$ .

of the coaxial aperture is presented in Figs. 6.11 and 6.12. Note that the dependence on  $r_e$  is also giving the dependence with the lattice filling fraction  $f$ , which is  $f = \pi(r_e/a)^2$  for the square lattice. The peak position is slightly connected with the coaxial radii. In case of variations in  $r_e$ , the peak position goes down in frequency when  $r_e$  increases; i.e., for larger cavities the TEM mode becomes more localized and decreases in frequency. On the other hand, when the inner radii  $r_i$  increases the peak position moves to higher frequencies since the annular aperture becomes thinner. However, note that the peak amplitude increases with the outer radii but is independent of the inner radii.

Figure 6.13 shows how the absorption peaks change in shape with the losses in the dielectric  $\xi$ , comparing the absorption spectrum for  $\xi = 0.025$ , 0.05, 0.1, for a structure with  $r_i/a = 0.1$ ,  $r_e/a = 0.4$ ,  $h/a = 0.7$ ,  $\ell/a = 0.1$ ,  $\theta = \pi/4$  and  $\phi = 0$ . Note that the peak position does not depend on the

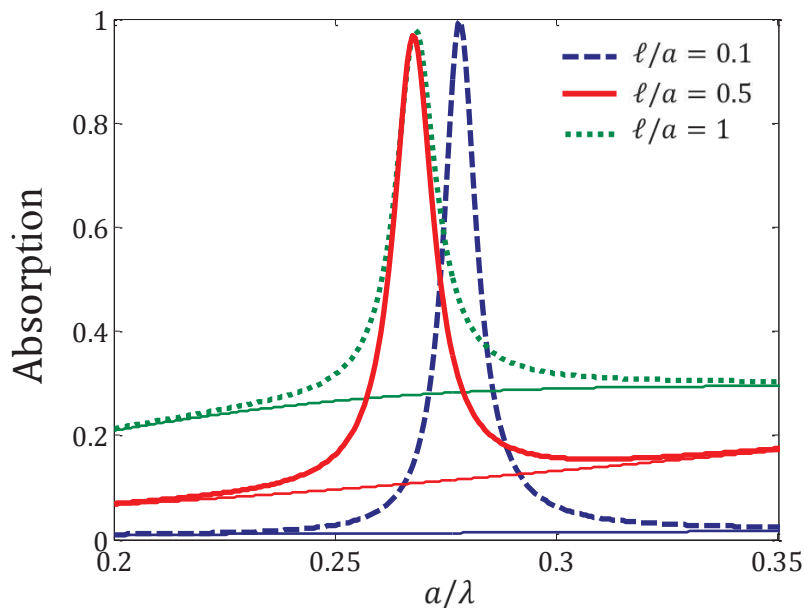


Figure 6.14: Absorbance of a dielectric slab with permittivity  $\varepsilon_d = 2 + i0.1$  for three different thicknesses. The annular cavities on the metallic surface have dimensions  $r_i/a = 0.1$ ,  $r_e/a = 0.4$ ,  $h/a = 0.7$ . Continuous lines under the peaks represent the absorption without the metallic metasurface. Results are obtained for the incident angles  $\theta = \pi/4$  and  $\phi = 0$ .

dielectric losses in the slab. Note that perfect absorption (unity absorption) is obtained for  $\xi = 0.05$  and not for the larger value  $\xi = 0.1$ , indicating that  $\xi$  should be optimized for a given structure in order to achieve perfect absorption.

Finally, Fig. 6.14 shows the absorption for three thicknesses of the dielectric slab. Notice that the peak amplitude is independent of the dielectric thickness, meaning that with the proper design perfect absorption is obtained independently of the thickness of the absorbing layer. However, also note that the peak profile becomes broader for larger thickness, indicating that absorption is proportional to the volume of the active layer.

### 6.3.2 Other absorption mechanisms

Now, two additional mechanisms of absorption by thin films are studied and, although it will be shown that they are less efficient, they may offer more



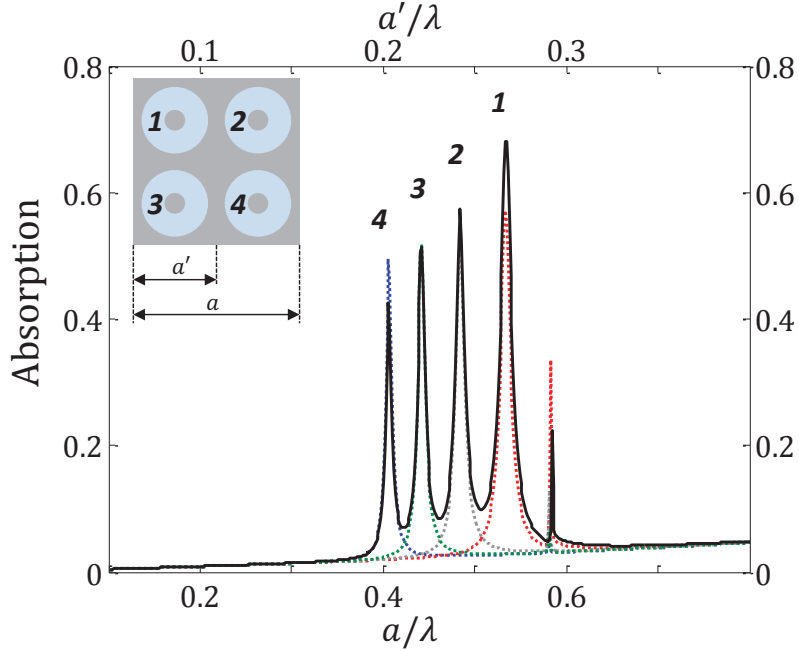


Figure 6.15: Absorbance of a dielectric slab with thickness  $\ell/a = 0.1$  and permittivity  $\varepsilon_d = 2 + i0.1$  on top of a metallic metasurface containing four annular cavities in the units cell (see the inset). The four cavities have the same cylindrical section ( $r_{i1,2,3,4}/a = 0.1$ ,  $r_{e1,2,3,4}/d = 0.2$ ), but their lengths are different:  $h_1/a = 0.35$ ,  $h_2/a = 0.4$ ,  $h_3/a = 0.45$  and  $h_4/a = 0.5$ . Results are obtained for the incident angles  $\phi = 0$  and  $\theta_0 = \pi/4$ .

degrees of freedom to improve the absorption by the thin film.

The first mechanism considers the possibility of using a non-Bravais lattice; i.e., by having more than one cavity in the unit cell. The second takes into account the excitation of guided modes in the slab by the metallic grating underneath.

### Non-Bravais lattices

Let us consider now the case in which more than one cavity is associated to one point of a Bravais lattice.

Figure 6.15 shows the absorption spectra for a square lattice containing four cavities per unit cell. All the four cavities have the same inner and outer radii, given by  $r_i/a = 0.1$  and  $r_e/a = 0.2$ , respectively, but different

depths, being  $h_1/a = 0.35$ ,  $h_2/a = 0.4$ ,  $h_3/a = 0.45$  and  $h_4/a = 0.5$ . The dielectric slab with thickness  $\ell/a = 0.1$  has a permittivity  $\varepsilon = 2 + i0.1$ . This result is obtained for the incident angle is  $\theta_0 = \pi/4$ . It is clear that there is no coupling between the cavity resonances, since the response of the complete system can be understood as the superposition of the responses of four different cells, each one corresponding to the holes with respective depths  $h_1, h_2, h_3$  or  $h_4$ , which has been depicted in the figure by dotted lines. This lack of interaction can be confirmed by the fact that the interaction matrix  $\chi_{\alpha\beta}$  has only significant values in the diagonal elements when  $\alpha = \beta$ . The individual resonances of each cavity have very low coupling to neighboring cells and, therefore, these super-cells can be employed for designing multi-frequency absorbing layers.

### Guided modes in slab

The excitation of guided modes of the dielectric layer can also produce absorptive peaks. These modes propagate along the lateral dimension of the slab and, consequently, their optical paths can be much larger than that corresponding to the vertical dimension. Remember that the excitation of these modes from the far field is not possible since the parallel wavenumber required for this excitation cannot be provided by a free space propagating wave. The role of the array of resonators is precisely to provide this additional wave number by the excitation of a set of diffracted waves.

Figure 6.16(a) shows the absorption spectra for three values of the permittivity:  $\varepsilon_d = 2(1 + i0.05)$  (continuous line),  $\varepsilon_d = 2(1 + i0.005)$  (dashed line) and  $\varepsilon_d = 2(1 + 0.15i)$  (dotted line). Results are obtained for the incident direction defined by the angles  $\theta = \pi/4$  and  $\phi = 0$  and the parameters of the structure are reported in the caption. The absorptive peaks denoted by  $G_1$ ,  $G_2$  and  $G_3$  are caused by the excitation of hybrid modes that are guided along the dielectric slab. They are excited thanks to the transverse component  $k_{G_i}$  of the diffracted modes, as explained below.

The  $P$ -polarized guided modes of a dielectric slab with a metallic grating underneath are obtained by setting  $C_\alpha = 0$  in (6.46) and inserting the condition obtained for  $B_{GP}^\pm$  into equations (6.20) and (6.21). In addition, by assuming that there is no incident field, the condition for the existence of a

guided mode can be written as

$$-iY_{GP}^0 \sin(p_G \ell) + Y_{GP}^d \cos(p_G \ell) = 0 \quad (6.116)$$

This expression is contained in the denominator of the term  $\chi(\omega)$ . When this condition is fulfilled a peak in the absorption spectrum will appear, as it is shown in Fig. 6.16(b), where the dispersion diagram of the dielectric slab (black line) and the transverse components of the diffracted modes (dotted lines) are depicted. Notice that the crossing points between both of them mark the peak positions. The reciprocal vectors at which the peaks appear are  $\mathbf{G}_1 = (-1, 0)$ ,  $\mathbf{G}_2 = (-1, 1) = (1, -1)$ , and  $\mathbf{G}_3 = (-2, 0)$ , using the labeling  $\mathbf{G} = (m_1, m_2)$  of Eq. (1).

The dependence on the incident direction is depicted in Fig. 6.17 where it is clearly shown the angle dependence predicted by condition (6.116). Notice that, on the contrary, no dependence is found for the low frequency peak, which corresponds to the fundamental cavity mode.

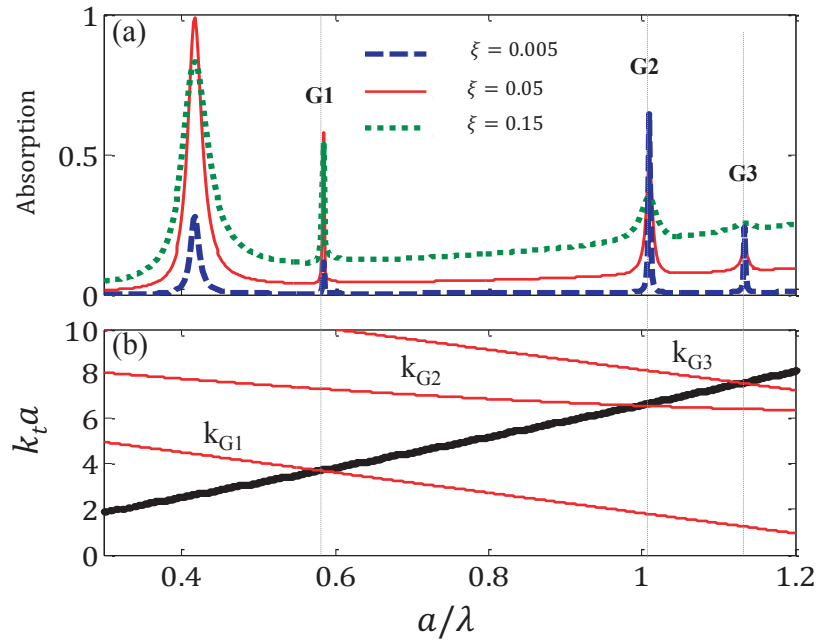


Figure 6.16: (a) Absorbance with a dielectric slab of thickness  $\ell/a = 0.1$  and permittivity  $\varepsilon_d = 2(1+i\xi)$ . Absorbance has been calculated for three values of  $\xi$ . (b) Dispersion diagram of the guided modes inside the slab. The annular cavities on the metallic metasurface have dimensions  $r_i/a = 0.1$ ,  $r_e/a = 0.4$  and  $h/a = 0.4$ . Results are calculated for the incidence angles  $\theta_0 = \pi/4$  and  $\phi = 0$ .

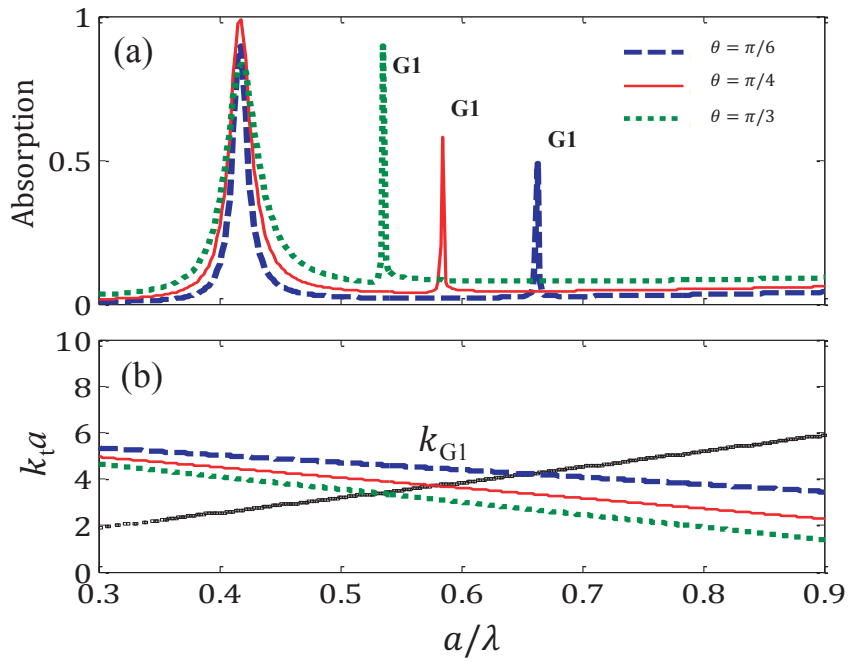


Figure 6.17: Dependence of the absorption for the incident angle  $\theta$  at fixed  $\phi = 0$ . Results are obtained with a slab with  $\ell/a = 0.1$  and permittivity  $\varepsilon_d = 2(1+i0.05)$ . (b) Dispersion diagram of the guided modes inside the slab. The annular cavities on the metallic metasurface have dimensions  $r_i/a = 0.1$ ,  $r_e/a = 0.4$  and  $h/a = 0.4$ .

# 7

## EXPERIMENTAL VERIFICATION OF TOTAL ABSORPTION

---

In this chapter, we experimentally study the absorbing system introduced in Chapter 6 and present a practical demonstration of the easy tunable system theoretically proposed. In particular, we develop a design method which allows engineering metasurfaces with total absorption. The designs are fabricated and experimentally characterized, studying the influence of the angle of incidence. The control of the peak frequency with the cavity length is demonstrated and the dependence of the peak amplitude with the dielectric thickness is also shown.

### Contents

---

<b>7.1</b>	<b>Design Methodology</b>	<b>136</b>
<b>7.2</b>	<b>Experimental setup</b>	<b>139</b>
<b>7.3</b>	<b>Results</b>	<b>140</b>
<b>7.4</b>	<b>Discussion</b>	<b>146</b>

---

## 7.1 Design Methodology

After the theoretical analysis described in Chapter 6, this section presents a method for designing total absorption devices. This method is based in the theoretical approximation for the low-frequency absorption peak that leads on to Eqs. (6.78) and (6.79). The methodology for the design of total absorption devices is organized as follows:

**Step 1:** Choose the material of the lossy thin layer

- (a) the material permittivity,  $\varepsilon_d$ .
- (b) the material thickness,  $\ell$

**Step 2:** Define the lattice. To produce total absorption by a thin layer, we use  $\ell \ll d$ . Moreover, we have to ensure that the operation frequency is below the diffraction limit.

**Step 3:** Choose the coaxial cross section,  $r_e$  and  $r_i$ , according with the fabrication limitations. In our case, these limitations are:

- (a)  $r_e - r_i > 2 \text{ mm}$  and  $r_i > 2$ .
- (b)  $d - 2r_e > 2 \text{ mm}$ .
- (c)  $h < 10 \text{ mm}$ .

**Step 4:** Starting from the previous analysis, we define the first design condition as:  $C_1 = \cot(k_h h) + \chi_I = 0$ . In this point, there are two options for the design:

- (a) Setting  $h$  and determine  $f$  (Design 1).
- (b) Setting  $f$  and determine  $h$  (Design 2).

Using  $C_1$  condition, we can find the unknown parameter.

**Step 5:** Ensure that the losses in the material,  $\xi$ , fulfils the design condition  $C_2 = H_{00}^2 - \chi_R = 0$  producing total absorption.

The dielectric chosen for the experimental demonstration is a standard glass-reinforced epoxy laminate material named FR4. At the working frequencies in this experiment the dielectric permittivity of this material is

$\varepsilon_d = 4.2(1 + 0.025i)$ . The small imaginary part of this permittivity indicates that FR4 has a poor performance as an absorber of microwaves frequencies. We have designed a metasurface made of aluminum which can enhance the absorption of a FR4 layer with  $\ell = 1.2$  mm, producing total absorption when the incidence angle is  $\theta = 45^\circ$ .

After choosing FR4 as dielectric, we have designed the coaxial-cavity grating for having the total absorption peak in the frequency range between 5 GHz and 10 GHz, which is our measurement regime. The incident angles are between  $20^\circ$  and  $60^\circ$ . To ensure that we work below the diffraction limit ( $f_{lim} = \sin \theta d/c$ ), we have chosen  $d = 10$  mm. Now, taking into account the physical limitations in the fabrication process, which are reported in the **Step 3**, the dimensions of each coaxial cavity are  $r_e = 4$  mm,  $r_i = 2$  mm. Due to the monomode approximation employed in the model, the internal radius and the external radius have to be as small as possible to avoid the effects of higher modes in the coaxial cavity.

Following Design 1, we set  $h = 10$  mm and find the operation frequency using  $C_1$ . The result obtained from this equation is shown in Fig. 7.1(a). The curve has a minimum that marks the frequency of the absorption peak,  $f = 5.62$  GHz. Once we have known the frequency in which the absorption peak appears, we check that the condition for having total absorption is satisfied. The condition  $C_2$  is evaluated and represented in Fig 7.1(b) as a function of the losses in the dielectric. The value for the losses in the FR4 is marked with a red arrow. This result confirms that  $C_2 = H_{00}^2 - \chi_R \approx 0$ .

Following Design 2, we set  $f = 7.1$  GHz and evaluate the  $h$  value satisfying the condition established in  $C_1$ . This equation is represented in Fig.7.2.(a) and determines that  $h = 7$  mm. Then, considering  $h = 7$  mm, we represent the condition for having total absorption as a function of the losses and confirm that the conditions is satisfied.

In order to characterize our designs and to study the capacity of tailoring the peak position, three different samples of the coaxial grating have been manufactured; all have the same cavity cross-section but different cavity lengths ( $h$ ). The dimensions of the cavity cross section are:  $r_e = 4$  mm and  $r_i = 2$  mm the external and internal radius respectively. The three different cavity lengths are  $h = 10$  mm (Sample 1), 7 mm (Sample 2) and 5 mm (Sample 3). The samples consist of 40 unit cells in the x-direction and



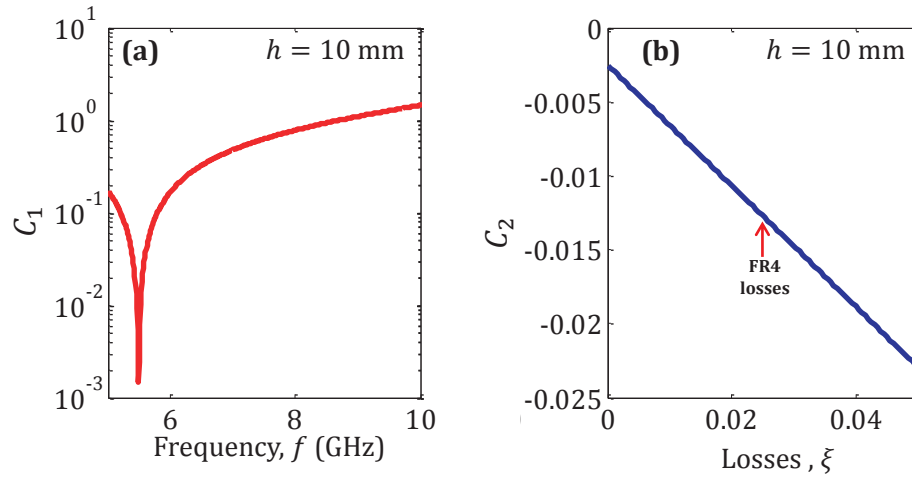


Figure 7.1: Design 1. Setting  $h = 10$  mm. (a) Representation of C1 condition for obtaining the operation frequency. (b) Representation of C2 condition obtaining the total absorption.

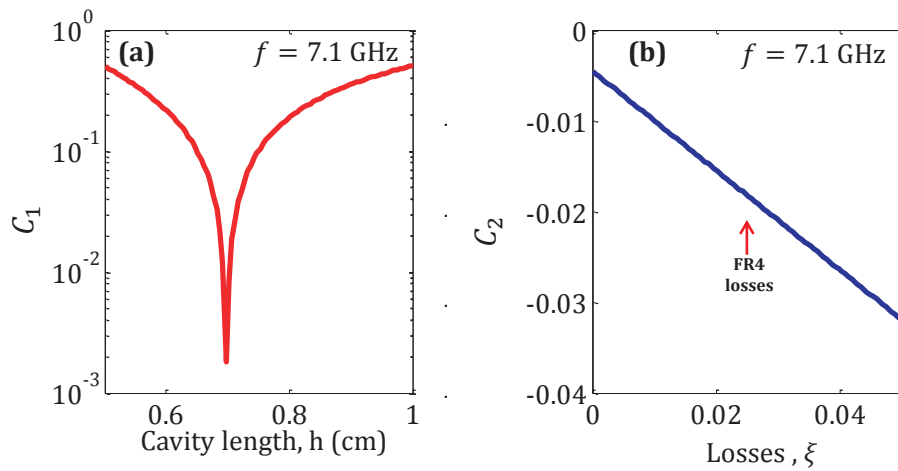


Figure 7.2: Design 2. Setting  $f = 7.1$  GHz. (a) Representation of C1 condition for obtaining cavity length,  $h$ . (b) Representation of C2 condition obtaining total absorption.

Dielectric Slab	Length (cm)	Width (cm)	Thickness (mm)
Slab 1	40	40	1.2
Slab 2	40	40	1.6
Slab 3	40	40	2.3
Coaxial Grating	$r_e$ (mm)	$r_i$ (mm)	$h$ (mm)
Sample 1	4	2	10
Sample 2	4	2	7
Sample 3	4	2	5

Table 7.1: Physical dimensions of the samples. The lattice period is  $d = 10$  mm for all the gratings.

40 unit cells in the y-direction, and the periodicity of the array is  $d = 10$  mm. The dielectric sheet entirely covers the metallic grating and it is fixed at the corners. Also we have characterized the coaxial-cavity grating with three different dielectric thicknesses,  $\ell = 1.2$  mm (Slab 1), 1.6 mm (Slab 2), 2.3 mm (Slab 3). Details of the three samples and the three dielectric slabs are reported in Table 7.1. Thus, a total number of nine different structures have been experimentally characterized.

A scheme of the structure under study is shown in Fig. 7.3(a). A photograph of one constructed metasurface is shown in Fig. 7.3(b), where the dielectric layers is slightly displaced from its original position for a better visualization of the square array of coaxial cavities.

## 7.2 Experimental setup

In the experimental setup, a microwave radiated from a rectangular horn antenna, which is placed at the focus of a collimating spherical mirror, impinges with an incident angle  $\theta$  the fabricated sample. The horn antenna is orientated and positioned such that the electric-vector of the radiation is in the plane of incidence (i.e. p- or TM polarized), and so that the plane of incidence is parallel to the xz-plane (keeping  $\phi = 0^\circ$ ). The reflected beam is collected by a receiver horn antenna, which is orientated to detect only p-polarized radiation and placed at the focus of a second mirror tilted an angle  $\theta$  with respect to the normal vector of the sample surface. The angle

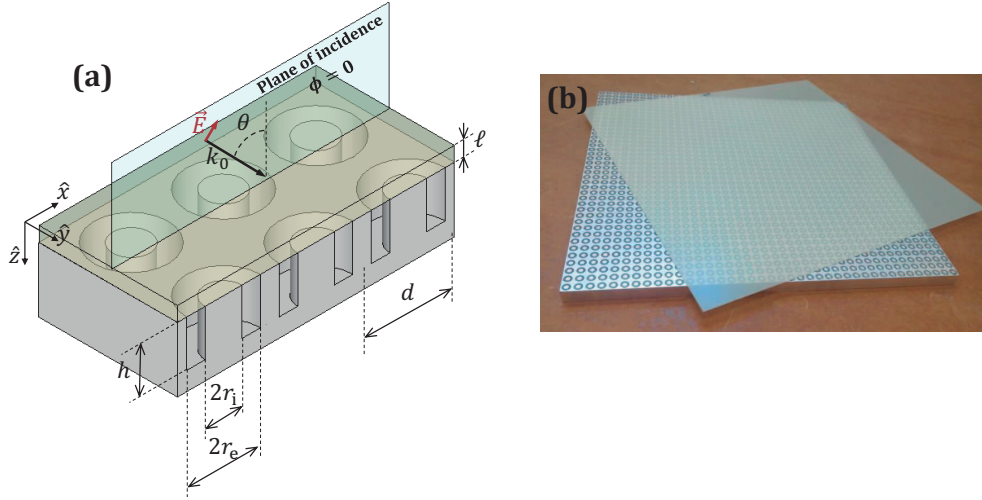


Figure 7.3: (a) Schematic representation of the experimental sample comprising of an array of coaxial cavities in a metal covered by a dielectric sheet. The plane of incidence is also shown. (b) Photograph of one constructed device. The FR4 dielectric layer is displaced for a better observation of the patterned surface ( $r_i = 2$  mm,  $r_e = 4$  mm and  $h = 10$  mm).

of incidence is shifted manually by changing the position and rotation of the transmission and the detection horns [see Fig. 7.4]. A photograph of the experimental setup is shown in Fig. 7.5.

A reference measurement is needed for obtaining the absorption spectra. This reference measurement is taken by using an aluminum plate with the same area and thickness than that of the sample (with the dielectric layer). The reflectivity is obtained for the same frequency ( $f$ ) values. Using this method, the sample absorption ( $A$ ) can be calculated from

$$A(f) = 1 - \frac{R_{sample}}{R_{ref}}, \quad (7.1)$$

where  $R_{sample}$  and  $R_{ref}$  are the reflectivity spectra for the sample and the aluminum plate respectively.

### 7.3 Results

Figure 7.6 summarizes the experimental characterization of Sample 1 ( $h = 10$  mm) with Slab 1 ( $\ell = 1.2$  mm) on top. In Fig. 7.6 (a), the absorption

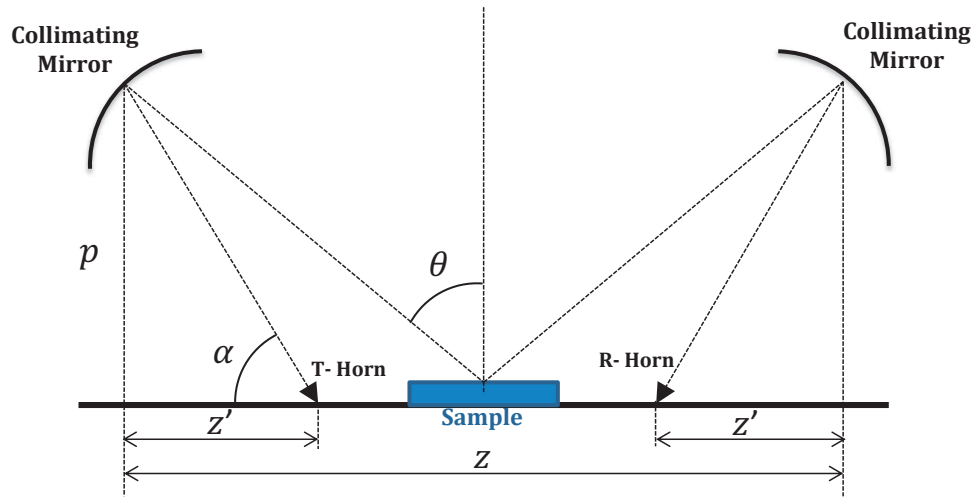


Figure 7.4: Schematic representation of the experimental setup

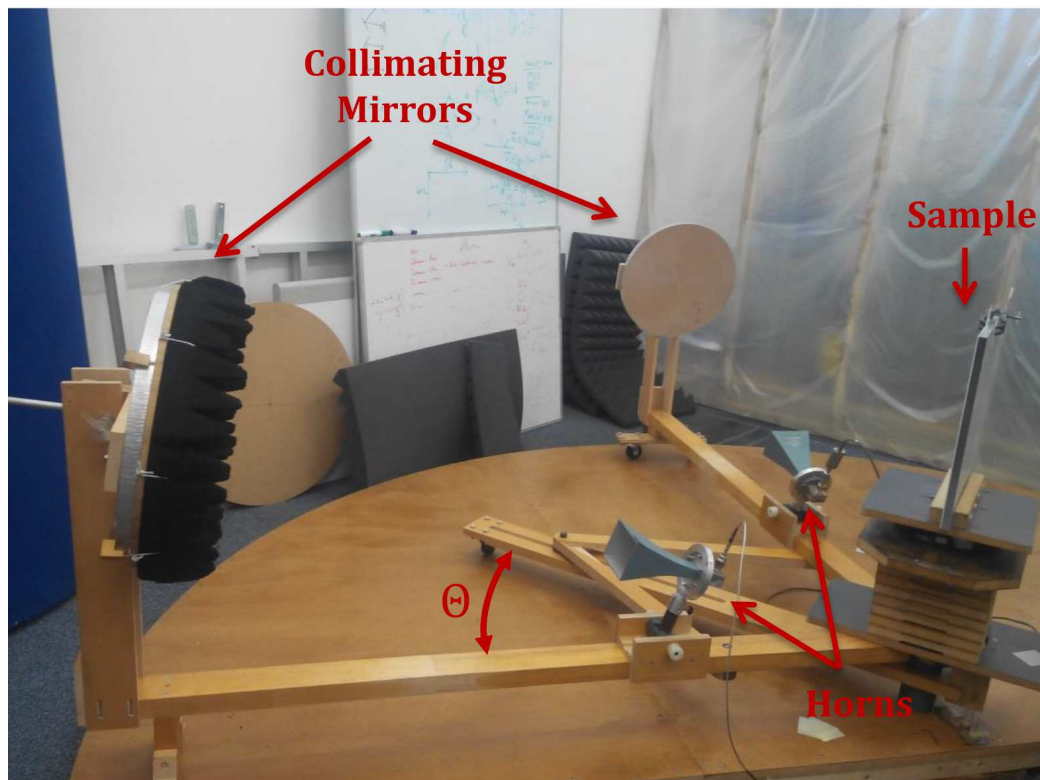


Figure 7.5: Photograph of the experimental setup

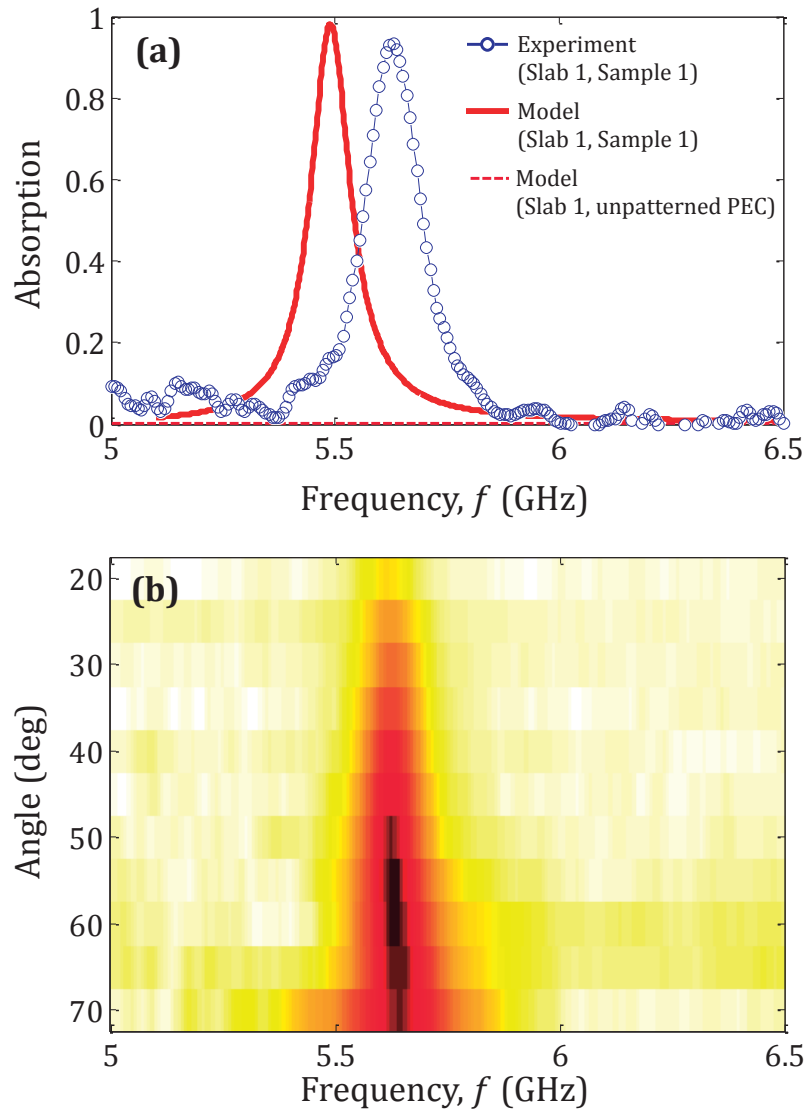


Figure 7.6: (a) Absorption spectrum obtained with an incident p-wave with  $\theta = 45^\circ$ . The structure is formed by a combination of Sample 1 ( $h = 10$  mm) with Slab 1 ( $\ell = 1.2$  mm). (b) Experimental absorption spectra taken for several incidence angles  $\theta$ , where the darkest color corresponds to the strongest absorption.

spectrum is shown when the incident angle is  $\theta = 45^\circ$ . The symbols represent the experimental data while the continuous line is the calculated with the model reported in Chapter 6. The dashed line corresponds to the absorption produced with the dielectric layer (Slab 1) covering an unpatterned aluminum surface. It is observed that the calculated spectrum is in good agreement with the experimental one except for a small frequency shift: the measured peak centered at 5.62 GHz gives absorption of 93% while the calculated peak is centered at 5.5 GHz with 98% absorption. The shifting of the measured peak towards high frequencies is about 2% and is due to an unavoidable air film existing between the metal grating and the dielectric layer. This film of air or air gap appears because of the defects (raised edges) produced during the manufacturing process of the coaxial cavities edges, and because of the mechanical stress of the dielectric layer, which is not completely flat. The effect of the non-perfect contact between the dielectric and the metasurface is discussed later.

In Fig. 7.6 (b), the same type of measurement has been performed for several incident angles; from  $\theta = 20^\circ$  to  $\theta = 75^\circ$ . The observed insensitivity of the peak position with the impinging angle supports the predictions of the model. Nevertheless, the absorption amplitude changes, a maximum value is achieved for  $\theta = 60^\circ$  while for higher or lower angles the absorption decreases. Also, it is easy to observe that, when the incidence angle is close to normal incidence ( $\theta \approx 0^\circ$ ), the absorption vanishes because the impinging wave cannot excite the resonant modes in the coaxial cavities without a phase variation across the surface.

Now, we experimentally study the feasibility of tuning the peak position with the cavity length,  $h$ . To do that, we have employed the dielectric layer with  $\ell = 1.2$  mm (Slab 1) and the three metallic samples. The corresponding spectra are shown in Fig. 7.7. The experimental data (symbols) are compared with the theoretical results (continuous lines). The measured (calculated) peaks appear at 5.62(5.5) GHz, 7.24(7.09) GHz and 9.14(8.83)GHz, for  $h = 10$  mm,  $h = 7$  mm and  $h = 5$  mm, respectively. These results demonstrate the tuning capability of the absorption peak with  $h$  while keeping its high absorption ( $> 90\%$ ). The measured (calculated) peak amplitudes are 0.93 (0.98), 0.99 (0.99) and 0.97 (0.99) for  $h = 10$  mm,  $h = 7$  mm and  $h = 5$  mm, respectively. From these results one confirms the design method-

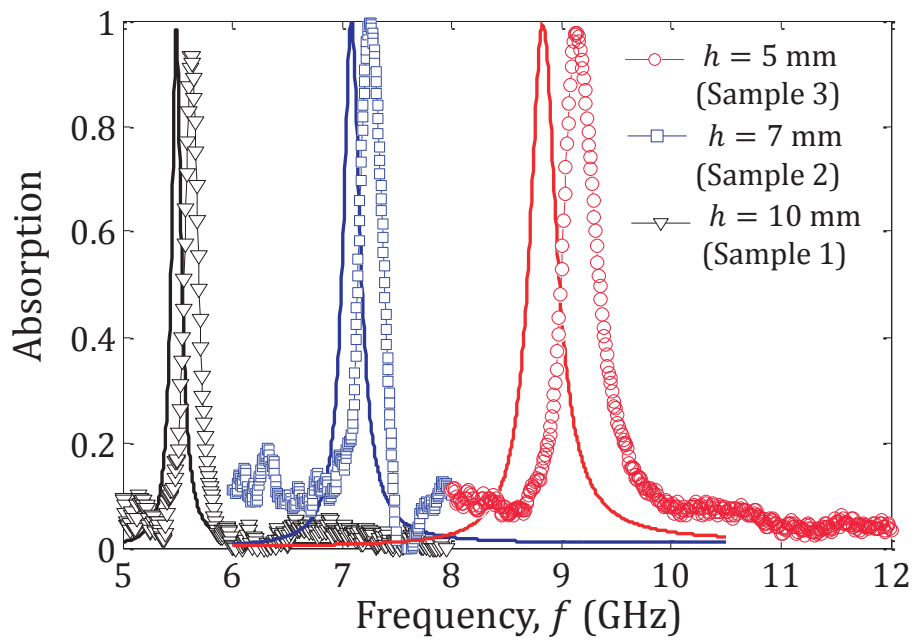


Figure 7.7: Absorption spectra for three values of cavity length,  $h$ . The dielectric thickness is  $\ell = 1.2$  mm (Slab 1) and the angle of incidence is  $\theta = 45^\circ$ .

ology described in Section 7.1, allowing the design of structures with total absorption at prefixed frequencies. The same effect noticed in the previous experiment also appears in these results, a frequency shift is produced in the experimental absorption spectra due to the non perfect contact between the coaxial grating and the dielectric sheet.

The third experiment analyzes the effects that the thickness of the dielectric layer,  $\ell$ , produces in the amplitude and position of the absorption peak. Figure 7.8(a) represents such dielectric thickness dependence, the dark areas define the regions with larger absorption. It is observed that  $\ell$  has effects not only on the peak frequency but also in its amplitude. However, we can conclude from Fig. 7.8(a) that changing  $\ell$  is not very efficient for tuning the peak position. It is observed that the frequency interval where the peak is highly absorptive (between 6.5 GHz and 7.5 GHz) is not as broad as the change produced by varying the cavity length  $h$ , which shifts the peak between 5 GHz and 10 GHz, keeping its maximum amplitude. Figure 7.8(a) shows that the absorption amplitude increases with the dielectric thickness, until it rises to one at  $\ell = 0.8$  mm (horizontal dashed line) and remains constant for higher values. This is the region with total absorption, which is represented by the shadowed area in Fig. 7.8(b). The first value producing total absorption can be considered as the optimum for designing the absorptive structure. For example, for the cavity length studied here ( $h = 7$  mm), the optimum value is  $\ell_{opt} = 0.8$  mm. In other words, a correct design of a total absorption device has to ensure that  $\ell \geq \ell_{opt}$ , but the optimal value will reduce the cost of the dielectric layer.

To confirm the role that the dielectric layer thickness ( $\ell$ ) plays in determining the amplitude and frequency position of the total absorption peak produced by a given patterned surface a second experiment is performed. We have considered the metasurface Sample 2 having patterned cavities with  $h = 7$  mm which is successively covered with the three dielectric slabs (all having thickness over the optimum value of  $\ell$ ). Figure 7.9 shows the three absorption spectra obtained for  $\theta = 45^\circ$ , the symbols represent the measurements while the continuous lines illustrate the theoretical simulations. It is observed that changes of the layer thickness are accompanied with changes in the position of the absorption peak. The measured (calculated) frequencies of the absorption peaks are 7.25(7.09) GHz, 7.09 (6.88)GHz and 6.92



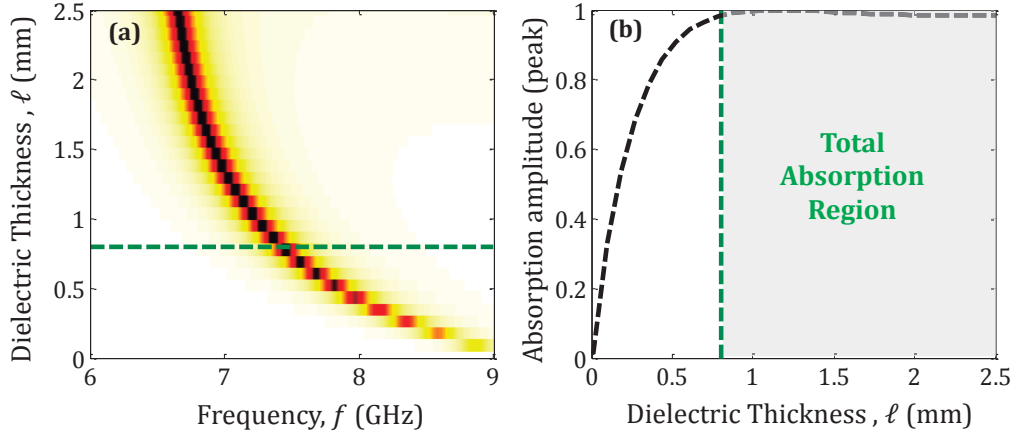


Figure 7.8: (a) Calculated absorption for the Sample 2 ( $h = 7$  mm) as a function of the dielectric layer thickness ( $\ell$ ). For values  $\ell \geq 0.8$  (horizontal dashed line) the absorption peak is unity. (b) Amplitude of the absorption peak as a function of  $\ell$ . The vertical dashed line defines the onset of total absorption.

(6.68) GHz, for  $\ell = 1.2$  mm,  $\ell = 1.6$  mm and  $\ell = 2.3$  mm mm, respectively. The profiles show an asymmetrical profile not shown in the numerical simulations. This asymmetry is probably due to an artifact of our experimental setup which uses finite size samples, a feature that is hard to include in our simulations. In other words, the receiver antenna is not symmetrically located with respect to the borders of the samples and, therefore, the waves radiated from the sample borders arrive to this antenna with low but different amplitudes, producing interference effects in the recorded spectra. This interference effects are clearly observed in the wiggling observed at the lower (absorption) parts of the spectra. The measured (calculated) peak amplitudes are, 0.99(0.99) , 0.98(0.99) and 0.99(0.99) for  $\ell = 1.2$  mm,  $\ell = 1.6$  mm and  $\ell = 2.3$  mm mm, respectively. In these measurements the frequency shift produced by the airgap between the metal and the dielectric is also noticed.

## 7.4 Discussion

To get a physical insight of the frequency shift observed between theory and experiment, we have extended the model introduced in Chapter 6 to the case

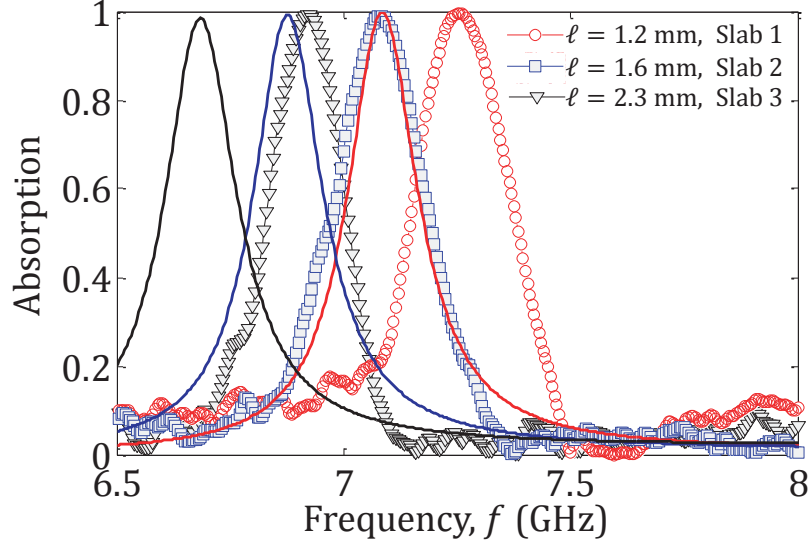


Figure 7.9: Absorption for the Sample 2 ( $h = 7$  mm) with three different dielectric thicknesses. The angle of incidence is  $\theta = 45^\circ$ . Symbols represent the measurements and solid lines the theoretical results.

that considers an air gap between the dielectric layer and the metal grating [see Fig. 7.10]. To do that, we use the same methodology that in the previous case and taking into account only the P-polarization (we have demonstrated in Chapter 6 that the system is not affected by S-polarized waves).

First, fields in the air region are expressed as:

$$|\mathbf{E}_t^0\rangle = A_0^- e^{-iq_0(z-\ell)} |\mathbf{k}_t\rangle + \sum_G A_G^+ e^{iq_G(z-\ell)} |\mathbf{k}_G\rangle, \quad (7.2)$$

$$|-\hat{\mathbf{z}} \times \mathbf{H}_t^0\rangle = -Y_0^0 A_0^- e^{-iq_0(z-\ell)} |\mathbf{k}_t\rangle + \sum_G Y_G^0 A_G^+ e^{iq_G(z-\ell)} |\mathbf{k}_G\rangle, \quad (7.3)$$

where  $A_0^-$  is the amplitude of the incident wave and  $q_G^2 = (\omega/c_0)^2 - |\mathbf{k}_G|^2$ . The normalized expressions of the fields remain equal and can be written as:

$$\langle \mathbf{r} | \mathbf{k}_G \rangle \equiv \frac{1}{\sqrt{\Omega}} e^{i\mathbf{k}_G \cdot \mathbf{r}} \hat{\mathbf{u}}_G, \quad (7.4)$$

where  $\Omega$  represents the area of the unit cell. The modal admittances for the P-polarized waves in the air region are

$$Y_G^0 = \frac{k_\omega}{q_G} \sqrt{\frac{\varepsilon_0}{\mu_0}} \quad (7.5)$$

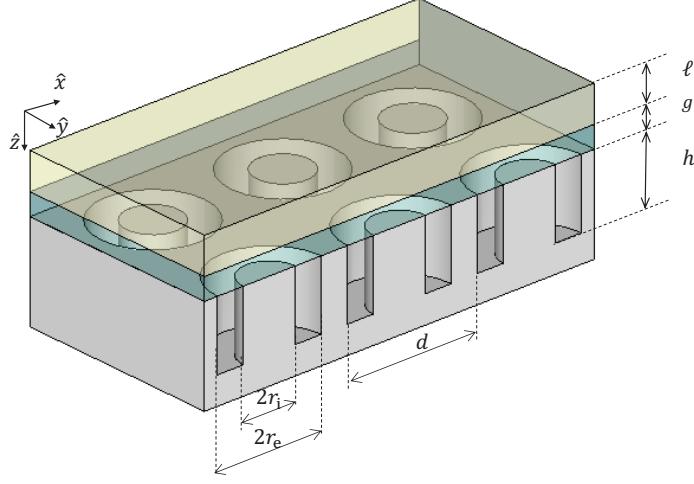


Figure 7.10: Schematic representation of the system under study with a film of air (air gap) with thickness  $g$  between the coaxial grating and the dielectric sheet.

and the unit vectors are

$$\hat{\mathbf{u}}_G = \frac{\mathbf{k}_G}{|\mathbf{k}_G|} \quad (7.6)$$

Then, fields in the dielectric region are

$$|\mathbf{E}_t^d\rangle = \sum_G (B_G^+ e^{ip_G(z-\ell)} + B_G^- e^{-ip_G(z-\ell)}) |\mathbf{k}_G\rangle, \quad (7.7)$$

and

$$|-\hat{\mathbf{z}} \times \mathbf{H}_t^d\rangle = \sum_G Y_G^d (B_G^+ e^{ip_G(z-\ell)} - B_G^- e^{-ip_G(z-\ell)}) |\mathbf{k}_G\rangle, \quad (7.8)$$

with  $p_G^2 = k_d^2 - |\mathbf{k}_G|^2$ ,  $k_d = k_0 \sqrt{\varepsilon_d \mu_d}$  and the modal admittance

$$Y_G^d = \frac{k_\omega}{p_G} \sqrt{\frac{\varepsilon_d}{\mu_d}}. \quad (7.9)$$

We add the fields in the air gap region which can be expressed as:

$$|\mathbf{E}_t^g\rangle = \sum_G (C_G^+ e^{iq_G(z-\ell)} + C_G^- e^{-iq_G(z-\ell)}) |\mathbf{k}_G\rangle, \quad (7.10)$$

and

$$|-\hat{\mathbf{z}} \times \mathbf{H}_t^g\rangle = \sum_G Y_G^0 (C_G^+ e^{iq_G(z-\ell)} - C_G^- e^{-iq_G(z-\ell)}) |\mathbf{k}_G\rangle. \quad (7.11)$$

Inside the cavities the fields are

$$|\mathbf{E}_t^\alpha\rangle = D_\alpha(e^{ik_h z} + \Gamma_\alpha e^{-ik_h z})|\alpha\rangle, \quad (7.12)$$

$$|-\hat{\mathbf{z}} \times \mathbf{H}_t^\alpha\rangle = Y_\alpha D_\alpha(e^{ik_h z} - \Gamma_\alpha e^{-ik_h z})|\alpha\rangle, \quad (7.13)$$

where, using the monomode approximation, the modal admittance is  $Y_\alpha = \sqrt{\varepsilon_h/\mu_h}$ , the reflection coefficient at the cavity bottom is  $\Gamma_\alpha = -e^{-2ik_h h}$  and the normalized TEM mode is

$$\langle \mathbf{r} | \alpha \rangle = -\frac{1}{\sqrt{2\pi}} \frac{e^{i\mathbf{k}_G \cdot \mathbf{R}_\alpha}}{\sqrt{\ln(r_e/r_i)}} \frac{1}{r} \hat{\mathbf{r}}, \quad (7.14)$$

Applying boundary conditions and projecting the electric fields with the mode  $\langle \mathbf{k}_G \sigma |$  and the magnetic field with cavity mode  $\langle \alpha |$ , we obtain the following system of equations:

Interface  $z = 0$  (air-dielectric)

$$A_G^+ + A_0^- \delta_{G0} = B_G^+ + B_G^- \quad (7.15)$$

$$Y_G^0(A_G^+ - A_0^- \delta_{G0}) = Y_G^d(B_G^+ - B_G^-) \quad (7.16)$$

Interface  $z = \ell$  (dielectric-air)

$$B_G^+ e^{-ip_G \ell} + B_G^- e^{ip_G \ell} = C_G^+ e^{-iq_G \ell} + C_G^- e^{iq_G \ell} \quad (7.17)$$

$$Y_G^d(B_G^+ e^{-ip_G \ell} - B_G^- e^{ip_G \ell}) = Y_G^0(C_G^+ e^{-iq_G \ell} - C_G^- e^{iq_G \ell}) \quad (7.18)$$

Interface  $z = \ell + g$  (air-coaxial grating)

$$C_G^+ e^{-iq_G(\ell+g)} + C_G^- e^{iq_G(\ell+g)} = D_\alpha(1 + \Gamma_\alpha) \langle G | \alpha \rangle \quad (7.19)$$

$$\sum_G Y_G^0 (C_G^+ e^{-iq_G(\ell+g)} - C_G^- e^{iq_G(\ell+g)}) \langle \alpha | G \rangle = Y_\alpha D_\alpha (1 - \Gamma_\alpha) \quad (7.20)$$

More details about the coupling integrals  $\langle \alpha | G \rangle$  and  $\langle G | \alpha \rangle$  are reported in Chapter 6.

From these equations one can obtain the coefficients  $D_\alpha$  inside the cavities as

$$D_\alpha = -\frac{4}{M} \frac{Y_0^0}{Y_\alpha} \frac{Y_0^0}{Y_0^H} e^{iq_0 g} \langle \alpha | 0 \rangle A_0^-, \quad (7.21)$$

where

$$Y_G^H = Y_G^0 \left( (\cos p_G \ell - i \rho_d \sin p_G \ell) - e^{2iq_G g} (\cos p_G \ell + i \rho_d \sin p_G \ell) \right) - Y_G^d \left( (i \sin p_G \ell - \rho_d \cos p_G \ell) - e^{2iq_G g} (i \sin p_G \ell + \rho_d \cos p_G \ell) \right), \quad (7.22)$$

and

$$M = (1 - \Gamma_\alpha) - (1 + \Gamma_\alpha)(\chi^{(1)} + \chi^{(2)}). \quad (7.23)$$

Terms  $\chi^{(1)}$  and  $\chi^{(2)}$  are

$$\chi^{(1)} = \sum_G \frac{Y_G^0}{Y_\alpha} \langle G|\alpha \rangle \langle \alpha|G \rangle \quad (7.24)$$

and

$$\chi^{(2)} = 2 \sum_G \frac{Y_G^0 Y_G^D}{Y_\alpha Y_G^H} e^{2iq_G g} \langle \alpha|G \rangle \langle G|\alpha \rangle, \quad (7.25)$$

with  $Y_G^D$  being

$$Y_G^D = Y_G^0 (\cos p_G \ell + i \rho_d \sin p_G \ell) - Y_G^d (i \sin p_G \ell + \rho_d \cos p_G \ell), \quad (7.26)$$

where  $\rho_G = \frac{Y_G^0}{Y_G^d}$ . The coefficients of the reflected waves are:

$$A_G^+ = R_d A_0^- \delta_{G0} + D_\alpha (1 + \Gamma_\alpha) \langle G|\alpha \rangle e^{iq_G g} N \quad (7.27)$$

with

$$R_d = -1 + 2 \frac{Y_G^0}{Y_G^H} \left( (\cos p_G \ell - i \rho_G \sin p_G \ell) - e^{2iq_G g} (\cos p_G \ell + i \rho_G \sin p_G \ell) \right) \quad (7.28)$$

and

$$N = (\cos p_G \ell + i \rho_G \sin p_G \ell) - \frac{Y_G^D}{Y_G^H} \left( (\cos p_G \ell - i \rho_G \sin p_G \ell) - e^{2iq_G g} (\cos p_G \ell + i \rho_G \sin p_G \ell) \right). \quad (7.29)$$

Therefore, the absorption  $A(\omega) = 1 - R(\omega)$  can be cast as

$$A(\omega) = 1 - \frac{\sum_G Y_G^0 |A_G^+|}{Y_0^0 |A_0^-|} \quad (7.30)$$

### Equation determining the frequency position of the peak

The absorption peak of interest here always appears below the diffraction limit. So, the absorption can be expressed as:

$$A(\omega) = 1 - \frac{|A_0^+|}{|A_0^-|} = 1 - R_0 \quad (7.31)$$

Considering that  $q_0\ell \ll 1$  and  $p_0\ell \ll 1$  and following the same procedure that in Ref.[16], the reflectance can be written as follows:

$$R_0 \approx -\frac{\cos k_h h + i \sin k_h h (\chi + 2H_{00}^2)}{\cos k_h h - i \sin k_h h \chi}, \quad (7.32)$$

where  $\chi$  is a lattice sum that can be decomposed as  $\chi = \chi_R + i\chi_I$ . This expression has a minimum value when

$$\cot k_h h + \chi_I(\omega) = 0. \quad (7.33)$$

This equation gives the condition for obtaining a peak in the absorption. It is similar to the one already developed in without the air gap but now the dependence on the air gap ( $g$ ) is embedded in  $\chi$ .

Figures 7.11 summarize the variation produced by the air gap in the position and amplitude of the peak. Figure 7.11(a) plots the solution of this expression as a function of the airgap thickness  $g$  when  $h = 10$  mm (Sample 1) with  $\ell = 1.2$  mm (Slab 1) and the incidence angle is  $\theta = 45^\circ$ . This result shows that an increase of the air gap thickness shifts the peak to higher frequencies. This behavior supports our previous claim suggesting that an unavoidable air gap explains the discrepancy between theoretical results and experimental data observed. Moreover, it is observed in Fig. 7.11(b) that there is a  $g$  value for which the peak amplitude is maximum. However, this result has no much interest since the air gap is out of control in the experimental setup.

A parametrical study of the air gap thickness, denoted by  $g$ , has been performed for  $\theta = 45^\circ$  using Slab 1 on top of Sample 1. Figure 7.12 (a) represents the absorption spectra calculated for several values  $g$  showing how the existence of an air gap shifts the absorption peak to higher frequencies. This behavior supports our previous observed in Fig. 7.11. Moreover, in Fig. 7.12 (b) the frequency position of the peak is represented as a function of  $g$ .

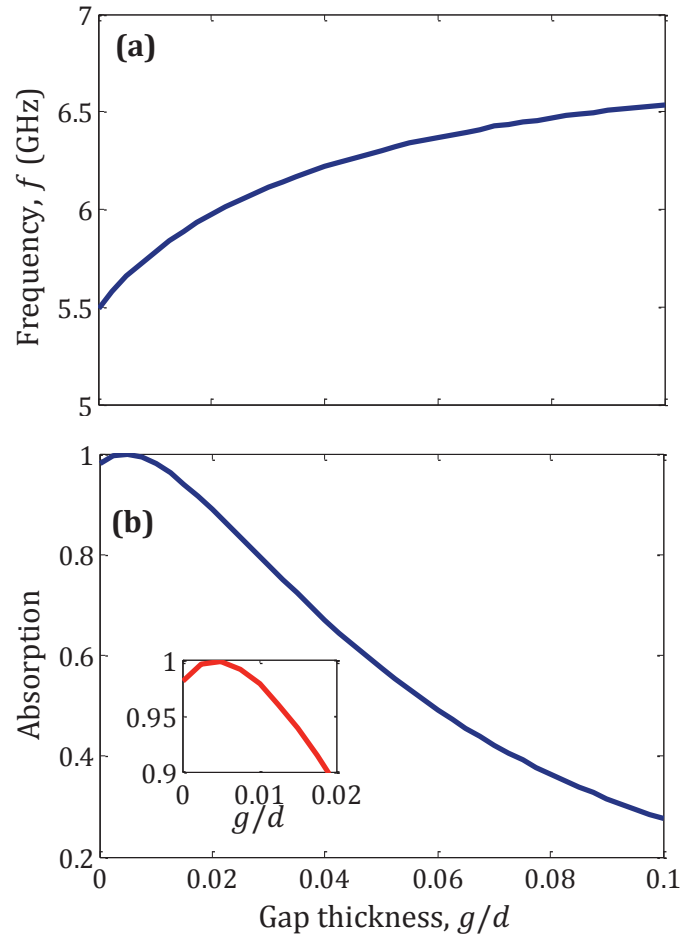


Figure 7.11: Sample 1 ( $h = 10$  mm) with the Slab 1 ( $\ell = 1.2$  mm) when the incidence angle is  $\theta = 45^\circ$ . (a) Frequency position of the absorption peak as a function of the air gap thickness,  $g$ . (a) Amplitude of the peak as a function of  $g$ .

	MM model ( $g = 0$ )	MM model		Experiment
	$f$ (GHz)	$g$ (mm)	$f$ GHz	$f$ GHz
<b>Sample 1 + Slab 1</b>	5.5	36	5.62	5.62
<b>Sample 2 + Slab 1</b>	7.09	30	7.24	7.24
<b>Sample 3 + Slab 1</b>	8.83	41	9.14	9.14
<b>Sample 2 + Slab 2</b>	6.88	36	7.09	7.09
<b>Sample 2 + Slab 3</b>	6.68	41	6.92	6.92

Table 7.2: Effect of an air gap on the frequency of the peak showing total absorption. The  $g$  values are obtained from the fitting to the measured peak position.

This curve is obtained using Eq. (7.33). In this figure, the horizontal lines correspond to air gap thicknesses of the spectra shown in Fig. 7.12(a). We can see that the Eq. (7.33) predicts the position of the absorption peak.

The effect of the air gap has been studied in all the measurements presented in this work and the results of these studies are reported in Table 7.2.

Figure 7.13 shows a comparison between the experimental data reported in 7.7 and the calculated absorption spectra using the airgap correction. The measured (calculated) peaks appear at 5.62(5.62) GHz, 7.24(7.24) GHz and 9.14(9.14)GHz, for  $h = 10$  mm,  $h = 7$  mm and  $h = 5$  mm. The calculated profiles are fitted using the following air gap thicknesses:  $g=36$   $\mu\text{m}$ , 30  $\mu\text{m}$ , and 41  $\mu\text{m}$ , respectively.

Moreover the experimental data shown in Figure 7.9 are compared with the air gap model in Figure 7.14. The measured (calculated) frequencies of the absorption peaks are 7.25(7.25) GHz, 7.09 (7.09)GHz and 6.92 (6.92) GHz, for  $\ell = 1.2$  mm,  $\ell = 1.6$  mm and  $\ell = 2.3$  mm mm, respectively. The calculated spectra are obtained using an air layer with  $g = 30$   $\mu\text{m}$ , 36  $\mu\text{m}$ , and 41  $\mu\text{m}$ , respectively.



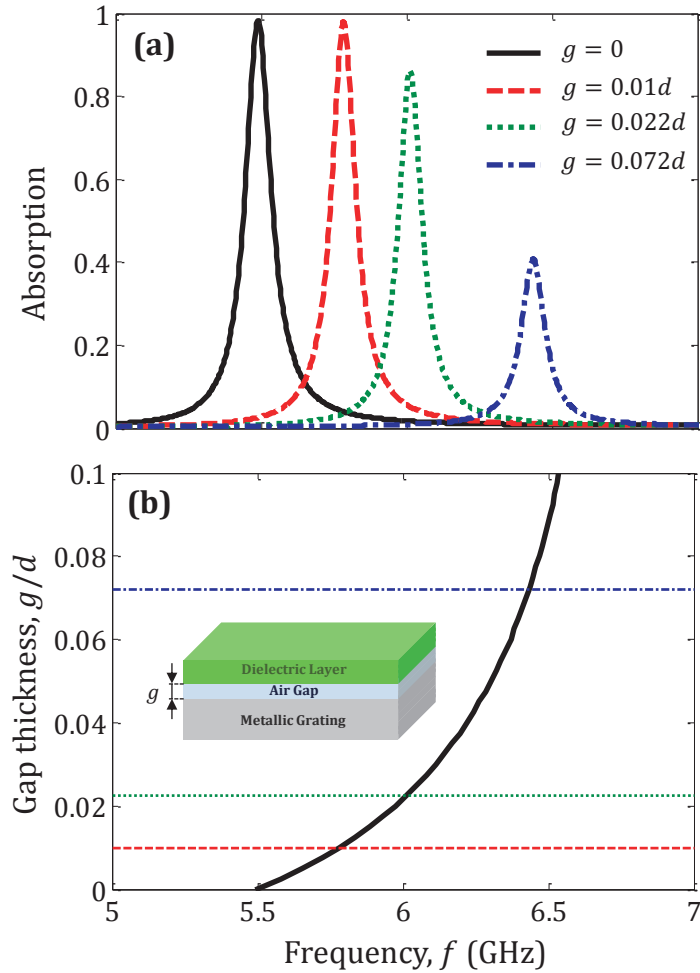


Figure 7.12: Effect of non-perfect contact between the dielectric layer and the metallic grating on the frequency of the absorption peak (numerical predictions) for the Sample 1 ( $h = 10$  mm) with the Slab 1 ( $\ell = 1.2$  mm) when the incidence angle is  $\theta = 45^\circ$ . (a) Calculated absorption spectra for several values of air gap thickness,  $g$ . (b) Calculated position of the absorption peak as a function of the air gap thickness,  $g$ . The inset illustrates the structure studied here.

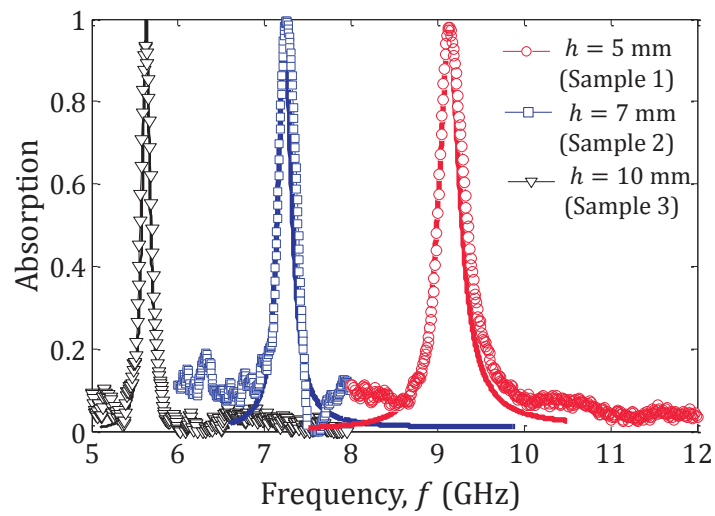


Figure 7.13: Absorption spectra for three values of cavity length  $h$ . The dielectric thickness is  $\ell = 1.2$  mm (Slab 1) and the angle of incidence is  $\theta = 45^\circ$ . Symbols represent the measurements and continuous lines represent the results obtained with the model described in this section. The calculated spectra are obtained using an air layer with  $g = 36 \mu\text{m}$ ,  $g = 30 \mu\text{m}$ , and  $g = 41 \mu\text{m}$  for  $h = 10$  mm,  $h = 7$  mm and  $h = 5$  mm, respectively.

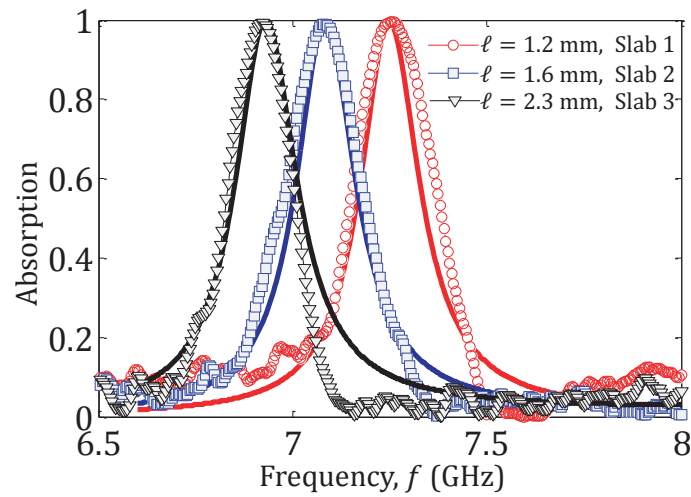


Figure 7.14: Absorption for the Sample 2 ( $h = 7$  mm) with three different dielectric thicknesses. The angle of incidence is  $\theta = 45^\circ$ . Symbols represent the measurements and solid lines the theoretical model. The calculated spectra are obtained using an air layer with  $g = 30 \mu\text{m}$ ,  $g = 36 \mu\text{m}$ , and  $g = 41 \mu\text{m}$  for  $\ell = 1.2$  mm,  $\ell = 1.6$  mm and  $\ell = 2.3$  mm, respectively.

# 8

## CONCLUDING REMARKS

---

This chapter summarizes the work reported in this manuscript and highlights the main contributions obtained during the thesis. Furthermore, in the second section, the future works connected with the results developed in this thesis are explained.

### Contents

---

<b>8.1</b>	<b>Summary and Conclusions</b> . . . . .	<b>158</b>
<b>8.2</b>	<b>Future Work</b> . . . . .	<b>158</b>

---

## 8.1 Summary and Conclusions

In the first part of this thesis, the resonant properties of the RPC shell have been studied in depth. Particularly, we have analyzed the existence of low-Q whispering gallery modes at the interface of these anisotropic and inhomogeneous metamaterials shells. Low-Q whispering gallery modes present a resonant frequency independent of the shell thickness and their quality factor can be adapted by changing the dielectric thickness. These features make possible the use of these modes for the energy exchange with the electromagnetic energy in the surrounding background, so they can be used in energy harvesting systems. In addition, Fabry-Perot modes, which are allowed in these shells, have been proposed as a solution for other applications. Particularly, we have study the strong coupling produced between two RPC shells for wireless power transfer and the use of a pair of RPC shells as a position sensor. This part also contains the first experimental verification of a RPC shell implementation.

The second part of this thesis deals with the absorption enhancement produced by a periodic grating placed on the bottom of a lossy thin layer. We have developed a theoretical model which allows a comprehensive study of the absorption mechanism in the system. Moreover, the experimental data demonstrate how the resonances produced by the metallic grating enhance over 3300% the absorption in the low-loss dielectric layer, compared to the response with an unpatterned metal backing.

## 8.2 Future Work

The present study leaves some points to be treated in more depth in further works.

The feasibility of using the RPC as resonators with evanescent field patterns for efficient wireless non-radiative energy transfer has been demonstrated, but a future line of research is the development of simplified structures allowing easy implementations and experimental verifications of these results. Another interesting point is the scaling of the structures to work at other frequencies ranges. For example, by changing the unit cell, RPCs can be designed for working at higher frequency. This fact can be useful to develop position or frequency sensor at the Terahertz range.

---

An interesting work is the development of a new theoretical model which includes the  $TE_{11}$  mode inside the coaxial. This study will reveal the effect produced by these evanescent wave in the low-frequency absorption peak. Finally, the study of random surfaces is another interesting line of research. Due to the high speed of calculus we can study deeply the effects of disordered media in the absorption enhancement. The knowledge of such simple structure will allow understanding the role that the disorder plays in the absorption.



# Part III

APPENDIX





# A

## MATHEMATICAL NOTES

---

### A.1 Bessel Functions

The Bessel's differential equation is defined as:

$$x^2 \frac{d^2 y}{dx^2} + x \frac{dy}{dx} + (a^2 x^2 + q^2)y = 0 \quad (\text{A.1})$$

Two different and independent solutions of this equation are the Bessel and Neuman functions,  $J_q(x)$  and  $Y(x)$  respectively. The solution for Bessel equation can be written as:

$$y = AJ_q(ax) + BY_q(ax) \quad (\text{A.2})$$

The functions  $J_q(x)$  are the Bessel functions of first kind and are defined as:

$$J_q(x) = \sum_{m=0}^{\infty} \frac{(-1)^m}{m!(m+q)!} \left(\frac{x}{2}\right)^{2m+q}, \quad (\text{A.3})$$

where  $q$  is the order of the Bessel function. A representation of the Bessel functions of first kind is shown in Fig A.1(a). In Figure A.1(b) the derivatives of these equations are also represented. The Neuman functions  $Y_q(x)$ , also named Bessel functions of second kind, have the form:

$$Y_q(x) = \frac{J_q(x) \cos(q\pi) - J_{-q}(x)}{\sin(q\pi)}. \quad (\text{A.4})$$

In Fig. A.2(a) and Fig. A.2(b) are represented the Bessel functions of second kind and their derivatives. Also it is necessary to define the Hankel functions, which are related with the Bessel and Neuman functions as:

$$H_q^{(1)}(x) = J_q(x) + iY_q(x) \quad (\text{A.5})$$

$$H_q^{(2)}(x) = J_q(x) - iY_q(x) \quad (\text{A.6})$$

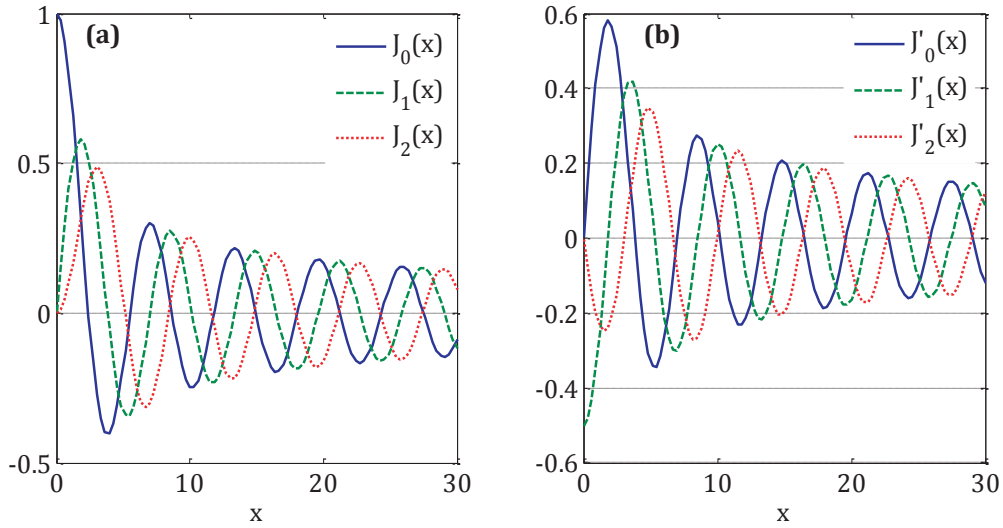


Figure A.1: (a) Bessel functions of the first kind and (b) Derivative of Bessel functions of the first kind.

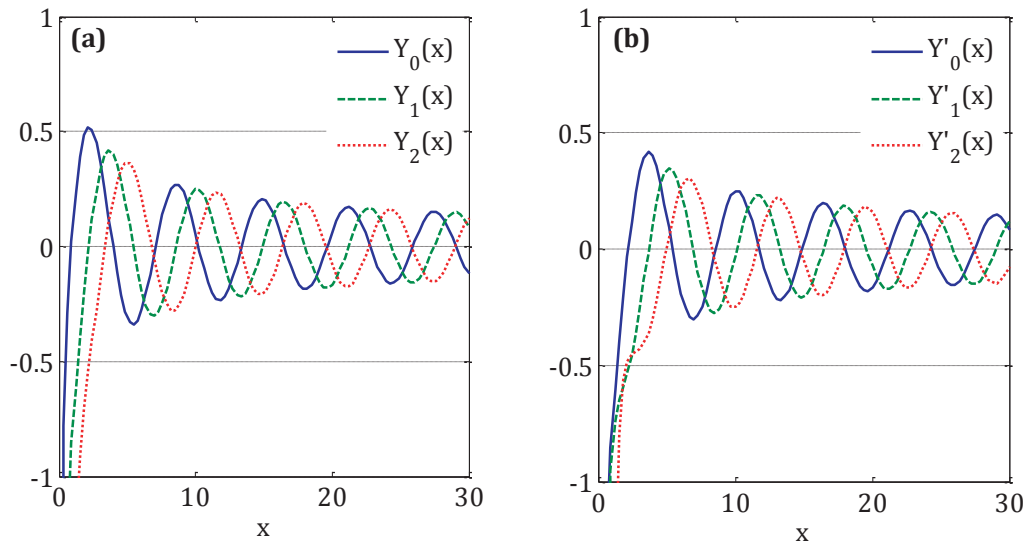


Figure A.2: (a) Bessel functions of the second kind and (b) Derivative of Bessel functions of the second kind.

where  $i$  is the imaginary unit.

### A.1.1 Properties

Now, we list some properties of the Bessel functions. Being  $\Psi = J, Y, H$ :

1.  $\frac{\delta \Psi_q(kr)}{\delta r} = k \Psi'_q(kr)$
2.  $\Psi'_q(x) = \frac{1}{2} (\Psi_{q-1}(x) - \Psi_{q+1}(x))$
3.  $\Psi_{-q}(x) = (-1)^q \Psi_q(x)$
4.  $\Psi_q(x) = \frac{x}{2q} (\Psi_{q-1}(x) + \Psi_{q+1}(x))$

## A.2 Chebyshev Identity

In this section, we derive the  $N$ th power of a unimodular matrix also known as Chebyshev identity. Let us analyze the eigenvalues and the eigenvectors of the matrix. The eigenvector problem can be written as:

$$\begin{pmatrix} A & B \\ C & D \end{pmatrix} V_{\pm} = e^{\pm K\Lambda} V_{\pm}, \quad (\text{A.7})$$

where  $e^{\pm K\Lambda}$  represents the eigenvalues and  $V_{\pm}$  the eigenvectors. The eigenvalues are given by:

$$e^{\pm K\Lambda} = \frac{1}{2} (A + D) \pm \left\{ \left[ \frac{1}{2} (A + D) \right]^2 - 1 \right\}^{1/2} \quad (\text{A.8})$$

and the corresponding eigenvectors are:

$$V_{\pm} = \begin{pmatrix} \alpha_{\pm} \\ \beta_{\pm} \end{pmatrix}, \quad (\text{A.9})$$

being

$$\alpha_{\pm} = \frac{B}{[B^2 + (e^{\pm K\Lambda} - A)^2]^{1/2}} \quad \beta_{\pm} = \frac{e^{\pm K\Lambda} - A}{[B^2 + (e^{\pm K\Lambda} - A)^2]^{1/2}} \quad (\text{A.10})$$

To derive the Chebyshev identity we use the following relation:

$$\left\{ M \begin{pmatrix} A & B \\ C & D \end{pmatrix} M^{-1} \right\}^N = M \begin{pmatrix} A & B \\ C & D \end{pmatrix}^N M^{-1} \quad (\text{A.11})$$

This matrix equation is easy to see taking into account that  $MM^{-1} = I$ . The relation establishes that the Nth power of a transformed matrix is similar to transform of the Nth power of the original matrix. We are looking for M matrix that transform the original matrix into a diagonal matrix with the eigenvectors, such that

$$M \begin{pmatrix} A & B \\ C & D \end{pmatrix} M^{-1} = \begin{pmatrix} e^{iK\Lambda} & 0 \\ 0 & e^{-iK\Lambda} \end{pmatrix} \quad (\text{A.12})$$

Using equation (A.11) we can write

$$\begin{pmatrix} A & B \\ C & D \end{pmatrix}^N = M^{-1} \begin{pmatrix} e^{iNK\Lambda} & 0 \\ 0 & e^{-iNK\Lambda} \end{pmatrix} M \quad (\text{A.13})$$

The values of the  $M$  matrix and the inverse,  $M^{-1}$  are

$$M^{-1} = \frac{1}{\sqrt{\alpha_+\beta_- - \alpha_-\beta_+}} \begin{pmatrix} \alpha_+ & \alpha_- \\ \beta_+ & \beta_- \end{pmatrix} \quad (\text{A.14})$$

$$M = \frac{1}{\sqrt{\alpha_+\beta_- - \alpha_-\beta_+}} \begin{pmatrix} \beta_- & -\alpha_- \\ -\beta_+ & \alpha_+ \end{pmatrix} \quad (\text{A.15})$$

Finally the Nth power of the unimodular matrix is

$$\begin{aligned} \begin{pmatrix} A & B \\ C & D \end{pmatrix}^N &= \frac{1}{\sqrt{\alpha_+\beta_- - \alpha_-\beta_+}} \begin{pmatrix} \beta_- & -\alpha_- \\ -\beta_+ & \alpha_+ \end{pmatrix} \\ &\times \begin{pmatrix} e^{iNK\Lambda} & 0 \\ 0 & e^{-iNK\Lambda} \end{pmatrix} \begin{pmatrix} \beta_- & -\alpha_- \\ -\beta_+ & \alpha_+ \end{pmatrix} \end{aligned} \quad (\text{A.16})$$

After some simplifications, we can express this equation as

$$\begin{pmatrix} A & B \\ C & D \end{pmatrix}^N = \begin{pmatrix} AU_{N-1} - U_{N-2} & BU_{N-1} \\ CU_{N-1} & DU_{N-1} - U_{N-2} \end{pmatrix} \quad (\text{A.17})$$

where

$$U_N = \sin((N+1)K\Lambda) / \sin(K\Lambda) \quad (\text{A.18})$$

and

$$K\Lambda = \cos^{-1} \left( \frac{1}{2} (A + D) \right). \quad (\text{A.19})$$

# REDUCED PARAMETERS OF RADIAL PHOTONIC CRYSTALS

---

# B

The purpose of this study is the design of a simplified structure of a RPC shell with four layers (two layers with material A and two layers with material B), with  $r_{int} = 15$  mm,  $d_a = d_b = 5$  mm and whose constitutive parameters are described by:

$$\mu_{ra}(r) = \frac{d}{0.347r}, \quad \mu_{rb}(r) = \frac{d}{0.5r}, \quad (\text{B.1a})$$

$$\mu_{\theta a}(r) = \frac{0.08r}{d}, \quad \mu_{\theta b}(r) = \frac{0.04r}{d}, \quad (\text{B.1b})$$

$$\varepsilon_{za}(r) = \frac{d}{0.143r}, \quad \varepsilon_{zb}(r) = \frac{d}{0.1r}. \quad (\text{B.1c})$$

The simplified structure should be able to act as a resonator at the same frequencies that a RPC shell. The equation that models the electric field inside a 2D RPC shell can be written as:

$$\left[ -\frac{\partial}{\partial r} \left( \frac{r}{\mu_{\theta}(r)} \frac{\partial}{\partial r} \right) + \frac{q}{r\mu_r(r)} \right] \mathbf{E}_q(\mathbf{r}) = r\varepsilon_z(r)\omega^2 \mathbf{E}_q(\mathbf{r}). \quad (\text{B.2})$$

Terms  $\frac{r}{\mu_{\theta}(r)}$ ,  $\frac{1}{r\mu_r(r)}$  and  $r\varepsilon_z(r)$  define the normalized constitutive parameters and the propagations features in the RPC shell. The simplified design of the RPC shell has only radially dependent function for the angular permeability and keeping constant values of radial permeability ( $\mu_r(r) = \mu_r^{red}$ ) and permittivity ( $\varepsilon_z(r) = \varepsilon_z^{red}$ ). To obtain an equivalence between the complete

and the reduced system we analyze the average of these terms over the four layer. For the simplified structure we obtain the following expressions:

$$\langle r\varepsilon_z(r) \rangle_{red} = \frac{\int_{r_{int}}^{r_{ext}} r\varepsilon_z(r)dr}{r_{ext} - r_{int}} \approx \frac{r_{ext}^2 - r_{int}^2}{2(r_{ext} - r_{int})} \varepsilon_z^{red} \quad (B.3)$$

$$\left\langle \frac{1}{r\mu_r(r)} \right\rangle_{red} = \frac{\int_{r_{int}}^{r_{ext}} \frac{dr}{r\mu_r(r)}}{r_{ext} - r_{int}} \approx \frac{\ln(r_{ext}/r_{int})}{(r_{ext} - r_{int})} \frac{1}{\mu_r^{red}} \quad (B.4)$$

The same procedure apply to the RPC shells leads to

$$\langle r\varepsilon_z(r) \rangle_{RPC} = \frac{d_a \hat{\varepsilon}_{za} + d_b \hat{\varepsilon}_{zb}}{d} = \frac{\hat{\varepsilon}_{za} + \hat{\varepsilon}_{zb}}{2} \quad (B.5)$$

$$\left\langle \frac{1}{r\mu_r(r)} \right\rangle_{RPC} = \frac{\frac{d_a}{\hat{\mu}_{ra}} + \frac{d_b}{\hat{\mu}_{zb}}}{d} = \frac{1}{2} \left( \frac{1}{\hat{\mu}_{ra}} + \frac{1}{\hat{\mu}_{zb}} \right) \quad (B.6)$$

To ensure that both system are equivalent, it is necessary that

$$\langle r\varepsilon_z(r) \rangle_{RPC} = \langle r\varepsilon_z(r) \rangle_{red} \quad (B.7)$$

$$\left\langle \frac{1}{r\mu_r(r)} \right\rangle_{RPC} = \left\langle \frac{1}{r\mu_r(r)} \right\rangle_{red} \quad (B.8)$$

Applying these condition, we obtain the relation between the RPC parameters and the reduced profile:

$$\hat{\varepsilon}_{za} + \hat{\varepsilon}_{zb} = \frac{r_{ext}^2 - r_{int}^2}{(r_{ext} - r_{int})} \varepsilon_z^{red} \quad (B.9)$$

$$\frac{1}{\hat{\mu}_{ra}} + \frac{1}{\hat{\mu}_{zb}} = 2 \frac{\ln(r_{ext}/r_{int})}{(r_{ext} - r_{int})} \frac{1}{\mu_r^{red}} \quad (B.10)$$

Then, for the angular permeability, the values of the reduced profile are constant in each layer and equal to the respective layer at its center. This values are modeled by:

$$\mu_\theta(r) = \begin{cases} \mu_{\theta a}(r) = \hat{\mu}_{\theta a} \left( r_{int} + \frac{d_a}{2} + (n-1)d \right) \\ \mu_{\theta b}(r) = \hat{\mu}_{\theta b} \left( r_{int} + \frac{3d_b}{2} + (n-1)d \right) \end{cases} \quad n = 1, 2 \quad (B.11)$$

Table B summarizes the value of each parameter in each layer. In Fig. B.1, a comparison of the resonant modes in both structures is shown.

Ring resonator	1A	1B	2A	2B
$\mu_\theta$	0.14	0.09	0.22	0.13
$\varepsilon_z$	3.4	3.4	3.4	3.4
$\mu_r$	1	1	1	1

Table B.1: Constitutive parameters of the reduced profile

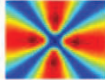
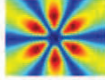
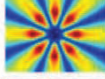
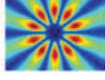
Mode pattern	Mode symmetry	Full profile RPC $f_r$ (GHz)	Reduced profile RPC $f_r$ (GHz)	Relative difference
	shell Bragg $q = 2$ $m = 1$	2.889	2.735	5.33%
	shell Bragg $q = 3$ $m = 1$	3.897	3.803	2.41%
	shell Bragg $q = 4$ $m = 1$	4.943	4.830	2.3%
	shell Bragg $q = 5$ $m = 1$	6.041	5.781	4.3%

Figure B.1: Comparison between the resonant modes in the complete RPC and in the reduced shell





# C

## HOMOGENIZATION OF THE SRR UNIT CELLS

---

In this appendix, the method used for the parameter retrieval of the SRR unit cells is explained in detail. First, we obtain the expressions which define the effective parameters. Then, an example of an extraction from a SRR unit cell is calculated.

### C.1 Transmission Matrix

We start with the analysis of the *Transmission Matrix* for a single dielectric slab. Considering an isotropic and homogeneous medium with  $\eta_a = \sqrt{(\mu_a/\varepsilon_a)}$ ,  $n_a = \sqrt{\mu_a\varepsilon_a}$  and  $k_a = n_ak_0$  and setting  $\mathbf{E}(z) = \hat{x}E(z)$  and  $\mathbf{H}(z) = \hat{y}H(z)$ , the forward and backward fields can be expressed as:

$$E(z) = E_a^+ e^{ik_a z} + E_a^- e^{-ik_a z} = E^+(z) + E^-(z), \quad (\text{C.1})$$

$$H(z) = \frac{1}{\eta_a} (E_a^+ e^{ik_a z} - E_a^- e^{-ik_a z}) = \frac{1}{\eta_a} (E^+(z) - E^-(z)). \quad (\text{C.2})$$

We can express the forward and backward amplitudes in terms of the total magnetic fields as:

$$E^+(z) = \frac{1}{2} (E(z) + \eta_a H(z)), \quad (\text{C.3})$$

$$E^-(z) = \frac{1}{2} (E(z) - \eta_a H(z)). \quad (\text{C.4})$$

Equations (C.1) and (C.3) can be written in a matrix form as:

$$\begin{bmatrix} E \\ H \end{bmatrix} = \begin{bmatrix} 1 & 1 \\ \eta_a^{-1} & -\eta_a^{-1} \end{bmatrix} \begin{bmatrix} E^+ \\ E^- \end{bmatrix}, \quad \begin{bmatrix} E^+ \\ E^- \end{bmatrix} = \frac{1}{2} \begin{bmatrix} 1 & \eta_a \\ 1 & -\eta_a \end{bmatrix} \begin{bmatrix} E \\ H \end{bmatrix}. \quad (\text{C.5})$$

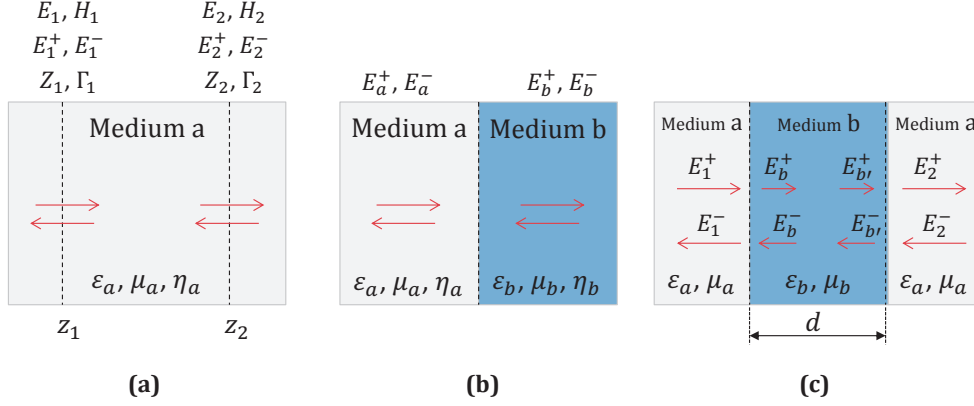


Figure C.1: Schematic representation of the field amplitudes. (a) Field amplitudes propagating between two positions of the same medium. (b) Field amplitudes across and interface. (c) Field amplitudes in a single dielectric slab.

Next, we obtain the *Propagation Matrix* which relates the propagation of the forward and backward waves from one point to another point separated  $d = z_2 - z_1$ . The amplitude of the waves are represented in Fig C.1(a). The field amplitudes in  $z_1$  and  $z_2$  can be written as:

$$E_2^+ = E_0^+ e^{ik_a z_2} \rightarrow E_1^+ = E_0^+ e^{ik_a z_1} = E_0^+ e^{ik_a(z_2-d)} = E_2^+ e^{-ik_a d} \quad (\text{C.6})$$

$$E_2^- = E_0^- e^{-ik_a z_2} \rightarrow E_1^- = E_0^- e^{-ik_a z_1} = E_0^- e^{-ik_a(z_2-d)} = E_2^- e^{ik_a d} \quad (\text{C.7})$$

Writing these equation in matrix form we lead to the *Propagation Matrix*:

$$\begin{bmatrix} E_1^+ \\ E_1^- \end{bmatrix} = \begin{bmatrix} e^{-ikd} & 0 \\ 0 & e^{ikd} \end{bmatrix} \begin{bmatrix} E_2^+ \\ E_2^- \end{bmatrix}. \quad (\text{C.8})$$

Then, we have to analyse the interface between two different media [see Figure C.1.(b)]. In this case, the Matching Matrix will related the field amplitudes at both size of the interface. To do that, we have to apply the boundary conditions that impose the continuity of the fields across the interface,  $E_a = E_b$ . and  $H_a = H_b$ . These conditions expressed in terms of the forward and backward waves are:

$$E_a^+ + E_a^- = E_b^+ + E_b^-, \quad (\text{C.9})$$

$$\frac{1}{\eta_a} (E_a^+ - E_a^-) = \frac{1}{\eta_b} (E_b^+ - E_b^-). \quad (\text{C.10})$$

The *Matching Matrix* is:

$$\begin{bmatrix} E_a^+ \\ E_a^- \end{bmatrix} = \frac{1}{\tau_a} \begin{bmatrix} 1 & \rho_a \\ \rho_a & 1 \end{bmatrix} \begin{bmatrix} E_b^+ \\ E_b^- \end{bmatrix}, \quad \begin{bmatrix} E_b^+ \\ E_b^- \end{bmatrix} = \frac{1}{\tau_b} \begin{bmatrix} 1 & \rho_b \\ \rho_b & 1 \end{bmatrix} \begin{bmatrix} E_a^+ \\ E_a^- \end{bmatrix}, \quad (\text{C.11})$$

where

$$\rho_a = \frac{\eta_b - \eta_a}{\eta_b + \eta_a}, \quad \tau_a = \frac{2\eta_b}{\eta_b + \eta_a}, \quad (\text{C.12})$$

$$\rho_b = \frac{\eta_a - \eta_b}{\eta_a + \eta_b}, \quad \tau_b = \frac{2\eta_a}{\eta_a + \eta_b}. \quad (\text{C.13})$$

Now, we are ready to study the Transmission Matrix of a single slab. The system under study is represented in Fig C.1(c) where the notation used for the field amplitudes is shown. Applying the *Matching Matrix* and the *Propagation Matrix* we can calculate the relation between the field in the left and right sides of the dielectric slab. The procedure is:

$$\begin{aligned} \begin{bmatrix} E_1^+ \\ E_1^- \end{bmatrix} &= \frac{1}{\tau_a} \begin{bmatrix} 1 & \rho_a \\ \rho_a & 1 \end{bmatrix} \begin{bmatrix} E_b^+ \\ E_b^- \end{bmatrix} = \frac{1}{\tau_a} \begin{bmatrix} 1 & \rho_a \\ \rho_a & 1 \end{bmatrix} \begin{bmatrix} e^{-ik_b d} & 0 \\ 0 & e^{ik_b d} \end{bmatrix} \begin{bmatrix} E_{b'}^+ \\ E_{b'}^- \end{bmatrix} \\ &= \frac{1}{\tau_a} \begin{bmatrix} 1 & \rho_a \\ \rho_a & 1 \end{bmatrix} \begin{bmatrix} e^{-ik_b d} & 0 \\ 0 & e^{ik_b d} \end{bmatrix} \frac{1}{\tau_b} \begin{bmatrix} 1 & \rho_b \\ \rho_b & 1 \end{bmatrix} \begin{bmatrix} E_2^+ \\ E_2^- \end{bmatrix} \end{aligned} \quad (\text{C.14})$$

Moreover, the relation between the electric and magnetic fields in both side of the dielectric slab is:

$$\begin{aligned} \begin{bmatrix} E_1 \\ H_1 \end{bmatrix} &= \begin{bmatrix} 1 & 1 \\ \eta_b^{-1} & -\eta_b^{-1} \end{bmatrix} \begin{bmatrix} E_b^+ \\ E_b^- \end{bmatrix} = \begin{bmatrix} 1 & 1 \\ \eta_b^{-1} & -\eta_b^{-1} \end{bmatrix} \begin{bmatrix} e^{-ik_b d} & 0 \\ 0 & e^{ik_b d} \end{bmatrix} \begin{bmatrix} E_{b'}^+ \\ E_{b'}^- \end{bmatrix} \\ &= \frac{1}{\tau_a} \begin{bmatrix} 1 & 1 \\ \eta_b^{-1} & -\eta_b^{-1} \end{bmatrix} \begin{bmatrix} e^{-ik_b d} & 0 \\ 0 & e^{ik_b d} \end{bmatrix} \begin{bmatrix} 1 & \eta_b \\ 1 & \eta_b \end{bmatrix} \begin{bmatrix} E_2 \\ H_2 \end{bmatrix} \end{aligned} \quad (\text{C.15})$$

This matrix is known as *Transmission Matrix* and can be written as:

$$\begin{bmatrix} E_1 \\ H_1 \end{bmatrix} = \begin{bmatrix} T_{11} & T_{12} \\ T_{21} & T_{22} \end{bmatrix} = \begin{bmatrix} \cos(k_b d) & i\eta_b \sin(k_b d) \\ i\eta_b^{-1} \sin(k_b d) & \cos(k_b d) \end{bmatrix} \begin{bmatrix} E_2 \\ H_2 \end{bmatrix} \quad (\text{C.16})$$

The relations of the elements of this matrix with the S-parameters are [47]:

$$T_{11} = \frac{(1 + S_{11})(1 - S_{22}) + S_{21}S_{12}}{2S_{21}} \quad (\text{C.17})$$

$$T_{12} = \frac{(1 + S_{11})(1 + S_{22}) - S_{21}S_{12}}{2S_{21}} \quad (\text{C.18})$$

$$T_{21} = \frac{(1 - S_{11})(1 - S_{22}) - S_{21}S_{12}}{2S_{21}} \quad (\text{C.19})$$

$$T_{22} = \frac{(1 - S_{11})(1 + S_{22}) + S_{21}S_{12}}{2S_{21}} \quad (\text{C.20})$$

For the symmetry of the problem  $S_{11} = S_{22}$  and  $S_{21} = S_{12}$ . From the first element of the Transmission Matrix we can obtain the value of  $n_b$  as a function of the S-parameters:

$$\cos(n_b k_0 d) = \frac{1 - S_{11}^2 + S_{12}^2}{2S_{21}} \rightarrow n_b = \frac{1}{k_0 d} \cos^{-1}\left(\frac{1 - S_{11}^2 + S_{12}^2}{2S_{21}}\right). \quad (\text{C.21})$$

From  $T_{12}$  and  $T_{21}$  we can obtain the value of the wave impedance  $\eta_b$  in terms of the S-parameters:

$$\eta_b^2 = \frac{T_{12}}{T_{21}} \rightarrow \eta_b = \sqrt{\frac{(1 - S_{11})^2 - S_{12}^2}{(1 + S_{11})^2 - S_{12}^2}} \quad (\text{C.22})$$

The relation between the constitutive parameters with the wave impedance,  $\eta_b$ , and the refractive index,  $n_b$ :

$$\varepsilon_b = \frac{n_b}{\eta_b} \quad \mu_b = n_b \eta_b. \quad (\text{C.23})$$

## C.2 Effective Parameters of SRR Unit Cells

In Sec. 4.3, a practical implementation of the constitutive parameters of each RPC layer is performed by an arrayed microstructure using a unitary cell composed of a SRR. The method used to obtain the material parameters of these metamaterials is based on the previous analysis [48]. The S-parameters for the unit cell of Fig C.2(a) are computed using HFSS Ansoft. S-parameters are presented in Fig. C.2(b) and Fig. C.2(c).

Now, the effective permittivity and effective permeability are calculated based on the assumption that the slab can be accurately described as a homogeneous material with these parameters. The permeability of an array

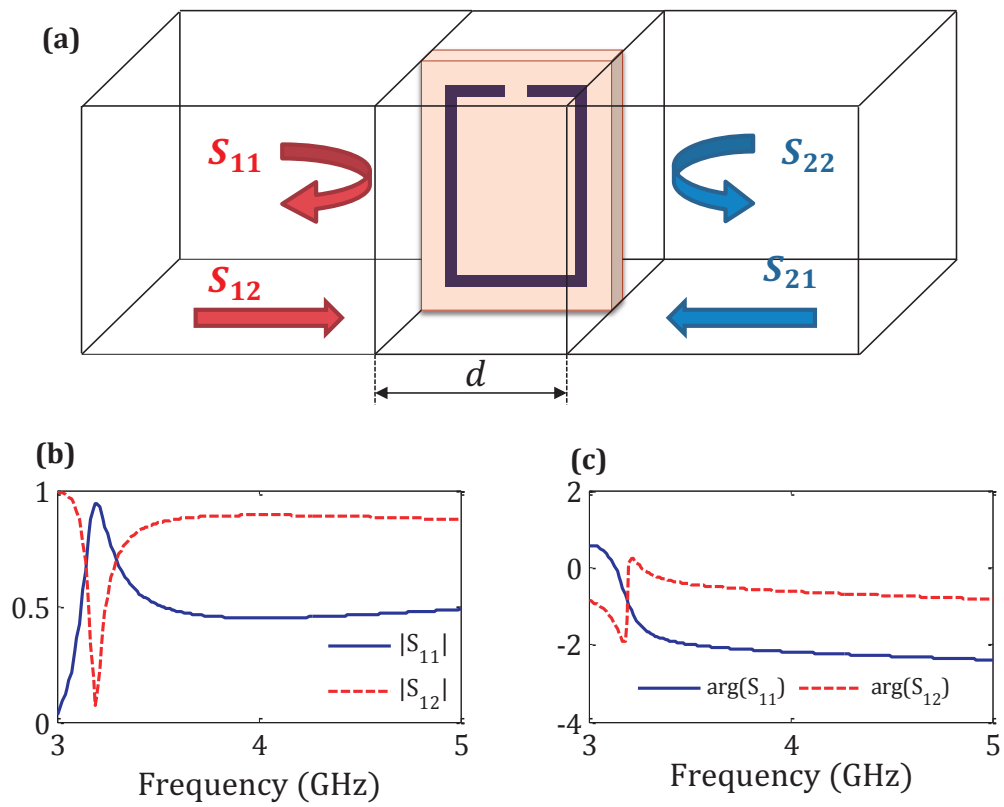


Figure C.2: (a) A single unit cell of a negative index metamaterial. (b) and (c) Magnitude and phase of the S-parameters calculated with HFSS.

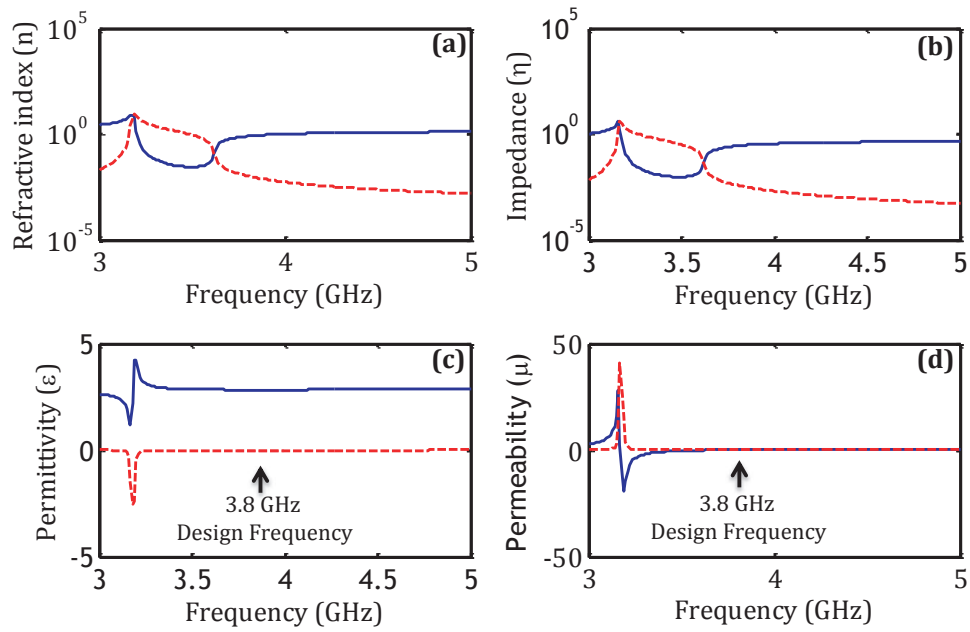


Figure C.3: Real and imaginary parts of the retrieved index (a), impedance (b), permittivity (c) and permeability (d)

of SRRs can be modelled by a Lorentz-type function with the resonant frequency separating positive and negative values of the effective permeability. The characteristic effective parameters of this material have a typical behavior given in Fig C.3(c) and Fig C.3(d).





# D

## MERITS OF THE AUTHOR

---

### D.1 International Journals

The following papers have been derived from the work of the thesis:

1. **Ana Díaz-Rubio**, Alastair P. Hibbins, Jorge Carbonell and José Sánchez-Dehesa. *Experimental verification of total absorption by a low-loss thin dielectric layer*. Applied Physics Letter 106, 241604, pp. 1-4 (2015).
2. **Ana Díaz-Rubio**, Daniel Torrent, Jorge Carbonell and José Sánchez-Dehesa. *Extraordinary absorption by a thin dielectric slab backed with a metasurface*. Physical Review B, 89, no 24, 245123, pp. 1-10 (2014).
3. **Ana Díaz-Rubio**, Jorge Carbonell and José Sánchez-Dehesa. *Wireless energy transfer between anisotropic metamaterials shells*. Annals of Physics, 345, pp. 55 - 62 (2014).
4. **Ana Díaz-Rubio**, Jorge Carbonell, Daniel Torrent and José Sánchez-Dehesa. *Low-Q whispering gallery modes in anisotropic metamaterials shells*. Physical Review B, 88, 115118 pp. 1-11 (2013).
5. Jorge Carbonell, **Ana Díaz-Rubio**, Daniel Torrent, Francisco Cervera, Matt Kirleis, M. A., Alberto Piqué and José Sánchez-Dehesa. *Radial Photonic Crystal for detection of frequency and position of radiation sources*. Scientific Reports, 2, pp. 1-8 (2012).

Other contributions by the author not included in the thesis:

6. Jorge Carbonell, Francisco Rodríguez-Fortuño, **Ana Díaz-Rubio**, Alejandro Martínez, Francisco Cervera and José Sánchez-Dehesa *Directive excitation of guided electromagnetic waves through polarization control*. Physical Review B, 89, no 15, 155121, pp. 1-7 (2014).
7. Jorge Carbonell, Daniel Torrent, **Ana Díaz-Rubio** and José Sánchez-Dehesa *Multidisciplinary approach to cylindrical anisotropic metamaterials*. New Journal of Physics, 13, 103034, pp. 1-20 (2011).
8. Victor Manuel Gracia-Chocano, Lorenzo Sanchis, **Ana Díaz-Rubio**, Martínez-Pastor, Francisco Cervera, Rafael Llopis-Pontiveros and José Sánchez-Dehesa *Acoustic cloak for airborne sound by inverse design*. Applied Physics Letters, 99, 74102, pp. 1-3 (2011).

## D.2 International Meetings and Conferences

1. **Ana Díaz-Rubio**, Alastair P. Hibbins, Jorge Carbonell and José Sánchez-Dehesa. *Total absorption by a low-loss dielectric thin layer on top of a metallic metasurface*. 9th International Congress on Advanced Electromagnetic Materials in Microwaves and Optics (Metamaterials 2015). Oxford (UK), 2015.
2. Jorge Carbonell, Francisco Rodríguez-Fortuño, **Ana Díaz-Rubio**, Alejandro Martínez, Francisco Cervera and José Sánchez-Dehesa. *Spatial sorting and routing of electromagnetic waves based on polarization control*. 8th International Congress on Advanced Electromagnetic Materials in Microwaves and Optics (Metamaterials 2014). Copenhagen (Denmark), 2014.
3. **Ana Díaz-Rubio**, Daniel Torrent, Jorge Carbonell and José Sánchez-Dehesa. *Metasurface for absorption enhancement*. 8th International Congress on Advanced Electromagnetic Materials in Microwaves and Optics (Metamaterials 2014). Copenhagen (Denmark), 2014.
4. Victor Manuel Garcia, Francisco Cervera, **Ana Díaz-Rubio**, Alfonso Climente, Daniel Torrent and José Sánchez-Dehesa. *Acoustic cloaking for airborne sound based on inclusions of rigid scatterers*. 166th

Meeting of the Acoustical Society of America. San Francisco (EEUU), 2013.

5. José Sánchez-Dehesa, Victor Manuel Garcia, Daniel Torrent, **Ana Díaz-Rubio**, Alfonso Climente and Francisco Cervera, . *Acoustic Cloaks for Airborne Sound*. International Symposium on the Theory and Application of Artificial Periodic Structures (ISAPS). Changsha (China), 2013.
6. Jorge Carbonell, **Ana Díaz-Rubio**, Daniel Torrent and José Sánchez-Dehesa. *Metamaterial shells based on Radial Photonic Crystals: Theory and Applications*. 7th International Congress on Advanced Electromagnetic Materials in Microwaves and Optics (Metamaterials 2013). Bordeaux (France), 2013.
7. **Ana Díaz-Rubio**, Jorge Carbonell, Daniel Torrent, Francisco Cervera, Matt Kirleis, M. A., Alberto Piqué and José Sánchez-Dehesa. *Radial photonic crystals for microwave operation*. 6th International Congress on Advanced Electromagnetic Materials in Microwaves and Optics (Metamaterials 2012). Saint Petersburg (Russian), 2012

### D.3 National Meetings and Conferences

1. **Ana Díaz-Rubio**, Alastair P. Hibbins, Jorge Carbonell and José Sánchez-Dehesa. *Experimental demonstration of total absorption by thin layers*. XXX Symposium Nacional de la Unión Científica Internacional de Radio (URSI). Pamplona, Spain, 2015.
2. Jorge Carbonell, Francisco Rodríguez-Fortuño, **Ana Díaz-Rubio**, Alejandro Martínez, Francisco Cervera and José Sánchez-Dehesa. *Directividad y selectividad espaciales basadas en el control de la polarización*. XXIX Symposium Nacional de la Unión Científica Internacional de Radio (URSI). Valencia, Spain, 2014.
3. Jorge Carbonell, **Ana Díaz-Rubio**, Daniel Torrent and José Sánchez-Dehesa. *Modos altamente radiativos en estructuras basadas en metamateriales*. XXXIV Reunión Bienal de la Sociedad Española de Física. Valencia, Spain, 2013

## D.4 Patents

1. Jorge Carbonell, **Ana Díaz-Rubio**, José Sánchez-Dehesa and Daniel Torrent. *Wireless Power Transfer Device*. *Polytechnic University of Valencia*. P201331500.

## BIBLIOGRAPHY

---

- [1] D. Torrent and J. Sánchez-Dehesa, “Radial wave crystals: radially periodic structures from anisotropic metamaterials for engineering acoustic or electromagnetic waves,” *Physical Review Letters*, vol. 103, no. 6, p. 064301, 2009.
- [2] K. Sakoda, *Optical properties of photonic crystals*, vol. 80. Springer, 2005.
- [3] J. D. Joannopoulos, S. G. Johnson, J. N. Winn, and R. D. Meade, *Photonic crystals: molding the flow of light*. Princeton University Press, 2011.
- [4] A. Yariv and P. Yeh, “Electromagnetic propagation in periodic stratified media. i . general theory,” *Journal of the Optical Society of America*, vol. 67, no. 4, pp. 438–447, 1977.
- [5] S. Guo and S. Albin, “Simple plane wave implementation for photonic crystal calculations,” *Optics Express*, vol. 11, no. 2, pp. 167–175, 2003.
- [6] N. Engheta and R. W. Ziolkowski, *Metamaterials: physics and engineering explorations*. John Wiley & Sons, 2006.
- [7] R. Marqués, F. Martín, and M. Sorolla, *Metamaterials with negative parameter: theory, design, and microwave applications*. John Wiley & Sons, 2008.
- [8] V. G. Veselago, “The electrodynamics of substances with simultaneously negative values of  $\epsilon$  and  $\mu$ ,” *Physics-Uspeski*, vol. 10, no. 4, pp. 509–514, 1968.

- 
- [9] W. Cai, D. A. Genov, and V. M. Shalaev, “Superlens based on metal-dielectric composites,” *Physical Review B*, vol. 72, p. 193101, Nov 2005.
- [10] J. B. Pendry, D. Schurig, and D. R. Smith, “Controlling electromagnetic fields,” *science*, vol. 312, no. 5781, pp. 1780–1782, 2006.
- [11] N. Landy, S. Sajuyigbe, J. Mock, D. Smith, and W. Padilla, “Perfect metamaterial absorber,” *Physical Review Letters*, vol. 100, no. 20, p. 207402, 2008.
- [12] D. Torrent and J. Sánchez-Dehesa, “Acoustic resonances in two-dimensional radial sonic crystal shells,” *New Journal of Physics*, vol. 12, no. 7, p. 073034, 2010.
- [13] N. Horiuchi, Y. Segawa, T. Nozokido, K. Mizuno, and H. Miyazaki, “High-transmission waveguide with a small radius of curvature at a bend fabricated by use of a circular photonic crystal,” *Optics Letters*, vol. 30, no. 9, pp. 973–975, 2005.
- [14] P.-T. Lee, T.-W. Lu, J.-H. Fan, and F.-M. Tsai, “High quality factor microcavity lasers realized by circular photonic crystal with isotropic photonic band gap effect,” *Applied Physics Letters*, vol. 90, no. 15, p. 151125, 2007.
- [15] A. Díaz-Rubio, J. Carbonell, D. Torrent, and J. Sánchez-Dehesa, “Low- $q$  whispering gallery modes in anisotropic metamaterial shells,” *Physical Review B*, vol. 88, no. 11, p. 115118, 2013.
- [16] D. Torrent and J. Sánchez-Dehesa, “Acoustic cloaking in two dimensions: a feasible approach,” *New Journal of Physics*, vol. 10, no. 6, p. 063015, 2008.
- [17] O. M. Ramahi, T. S. AlMoneef, M. AlShareef, and M. S. Boybay, “Metamaterial particles for electromagnetic energy harvesting,” *Applied Physics Letters*, vol. 101, no. 17, 2012.
- [18] A. M. Hawkes, A. R. Katko, and S. A. Cummer, “A microwave metamaterial with integrated power harvesting functionality,” *Applied Physics Letters*, vol. 103, no. 16, 2013.

- [19] Y. Yao, J. Yao, V. K. Narasimhan, Z. Ruan, C. Xie, S. Fan, and Y. Cui, “Broadband light management using low-q whispering gallery modes in spherical nanoshells,” *Nature Communications*, vol. 3, p. 664, 2012.
- [20] C. Navau, J. Prat-Camps, and A. Sanchez, “Magnetic energy harvesting and concentration at a distance by transformation optics,” *Physical Review Letters*, vol. 109, no. 26, p. 263903, 2012.
- [21] N. Tesla, “System for transmission of electrical energy,” *US Pat*, vol. 000645576, 1900.
- [22] A. Volokitin and B. N. Persson, “Near-field radiative heat transfer and noncontact friction,” *Reviews of Modern Physics*, vol. 79, no. 4, p. 1291, 2007.
- [23] A. Noda and H. Shinoda, “Selective wireless power transmission through high-flat waveguide-ring resonator on 2-d waveguide sheet,” *Microwave Theory and Techniques, IEEE Transactions on*, vol. 59, no. 8, pp. 2158–2167, 2011.
- [24] R. E. Hamam, A. Karalis, J. Joannopoulos, and M. Soljačić, “Efficient weakly-radiative wireless energy transfer: An eit-like approach,” *Annals of Physics*, vol. 324, no. 8, pp. 1783–1795, 2009.
- [25] Z. N. Low, R. A. Chinga, R. Tseng, and J. Lin, “Design and test of a high-power high-efficiency loosely coupled planar wireless power transfer system,” *Industrial Electronics, IEEE Transactions on*, vol. 56, no. 5, pp. 1801–1812, 2009.
- [26] A. Karalis, J. D. Joannopoulos, and M. Soljačić, “Efficient wireless; i; non-radiative mid-range; i; energy transfer,” *Annals of Physics*, vol. 323, no. 1, pp. 34–48, 2008.
- [27] Y. Chow, L.-M. Li, Z.-Q. Zhang, and C. Chan, “Resonant energy transfer between two defects in a photonic-band-gap system,” *Physical Review B*, vol. 60, no. 11, p. 8050, 1999.
- [28] H. A. Haus, *Waves and fields in optoelectronics*, vol. 464. Prentice-Hall Englewood Cliffs, NJ, 1984.



- [29] A. Karalis, R. Hamam, J. Joannopoulos, and M. Soljacic, “Wireless energy transfer, including interference enhancement,” 2009. US Patent App. 12/466,065.
- [30] J. Carbonell, A. Díaz-Rubio, D. Torrent, F. Cervera, M. Kirleis, A. Piqué, and J. Sánchez-Dehesa, “Radial photonic crystal for detection of frequency and position of radiation sources,” *Scientific Reports*, vol. 2, 2012.
- [31] H. Tao, N. I. Landy, C. M. Bingham, X. Zhang, R. D. Averitt, and W. J. Padilla, “A metamaterial absorber for the terahertz regime: Design, fabrication and characterization,” *Optics express*, vol. 16, no. 10, pp. 7181–7188, 2008.
- [32] Y. Cheng, Y. Nie, and R. Gong, “A polarization-insensitive and omnidirectional broadband terahertz metamaterial absorber based on coplanar multi-squares films,” *Optics & Laser Technology*, vol. 48, pp. 415–421, 2013.
- [33] A. P. Hibbins, J. R. Sambles, C. R. Lawrence, and J. R. Brown, “Squeezing millimeter waves into microns,” *Physical review letters*, vol. 92, no. 14, p. 143904, 2004.
- [34] J. S. White, G. Veronis, Z. Yu, E. S. Barnard, A. Chandran, S. Fan, and M. L. Brongersma, “Extraordinary optical absorption through sub-wavelength slits,” *Optics letters*, vol. 34, no. 5, pp. 686–688, 2009.
- [35] E. Stone and E. Hendry, “Dispersion of spoof surface plasmons in open-ended metallic hole arrays,” *Physical Review B*, vol. 84, no. 3, p. 035418, 2011.
- [36] E. Lansey, I. R. Hooper, J. N. Gollub, A. P. Hibbins, and D. T. Crouse, “Light localization, photon sorting, and enhanced absorption in sub-wavelength cavity arrays,” *Optics express*, vol. 20, no. 22, pp. 24226–24236, 2012.
- [37] H. Xiong, J.-S. Hong, C.-M. Luo, and L.-L. Zhong, “An ultrathin and broadband metamaterial absorber using multi-layer structures,” *Journal of Applied Physics*, vol. 114, no. 6, p. 064109, 2013.

- [38] Y. Avitzour, Y. A. Urzhumov, and G. Shvets, “Wide-angle infrared absorber based on a negative-index plasmonic metamaterial,” *Physical Review B*, vol. 79, no. 4, p. 045131, 2009.
- [39] Y. Cui, K. H. Fung, J. Xu, H. Ma, Y. Jin, S. He, and N. X. Fang, “Ultrabroadband light absorption by a sawtooth anisotropic metamaterial slab,” *Nano letters*, vol. 12, no. 3, pp. 1443–1447, 2012.
- [40] F. Ding, Y. Cui, X. Ge, Y. Jin, and S. He, “Ultra-broadband microwave metamaterial absorber,” *Applied Physics Letters*, vol. 100, no. 10, p. 103506, 2012.
- [41] J. Hao, É. Lheurette, L. Burgnies, É. Okada, and D. Lippens, “Bandwidth enhancement in disordered metamaterial absorbers,” *Applied Physics Letters*, vol. 105, no. 8, p. 081102, 2014.
- [42] F. Baida and D. Van Labeke, “Three-dimensional structures for enhanced transmission through a metallic film: annular aperture arrays,” *Physical Review B*, vol. 67, no. 15, p. 155314, 2003.
- [43] M. J. Lockyear, A. P. Hibbins, J. R. Sambles, and C. R. Lawrence, “Microwave transmission through a single subwavelength annular aperture in a metal plate,” *Physical review letters*, vol. 94, no. 19, p. 193902, 2005.
- [44] V. Lomakin, S. Li, and E. Michielssen, “Transmission through and wave guidance on metal plates perforated by periodic arrays of through-holes of subwavelength coaxial cross-section,” *Microwave and Optical Technology Letters*, vol. 49, no. 7, pp. 1554–1558, 2007.
- [45] A. Roberts, “Beam transmission through hole arrays,” *Optics express*, vol. 18, no. 3, pp. 2528–2533, 2010.
- [46] F. Baida, A. Belkhir, O. Arar, E. Barakat, J. Dahdah, C. Chemrouk, D. Van Labeke, C. Diebold, N. Perry, and M.-P. Bernal, “Enhanced optical transmission by light coaxing: Mechanism of the tem-mode excitation,” *Micron*, vol. 41, no. 7, pp. 742–745, 2010.
- [47] D. M. Pozar, *Microwave engineering*. John Wiley & Sons, 2009.

- [48] D. Smith, D. Vier, T. Koschny, and C. Soukoulis, “Electromagnetic parameter retrieval from inhomogeneous metamaterials,” *Physical Review E*, vol. 71, no. 3, p. 036617, 2005.